

The University of Nottingham

UNITED KINGDOM • CHINA • MALAYSIA

Refining Pore Size, Functionality and Stability in Porous Hybrid Frameworks

Adam Nevin

Thesis submitted to the University of Nottingham for the degree of

Doctor of Philosophy

September 2016

Declaration

Except where specific reference has been made to another source, the work presented in this thesis is the original work of the author, and has not been submitted, in whole or in part, for any other degree.

Signed: Adam Nevin

Dated:

Acknowledgements

I would firstly like to thank my supervisor, Professor Martin Schröder, for providing me with the right guidance, support and provisions for carrying out research into the interesting field of Metal-Organic Frameworks. Thanks also goes to Dr. Tim Easun, who played an instrumental part in aiding research and refining ideas, along with providing encouragement to see them through. I would also like to thank my second supervisor, Professor Neil Champness for all his support.

Further thanks and gratitude go to my colleagues and collaborators during my PhD study. In particular, Professor Sandy Blake and Dr. William Lewis who have supported me with countless hours of crystallography expertise, and Dr. Matt Lennox for his support and GCMC simulations.

I would also like to use this as an opportunity to thank those scientific colleagues who inspired me through discussions, and imparted their knowledge and wisdom in all areas from synthetic skills to technical help with instrumentation. Top of this list is Dr. Florian Moreau, whose patience and guidance throughout all years of my study have been helpful beyond words. Colleagues within the group who have played a key part in getting here include Dr. Sihai Yang, Dr. William Trenholme, Dr. Martyn Brown, Chris Morris and Jenny Eyley.

I would like to gratefully acknowledge financial support from EPSRC and the University of Nottingham.

My time in Nottingham (and brief stint in Manchester) has been thoroughly enjoyable, and this is largely thanks to the brilliant members of the group, past and present: Adam, Ben, Bo, Chris, Gemma, Harry, Jack, Jian, Lydia, Maggie,

Mat, Nick, Pete, Simona, Thien, and everyone else. Without these people, the years would not have been the same.

Finally, for the limitless love and support that have seen me through to this point, perhaps the greatest thanks of all goes to Rachel, who has been amazing throughout everything, and to my family (and future family!). Thank you.

Abstract

This thesis describes the utilisation of a new, facile route for rapid ligand synthesis for the design, synthesis and characterisation of metal-organic frameworks (MOFs), and the subsequent refinement of ligand synthesis to discover a 2-step green alternative synthetic route to an analogous ligand for use in the same. From these ligands, two series of MOFs are detailed; a Cu(II) series with simulated isotherms showing promising CH_4 and CO_2 high pressure uptake, and two Zr(IV) MOFs with enhanced stability and their measured high pressure isotherms.

Chapter 1 introduces the need for highly functional materials to answer the needs of current energy production crises; with the production of CO_2 from fossil fuels predicted to continue dangerously damaging the environment for decades to come, while the fossil fuel energy sources themselves run out, alternatives are clearly needed to continue powering society. MOFs are introduced as potential materials which can fulfil both of these needs.

Chapter 2 describes the synthesis of the H_4L^X series, which utilise the Suzuki-Miyaura cross-coupling reaction to generate a large quantity of a versatile ligand pre-cursor (3,5-di(p-carbethoxy)benzene boronic acid), which is then used to generate a large number of ligands via a further Suzuki-Miyaura cross-coupling reaction with a dihalogenated core. A green synthetic route to an analogous ligand to the first in the series (H_4L^{1P}, which differs from H_4L^1 by the replacement of two phenyl rings with pyridyls) is then described, which reduces the synthetic steps by 66% (2 steps instead of 6), and the cost by 95% (£0.51/g instead of £11.68/g).

Chapter 3 describes the design, synthesis, and characterisation of a series of Cu(II) metal-organic frameworks (MFM-191 to 198), and their respective simulated isotherms, which enable rapid identification of promising frameworks for materials which theoretically approach and even exceed the American Department of Energy's (DoE's) target value for CH_4 working capacity, and also potentially provide an alternative to current proposals for CO_2 storage and shipping. The discussion on these frameworks is split into two studies: Exploration of the effects of interpenetration and classes thereof on low and high pressure gas sorption (MFM-191,192 and 193), and analysis of attempts to fine tune the high pressure uptake of a series of non-interpenetrated isoreticular structures *via* extension and functionalisation of the central core of the ligand (MFM-193 to 198).

The first group of frameworks demonstrates how interpenetration aids low pressure uptake, but hinders maximum high pressure uptake. MFM-191 (which exhibits 2-fold interpenetration, class IIa) displays an uptake of CH_4 of 1.97 wt% at 1 bar and 21.40 wt% and 80 bar, 298 K and an uptake of CO_2 of 2.88 mmol/g at 1 bar, and 16.69 mmol/g at 30 bar, 298 K; while MFM-193 (a non-interpenetrated MOF with the same topology) demonstrates a greater difference between uptakes, with uptakes for CH_4 of 0.85 wt% at 1 bar and 47.06 wt% for 80 bar, 298 K, and uptakes for CO_2 of 0.65 mmol/g at 1 bar and 40.82 mmol/g at 30 bar, 298 K. This larger difference is due to the decreased host-guest interactions at low loadings, and works in favour of a better working capacity for CH_4 for the non-interpenetrated framework. Alteration of the class of interpenetration (from class IIa to class Ia) results in overall uptake behaviour which lies between the two, displaying an uptake for MFM-192 of

CH_4 of 2.11 at 1 bar, and 31.36 wt% at 80 bar, 298 K and an uptake of 2.89 2.89 mmol/g at 1 bar and 24.07 mmol/g at 30 bar for CO_2 at 298 K.

The non-interpenetrated series of MOFs (MFM-193 to 198), shows how upon functionalisation of the central core of ligand H_4L^1, the gas sorption properties are increases in accordance to the aromaticity of the ligand, with an increase in maximum volumetric uptake (at 80 bar, 298 K) of CH_4 from 233.29 to 251.89 cm^3/cm^3 from MFM-193 (with H_4L^1, a ligand with a phenyl ring as the central core) to MFM-195 (synthesised from H_4L^{AN}, a ligand with an anthracene moiety as its central core). Surprisingly, the amine-functionalised MOF (MFM-196) displays the lowest uptake of both CH_4 and CO_2 at high pressure compared to the other functionalised MOFs (MFM-194 and MFM-195) Extension of the ligand core from one phenyl ring to biphenyl and pyrene based ligands affords MFM-197 and MFM-198, which in turn display the highest theoretical gravimetric CH_4 working capacities 5-80 bar (48.51 wt% and 44.15 wt% at 298 K, respectively). Furthermore, working capacities calculated from the 273 K simulated isotherms for MFM-198 (the pyrene functionalised framework) show that this MOF is capable of exceeding the DoE target for gravimetric working capacity of 50 wt% (and nearing the volumetric target of 264 $cm^3\ cm^{-3}$), by delivering 52.3 wt% and 256.9 $cm^3\ cm^{-3}$ between 5-80 bar. However, upon attempts to activate these Cu(II) frameworks, none were stable enough to obtain a permanent porosity, even from 'soft' activation methods such as supercritical CO_2; therefore, new frameworks were sought which would be designed to have enhanced stability.

Chapter 4 describes the synthesis of two Zr(IV) MOFs, synthesised from H_4L^1 and H_4L^{1P} (MFM-421 and MFM-422) designed to display enhanced stability

over the Cu(II) MOF series, and allow acquisition of experimentally gathered high pressure data. This is particularly interesting for the MOF synthesised from H_4L^{1P}, as the green, cost-effective synthesis conditions of the ligand are potentially valuable for industrial applications. Both MOFs display an increase in stability over the Cu(II) series, with a measureable BET of 3,300 m^2/g for MFM-421 and 2,500 m^2/g for MFM-422. The high pressure CH_4 and CO_2 capacities of both frameworks were measured, and, while they were lower than the simulated Cu(II) series, they were highly competitive compared to published MOFs. MFM-421 is shown to have the fourth highest CH_4 gravimetric working capacity at 298 K (compared to a list of the highest experimentally recorded MOFs for methane working capacity), and MFM-422 the sixth, measuring values of 25.7 wt% and 22.8 wt%, compared to the three highest of 31.0 wt%, 35.0 wt% and 42.3 wt% for MOF-177, MOF-205 and Al-soc-MOF-1, respectively. Importantly, compared to HKUST-1 (the only framework amongst this list that is cheaper than H_4L^{1P} to buy/synthesise), both of these frameworks exhibit higher gravimetric working capacities (which for HKUST-1 is 16.3 wt% at 298 K). The analysis of CO_2 high pressure isotherms for potential in storage and shipping shows that these MOFs exhibit an increase in storage capacity at 298 K, 30 bar over capacity of a tank at the same conditions of over 500% for MFM-421 (7,708 mol/m^3 compared to 1,458 mol/m^3) and over 650% for MFM-422 (9,605 mol/m^3). While the highest of these values still stands at only 43% of the value of a tank at 26.5 bar and 263 K, the ability to store this much CO_2 at ambient temperatures allows more flexibility in route and less energy intensive storage conditions.

Chapter 5 summarises the CH_4 and CO_2 storage properties of these structures and draws overall conclusions from the work.

Table of Contents

Chapter 1 .....
1.1 Current Challenges in the Energy Sector 1
1.1.1 The Need for Highly Functional Materials 1
1.1.2 The Role of CH_4 as an Alternative Fuel 2
1.1.3 The Growing Concern of CO_2 Emissions 4
1.2 High Pressure Storage 5
1.2.1 High Pressure Storage - Current Technology CH_4 6
1.2.2 High Pressure Storage – Current Technology CO_2 7
1.2.3 Highly Functional Porous Materials 8
1.3 Metal-Organic Frameworks 10
1.3.1 An Overview of Metal-Organic Frameworks 10
1.3.2 Design of Metal-Organic Frameworks 13
1.3.1 MOFs for High Pressure Storage – CH_4 15
1.3.2 MOFs for High Pressure Storage – CO_2 16
1.4 The scope of this thesis 19
Chapter 2 .....
2.1 Introduction 25
2.1.1 Organic linkers as key area of research in MOFs 25
2.1.2 Importance of design of ligand for MOFs 28
2.1.3 Cost implications of ligand synthesis 30
2.1.4 Aims and Objectives 32
2.2 Results and Discussion 33
2.2.1 Synthesis of ligand series H_4L^X 34
2.2.2 Cost of current methods and development of sustainable linker preparation 37
2.2.3 Comparison to Literature Synthetic Routes 45
2.3 Conclusion 47
2.4 Experimental 49
Chapter 3 .....
3.1 Introduction 68
3.1.1 A Brief Overview of Interpenetration 68
3.1.2 Classes of Interpenetration 70
3.1.3 Methods of Preventing Interpenetration 74
3.1.4 Aims and Objectives 80
3.2 Results and Discussion 81

3.2.1 Crystal Structure Description of MFM-191 81
3.2.2 Crystal Structure Description of MFM-192. 89
3.2.3 Crystal Structure Description of MFM-193 97
3.2.4 Comparison of Interpenetrated Frameworks 101
3.2.5 Simulated Isotherms for MFM-191, MFM-192 and MFM-193 103
3.2.6 Formation of Isoreticular Series Based Upon MFM-193 113
3.2.7 Description of MFM-19X Series 114
3.2.8 Simulated Isotherms for Isoreticular Copper Series 128
3.2.9 Applications – CO_2 Shipping 137
3.2.10 Applications – CH_4 Storage for Vehicular Transport 138
3.2.11 Isolation and Purification of Phase Pure Compounds 142
3.2.12 Activation of MFM-19X Series 146
3.3 Conclusion 154
3.4 Experimental 157
3.4.1 Solvothermal Syntheses of MFM-19X Series 157
3.4.2 Single Crystal Structure Determination for MFM-19X Series 160
3.4.3 Crystal Data for MFM-19X Series 161
3.4.4 Simulation Details for MFM-19X Series 164
3.4.5 Simulated N_2 Isotherms for MFM-19X Series 166
3.4.6 BET Plots and Rouquerol Plots for MFM-19X Series 166
3.4.7 Gas Adsorption Measurements on MFM-19X Series 170
3.4.8 Experimental BET Plots 170
Chapter 4 .....
4.1 Introduction 178
4.1.1 Selection of Secondary Building Units for Stability Enhancement in MOFs 178
4.1.2 Utilising Highly Connected Secondary Building Units to Stabilise MOFs 180
4.1.3 Interesting Features of Zr(IV) Structures in Literature 181
4.1.4 Aims and Objectives 183
4.2 Results and Discussion 183
4.2.1 Crystal Structure Description of MFM-421 184
4.2.2 Gas Sorption Measurements of MFM-421 191
4.2.3 MFM-422 201
4.2.4 Gas Sorption Measurements of MFM-422 207

4.2.5 Applications – CO_2 Shipping.....214
4.2.6 Applications – CH_4 Storage for Vehicular Transport.....216
4.3 Conclusion.....221
4.4 Experimental.....224
4.4.1 Preparation of MFM-42X.....224
4.4.2 Crystal Structure Descriptions of MFM-42X.....225
4.4.3 Gas Adsorption Measurements on MFM-19X Series.....225
4.4.4 BET Surface Plots.....226
Chapter 5.....
5.1 Conclusion.....231
Appendices.....235

CHAPTER 1

Introduction

1.1 Current Challenges in the Energy Sector

1.1.1 The Need for Highly Functional Materials

Over the past few decades, the necessity to find an alternate energy structure has become more and more pressing.[1] Particularly, the need for alternative fuels from those harnessed from coal and oil, the so called 'fossil fuels', has been increasingly capturing the attention of political figures and the media. The need is becoming ever pressing within the transport sector, as the expectation of travelling thousands of miles a year becomes commonplace, with the total distance travelled by people within Great Britain alone rising over 95% between 1972 and 2014 (Figure 1).[2]

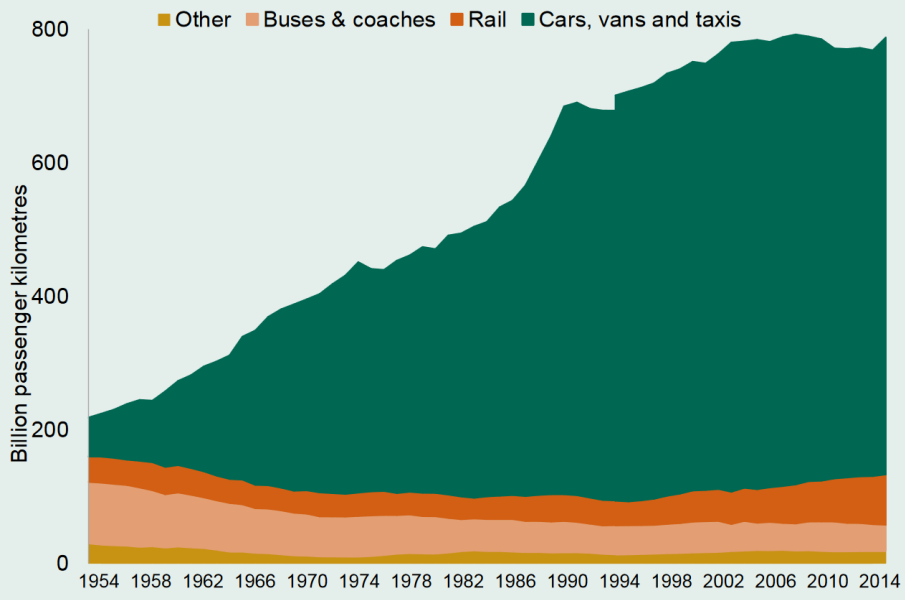


Figure 1. Passenger kilometres by mode 1954-2014.[2]

Furthermore, beyond solely the sourcing of the fuel, the annual production of over 35 gigatonnes of CO_2 from burning fossil fuels (data from 2014 global carbon budget)[3] has been identified as a major crisis area.[4] As such, the 2015 Paris Climate Conference agreement to limit emissions[5] and keep global warming below 2 °C was a monumental moment for environmental scientists.

Therefore, materials which are highly functional, and possess the ability to be finely tuned to suit a variety of purposes, such as fuel storage or CO_2 capture, transport and storage, are valuable research targets.[6]

Since the scale of the problem was first realised, a number of suggestions for alternative fuel have arisen, with a couple of the ideas standing prominent above the rest in terms of feasibility and ease of adaptability; these are given below.

- The synthesis of petroleum, from biomass[7] and *via* the Fischer-Tropsch method[8]
- The use of compressed natural gas, or methane, as combustible fuel[9]
- The use of hydrogen fuel cells to generate electricity[10]
- The use of electric cars which can be recharged by any form of industrial generator (coal, nuclear, wind, solar etc.)[11]

All of the suggestions have both their advantages and their disadvantages, and to date no individual idea has succeeded in excluding the need for research into others.

1.1.2 The Role of CH_4 as an Alternative Fuel

Of all the alternative fuels being researched at the moment, perhaps the most promising, in terms of both transfer of current technology over to the new system, and potential for sustainability is the use of compressed natural gas (CNG), or, more specifically, methane. Most modern engines can be easily modified to run on methane,[12] thus making the transfer one which can be easily adopted. Additionally, while methane is currently obtained mainly from fossil

fuels,[13] renewable sources can be found. Most landfills produce methane as a byproduct of decomposition, and many are starting to capture it and use it as a fuel.[14] The lifespan of this methane production from microbial breakdown of waste is shown below (Figure 2); it takes 20 years to reach phase IV where the gas is collectable for fuel (after separation from CO_2), and from there the production is steady for a further 30 years.[15]

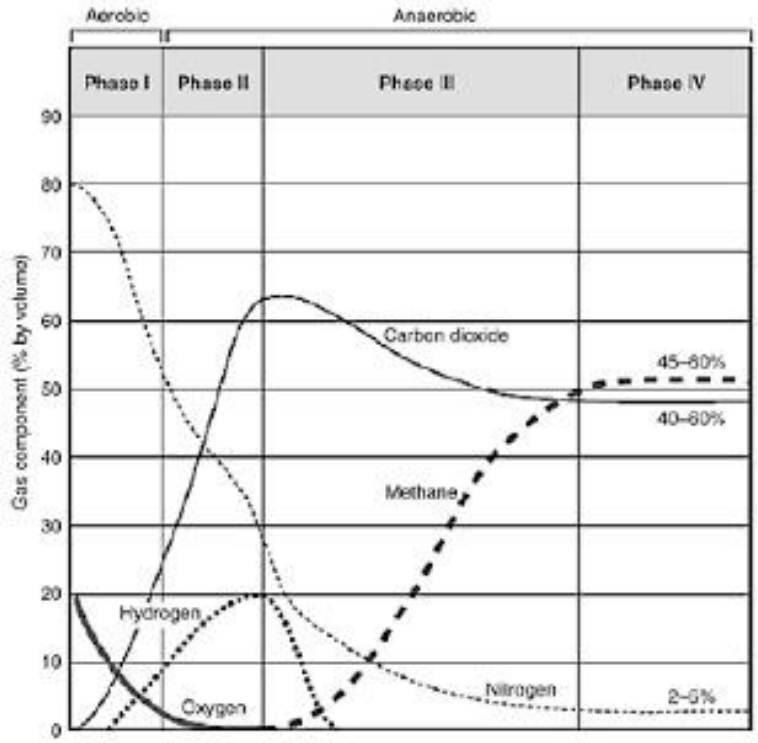


Figure 2. Lifecycle of decomposition by bacteria in landfills.[15]

For a more ideal scenario, these sources of natural gas can be phased out in favour of methane generated from CO_2 and H_2O, *via* electrolysis of water and subsequent Sabatier reaction between H_2 and CO_2.[16] Therefore the use of methane as an alternative fuel gives an immediate possibility for change (from landfill gas and current underground reservoirs), but also a long term sustainable solution.

1.1.3 The Growing Concern of CO_2 Emissions

Estimates predict that, even with stringent regulations and control, CO_2 emissions will continue to be a problem well into the coming century (Figure 3).[17] Three predictions are shown, all along the A1 storyline, which predicts a future of rapid economic growth and a global population that peaks mid-century and then begins to decline. This scenario also includes the rapid introduction of new, more efficient technologies, and a population more concerned with personal wealth than environmental change. The three predictions are A1T (technology based upon non-fossil fuel energy sources), A1FI (a fossil fuel intensive future) and A1B (a balanced situation); as shown, even the most optimistic scenario, where technology has moved largely away from fossil fuels (A1B) has CO_2 emissions which remain in the $GtCO_2$ region throughout the next hundred or so years. As such, it is imperative that methods of removing CO_2 from power station waste streams (flue gas) are researched, along with efficient transport and storage of the waste gas.

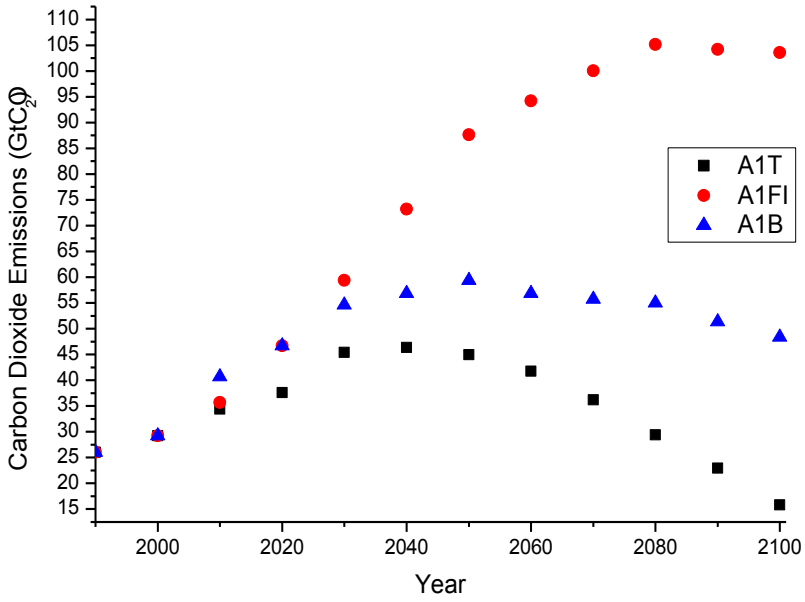


Figure 3. Total CO_2 emissions based on ISAM predictions until 2100 for fossil intensive (A1FI), alternative energies (A1T) and balanced (A1B) scenarios.[17]

1.2 High Pressure Storage

Materials capable of storing and delivering large amounts of gas are required for both CH_4 storage for fuelling vehicular transport, and CO_2 storage and transportation after it has been sequestered from the flue gas stream. The current industry standard for high pressure storage of gases is the use of steel-walled cylinders. While simple and effective, these methods of storage can be limited due to the pressure required for storing large volumes of gas (up to 300 bar), and highly dangerous in the event of rupture of the cylinder. This renders them unsatisfactory for a variety of situations where either a specifically large volume of gas needs to be transported, or where the danger of explosion is too great to consider safely implementing it on a global scale. Due to these reasons the current use of compressed natural gas in vehicles has significant drawbacks (liquefied natural gas is not considered here due to the additional implications

of cryogenics). A prime example of this technology is the Honda Civic GX (produced between 1998-2015), which was factory-built to run on CNG, and as such suffered from the associated drawbacks, with a tank pressurised to 250 bar and a range of under 200 miles (a factor considered by many to be the reason behind the slow adoption of CNG vehicles),[18] thus highlighting the need for improved storage of CH_4 in vehicles.



Figure 4. Refuelling a Honda Civic GX.[19]

1.2.1 High Pressure Storage - Current Technology CH_4

The use of methane as a fuel relies on a number of prerequisites for commercial viability, such as production and refinement of methane, storage for use in transport and other applications, and engines capable of efficient combustion of the fuel. These are all current topics of extensive research as the world searches for a new source of fuel to ease the burden on the dwindling oil supplies. This thesis, however, will focus solely on the storage aspect, specifically under the high pressures required for use in the transport industry.

Currently, the prototype vehicles equipped with methane storage tanks are almost exclusively utilising steel-walled cylinders filled with methane gas under high pressure (around 250 bar). However, as discussed above, this is not an ideal

situation when considering the size, weight and capacity of the tank. Therefore, to transition from a novel alternative fuel to widely adopted commercially viable vehicles, a method of storing large volumes of gas under safer, more practical conditions is required.

1.2.2 High Pressure Storage – Current Technology CO_2

Storage of CO_2, while seemingly simpler in concept, is also multi-faceted in its requirements as its sequestration is often from a mixture of gases, thus needing a degree of selectivity and refinement in the process. The storage of the sequestered CO_2 then falls often into two categories: short term and long term. A current leading global option of long term storage is geo-storage,[20] where the CO_2 is pumped into underground reservoirs to be kept at high temperatures and pressures, often in the recently emptied locations of crude oil.[21,22] Short term storage is herein described as that which could also fall under the term 'transport', as there is often a need to relocate the CO_2 to offshore sites in cases where the single-source single-sink scenario (where fuel is removed from a source, consumed, and the resultant CO_2 is pumped into the same site), is not applicable.[23] The transport of CO_2 from the source of production at the power plant to the final destination involves such large quantities that high-pressure cylinder storage is not a cost-effective solution, and therefore is currently done using pipelines which are able to effectively transport huge volumes with great speed across relatively large distances.[24] However, these pipelines are not suitable for situations where the CO_2 needs to be transported to offshore locations, or where the exact route is uncertain and likely to change, as is the case with many CO_2 geo-storage solutions.[23,25]

1.2.3 Highly Functional Porous Materials

One method of storing gas under milder conditions is adsorption in porous materials such as zeolites. These are naturally occurring porous aluminosilicate materials, typically with pore sizes between 2-8 Å, and a pore volume of 0.2-0.4 cm^3/g.[26] Typically, the framework is negatively charged, and thus positive counter-ions reside in the pores, reducing the pore volume, but providing an ideal situation for low pressure applications,[27] where the small pores increase interactions between the zeolite and the guest molecule at low loadings. Further enhancement of these interactions can be gained by cation exchange.[28]

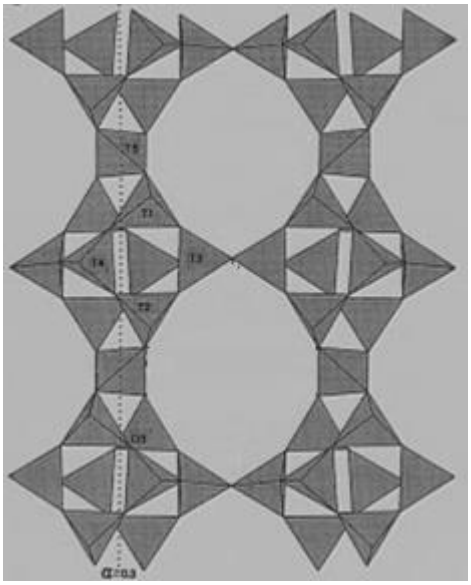


Figure 5. Stilbite, one of the first zeolites discovered.[29]

One of the major drawbacks of zeolites, however, is that they typically have poor high pressure uptake, as their low porosity limits the maximum uptake.[30,31]

A promising candidate for high pressure storage is the 'metal-organic framework' (MOF),[32] which has the possibility of possessing great porosity and stability,[33] potentially enabling a reproducible cycle of gas uptake and removal without damaging the framework.[34] Moreover, it can possess a high heat of gas

adsorption energy, Q_{ads}. This is a measure of how favourable the interactions between the gas molecules and the structure are; it has been suggested that for optimum methane storage and release from an adsorptive material, a heat of CH_4 adsorption of 15-20 kJ mol^{-1} is required.[35]

An additional property of metal-organic frameworks to consider is the Brunauer–Emmett–Teller (BET) surface area,[36] which is a measure of the surface area of a solid available for gas adsorption. Generally, the higher the BET surface area, the more gas can be theoretically stored inside it. This holds true at high pressures, as there is greater room to store the gas. However, this benefit is often off-set by a decrease in the ability of the gas to stay within the pores, as the orbital protrusion from the pore walls is small in comparison to the central void when the pore is larger; therefore the orbital overlap between ligand and gas is smaller, resulting in a less favourable interaction.[37] This is most relevant in low pressure applications, such as CO_2 scrubbing from flue gas. For high pressure applications, such as methane storage, this decrease in interaction between the gas molecule and the framework becomes relatively less important; indeed it can be argued that a decrease in uptake at low pressures can be beneficial to CH_4 storage, due a property often quoted, known as the 'working capacity'.[38] This is the difference in uptake between two pressures, and thus the quantity of gas capable of being released between the two. For CH_4 in vehicular transport, it is widely accepted that a minimum pressure of 5 bar is required to allow a pressure differential to drive fuel movement within the engine, and as such most working capacities for CH_4 storage for alternative fuel in transport are quoted between 5 and 80 bar. Therefore, a decrease in orbital overlap between framework and guest molecules, which is of great importance at low

pressure, can actually positively impact the working capacity, maximising the difference in uptake between the two pressures. This puts MOFs into a unique positions in comparison to zeolites, as MOF BET surface areas can range anywhere from 500-7,000 m^2/g (with a theoretical maximum of 14,600 m^2/g posturized by Hupp),[39] therefore allowing optimisation for pretty much any application, whereas zeolite BET surface areas are limited mostly up to 1,500 m^2/g, and are therefore more suited to low pressure applications.[40] As such, this thesis will focus on the unique ability for high pressure storage of MOFs.

Importantly, gas sorption in metal-organic frameworks is not limited to CH_4, many gases of interest can be stored inside them, such as CO_2,[41] N_2O,[42] propane,[43] acetylene[44] and hydrogen,[45] which can also be used to power transport.

1.3 Metal-Organic Frameworks

1.3.1 An Overview of Metal-Organic Frameworks

The term 'Metal-Organic Framework' was first coined by Omar Yaghi in 1995,[46] in a paper which built upon the history of co-ordination polymers (another type of metal-organic structure),[47] and extended the idea to create porous co-ordination polymers, with a new name 'MOFs'.[48]

MOFs are a class of crystalline, microporous materials[49] which consist of iono-covalently bound organic and inorganic fragments, propagated in an ordered, extended array. Within the generated framework, the metal centres form secondary building units (SBUs), often incorporating the organic ligands. These SBUs have multiple points of extension, which allow the generation of dimensionality within the framework. An example of an SBU is the copper paddlewheel, in which two copper atoms and four carboxylate groups form a

cluster which has 4 points of extension, and two open metal binding sites on the copper atoms, usually occupied by solvent molecules after synthesis (shown in Figure 6).[50]

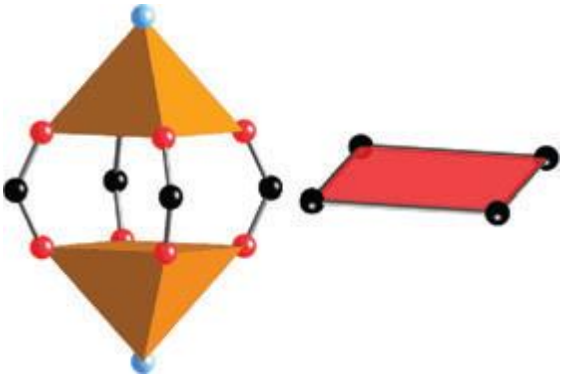


Figure 6. Square paddle-wheel: Cu, gold; C, black; O, red; N, blue.[44]

This method of construction provides an opportunity to form a porous, 3-dimensional structure in which the ligands act as 'walls' to pores or channels which run throughout the MOF crystal. The dimensions of the pores generated by the ligands are typically no larger than 20 angstroms for a microporous structure, but there are examples of mesoporous MOFs with larger pore sizes.[51]

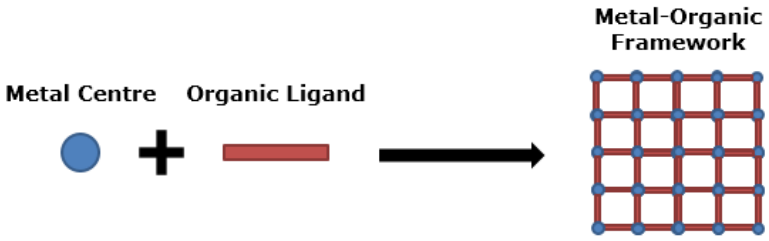


Figure 7. Schematic Diagram of MOF Synthesis.

It is possible, by altering the design of the ligand, to dramatically change one or many properties of the resultant MOF.[52] For example, the inclusion of nitrogen groups which are not involved in metal bonding can provide a strong

carbon dioxide interaction site on the ligand,[53] which increases the heat of adsorption of the CO_2 and displays a selectivity for preferential binding of carbon dioxide over other gases. [35,54]

There is also the possibility of altering the properties of a MOF by creating a series of 'isoreticular' frameworks. An isoreticular series of MOFs is one which retains the same topology (the general connectivity and arrangement of a single framework net), yet changes the nature of the ligand throughout the series (usually by the extension of the length).

A good example of this is the lengthening of a ligand from one framework to the next (as demonstrated in Figure 8, which shows an IR-MOF series).[55] This enlarges the pores according to the length of the ligand, providing a larger area for gas uptake.

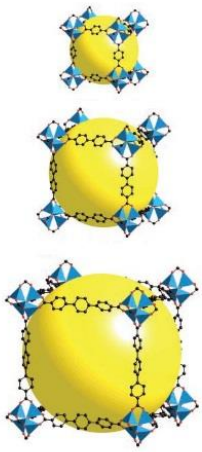


Figure 8. A series of isoreticular MOFs.[55]

Another way in which the nature of the MOF can be changed is by the control of open metal binding sites, which increase the heat of gas adsorption.[56] These can be included by careful consideration of the metal cluster used in the MOF, for example the paddlewheel cluster can be activated to give two binding sites

where solvent molecules initially reside (as shown in Figure 9). Open metal sites can also be introduced after synthesis (a process known as post-synthetic modification),[57] for example the binding of chromium tricarbonyl fragment to the pi-electron clouds of aromatic rings on the ligand.[58]

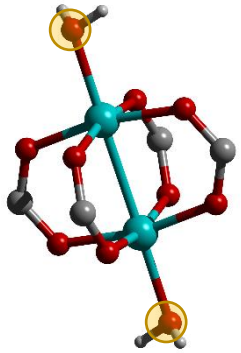


Figure 9. Copper paddlewheel with water-bound open metal sites highlighted.

1.3.2 Design of Metal-Organic Frameworks

To obtain a MOF, one must first synthesise a suitable ligand. This must be a molecule which can react with a metal precursor (usually a metal salt) to form a stable, inorganic secondary building unit (SBU). This requires a binding of the ligand to the metal - through a functional group such as a carboxylic acid – which is strong enough to produce a stable product, yet labile so that the structure can rearrange itself to remove defects.[59] Providing the ligand with multiple points of extension encourages crystallisation in more than 2 directions, to give a 3-dimensional structure.

Preferably, the ligand should have a rigid structure to allow for predictable crystallisation with a single phase. This rigidity is usually introduced by the incorporation of phenyl rings into the design, which has the additional benefit of providing large orbital overlap emanating from the aryl pi electron clouds.

An example of a typical ligand is shown in Figure 10, displaying the points of extension and incorporation of rigidity to provide a well characterised structure (NOTT-100).[60]

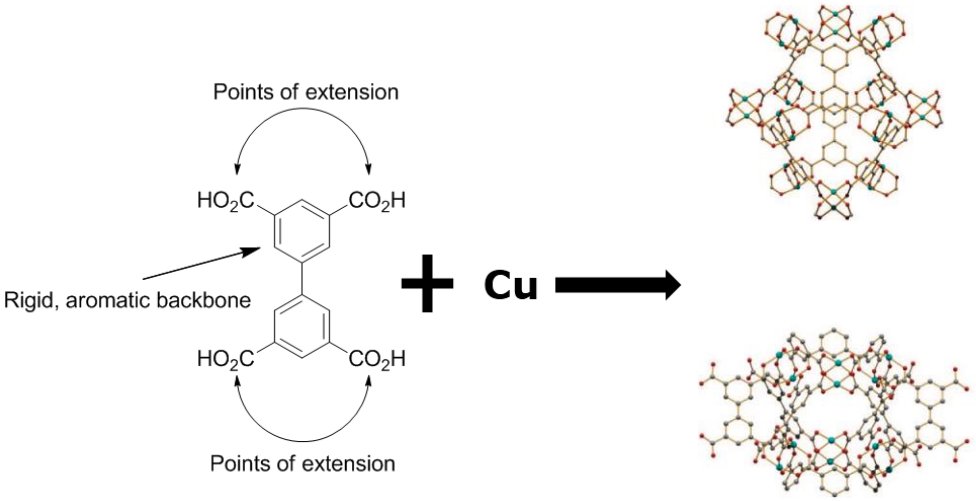


Figure 10. Example of ligand incorporation into metal-organic framework.

It is worth noting that the charges associated with the metal and the ligand must be taken into account when designing a MOF, as an imbalance can result in bulky counter-ions residing in the pores,[61] thus decreasing the pore volume.

The process of combining the ligand and the metal to get a metal-organic framework is a very capricious one, which requires different conditions for almost every MOF desired, resulting in a large amount of trial and error in the final step. This is not only time consuming, but also requires a large stock of ligand from which ~10 mg can be used each time a small scale MOF trial is performed, thus necessitating an optimisation of the ligand synthesis itself so that high quantities of ligand can be obtained in high yields for maximum efficiency.

1.3.1 MOFs for High Pressure Storage – CH_4

One of the most promising applications for metal-organic frameworks is the storage of methane at a medium-high pressure (60-80 bar) for use in methane powered vehicular transport. The current aim for porous materials, as set by the US Advanced Research Project Agency-Energy (ARPA-E), as part of their Methane Opportunities for Vehicular Energy (MOVE), is to deliver over 50 wt% and 350 cm^3/cm^3.[62] The pressures between which this is to be achieved are generally considered to be from 5 bar (as there needs to be a pressure differential between the tank and the engine to drive fuel) to 80 bar (as a tank that can hold this pressure is relatively easily and cheaply acquired compared to the current 250 bar cylinders). The temperature at which this should be achievable is typically stated as 298K, to avoid additional complications of cooling or liquefying the gas and allow for a long term storage solution. A number of materials have been tested for such a purpose, with the highest volumetric working capacity being 230 cm^3/cm^3 for MOF-519, and the highest gravimetric working capacity belonging to Al-soc-MOF-1, which reaches 42 wt%. However, as shown, none have yet managed to exceed the ARPA-E target capacity, which has been set at 25% over the energy density of CNG at 250 bar, in order to be a competitor for current technology (the extra 25% is to account for losses during pelletisation and packing when scaling up to commercial use). There has even been research into the limits of porous media, performed by computational researchers (Snurr, Smit et. al),[67] who screened thousands of MOFs computationally in a high-throughput method. Their research covered MOFs, ZIFs (zeolitic imidazolate frameworks), zeolites and PPNs (porous polymer networks), all current research targets by experimental chemists to test

if any exceeded the target set by ARPA-E. They found that while there were candidates which approached the target (and certainly far exceeded an empty tank), none were able to obtain the 350 cm^3/cm^3 working capacity of methane required. However, the method of computational screening was severely limited to pre-chosen topologies and linkers, and therefore offers only a very small glimpse into the real attainable values from synthesised frameworks, leaving much left to do for the synthetic chemist in generating ligands with rare or unknown topologies and highly functionalised ligands to generate exceptional interactions with guest molecules.

1.3.2 MOFs for High Pressure Storage – CO_2

An often overlooked application of metal-organic frameworks is the use in high pressure storage of CO_2 for use in shipping large quantities of it from a power station to an offshore site where it will be pumped underground into recently emptied oil reservoirs to be kept in place by the natural high pressure surroundings, namely those areas not covered by a 'single-sink-single-source' scenario. This is most necessary for countries in East Asia, where there are ocean-side storage sites which may be shared collaboratively by carbon-intensive countries in this region.[23] The presence of pipeline technology in Western Europe and North America which is the preferred method of CO_2 transport where it is available,[24] may contribute to the factors why MOFs are not extensively tested for this purpose; however with their affinity for gas molecules and potential for high pressure uptake, they may be a promising alternative to the current proposed methods. Figure 11 shows the path of CO_2 from source to a tanker ready to move it to long term storage locations.

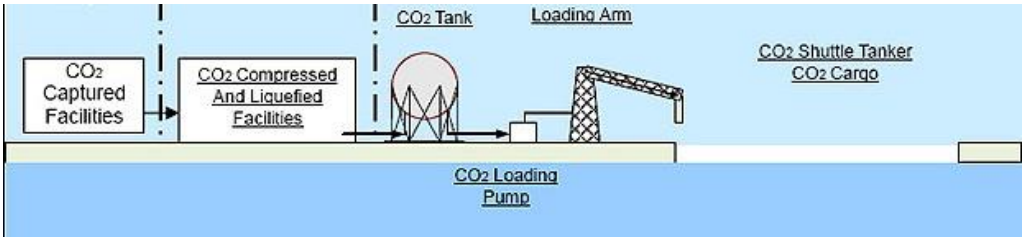


Figure 11. Outline of CO_2 shipping plans, where the right hand section of the diagram shows the storage and transport of gas to necessary locations.[63]

The current leading technology for this application is low temperature, high pressure cylinders of CO_2 on ships (Figure 12),[23] which require a moderate amount of energy to pump the CO_2 into initially, as the resting pressure is 26.5 bar, however further energy is required both in the cooling of the entire cylinder to -10 °C,[64] and subsequent warming of CO_2 at the deposit site (although this can be done by seawater in tropical locations for an ideal lower energy outcome).[65] It is proposed, therefore, that MOFs, as highly porous media often used in high pressure storage of methane, might be a suitable replacement to enable low energy cost, reusable shipping containers for movement of CO_2 to desired locations across the globe (as shown in Figure 13).

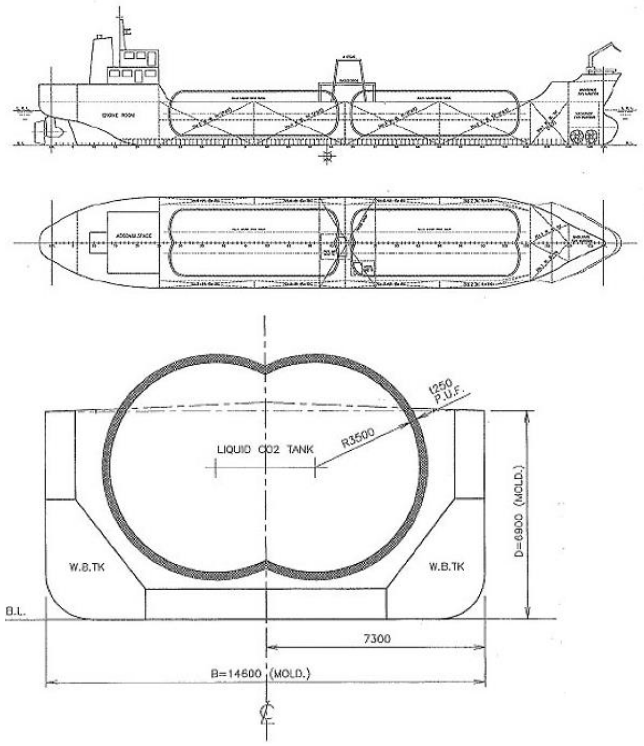


Figure 12. Current proposed storage of CO_2 as liquid for transport to offshore locations.[63]

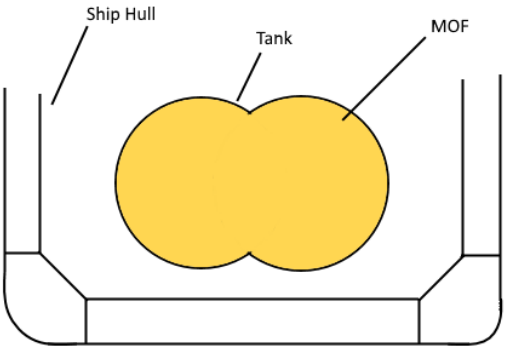


Figure 13. Representation of MOFs as storage medium for CO2 at ambient temperatures.

For a porous material to be of sufficient benefit in this application, it must be able to be put into mass production at low cost, to match the current steel cylinder technology, which is relatively cheap and readily accessible (however the cost of cooling does somewhat counter this, making a low cost MOF alternative appealing); it must also be capable of adsorbing, at room temperature and ~26.5 bar, a competitive quantity of CO_2 in comparison to that of the

cylinder at the same pressure and -10 °C (although MOF storage pressures up to 30 bar are comparable, as the liquid CO_2 tank must withstand expansion of the stored gas by gradual heating over the journey to the CO_2 sink, as the tank relies solely on insulation to keep at -10 °C). The quantity of CO_2 capable of being stored under these conditions is 983.78 kg/m^3 (22,354 mol/m^3), which allows the transport of a total of 3,000 tonnes of CO_2 per ship. There has also been investigation into transport at 7 bar and -50 °C, which would allow the transport of 1155.2 kg/m^3.[66] Without the need for liquefaction or heating of CO_2 at the other side, this proposed route could save over 72 GJ each time a cylinder is filled, totalling a saving of 2 million USD per ship per year.[66]

1.4 The scope of this thesis

This thesis explores the versatile synthesis of a new series of ligands, the H_4L^X series, which are suitable for use in reticular MOF chemistry, and as such allow detailed study into the high pressure uptake capacity of both CO_2 and CH_4 within these frameworks. Chapter 2 describes these linkers, their synthesis, and the implications of a route which enables functionalisation and extension at little to no extra synthetic effort or cost. A green, efficient route to an analogue of the most ubiquitous ligand is also shown. The isoreticular Cu(II) MOF series, MFM-19X, generated from the H_4L^X ligands (shown below in Figure 14) is discussed in Chapter 3, along with their simulated isotherms, potential applications, and ultimate instability and consequential reduced permanent porosity.

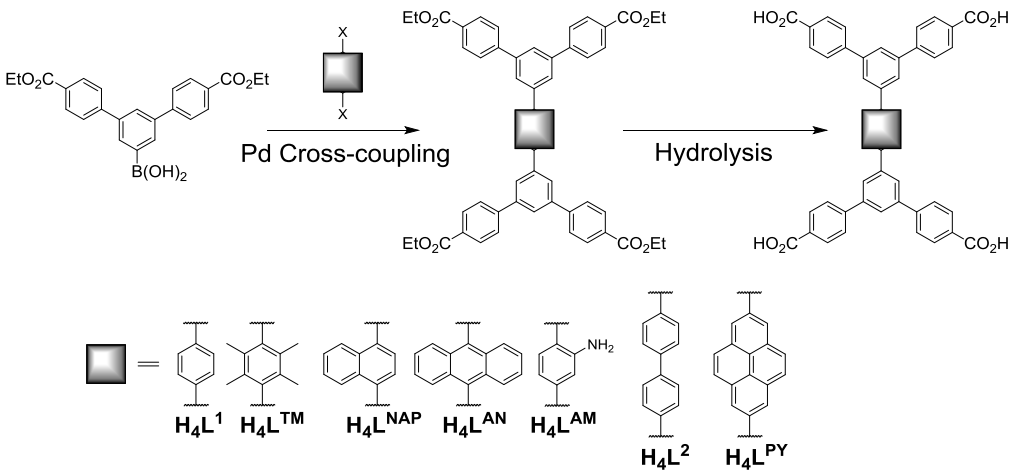


Figure 14. Simplified building block scheme for ligand series H_4L^X.

Chapter 4, the final results and discussion Chapter, remedies some of the problems seen in the Cu(II) MFM-19X series, by describing the synthesis and gas sorption properties of two highly stable Zr(IV) MOFs, MFM-411 and MFM-412, culminating in a comparison of the gas sorption properties of these stable MOFs against the idealised theoretical isotherms of the unstable MFM-19X series.

References

1. De Jong, S. *Rev. Int. Polit. développement*, **2011**, *2*, 21-43.
2. DFT. *Dep. Transp.* **2015**, 1–25.
3. Le Quéré, C. *et al., Earth Syst. Sci. Data,* **2015**, *7*, 349–396.
4. Delbeke, J. & Vis, P. *EU climate policy explained*.
5. Lykketoft, M. Adoption of the Paris Agreement.
6. Kilner, J. A. *Functional materials for sustainable energy applications*. (Woodhead Pub, 2012).
7. Braden, D. J., Henao, C. a, Heltzel, J., Maravelias, C. C. & Dumesic, J. a. *Green Chem.* **2011**, *13*, 1755.
8. Craxford, S. R. The Fischer-Tropsch synthesis of hydro-carbons, and some related reactions. **1939**, 946–958.
9. Malenshek, M. & Olsen, D. B. *Fuel,* **2009**, *88*, 650–656.
10. Bashyam, R. & Zelenay, P. *Nature* **2006,** *443*, 63–6.
11. Wong, K.-F. V. & Perilla, N. *IMECE2009,* **2010,** *6*, 447–458.
12. Uchechukwu Okeke, E. & Thaddeus Lebele-Alawa, B. *Int. J. Eng.*

Technol. Innov. **2013,** *3*, 86–94.

13. *Natural Gas Information 2016*. (2016).
14. Pilarczyk, E., Henning, K.-D. & Knoblauch, K., **1987**, *14*, 283–294.
15. Speight, J. G. *Synthetic fuels handbook : properties, process, and performance*. (McGraw-Hill, **2008**).
16. Sterner, M. *Transformation*, **2009,** 14.
17. Houghton JT *et al.*, *Clim. Chang.*, **2001,** 881.
18. Wegrzyn, J. & Gurevich, M. *Appl. Energy* **1996**, *55*, 71–83.
19. IFCAR. **2009**
20. Bennaceur, K. *et al.*, *Oilf. Rev.* **2004**, 44–61.
21. Liang, Z., Shu, W., Li, Z., Shaoran, R. & Qing, G. *Pet. Explor. Dev.*, **2009**, *36*, 737–742.
22. Yang, W., Peng, B., Wu, M., Li, J. & Ni, P. *Energy Procedia*, **2016**, *86*, 41–46.
23. Chiyoda Corporation et al. *Preliminary feasibility study on CO_2 carrier for ship-based CCS*. (**2011**).
24. Noothout, P., Wiersma, F., Hurtado, O., Roelofsen, P. & Macdonald, D. *Glob. CCS Inst.*, **2014**.
25. Hedley, B. J., Davies, R. J., Mathias, S. A., Hanstock, D. & Gluyas, J. G. *Greenh. Gases Sci. Technol.*, **2013**, *3*, 212–230.
26. Acton, Q. A. *Aluminum Silicates—Advances in Research and Application: 2013 Edition*. (**2013**).
27. Cheung, O. & Hedin, N., *RSC Adv.* **2014**, *4***,** 14480.
28. Zhang, J., Singh, R. & Webley, P. A., *Microporous Mesoporous Mater.* **2008,** *111*, 478–487.
29. Ferrara, I., Milano, I. & Modena, I. **1997**, *82*, 729–739.
30. Feng, C., Khulbe, K. C., Matsuura, T., Farnood, R. & Ismail, F. *J. Membr. Sci. Res.* **2015**, *1*, 49–72.
31. Zhang, S. Y., Talu, O. & Hayhurst, D. T. *J. Phys. Chem.* **1991**, *95*, 1722–1726.
32. Suh, M. P., Park, H. J., Prasad, T. K. & Lim, D.-W., *Chem. Rev.* **2012**, *112*, 782–835.
33. Dybtsev, D. N., Chun, H., Yoon, S. H., Kim, D. & Kim, K., *J. Am. Chem. Soc.* **2004**, *126*, 32–3.
34. Janiak, C. *Dalt. Trans.*, **2003,** 2781.
35. Bhatia, S. K. & Myers, A. L. *Langmuir* **2006**, *22*, 1688–700.
36. Emmett, P. H. **1936**, 407.
37. Chen, B. *et al.*, *J. Am. Chem. Soc.*, **2008,** *130*, 6411–23.
38. Gándara, F., Furukawa, H., Lee, S. & Yaghi, O. M., *J. Am. Chem. Soc.*, **2014**, *136*, 5271–5274.

39. Farha, O. K. *et al., J. Am. Chem. Soc.*, **2012,** *134,* 15016–15021.
40. Van Steen, E. (Eric), Callanan, L. H. (Linda H. . & Claeys, C. *Recent advances in the science and technology of zeolites and related materials. Part A : proceedings of the 14th International Zeolite Conference, Cape Town, South Africa, 25-30th April 2004*. (Elsevier, **2004**).
41. Millward, A. R. & Yaghi, O. M. *J. Am. Chem. Soc*. **2005,** *127,* 17998–9.
42. Saha, D. & Bao, Z. **2010**, *44,* 1820–1826.
43. Lamia, N. *et al., Chem. Eng. Sci.*, **2009,** *64,* 3246–3259.
44. Zhang, Z., Xiang, S. & Chen, B., *CrystEngComm* **2011,** *13,* 5983.
45. Sun, D., Ma, S., Ke, Y., Collins, D. J. & Zhou, H.-C., *J. Am. Chem. Soc.,* **2006,** *128,* 3896–3897.
46. Yaghi, O. M. & Li, H. *J. Am. Chem. Soc.*, **1995,** *117,* 10401–10402.
47. Hoskins, B. F. & Robson, R. **1989**, 5962–5964.
48. Batten, S. R. *et al., CrystEngComm* **2012,** *14,* 3001.
49. Davis, M. E., *Nature* **2002,** *417,* 813–821.
50. Tranchemontagne, D. J., Mendoza-Cortés, J. L., O'Keeffe, M. & Yaghi, O. M., *Chem. Soc. Rev.* **2009,** *38,* 1257–83.
51. Llewellyn, P. L. *et al., Langmuir* **2008,** *24,* 7245–50.
52. Kumar, R. M., Sundar, J. V. & Subramanian, V., *Int. J. Hydrogen Energy,* **2012,** *37,* 16070–16077.
53. Zheng, B., Bai, J., Duan, J., Wojtas, L. & Zaworotko, M. J., *J. Am. Chem. Soc.* **2011,** *133,* 748–51.
54. Demessence, A., D'Alessandro, D. M., Foo, M. L. & Long, J. R., *J. Am. Chem. Soc.,* **2009,** *131,* 8784–6.
55. Eddaoudi, M. *et al., Science* **2002,** *295,* 469–72.
56. Kong, X. *et al. J. Am. Chem. Soc.,* **2012,** *134,* 14341–4.
57. Cohen, S. M., *Chem. Rev.* **2012,** *112,* 970–1000.
58. Kaye, S. S. & Long, J. R., **2008**, 806–807.
59. Haque, E., Jeong, J. H. & Jhung, S. H., *CrystEngComm* **2010,** *12,* 2749.
60. Lin, X. *et al., J. Am. Chem. Soc.,* **2009,** *131,* 2159–71.
61. Du, J.-L., Hu, T.-L., Li, J.-R., Zhang, S.-M. & Bu, X.-H.. *Eur. J. Inorg. Chem.* **2008,** 1059–1066.
62. Advanced Research Projects Agency - Energy. *Methane Opportunities for Vehicular Energy*. (**2012**).
63. Chiyoda Corporation et al. Preliminary feasibility study on CO2 carrier for ship-based CCS. Phase 2: unmanned offshore facility. (**2012**).
64. Ozaki, M., Ohsumi, T. & Kajiyama, R., *Energy Procedia* **2013,** *37,* 3184–3190.
65. Kokubun, N., Ko, K. & Ozaki, M., *Energy Procedia* **2013,** *37,* 3160–

3167.

66. Skagestad, R. *et al.* Ship transport of CO_2. (**2014**).

67. Simon, C. M. *et al.*, *Energy Environ. Sci.* **2015,** *8*, 1190–1199.

CHAPTER 2

Development of efficient synthetic routes to highly functionalised organic building blocks

2.1 Introduction

2.1.1 Organic linkers as key area of research in MOFs

The design and synthesis of MOFs is an area which has received a lot of interest in recent years, and indeed the number of published MOFs has increased exponentially in recent decades (Figure 15).[1] This is due to the promising potential of highly porous frameworks which can be used in a wide variety of applications, by 'tuning' the material pore walls to be suitable for specific purposes.

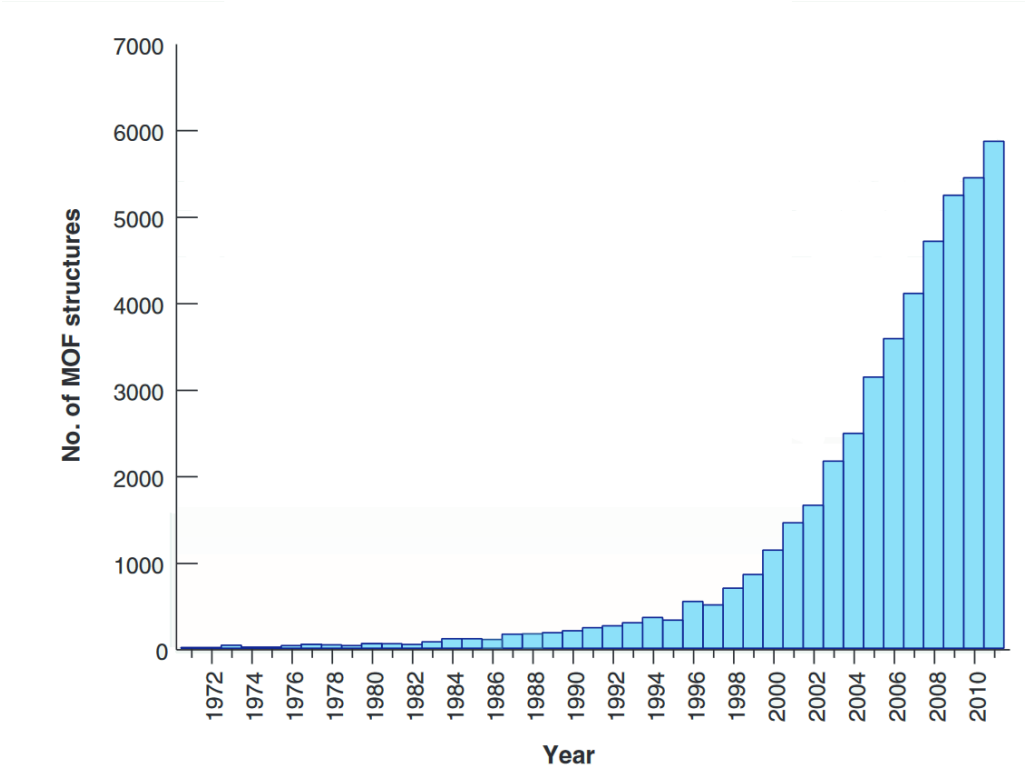


Figure 15. Number of MOF structures reported in the CSD between 1971-2011.[1]

However, many of the most promising applications identified, such as hydrogen storage, or methane storage, have targets which have not yet been reached by MOFs reported to date, and there are some arguments that the targets are almost impossible to reach with MOFs.[2,3] This is due to a number of high-throughput

simulations performed on a library of theorised MOFs, in which there seems to be an upper limit which the simulations do not predict being broken (Figure 16).

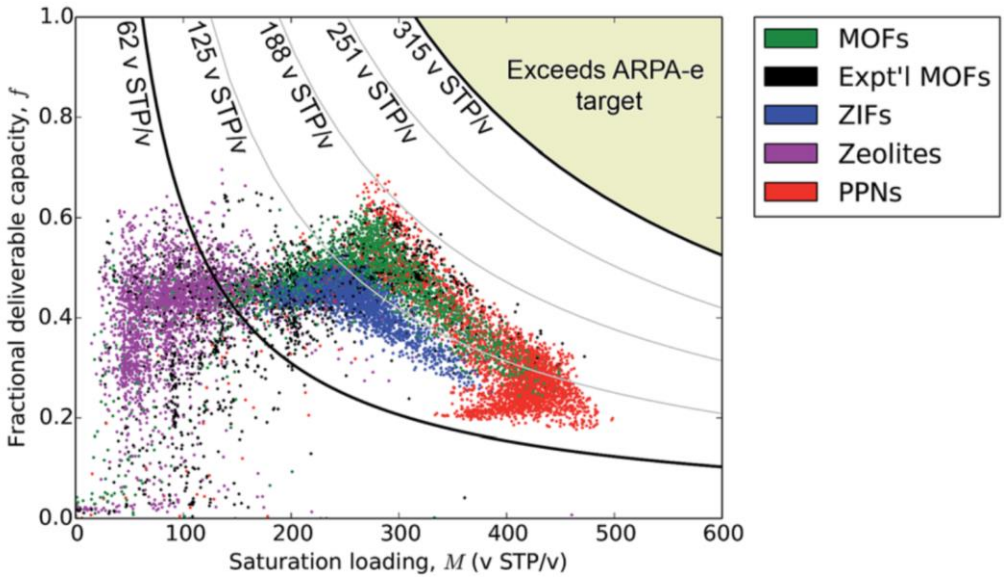


Figure 16. Fractional deliverable capacity of CH_4 against saturation loading for simulated MOFs, published MOFs, ZIFs (zeolitic imidazolate frameworks), zeolites and PPNs (porous polymer networks). The bottom and top hyperbolas give the deliverable capacity of a free space tank and the APRA-E target, respectively.[3]

However, the library of MOFs (the majority of which have not been synthesised), is based upon known topologies, ligands and metal clusters, thus limiting the reach of the study. Therefore, to push the boundaries of gas storage in MOFs, new ligands and new topologies must be discovered from the almost limitless number of plausible options. A study of theoretically stable 3D tetrahedral frameworks, the hypothetical zeolite structure database (designed for zeolite topologies, but applicable to MOFs), lists more than 100,000 unique topologies.[4] Extending the search to nets with a connectivity of more than 4 gives a fathomless number of novel structures for the synthetic MOF chemist to discover. Therefore, extensive research into new ligands is necessary, as with

new ligand shapes, sizes and functionalities comes the potential for topologies which are extremely rare, or perhaps completely new.

Gas sorption within a framework is altered greatly not just by the ligand functionality or open metal site availability, but by the topology, and hence the accessibility of the various cages throughout the MOF.[5] Figure 17 shows two methods of simulating gas sorption – adsorption at all sites and adsorption only in cages large enough to accommodate the guest molecule – and demonstrates how considering the size of cages is more realistic and matches experimental data, and is far below an 'ideal' scenario where all cages are accessible. As such, a topology which did not block access to any of the cages throughout the framework would adsorb much more gas than one which contained cages too small for gas entry and exit.

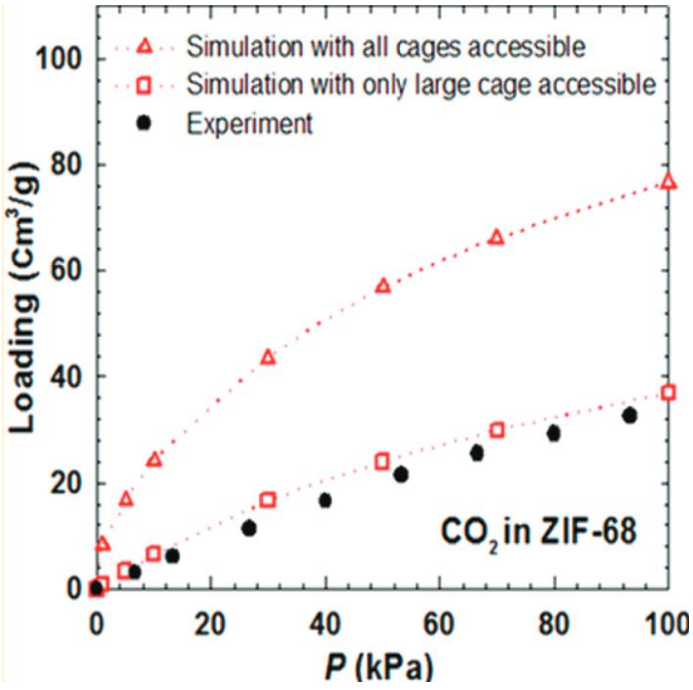


Figure 17. Comparison of simulated gas isotherms when topological features are considered.[5]

2.1.2 Importance of design of ligand for MOFs

When designing ligands for MOF synthesis, it is not only important to consider the resultant topology (which can be estimated by evaluation of the degrees of freedom in the ligand and the metal nodes in the reaction), but also the functionality of the ligand. These factors work in tandem with the overall connectivity of the 3D framework to provide optimum interactions between the framework and any guest molecules. Access to new topologies can be gained by simple changes in the connectivity and length of a ligand. For example, HKUST-1 is synthesised from benzene-1,3,5-tricarboxylic acid (H_3BTC) and Cu(II) paddlewheels, and exhibits the **tbo** topology,[6] whereas the simple extension of the ligand to benzene-1,3,5-tribenzoic acid (H_3BTB), with Cu(II), gives MOF-14 which crystallises in the **pto** topology (Figure 18).[7] This radical difference in topology from a simple extension of ligand was explored in depth by the Schmid group,[8] who not only applied a molecular mechanics force field to predict the observed behaviour, but also designed a bromine functionalised H_3BTB analogue which could force the structure back to the more open **tbo** topology, thus illustrating again the large differences to overall structure gained from simple changes to the ligand.

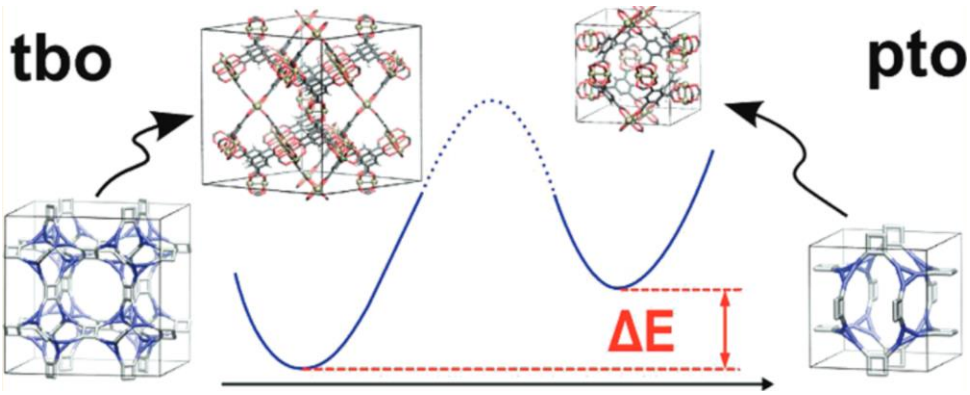


Figure 18. Energy minima of different topologies formed from Cu(II) and H_3BTC and H_3BTB ligands.

Conversely, isoreticular frameworks can be formed by dramatically different ligands when the connectivity of the SBU is considered. For example, the **tbo** topology of HKUST-1, while lost upon extension of the ligand, can be accessed by reducing the topology down to its constituent parts, and recreating the building blocks with specifically designed ligands. The most successful example of this is Cu-tbo-MOF-5, reported by Spanopoulos *et al.*,[9] in which they replaced one of the 'square' motifs of the simplified tiled net and replaced it with an octacarboxylate linker, as shown below in Figure 19. This generated a framework isoreticular to HKUST-1, with a vastly different ligand, and an improved methane uptake.

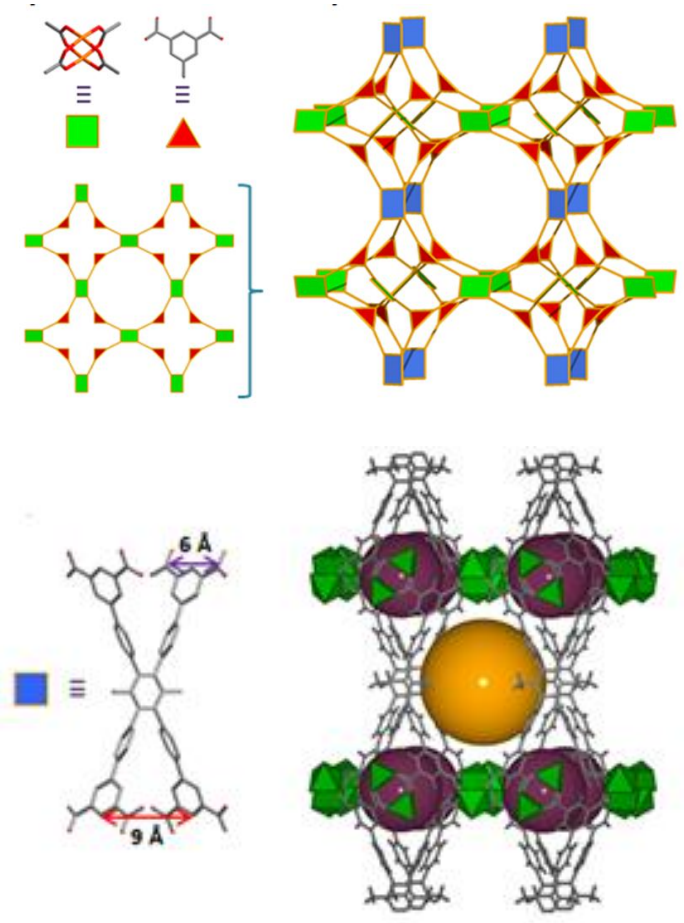


Figure 19. HKUST-1 linker and simplified net (top), and Cu-tbo-MOF-5 linker and net (bottom).[9]

The extension of the ligand in the example above is of great benefit to the gas sorption properties (resulting in a CH_4 gravimetric working capacitybetween 5-80 bar at 298 K of 22 wt% over the 16 wt% for HKUST-1), and exemplifies the general trend towards more aromatic, longer ligands seen in general throughout MOF literature.[10] The reason behind this can be seen when considering the interactions of guest molecules with the framework, as shown in Figure 20, which plots the binding energy of CH_4 to the delocalised π systems of various polycyclic aromatic hydrocarbons (PAHs), and shows that this interaction increases in strength from -1.43 kcal mol^{-1} to -2.12 kcal mol^{-1}, with an increase in the aromaticity of the system to naphthalene. This is also accompanied by a change in binding mode from singly-coordinated to triply-coordinated CH_4.

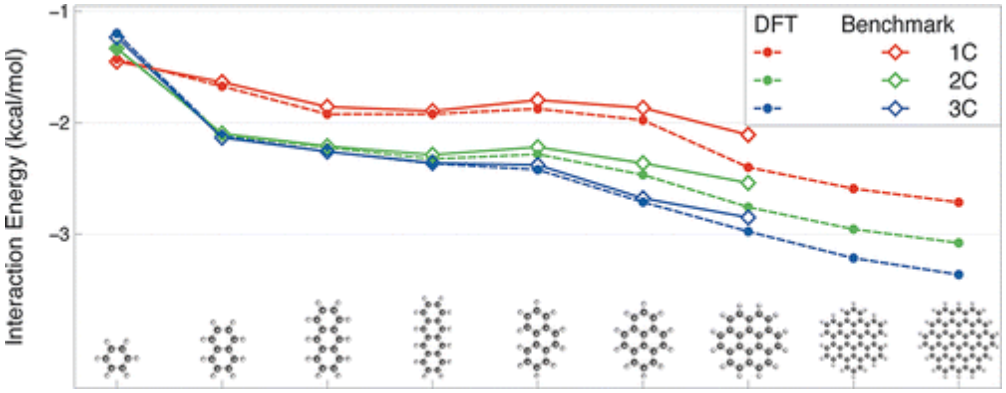


Figure 20. Interaction energies of methane binding through singly coordinated π-H mode (1C), double (2C) or triple (3C) to a series of polycyclic aromatic hydrocarbons.[11]

2.1.3 Cost implications of ligand synthesis

The importance of highly aromatic, long ligands which are capable of generating porous materials with unique sorption properties is, therefore, a main drive in MOF research. However, the main potential of research into CH_4 and H_2 storage in MOFs is the consequent use in industrial applications, such as vehicular transport. Therefore, as an increase in ligand complexity often results

in an exponential increase in cost (for example, MOF-5, from H_2BDC, costs \$200/kg, while MOF-177, from H_3BTB, costs in excess of \$130,000/kg), there is typically a trade-off between functionality/size of ligand and cost/feasibility of scale up. One of the main causes of increase synthetic cost is the use of precious metal catalysed cross-coupling reactions often inherent in ligand extension design. Consequently, methods of accessing large, highly aromatic linkers without the need for cross coupling reactions are a necessity for the design of MOFs which may be capable of realising their full potential in gas sorption applications.

One such method is the use of amines to form amide bridges between aromatic molecules, as demonstrated in the synthesis of an extended version of H_3BTC molecule by Chen *et al.*, where the central phenyl ring is extended *via* amide bridges (Figure 21).[12] The MOF exhibits excellent CO_2 uptake, which shows the benefit of this method of extension of ligands, as amide functionalities are known to improve CO_2 interactions.[13]

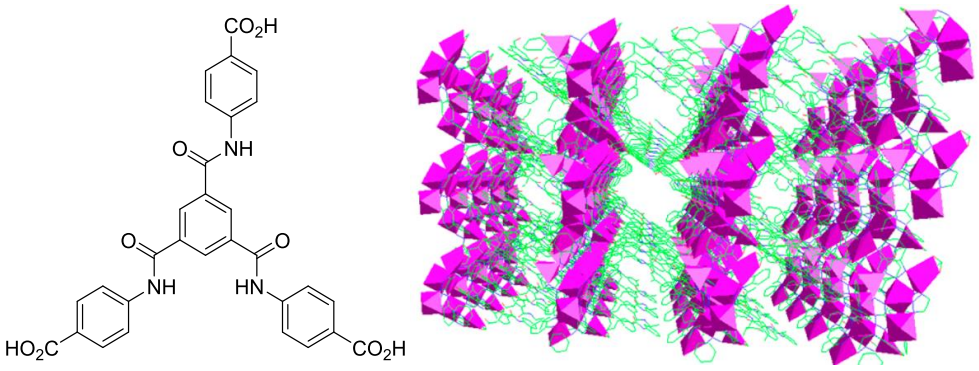


Figure 21. An amide functionalised ligand (left) and corresponding Zn(II) MOF (right).[12]

Another method of increasing the molecular weight and complexity of a molecule is cyclisation. For example, the synthesis of another H_3BTB analogue

with a triazine core synthesised by the Zhou group is shown in Figure 22.[14] This MOF forms a framework with Cu(II) of **pto** topology, which is isostructural to MOF-14, and as such highlights how the cyclisation step involved in this MOF allows rapid access to a H_3BTB/MOF-14 analogue without the need for cross-coupling reactions.

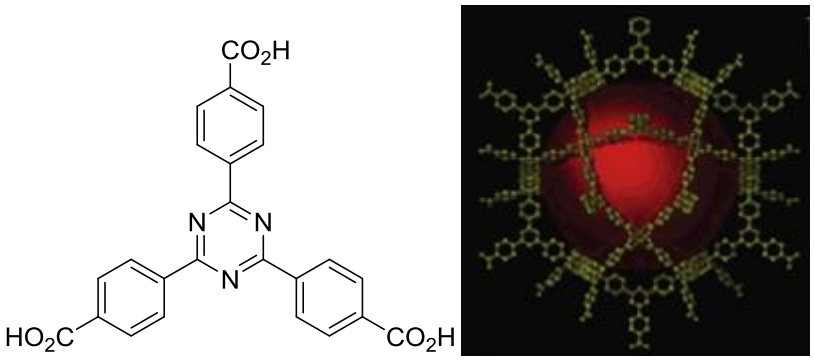


Figure 22. A triazine based ligand (left) and corresponding Cu(II) MOF (right).

As MOFs are still a relatively new field, the majority of focus is on generating frameworks with interesting properties, and the cost of ligand synthesis is not often contemplated. However, the importance of this can be seen in the commercial availability of metal-organic frameworks, where the majority of those on the market are from simple ligands which require no expensive procedures to synthesise, such as trimesic acid, used in the synthesis of Basolite C300 (HKUST-1).

2.1.4 Aims and Objectives

This chapter describes the synthesis and characterisation of a series of ligands designed for the generation of isoreticular MOFs. It details the versatile 'building block' methodology, which enables rapid access to a variety of functionalised and extended ligands, at no detriment to the ease of synthesis due to the ubiquitous nature of the dihalogenated compounds used for the core. The

discussion then moves to the cost of synthesis of the ligand series, considering all steps and cross-coupling reactions, with a brief comparison to some of the highest performing MOFs in literature for high pressure storage of CH_4 and CO_2. The chapter ends with the synthesis of a ligand which is analogous to the series in the first half, yet is accessible *via* a cyclisation to rapidly increase the molecular weight and reduce the synthesis from six steps down to two.

2.2 Results and Discussion

In order to rationally design a series of ligands for use in an isoreticular series of MOFs, it was necessary to plan a synthetic route which was versatile and rapid. To do this, the ligand was designed in stages. Firstly, the overall connectivity was considered, as this would dictate the nature of the frameworks likely to be produced. A ligand with four points of extension was decided upon, based around the NOTT-100 series (Figure 23), as lengthening of the carboxylate distances laterally (distance **a**) would enable potential access to a new set of structures, and ideally new topologies for exploring outside the limit of known topologies probed by high throughput methods.

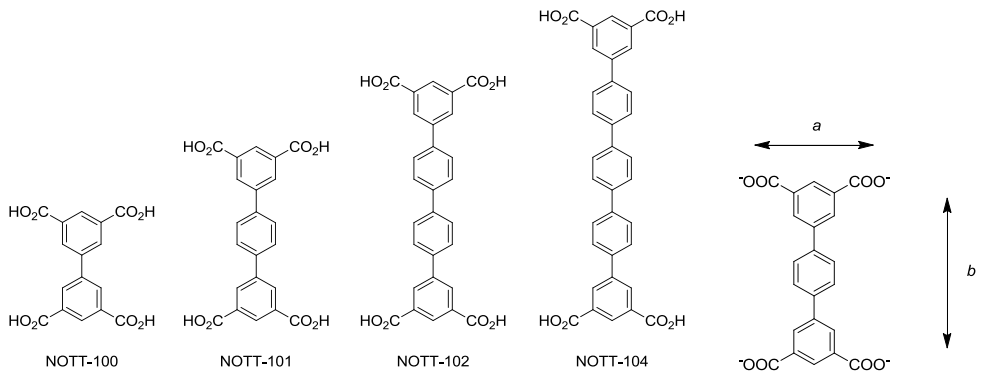


Figure 23. Ligands used in synthesis of NOTT-10X series (left) and carboxylate distances **a** and **b** in the ligand (right).

Once the connectivity of the ligand was decided, it was necessary to break the ligand down into its constituent parts to assess possible synthetic routes which would enable rapid functionalisation and extension. Therefore, the ligand was visualised as an assembly of building blocks, based around a core which could be exchanged for one with added functionality or length, as shown in Figure 24.

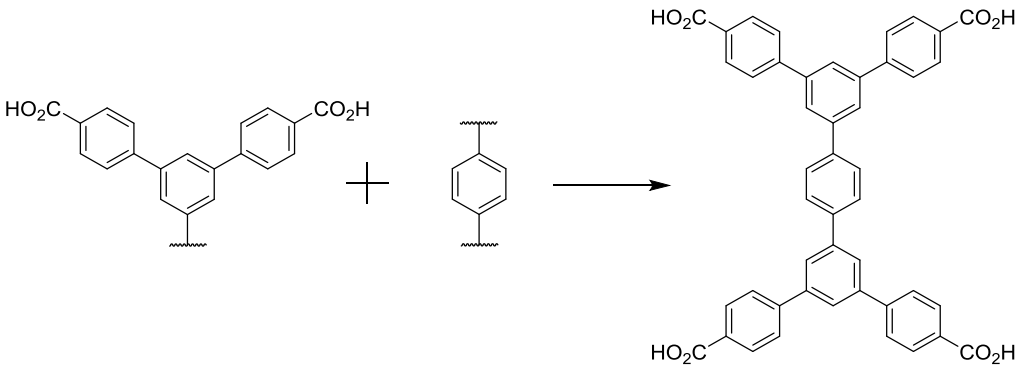


Figure 24. Visualisation of potential building blocks for synthesis of H_4L^1.

2.2.1 Synthesis of ligand series H_4L^X

The best method for formation of aryl-aryl bonds was identified in this case as a Suzuki-Miyaura cross-coupling reaction,[15] as these are highly efficient and versatile methods which are known to be robust and proceed in a wide variety of conditions. Due to the commercial availability of a wide variety of dihalogenated compounds suitable as core building blocks, the 'arms' were designed as boronic acids, as shown in Figure 25, enabling efficient and rapid coupling reactions affording the series shown below, with only small variations in the ease of synthesis between them.

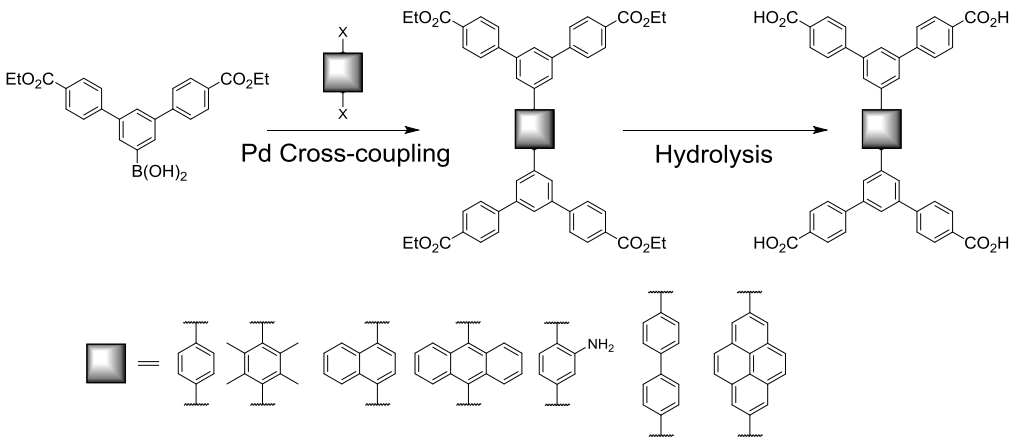


Figure 25. Simplified building block scheme for ligand series H_4L^X.

Using this approach, the large scale synthesis of the meta-terphenyl arms was highly important, as from here, coupling to a wide variety of dihalogenated cores would afford various ligands in high yields relatively easily and rapidly.

Synthesis of protected 3,5-di(p-carbethoxy)benzene boronic acid (DPCB)

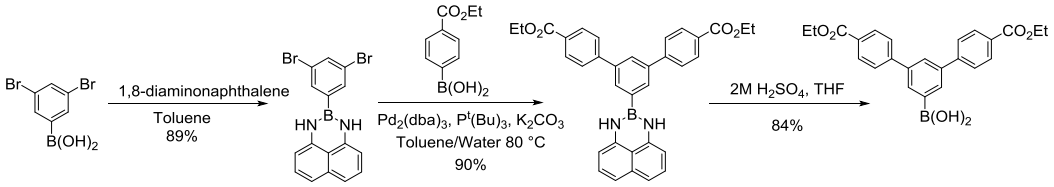


Figure 26. Synthetic procedure to obtain 'arm' precursor boronic acid.

The synthesis of the boronic acid precursor (shown above in Figure 26) proceeded smoothly from the 3,5-dibromobenzene boronic acid starting material. 3,5-Dibromobenzene boronic acid was reacted with 1,8-diaminonapthalene to protect the boronic acid and prevent self-coupling in a following Suzuki-Miyaura cross-coupling procedure. Next, a cross-coupling reaction was performed with 2.8 equivalents of 4-carbethoxybenzene boronic acid (synthesised by the esterification shown in Figure 27) and the product easily deprotected using sulphuric acid, affording DPCB. The carboxylic acid

functionalities were protected in this instance by an esterification with an ethyl group as free carboxylic acid groups would interfere with the palladium coupling reactions. Additionally, the ethyl ester groups improve the solubility of the boronic acid and are stable to the conditions used throughout the procedure, yet labile enough to be removed under relatively mild conditions.

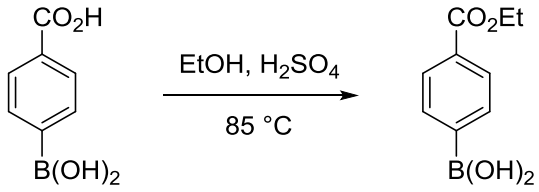


Figure 27. Synthetic procedure for esterified boronic acid.

The power of this building block method can be seen below, where the coupling of DPCB to any of the dihalogenated cores shown generates the large series of ligands in good yields. Therefore, scale up of the initial synthesis route to DPCB gives a large stock of this (up to 10 grams of the final product can be synthesised at a time without affecting the yield dramatically), which then can be used to generate at least one gram of each ligand below with no alteration to the procedure. The exploratory nature of MOF synthesis, which often requires a large amount of trial and error (using ~10 mg in each MOF trial), necessitates a large amount of ligand; as such the synthesis of a gram of ligand at a time is of great value. This method is ideal for generating a series of isoreticular MOFs where all frameworks are comparable in ease of synthesis, thus giving true ability to tune the properties of the MOF to the desired degree without any negative impact on feasibility of scale up.

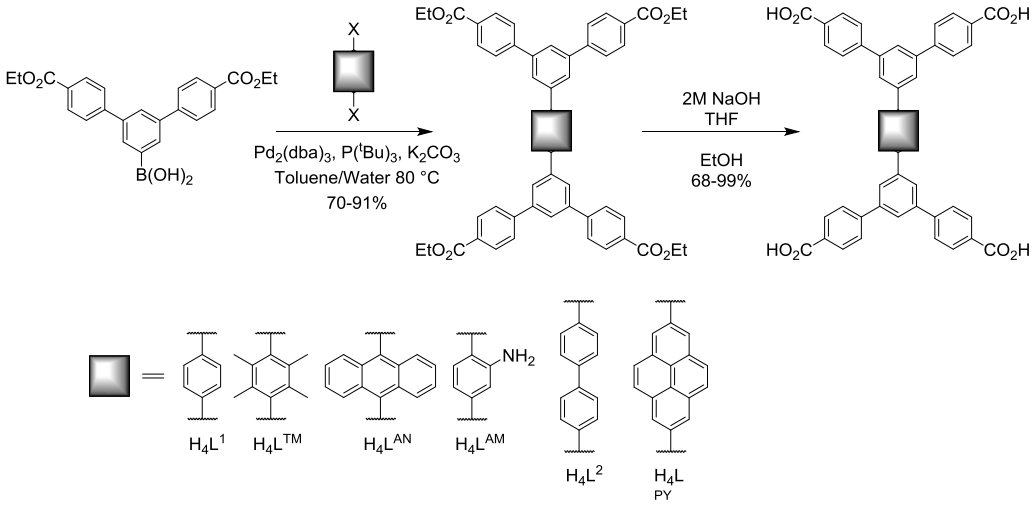


Figure 28. Synthesis conditions, yields, and naming system for ligand series H_4L^X.

The versatility of this method for functionalising the central core is shown in Figure 28, and it is evident that the yield of each reaction is not only very high, but very consistent throughout the series. All dihalogenated cores are available for purchase for relatively low cost (prices range from £0.09 to £2 per gram), with the noted exceptions of 2,7-dibromopyrene, which is orders of magnitude more expensive, and 3,6-dibromodurene, which is accessible *via* a simple one-step reaction from the inexpensive durene.

2.2.2 Cost of current methods and development of sustainable linker preparation

One very important, yet often neglected feature of a MOF for industrial application is the cost of synthesis, not only of the framework, but also of the ligand itself. While the methods described in Section 2.2.1 are highly efficient and versatile in terms of reaction steps to a wide variety of ligands, the cost involved in the synthesis of each gram of product is still very high, as there are too many steps to be cost-effective. Additionally, there are two Suzuki-Miyaura cross-coupling reactions involved in the synthesis, which brings the price for a

gram of the simplest ligand to £11.63, assuming 90% yield in all reactions, and not factoring in the cost of the palladium catalyst.

While it is possible to use simple starting materials, such as benzenedicarboxylate, or trimesic acid, these ligands give a limited number of structures, and do not possess the same benefits as structures with longer ligands, such as high pore volumes or accessibility to highly functionalised MOFs for a wide variety of purposes. Therefore, using the H_4L^X ligand series as an example of such multifunctional ligands, a new route to the same or analogous ligands was pursued. The criteria for the new ligand synthesis were that it must be a significantly shorter synthetic pathway, which must not involve the use of any precious metal catalyst, and that the starting materials must be cheap (ideally for a total of less than £1.00 per gram on a laboratory scale). From these selection criteria, the ligand shown in Figure 29 was proposed as a potential target, as it became clear that cyclisation could play a key part in both minimizing cost and cutting down the steps, as from simple starting materials the molecular weight can be vastly increased in a single step.

Formazan cyclisation as a route to highly functionalised materials

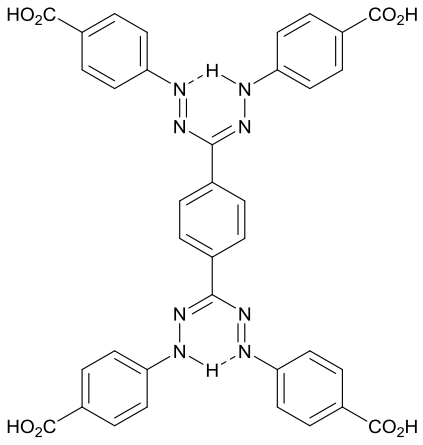


Figure 29. Proposed formazan-based ligand.

Research into formazan cyclisation gave the following reaction (Figure 30), which was used as the basis of a new target (Figure 31) which could be synthesised first to test the reaction conditions.

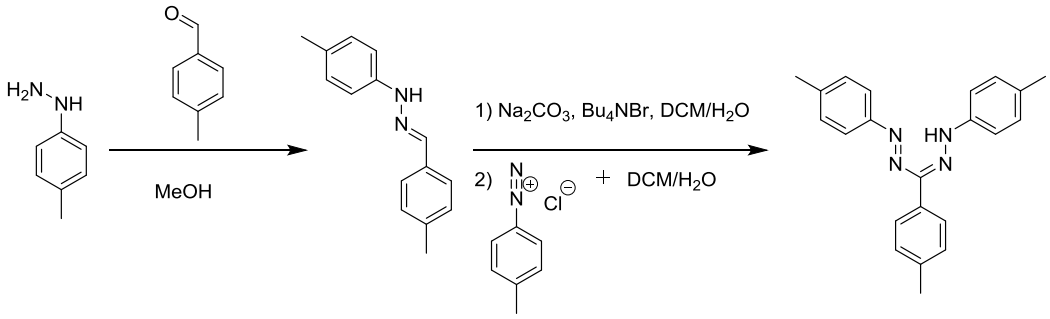


Figure 30. Reaction scheme to form tritolylformazan.

The mechanism of the cyclisation shown above, as discussed by Katritzky *et. al.*, was known to be versatile regarding the substituents in the 4- position on the phenyl rings, with the caveat that electron withdrawing groups slowed the reaction down slightly. Therefore, the synthesis of the compound shown in Figure 31 was performed over a longer period.

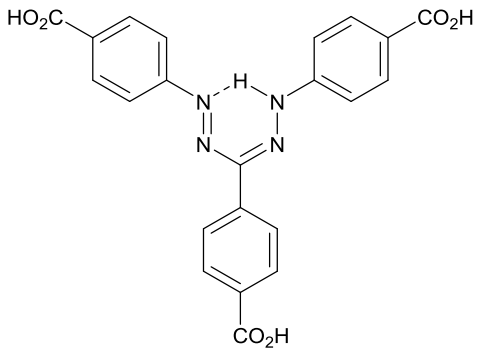


Figure 31. First formazan target; Tricarboxyphenyl formazan.

Synthesis of 1,3,5-tricarboxyphenyl formazan

In this reaction, an equimolar mixture of 4-hydrazinobenzoic acid and 4-formylbenzoic acid were reacted with triethylamine in excess in ethanol to produce the intermediate hydrazine. In a separate flask, 4-aminobenzoic acid in

water and HCl is cooled to -5 °C and stirred with sodium nitrite to form a highly reactive diazonium salt, which is immediately added dropwise to a cooled solution of the hydrazine intermediate. The resulting solution is stirred over 24 hours to form a dark red solution. Acidification and filtration of the resulting suspension yields the crude formazan product, which can be washed with ethyl acetate to purify it as a red solid.

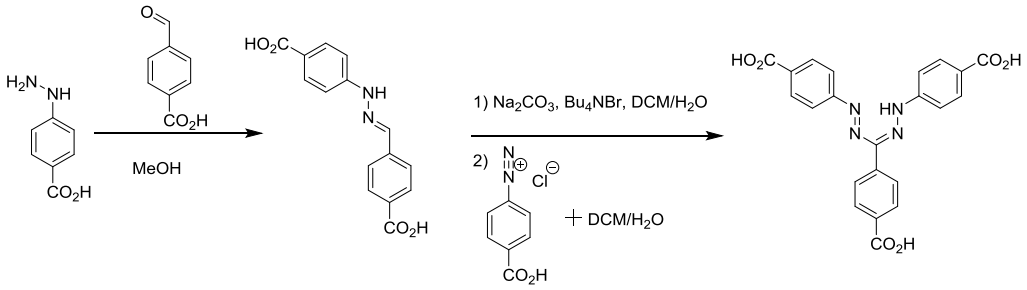


Figure 32. One-pot reaction to form formazan product in 45% yield.

Synthesis attempt of diformazan H_4L^1 analogue

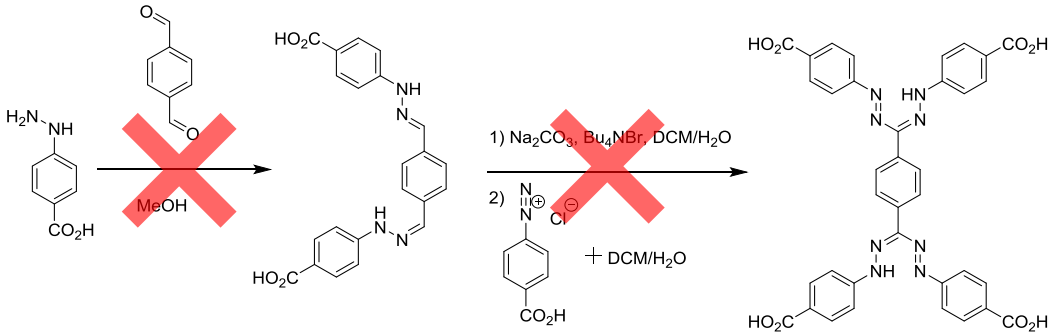


Figure 33. One-pot reaction attempt to form diformazan product.

As shown in Figure 33, the attempt to synthesise the diformazan product was unsuccessful, and yielded a mixture of products in NMR, identified as the mono-coupled and a trace of the product. As this method was to find a synthetic

route for cheap, bulk synthesis of ligands, purification of this was not pursued, and alternative cyclisation routes were analysed.

Pyridine cyclisation as a method of rapid structure growth

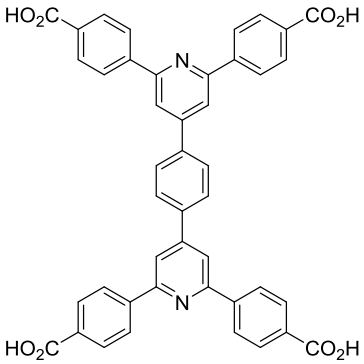


Figure 34. Proposed pyridine-based ligand.

Research into pyridine cyclisation yielded the following reaction (Figure 35), which is an improvement on the Kröhnke pyridine synthesis, avoiding the need for prior preparation of pyridinium salts and α-β-unsaturated ketones, which dramatically simplifies the synthetic route. The method, first proposed by Cave and Raston,[16] synthesises pyridine *via* sequential solventless aldol condensation and Michael addition with solid NaOH, followed by treatment with ammonium acetate in acetic acid as a one pot reaction.

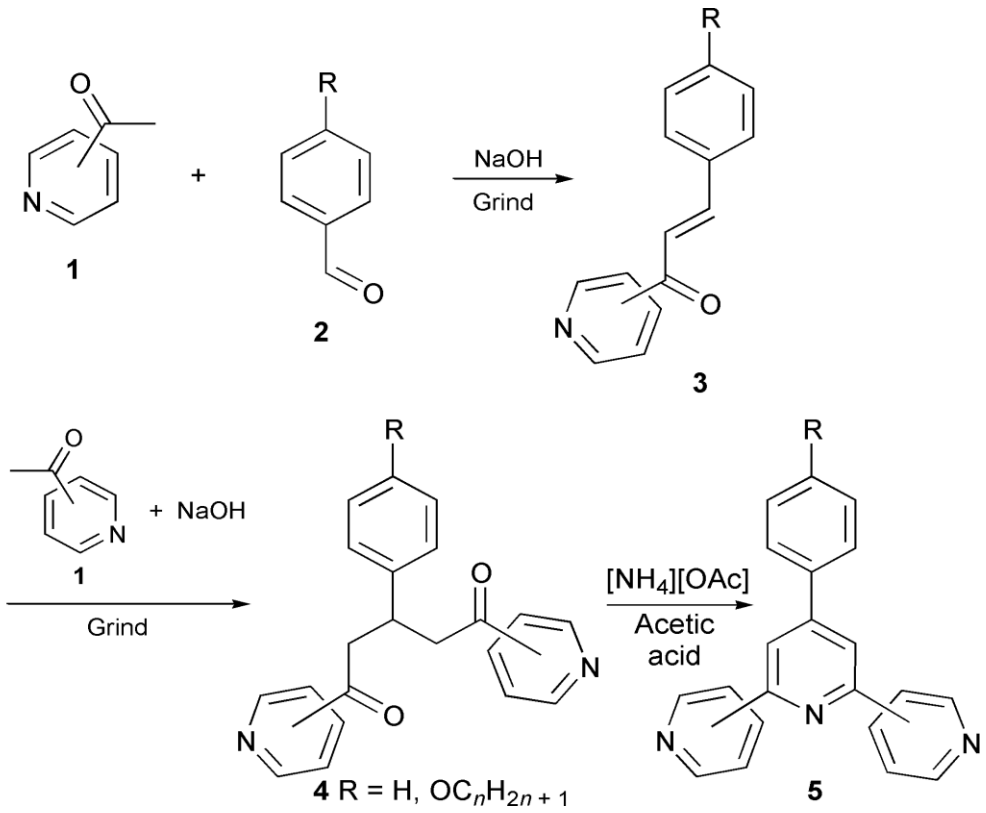


Figure 35. Generic scheme for synthesis route to asymmetrically functionalised pyridines.[16]

Based on the efficient one pot reaction shown above, the following synthetic route was proposed (Figure 36), based on a route to a similar compound accessed *via* the tetramethyl molecule which has been synthesised by a group using it for research into OLED candidates due to the extended conjugation of their final product.[17]

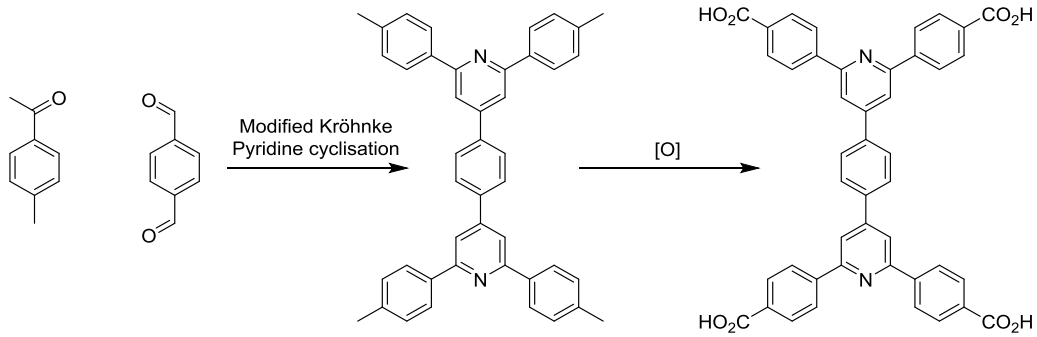


Figure 36. Proposed route to H_4L^{1P}.

Synthesis of 1,4-bis(2,6-di-p-tolylpyridin-4-yl)benzene

In this reaction, five equivalents of 4'-methylacetophenone are ground in a pestle and mortar for 20 minutes with one equivalent of terephthalaldehyde and six equivalents of sodium hydroxide. The resultant yellow powder is then stirred into a solution of ammonium acetate (in stoichiometric excess) in ethanol, and heated for 18 hours to give the crude product. This can then be recrystallized from toluene to give the tetramethyl product as a pure white solid.

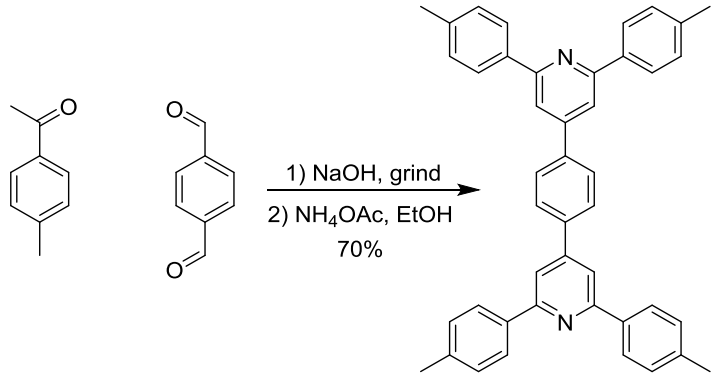


Figure 37. Synthetic procedure to obtain tetramethyl precursor to H_4L^{1P}.

Oxidation of tetramethyl precursor

Oxidation of 1,4-bis(2,6-di-p-tolylpyridin-4-yl)benzene was attempted using the standard conditions within the Schröder group, using potassium permanganate in a ^{t}butanol/water mixture with sodium hydroxide to aid solubility of the oxidised compound and theoretically help pull the reaction to completion (Figure 38). However, it was found that after all of the $KMnO_4$ had been added, and the reaction left for a few days, the filtrate contained no product. The usual manganese oxide 'cake' which is filtered off after the reaction was found to contain white flecks throughout the usual brown mass, indicating that the initial starting material had not gone into solution, and the

solid left on top was the tetramethyl starting material (as the tetracarboxylate anion would be soluble in water).

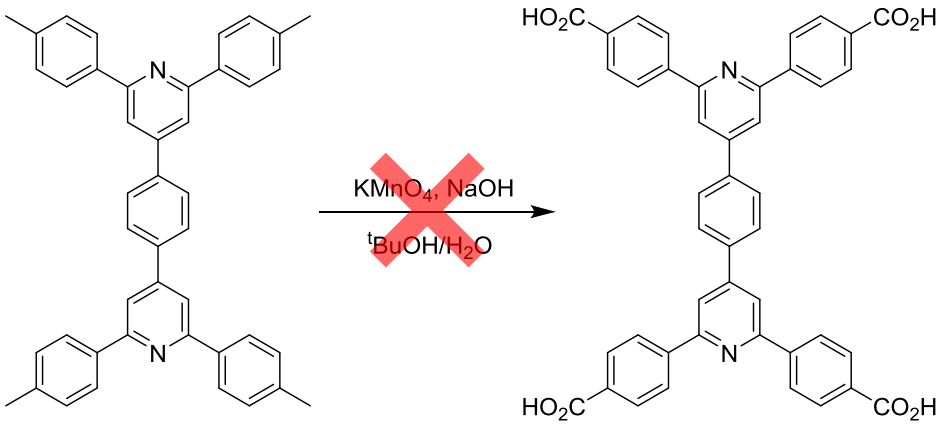


Figure 38. Oxidation attempt to obtain the pyridyl tetracaboxylic acid linker.

As the above reaction was unsuccessful, other oxidation conditions were researched, and a method which involved heating the starting material in a sealed bomb at 180 °C for 18 hours with a water/nitric acid mixture was used (Figure 39). The supercritical nature of the water at this temperature and pressure should solubilise the starting material, allowing oxidation to take place, and upon cooling, the compound could simply be filtered and washed with water to neutralise any remaining acid.

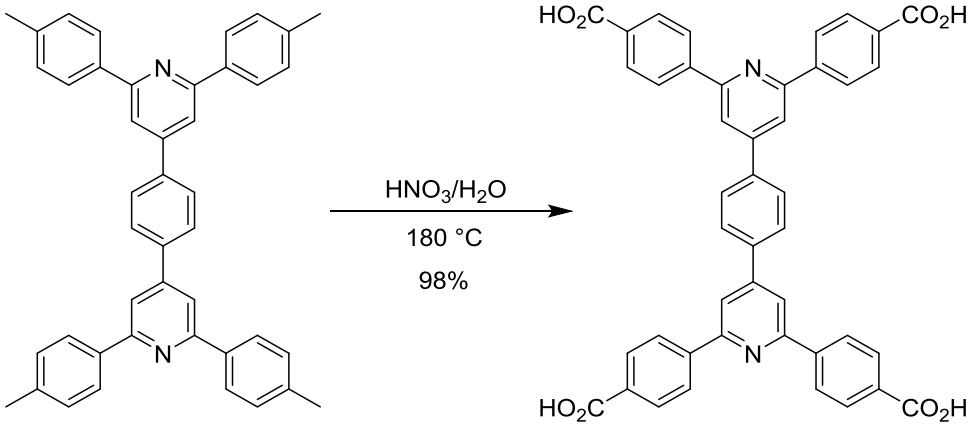


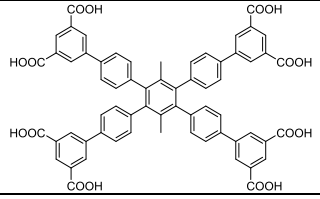
Figure 39. Oxidation of tetramethyl precursor with nitric acid in a sealed bomb.

Acquisition of the tetramethyl molecule and further oxidation was utilised to generate H_4L^{1P} in a 2 step reaction from very simple starting materials. The cost of the reaction overall was calculated to be £0.51/g at a laboratory scale, which shows very promising signs for a candidate to be scaled up and used in industrial processes. Furthermore, the ligand is a prime example of green synthesis, with an initial solvent-free reaction, followed by heating in a reasonably green solvent, ethanol. This, followed by a green alternative oxidation route, results in a highly favourable ligand for use in economically viable, sustainable MOF synthesis.

2.2.3 Comparison to Literature Synthetic Routes

Comparison to a wide variety of ligands used in the top performing MOFs in literature (Table 1) was also useful, as this highlights how optimising for high pressure storage of gases often results in an increase in complexity, and thus cost, of ligand. The method of ligand cost calculation was based upon yields of 90% for each step, without factoring in cost of catalyst or solvent (this is most significant for reactions with precious metal cross coupling), as synthetic pathways may vary, yet the inherent cost associated with the most accessible starting materials will not change. These starting materials were identified as those which were most cost effective, as some ligands are commercially available at a much higher price, which would not allow effective comparison.

Table 1. All costs *via* multiple step routes assume that each step has a yield of 90%. *These methods involve at least one Suzuki coupling reaction or other precious metal reaction. **These ligands are available to buy, but are far more expensive, so the cheapest route has been identified.

MOF	Ligand	Steps to Ligand	Cost of Ligand
N/A	**H_4L^1**	**6***	**£11.68/g**
N/A	**H_4L^X**	**6***	**£11.68-£257.27/g**
N/A	**H_4L^{1P}**	**2**	**£0.51/g**
Al-soc-MOF-1[24]	3,3",5,5"-tetrakis(4-carboxyphenyl)-p-terphenyl (H_4L^1)	3*	£42.77/g
MOF-205	2,6-Naphthalenedicarboxylic acid	0	£2.02/g
MOF-177[18]	H_3BTB (1,3,5-tris(4-carboxyphenyl)benzene)	2*	£3.10/g**
MOF-520[19]	H_3BTB (1,3,5-tris(4-carboxyphenyl)benzene)	2*	£3.10/g**
Cu-tbo-MOF-5[9]		6*	£13.60/g
MOF-519[19]	H_3BTB (1,3,5-tris(4-carboxyphenyl)benzene)	2*	£3.10/g**
HKUST-1[6]	Trimesic Acid	0	£0.28/g
PCN-14[20]	5,5'-(9,10-Anthracenediyl)di-isophthalic acid	2*	£25.32/g
MOF-5[21]	Terephthalic Acid	0	£0.09/g
MOF-200[22]	1,3,5-Tris(4′-carboxy[1,1′-biphenyl]-4-yl)benzene (H_4BBC)	3*	£3.37/g
MOF-505[23]	Biphenyl-3,3′,5,5′-tetracarboxylic acid (H_4BPTC)	4*	£1.09

As shown above, the building block synthetic method is a powerful tool to access a wide variety of ligands, as the cost is roughly a quarter of the method employed in the literature method for Al-soc-MOF-1, which obtains the same resultant ligand (£11.68/g compared to £42.77/g). The pathway used in literature, however, is half the length of that discussed here, three steps for Al-

soc-MOF-1 rather than six for H_4L^1. Although this difference in length of synthetic route is somewhat countered by the ability to scale up the synthesis of the boronic acid 'arms' to generate a stockpile from which one can synthesise any one of eight different ligands in a single reaction and subsequent hydrolysis.

Furthermore, the use of cyclisation as a method of accessing large, highly aromatic ligands is shown to be highly effective at keeping the cost and length of synthetic route down. In comparison to the route employed here to synthesise H_4L^1, the cost is $1/20^{th}$ (£0.51/g compared to £11.68/g), and in comparison to the literature pathway to Al-soc-MOF-1, the cost is $1/84^{th}$, and the route is two steps rather than three. Moving further down the table, it is clear that the pathway to H_4L^{1P} is cheaper than almost all ligands used for high pressure methane storage.

2.3 Conclusion

In this chapter, the evaluation of a versatile building block approach was discussed. Through this method, it was possible to rapidly synthesise a large series of ligands for use in MOF synthesis by coupling the metaterphenyl 'arms' to a number of commercially available (or, with the exception of 2,7-dibromopyrene, easily synthesised) dihalogenated cores, giving the H_4L^X series. This method has wide ranging significance, as the same boronic acid blocks could be coupled to any number of other halogenated cores generating further series' of ligands with different connectivities and functionalities.

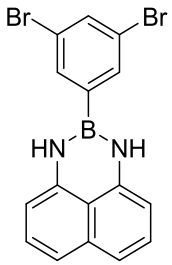
The next part of the chapter recognised the requirements of industry for readily available, cheap ligands for MOF applications, and discusses the preparation of a new ligand which could be synthesised *via* an incredibly short, cheap, and

green synthetic pathway. The versatility of this method is highlighted as something which requires further research, and could yield interesting results, as the ability to generate an isoreticular series of very cheap ligands would open up the possibility of MOFs as a true contender for current industrial applications. The problems foreseen with the versatility of this method, or lack thereof, fall into two categories. Firstly, the presence of certain functionalities on the central core could affect the synthesis (for instance, an aldehyde or ketone would cause side reactions to occur). Secondly, the availability of functionalised dialdehydes is certainly far less than that of dihalogenated cores, and therefore the selection may be far less than that based around the dihalogenated cores.

The chapter was concluded by comparison of ligands used in current leading MOFs, to evaluate the usefulness of the new synthetic pathway to H_4L^{1P}. It was found that this ligand was among the three cheapest to synthesise, just below H_3BTC and H_2BDC, two of the most ubiquitous ligands available. This was encouraging, as the complexity of the ligand was far greater than these, and could therefore give rise to highly porous materials for use in high pressure gas storage. Two clear results have arisen from this chapter – a series of ligands suited to the probing of interactions of host and guest in high pressure storage (the H_4L^X series), and two analogous ligands (H_4L^1 and H_4L^{1P}), which can be used to explore the potential industrial impact of designing highly functionalised, extended ligands which are accessible *via* facile, low cost, green synthetic conditions.

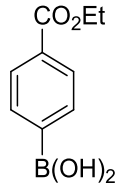
2.4 Experimental

Synthesis of **1**



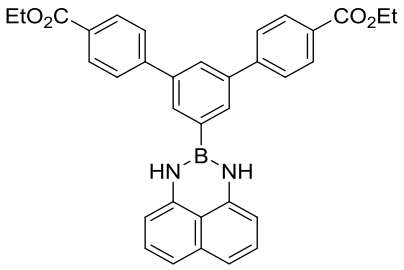
To a stirring solution of (3,5-dibromophenyl) boronic acid (10 g, 35.75 mmol) in toluene (170 ml) was added 1,8-diaminonapthalene (6.6 g, 41.72 mmol). The solution was heated to 100 °C in an open flask for 1 h. Once complete, the solvent was removed under vacuum to give the crude product as a brown solid. This was dissolved in a minimum amount of boiling dichloromethane, and petroleum ether (b.p 60-80 °C) was carefully added until precipitation of the product. The suspension was allowed to cool to room temperature before filtering and drying to obtain the pure product as a bright yellow solid (11.25 g, 78%). (Found: $[M+H]^+$, 402.90. $C_{16}H_{12}BBr_2N_2$ requires 402.9); ^{1}H NMR (400MHz, $CDCl_3$): δ = 5.95 (s, 2H, NH), 6.45 (dd, $^3J_{H,H}$ 7.2 Hz, $^3J_{H,H}$ 0.9 Hz, 2H, Ar), 7.09 (d, $^3J_{H,H}$ 0.7 Hz, 1H, Ar), 7.11 (d, $^3J_{H,H}$ 0.7 Hz, 1H, Ar), 7.15-7.20 (m, 2H, Ar), 7.69 (d, $^4J_{H,H}$ 1.9 Hz, 2H, Ar), 7.78 (t, $^4J_{H,H}$ 1.8 Hz, 1H, Ar) ppm. ^{13}C NMR (100 MHz, $CDCl_3$): δ = 106.4, 118.4, 119.9, 123.5, 127.6, 132.9, 135.5, 136.2, 136.2, 140.3 ppm.

Synthesis of **2**



To a stirring solution of 4-carboxyphenylboronic acid (15 g, 90 mmol) in ethanol (375 ml) was added concentrated sulphuric acid (4.5 ml). The solution was heated to 85 °C for 19 hours. Once the reaction was complete, the volume of the solution was reduced under vacuum until precipitation occurred. The resulting suspension was treated with an excess of water and filtered. The white product was washed with water until the pH of the filtrate was neutral, and subsequently dried to give the product as a fine white powder (15.37 g, 88%). (Found: $[M+H]^+$, 195.0. $C_9H_{12}BO_4$ requires 195.00); ^{1}H NMR (400MHz, $CDCl_3$): δ = 1.28 (t, $^3J_{H,H}$ 7.1 Hz, 3H, CH_3), 4.28 (q, $^3J_{H,H}$ 7.1 Hz, 2H, CH_2), 7.83-7.91 (m, 4H, Ar) ppm. ^{13}C NMR (100 MHz, $CDCl_3$): δ = 14.7, 61.1, 128.6, 131.2, 134.1 134.7, 166.5 ppm.

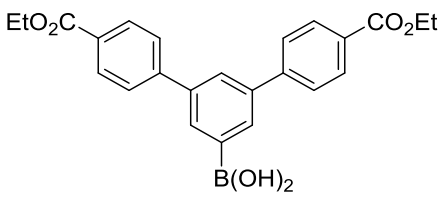
Synthesis of **3**



To a stirring, degassed suspension of compound **1** (6 g, 14.9 mmol), compound **2** (8.13 g, 41.2 mmol) and potassium carbonate (4.34 g, 31.4 mmol) in toluene (400 ml) and water (100 ml) at 60 °C was added tri-tert-butyl phosphine (1M in toluene, 2.4 ml, 2.4 mmol) and tris(dibenzylideneacetone)dipalladium(0) (1.34 g, 1.5 mmol). This suspension was heated to 80 °C for 1 hour and 30

minutes. The resulting suspension was filtered while hot, and the solid washed with dichloromethane (200 ml). This filtrate was separated, and the organic phase extracted, washed with water (2 x 200 ml), and dried with magnesium sulphate before removing the solvent under vacuum. The resulting yellowish solid was solubilised in a minimum amount of dichloromethane and partially purified through a silica plug (in ethyl acetate), the filtrate of which gave a dark brown solid after removal of the solvent under vacuum. The solid was dissolved in a minimum amount of boiling dichloromethane, and crashed out by the careful addition of petroleum ether (b.p 60-80 °C). The suspension was filtered to obtain the pure product as a yellow/orange solid (5.98 g, 74%). (Found: $[M+H]^+$, 541.3. $C_{34}H_{30}O_4N_2B$ requires 541.43); ^{1}H NMR (400MHz, $CDCl_3$): δ = 1.47 (t, $^3J_{H,H}$ 7.1 Hz, 6H, CH_3), 4.46 (q, $^3J_{H,H}$ 7.1 Hz, 4H, CH_2), 6.17 (s, 2H, NH), 6.50 (d $^3J_{H,H}$ 7.3 Hz, 2H, Ar), 7.10-7.23 (m, 4H, Ar), 7.78 (dt, $^3J_{H,H}$ 8.5 Hz, $^4J_{H,H}$ 1.9 Hz, 4H, Ar), 7.91 (d, $^4J_{H,H}$ 1.8 Hz, 2H, Ar), 7.95 (t, $^4J_{H,H}$ 1.8 Hz, 1H, Ar), 8.21 (dt, $^3J_{H,H}$ 8.5 Hz, $^4J_{H,H}$ 1.9 Hz, 4H, Ar) ppm. ^{13}C NMR (100 MHz, $CDCl_3$): δ = 14.4, 61.1, 106.3, 118.1, 112.0, 127.3, 127.6, 127.7, 128.2, 129.7, 130.1, 130.2, 136.4, 140.2, 140.8, 145.2, 166.5 ppm.

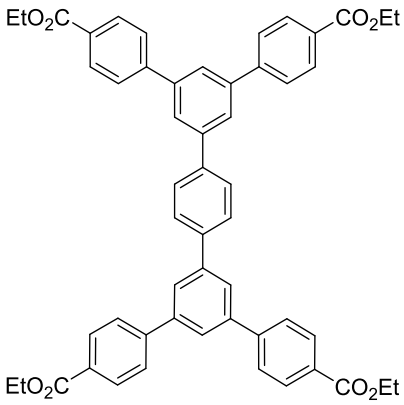
Synthesis of **4**



To a stirring solution of compound **3** (6.35 g, 11.75 mmol) in tetrahydrofuran (360 ml) was added sulphuric acid (2M in water, 73 ml). This solution was heated to reflux for 4 hours. The reaction mixture formed a suspension over

this time, which was filtered while hot, to remove the solid impurities. The volume of solvent in the filtrate was then reduced under vacuum until precipitation occurred. This suspension was then solubilised by heating to 70 °C, at which point an excess of water was added. This was then filtered and washed with a large amount of water until the pH of the filtrate was neutral. The solid was dried to give the product as an off white powder (4.44 g, 97%). (Found: [M - H], 417.1506. $C_{24}H_{22}O_6B^-$ requires 417.1515); ^{1}H NMR (400MHz, $CDCl_3$): δ = 1.35 (t, $^3J_{H,H}$ 7.1 Hz, 6H, CH_3), 4.35 (q, $^3J_{H,H}$ 7.1 Hz, 4H, CH_2), 7.96 (d $^3J_{H,H}$ 8.5 Hz, 4H, Ar), 8.08 (d, $^3J_{H,H}$ 8.5 Hz, 5H, Ar), 8.20 (d, $^4J_{H,H}$ 1.8 Hz, 2H, Ar) ppm. ^{13}C NMR (100 MHz, $CDCl_3$): δ = 14.7, 61.2, 127.7, 129.3, 130.2, 138.0, 139.3, 142.9, 145.2, 145.9, 166.1 ppm.

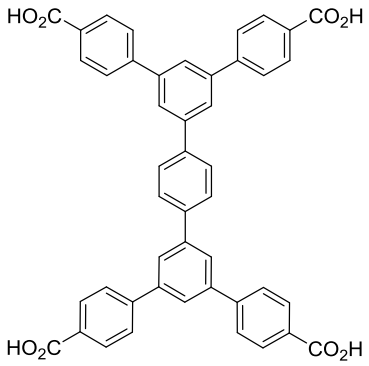
Synthesis of **5**



To a stirring, degassed solution of 1,4-dibromobenzene (281 mg, 1.19 mmol), compound **4** (1.39 g, 3.57 mmol) and potassium carbonate (920 mg, 6.65mmol) in toluene (105 ml) and water (20 ml) at 60 °C was added tri-tert-butyl phosphine (1M in toluene, 0.55 ml, 0.55 mmol) and tris(dibenzylideneacetone)dipalladium(0) (218 mg, 0.24 mmol). This suspension was raised in temperature to 80 °C for 1 hour and 40 minutes. The

resulting suspension was separated, and the organic phase extracted with dichloromethane and washed with water (2 x 100 ml). This was then dried with magnesium sulphate before removing the solvent under vacuum. The resulting brown solid was dissolved in a minimum amount of boiling dichloromethane, and crashed out by the careful addition of methanol. The suspension was filtered and the solid dried in an oven at 80 °C to obtain the pure product as an off-white solid (889 mg, 91%). (Found: [M], 822.42. $C_{54}H_{46}O_8$ requires 822.32); ^{1}H NMR (400MHz, $CDCl_3$): δ = 1.45 (t, $^3J_{H,H}$ 7.1 Hz, 12H, CH_3), 4.44 (q, $^3J_{H,H}$ 7.1 Hz, 8H, CH_2), 7.80 (dt, $^3J_{H,H}$ 8.5 Hz, $^4J_{H,H}$ 1.9 Hz, 8H, Ar), 7.85-7.88 (m, 6H, Ar), 7.92 (d, $^4J_{H,H}$ 1.8 Hz, 4H, Ar), 8.19 (dt, $^3J_{H,H}$ 8.6 Hz, $^4J_{H,H}$ 1.8 Hz, 8H, Ar). ^{13}C NMR (100 MHz, $CDCl_3$): δ = 14.4, 60.4, 125.3, 125.9, 127.3, 127.8, 128.7, 129.7, 130.3, 138.4, 138.7, 147.9, 174.3 ppm. CHN analysis – Expected: C 78.81; H 5.63;. Found (average): C 78.59; H 5.66.

Synthesis of **6 (H_4L^1)**[24]

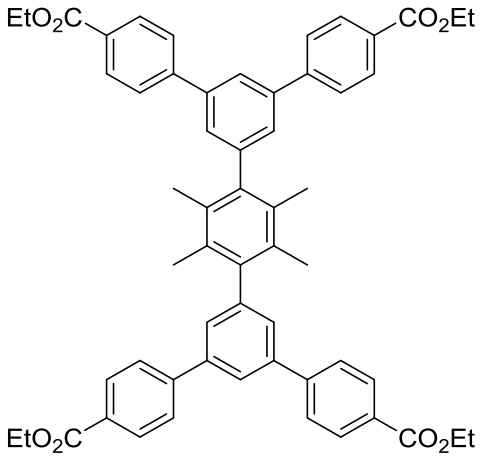


To a stirring solution of compound **5** (1.30 g, 1.58 mmol) in tetrahydrofuran (180 ml) and ethanol (180 ml) was added sodium hydroxide (2M in water, 180 ml), and the solution heated to 100 °C for 16 hours. The cooled solution was filtered, and the phases separated. The aqueous phase was extracted, acidified

with HCl (pH ~1), and the resulting suspension filtered and washed with an excess of water until the pH of the filtrate was neutral. The solid was dried to give the product as a white solid (0.77 g, 68%). (Found: [M], 709.68. $C_{46}H_{30}O_8$ requires 710.19); ^{1}H NMR (400MHz, $CDCl_3$): δ = 8.04-8.13 (m, 26H, Ar). ^{13}C NMR (100 MHz, CDCl3): δ = 125.8, 126.3, 127.9, 128.3, 130.4, 130.4, 139.7, 141.2, 141.9, 144.5, 167.6 ppm. CHN – Expected: C 77.74; H 4.25; Found (average): C 75.28; H 4.18.

The experimental values found here match those in literature.[24]

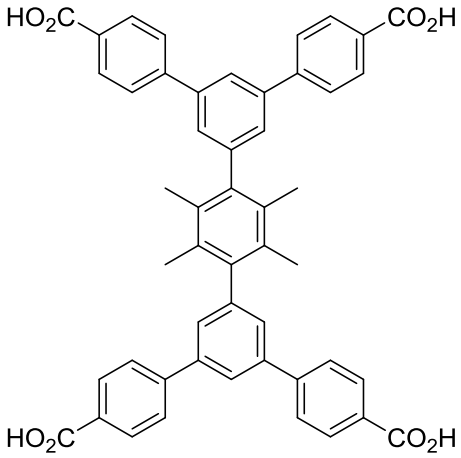
Synthesis of **7**



To a stirring, degassed solution of 3,6-dibromodurene (500 mg, 1.71 mmol), compound **4** (2.15 g, 5.13 mmol) and potassium carbonate (1.32 g, 9.57 mmol) in toluene (150 ml) and water (30 ml) at 60 °C was added tri-tert-butyl phosphine (1M in toluene, 0.79 ml, 0.79 mmol) and tris(dibenzylideneacetone)dipalladium(0) (313 mg, 0.34 mmol). This suspension was heated at 80 °C for 2 h. The workup procedure was the same as compound **5**. The product was a white solid (1.28 g, 85%). (Found: $[M-H]^-$, 878.7. $C_{58}H_{53}O_8$ requires 878.05); ^{1}H NMR (400MHz, $CDCl_3$): δ = 1.45 (t, $^3J_{H,H}$

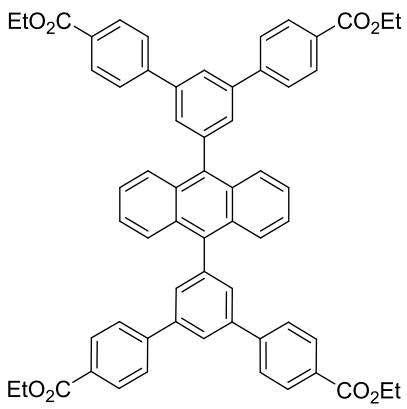
7.1 Hz, 12H, CH_3), 2.11 (s, 12H, CH_3) 4.44 (q, $^3J_{H,H}$ 7.1 Hz, 8H, CH_2), 7.55 (d, $^4J_{H,H}$ 1.7 Hz, 4H, Ar), 7.79 (m, 8H, Ar), 7.90 (t, $^4J_{H,H}$ 1.7 Hz, 2H, Ar), 8.17 (m, 8H, Ar) ppm. ^{13}C NMR (100 MHz, $CDCl_3$): δ = 14.4, 18.4, 61.1, 124.4, 127.2, 128.1, 129.6, 130.2, 132.2, 141.0, 141.1, 144.1, 145.1, 166.5 ppm. CHN – Expected: C, 79.25; H, 6.19, Found: C, 78.41; H, 6.01.

Synthesis of **8 (H_4L^{TM})**



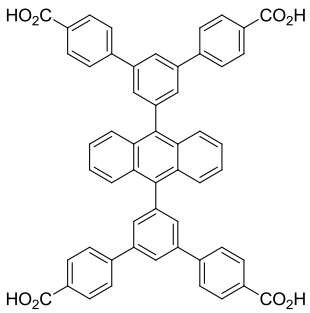
To a stirring, solution of compound **7** (1.28 g, 1.46 mmol) in tetrahydrofuran (190 ml) and ethanol (190 ml) was added NaOH (2M, 190 ml), and the solution heated to 100 °C for 23 h. The workup procedure was the same as H_4L^1. The product was an off-white solid (1.06 g, 95%). (Found: $[M+Na]^+$, 789.7. $C_{50}H_{38}O_8Na$ requires 789.3); ^{1}H NMR (400MHz, $CDCl_3$): δ = 2.03 (s, 12H, CH_3), 7.57 (d, $^4J_{H,H}$ 1.6 Hz, 4H, Ar), 7.97-8.10 (m, 16H, Ar), 8.11 (t, $^4J_{H,H}$ 1.6 Hz, 2H, Ar) ppm. ^{13}C NMR (100 MHz, $CDCl_3$): δ = 18.5, 127.7, 128.0, 128.1, 130.4, 130.5, 131.8, 140.6, 140.9, 144.1, 144.3, 167.8 ppm. CHN – Expected: C, 78.31; H, 5.00, Found: C, 77.94; H, 4.90.

Synthesis of **9**



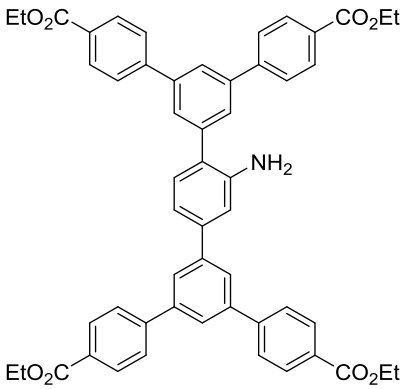
To a stirring, degassed solution of 9,10-dibromoanthracene (474 mg, 1.41 mmol), compound **4** (1.65 g, 4.23 mmol) and potassium carbonate (1.09 g, mmol) in toluene (133 ml) and water (34 ml) at 60 °C was added tri-tert-butyl phosphine (1M in toluene, 0.65 ml, 0.65 mmol) and tris(dibenzylideneacetone)dipalladium(0) (258 mg, 0.28 mmol). This suspension was heated to 80 °C for 2 h. The workup procedure was the same as compound **5**. The product was a yellow solid (1.06 g, 82%). (Found: [M], 922.21. $C_{62}H_{50}O_8$ requires 922.35); ^{1}H NMR (400MHz, $CDCl_3$): δ = 1.43 (t, $^3J_{H,H}$ 7.2 Hz, 12H, CH_3), 4.43 (q, $^3J_{H,H}$ 7.2 Hz, 8H, CH_2), 7.39-7.47 (m, 4H, Ar), 7.81-7.90 (m, 16H, Ar) 8.09 (t, $^4J_{H,H}$ 1.7 Hz, 2H, Ar), 8.17 (dt, $^3J_{H,H}$ 8.5 Hz, $^4J_{H,H}$ 1.9 Hz, 8H, Ar) ppm. ^{13}C NMR (100 MHz, $CDCl_3$): δ = 14.4, 61.1, 86.1, 107.2, 108.2, 125.6, 127.2, 129.3, 129.9 130.2, 131.4, 139.6, 141.1, 149.2, 171.4 ppm. CHN – Expected: C, 80.67; H, 5.46, Found: C, 80.42; H, 5.48.

Synthesis of **10 (H_4L^{AN})**



To a stirring, solution of compound **9** (1.00 g, 1.08 mmol) in tetrahydrofuran (140 ml) and ethanol (140 ml) was added NaOH (2M, 140 ml), and the solution heated to 100 °C for 23 hours. The workup procedure was the same as H_4L^1. The product was a brown solid (874 mg, 99%). (Found: [M], 810.06. $C_{54}H_{34}O_8$ requires 810.23); ^{1}H NMR (400MHz, $CDCl_3$): δ = 7.42-7.59 (m, 4H, Ar), 7.73-7.83 (m, 4H, Ar), 7.90 (s, 4H, Ar), 8.06 (s, 16H, Ar), 8.35 (s, 2H, Ar). ^{13}C NMR (100 MHz, $CDCl_3$): δ = 108.0, 111.4, 123.4, 123.8, 127.8, 128.2, 129.8, 130.4, 139.0, 140.8, 144.1, 156.6, 180.0 ppm. CHN – Expected: C, 79.99; H, 4.23, Found: C, 79.79; H, 4.22. The experimental values found here match those in literature.[25]

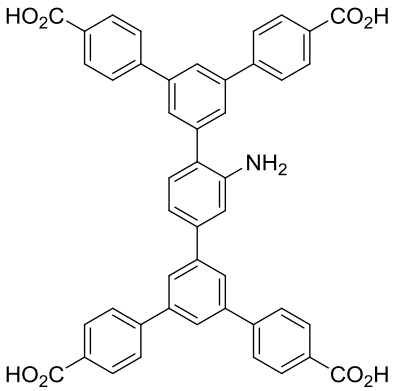
Synthesis of **11**



To a stirring, degassed solution of 2,5-dibromoaniline (500 mg, 1.99 mmol), compound **4** (2.50 g, 5.98 mmol) and potassium carbonate (1.54 g, 11.14 mmol)

in toluene (190 ml) and water (50 ml) at 60 °C was added tri-tert-butyl phosphine (1M in toluene, 0.92 ml, 0.92 mmol) and tris(dibenzylideneacetone)dipalladium(0) (368 mg, 0.40 mmol). This suspension was heated to 80 °C for 2 h. The workup procedure was the same as compound **5**. The product was a brown solid (1.17 g, 70%). (Found: [M-HCN+Na]$^+$, 832.3. $C_{53}H_{45}NaO_8$ requires 832.92); ^{1}H NMR (400MHz, $CDCl_3$): δ = 1.36 (td, $^3J_{H,H}$ 7.1, 2.2 Hz, 12H, CH_3), 4.43 (q, $^3J_{H,H}$ 7.1, 2.4 Hz, 8H, CH_2), 7.08 (s, 1H, Ar), 7.14 (dd, J=7.78, 1.53 Hz, 1H, Ar), 7.3 (dd, J=7.78, 1.53 Hz, 1H, Ar), 7.67-7.82 (m, 14H, Ar), 8.07-8.13 (m, 8H, Ar) ppm. ^{13}C NMR (100 MHz, $CDCl_3$): δ = 14.4, 61.1, 125.3, 125.4, 125.9, 127.2, 127.7, 129.7, 129.8, 130.2, 131.1, 141.4, 141.6, 144.8, 145.2, 166.4 ppm. CHN – Expected: C, 77.40; H, 5.65; N 1.67 Found: C, 78.02; H, 5.17; N, 2.02.

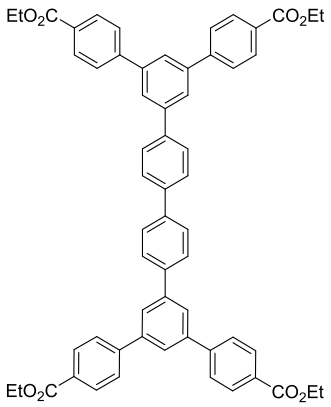
Synthesis of **12 (H_4L^{AM})**



To a stirring, solution of compound **11** (1.17 g, 1.40 mmol) in tetrahydrofuran (180 ml) and ethanol (180 ml) was added NaOH (2M, 180 ml), and the solution heated to 100 °C for 23 hours. The workup procedure was the same as H_4L^1. The product was a brown solid (914 mg, 90%). (Found: [M], 725.2. $C_{46}H_{31}NO_8$ requires 725.75); ^{1}H NMR (400MHz, $CDCl_3$): δ =7.33-7.39 (m, 2H, Ar), 7.87 (s, 2H, Ar), 7.99-8.12 (m, 21H, Ar) ppm. ^{13}C NMR (100 MHz,

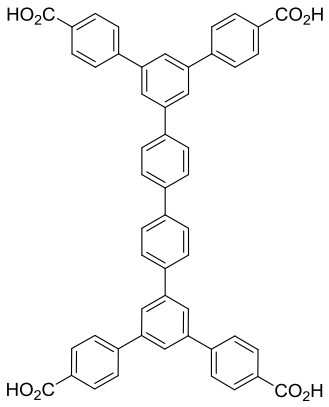
$CDCl_3$): δ = 125.3, 127.6, 127.8, 127.8, 128.6, 129.4, 130.4, 130.4, 130.5, 141.0, 141.1, 144.6, 144.6, 167.7 ppm. CHN – Expected: C, 76.13; H, 4.31; N 1.93 Found: C, 75.29; H, 4.51; N, 2.08.

Synthesis of **13**



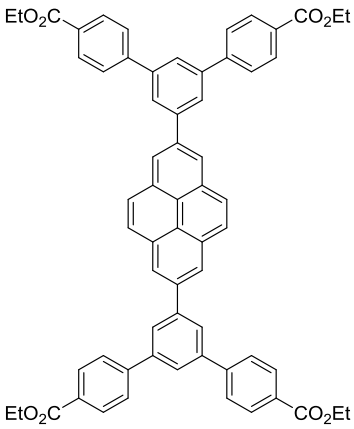
To a stirring, degassed solution of 4,4'-diiodobiphenyl (597 mg, 1.47 mmol), compound **4** (1.72 g, 4.41 mmol) and potassium carbonate (1.01 g, mmol) in toluene (180 ml) and water (45 ml) at 60 °C was added tri-tert-butyl phosphine (1M in toluene, 0.68 ml, 0.68 mmol) and tris(dibenzylideneacetone)dipalladium(0) (242 mg, 0.26 mmol). This suspension was heated to 80 °C for 3 h. The workup procedure was the same as compound **5**. The product was an off-white solid (1.15 g, 85%). (Found: [M], 898.23. $C_{60}H_{50}O_8$ requires 898.35); ^{1}H NMR (400MHz, $CDCl_3$): δ = 1.45 (t, $^3J_{H,H}$ 7.1 Hz, 12H, CH_3), 4.44 (q, $^3J_{H,H}$ 7.1 Hz, 8H, CH_2), 7.81 (dt, $^3J_{H,H}$ 8.4 Hz, $^4J_{H,H}$ 1.9 Hz, 8H, Ar), 7.83 (m, 8H, Ar) 7.86 (t, $^4J_{H,H}$ 1.7 Hz, 2H, Ar), 7.92 (d, $^4J_{H,H}$ 1.7 Hz, 4H, Ar), 8.19 (dt, $^3J_{H,H}$ 8.4 Hz, $^4J_{H,H}$ 1.9 Hz, 8H, Ar) ppm. ^{13}C NMR (100 MHz, $CDCl_3$): δ = 14.4, 61.1, 125.4, 125.9, 127.3, 127.6, 127.9, 129.7, 130.2, 139.8, 140.0, 141.6, 142.2, 145.2, 166.5 ppm. CHN – Expected: C 80.16; H 5.61; O 14.24. Found: C 79.91; H 5.62.

Synthesis of **14 (H_4L^2)**



To a stirring, solution of compound **13** (660 mg, 0.723 mmol) in tetrahydrofuran (88 ml) and ethanol (88 ml) was added NaOH (2M, 88 ml), and the solution heated to 100 °C for 16 hours. The workup procedure was the same as H_4L^1. The product was a white solid (560 mg, 98%). (Found: [M], 786.07. $C_{52}H_{34}O_8$ requires 786.23); ^{1}H NMR (400MHz, $CDCl_3$): δ = 7.92 (d, $^3J_{H,H}$ 8.3 Hz, 4H, Ar) 8.03-8.14 (m, 26H), 13.03 (s, 4H). ^{13}C NMR (100 MHz, $CDCl_3$): δ = 125.7, 127.5, 127.6, 127.9, 128.3, 130.4, 139.4, 139.5, 140.1, 141.2, 141.8, 144.5, 167.6 ppm. CHN – Expected: C 79.38; H 4.36; Found (average): C 76.08; H 4.37.

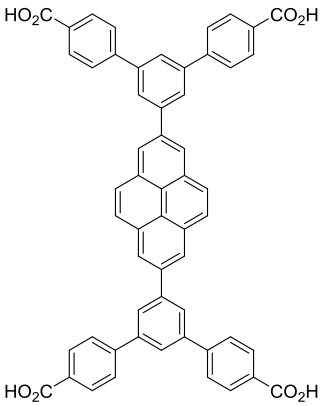
Synthesis of **15**



To a stirring, degassed solution of 2,7-dibromopyrene (500 mg, 1.39 mmol), compound **4** (1.74 g, 4.17 mmol) and potassium carbonate (1.08 g, 7.78 mmol)

in toluene (133 ml) and water (35 ml) at 60 °C was added tri-tert-butyl phosphine (1M in toluene, 0.64 ml, 0.64 mmol) and tris(dibenzylideneacetone)dipalladium(0) (258 mg, 0.28 mmol). This suspension was raised in temperature to 80 °C for 2 h. The workup procedure was the same as compound **5**. The product was a brown solid (1.12 g, 85%). (Found: [M], 947.3. $C_{64}H_{50}O_8$ requires 947.10); ^{1}H NMR (400MHz, $CDCl_3$): δ = 1.47 (t, $^3J_{H,H}$ 7.2 Hz, 12H, CH_3), 4.46 (q, $^3J_{H,H}$ 7.2 Hz, 8H, CH_2), 7.86-7.91 (m, 8H, Ar), 7.95 (t $^4J_{H,H}$ 1.6 Hz, 2H, Ar), 8.17 (d, $^4J_{H,H}$ 1.6 Hz, 4H, Ar), 8.21-8.26 (m, 12H, Ar), 8.55 (s, 4H, Ar) ppm. ^{13}C NMR (100 MHz, $CDCl_3$): δ = 14.4, 58.9, 108.2, 124.8, 126.9, 127.3, 128.5, 129.6, 130.2, 130.3, 131.5, 131.7, 137.0, 141.7, 152.4, 180.0 ppm. CHN – Expected: C 81.16; H 5.32. Found (average): C 82.01; H 5.08.

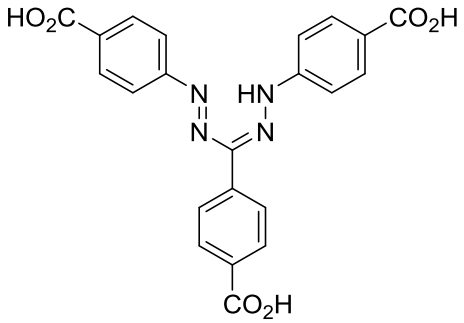
Synthesis of **16 (H_4L^{PY})**



To a stirring, solution of compound **15** (1.12 g, 1.18 mmol) in tetrahydrofuran (160 ml) and ethanol (160 ml) was added NaOH (2M, 160 ml), and the solution heated to 100 °C for 16 hours. The workup procedure was the same as H_4L^1. The product was a white solid (927 mg, 94%). (Found: [M], 834.5. $C_{56}H_{34}O_8$ requires 834.88); ^{1}H NMR (400MHz, $CDCl_3$): δ = 8.07-8.14 (m, 18H, Ar), 8.30-8.37 (m, 8H, Ar) 8.81-8.85 (m, 4H) ppm. ^{13}C NMR (100 MHz, $CDCl_3$):

δ = 123.6, 124.4, 126.7, 127.7, 127.8, 127.9, 128.5, 130.4, 131.7, 141.3, 142.5, 144.4, 144.5, 167.7 ppm. CHN – Expected: C 80.56; H 4.11. Found (average): C 78.90; H 4.31.

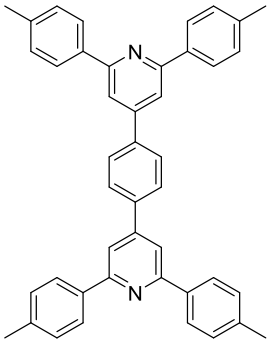
Synthesis of **17**



To a stirring solution of 4-hydrazinobenzoic acid (1.34 g, 8.79 mmol) in ethanol (15 mL) and triethylamine (2.21 mL, 1.60 g, 15.8 mmol) was added 4-formylbenzoic acid (8.80 mL, 1.32 g, 8.79 mmol) and the solution stirred for 10 minutes. Dichloromethane (50 mL) and water (50 mL) were added to form a biphasic mixture, after which sodium carbonate (3.17 g, 29.9 mmol) and tetrabutylammonium bromide (0.28 g, 0.88 mmol) were added, and the reaction mixture cooled to -5 □°C. In a separate flask, 4-aminobenzoic acid (1.23 g, 8.97 mmol) was added to a stirring solution of water (20 mL), and concentrated HCl (3.6 mL) was added, before the mixture was cooled to -5 °C. Sodium nitrite (0.69 g, 10 mmol) was added slowly to the mixture, and the reaction was cooled and stirred for 30 minutes to form a diazonium salt. This solution was then added dropwise to the biphasic reaction mixture over 10 minutes. The resulting solution was stirred for 24 hours at room temperature. The resulting solution was acidified (2M HCl) and filtered. The solid was washed with ethyl acetate to afford the pure product as a red solid (1.71 g, 45%). (Found: [M], 432.4. $C_{22}H_{16}N_4O_6$ requires 432.39); ^{1}H NMR (400MHz,

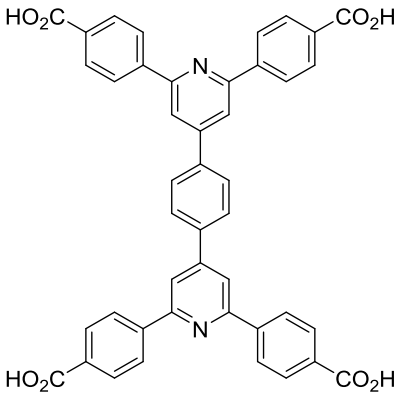
$CDCl_3$): δ = 8.06 (d, J = 8.8 Hz, 4H, Ar), 8.23 (d, J = 8.8 Hz, 4H, Ar), 8.29 (d, J = 8.6 Hz, 2H, Ar), 8.48 (d, J = 8.6 Hz, 2H, Ar) ppm. ^{13}C NMR (100 MHz, $CDCl_3$): δ = 95.1, 127.4, 128.2, 130.8, 131.4, 131.7, 135.7, 136.0, 136.4, 164.2, 166.0 ppm. CHN – Expected: C 61.11; H 3.73; N 12.96. Found (average): C 61.57; H 3.86; N 13.54.

Synthesis of **18**



4'-methylacetophenone (6.70 g, 6.67 mL, 49.93 mmol), terephthalaldehyde (1.34 g, 9.99 mmol) and NaOH pellets (2.4 g, 60 mmol) were grinded with a pestle and mortar for 20 minutes. The resultant yellow powder was added to a stirring solution of ammonium acetate (15 g, 195 mmol) in ethanol (300 mL). The solution was heated at reflux for 18 hours. The resultant precipitate was filtered, washed with water and dried. Recrystallisation from hot toluene afforded the pure product as a white solid (4.18 g, 70%). (Found: [M], 592.6. $C_{44}H_{36}N_2$ requires 592.79); ^{1}H NMR (400MHz, $CDCl_3$): δ = 2.46 (s, 12 H, CH_3), 7.35 (d, J=8.1 Hz, 8H, Ar), 7.91 (s, 8H, Ar), 8.14 (d, J= 8.1 Hz, 8H, Ar) ppm. ^{13}C NMR (100 MHz, $CDCl_3$): δ = 21.3, 116.3, 127.0, 127.9, 129.4, 136.8, 139.1, 139.7, 149.2, 157.6 ppm. CHN – Expected: C 89.15; H 6.12; N 4.73. Found (average): C 89.60; H 5.84; N 4.72.

Synthesis of **19 (H_4L^{1P})**



A slurry of compound **18** (0.5 g, 0.84 mmol), nitric acid (conc., 1 mL) and water (5 mL) was placed in a 30 mL bomb, which was consequently sealed and heated to 180 °C for 24 hours. Upon cooling, the resultant solid was washed several times with water until the pH of the washings were neutral, affording the product as an orange solid (0.59 g, 98%). (Found: $[M+H]^+$, 713.2. $C_{48}H_{29}N_2O_8$ requires 713.72); ^{1}H NMR (400MHz, $CDCl_3$): δ = 8.13 (d, J=8.24 Hz, 8H, Ar), 8.28 (s, 4H, Ar), 8.43 (s, 4H, Ar), 8.49 (d, J=8.24 Hz, 8H, Ar) ppm. ^{13}C NMR (100 MHz, CDCl3): δ = 118.1, 127.3, 128.2, 129.8, 131.4, 138.3, 142.5, 149.3, 155.8, 167.2 ppm. CHN – Expected: C 74.15; H 3.96; N 3.93. Found (average): C 74.53; H 3.55 N 4.01

References

1. Furukawa, H., Cordova, K. E., O'Keeffe, M. & Yaghi, O. M., *Science.*, **2013,** *341*, 1230444–1230444.
2. Lee, S. J. & Bae, Y. S., *J. Phys. Chem. C* **2014,** *118*, 19833–19841.
3. Simon, C. M. *et al.*, *Energy Environ. Sci.* **2015,** *8*, 1190–1199.
4. Treacy, M. M. J., Randall, K. H., Rao, S., Perry, J. A. & Chadi, D. J. *Proc. twelfth Int. Zeolite Conf.*, **1999,** *1*, 517–532.
5. Babarao, R., Dai, S. & Jiang, D., *J. Phys. Chem. C* **2011,** *115*, 8126–8135.
6. Chui, L., Charmant, O. & Williams. S. *Science* **1999,** *283*, 1148–50.
7. Chen, B., Eddaoudi, M., Hyde, S. T., O'Keeffe, M. & Yaghi, O. M., *Science* **2001,** *291*, 1021–3.
8. Amirjalayer, S., Tafipolsky, M. & Schmid, R., *J. Phys. Chem. C* **2011,** *115*, 15133–15139.
9. Spanopoulos, I. *et al.*, *J. Am. Chem. Soc.* **2016,** *138*, 1568–1574.
10. Düren, T., Sarkisov, L., Yaghi, O. M. & Snurr, R. Q., *Langmuir* **2004,** *20*, 2683–2689.
11. Smith, D. G. A. & Patkowski, K., *J. Chem. Theory Comput.* **2013,** *9*, 370–389.
12. Chen, Y. *et al. Inorg. Chem.*, **2014,** *53*, 8842–8844
13. Duan, J. *et al.*, *Chem. Commun.* **2012,** *48*, 3058.
14. Sun, D., Ma, S., Ke, Y., Collins, D. J. & Zhou, H.-C., *J. Am. Chem. Soc.* **2006,** *128*, 3896–3897.
15. Miyaura, N., Yamada, K. & Suzuki, A., *Tetrahedron Lett.* **1979,** *20*, 3437–3440.
16. Cave, G. W. V. *et al.*, *Chem. Commun.* **2000,** *36*, 2199–2200.
17. Yang, J.-X. *et al.*, *J. Am. Chem. Soc.* **2005,** *127*, 3278–3279.
18. Chae, H. K. *et al.*, *Nature* **2004,** *427*, 523–527.
19. Gándara, F., Furukawa, H., Lee, S. & Yaghi, O. M., *J. Am. Chem. Soc.* **2014,** *136*, 5271–5274.
20. Ma, S. *et al.*, *J. Am. Chem. Soc.* **2008,** *130*, 1012–1016.
21. Eddaoudi, M. *et al.*, *Science* **2002,** *295*, 469–72.
22. Furukawa, H. *et al.*, *Science*, **2010**, *329*.
23. Chen, B., Ockwig, N. W., Millward, A. R., Contreras, D. S. & Yaghi, O. M., *Angew. Chemie Int. Ed.* **2005,** *44*, 4745–4749.

24. Alezi, D. *et al.*, *J. Am. Chem. Soc.* **2015,** *137,* 13308–13318.

25. Gole, B., Bar, A. K., Mallick, A., Banerjee, R. & Mukherjee, P. S., *Chem. Commun. (Camb).* **2013,** *49,* 7439–41.

CHAPTER 3

Topology and interpenetration as a means of controlling host/guest interactions

3.1 Introduction

3.1.1 A Brief Overview of Interpenetration

Due to the nature of assembling a highly porous framework by reversible metal-carboxylate bond formation, it is often possible to obtain structures in which the framework has sufficient porosity to host two identical nets throughout, which are intertwined in such a way that they cannot be separated without the breaking of bonds. This is commonly referred to as interpenetration,[1] a pictorial example of which is shown in Figure 40.

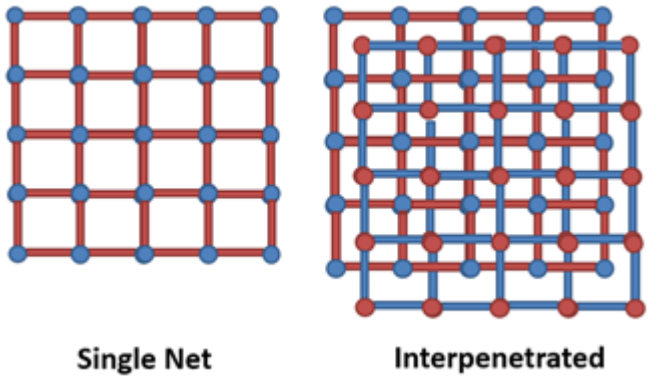


Figure 40. A schematic representation of interpenetration.

The synthesis of an interpenetrated framework can provide both positive and negative effects when compared to the non-interpenetrated analogue, depending on the desired application. For instance, the presence of two nets can reduce the porosity up to half that of the non-interpenetrated framework,[2] thus negatively impacting any high pressure gas uptake.[3] This has been demonstrated previously in the group, by a series of isoreticular MOFs (the NOTT-10X series, Figure 41),[4] which was designed in order to extend pore size and thus porosity (as discussed in Chapter 2); however, upon extension of the ligand series cores beyond two phenyl rings (NOTT-104), the framework became sufficiently porous to interpenetrate, and the porosity fell to 41.0%, a sharp 34.5% drop

compared to the steady increase of ~6% per additional phenyl spacer seen to this point.

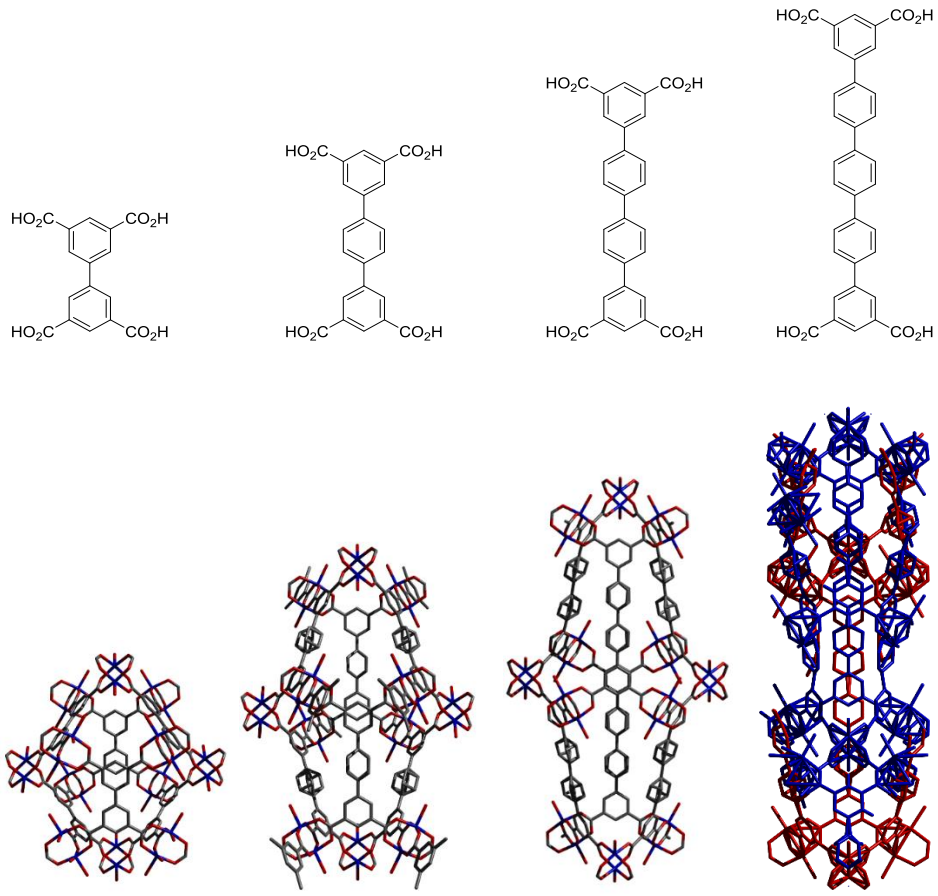


Figure 41. NOTT-10X frameworks as evidence of decrease in porosity upon over-extension of ligand series.[4]

Positive effects of interpenetration can also be seen, however, as the effect of a supporting framework where there would otherwise be just a pore can in fact bolster the stability of an otherwise fragile framework.[5] A relevant example of this is shown by Zhang *et al.*,[6] in Figure 42 below, where a non-interpenetrated photoactive MOF with an incorporated Ru metalloligand shows promising photocatalytic activity, yet is not very stable, and shows degradation over time. However, the incorporation of a second net by careful manipulation of the

ligand used in MOF synthesis (changing the position of the carboxylates from the 4,4' position to 5,5') gives the framework much greater stability, showing good photocatalytic durability and recyclability, and an increase in thermal and photo-stability in comparison with the non-interpenetrated counterpart.

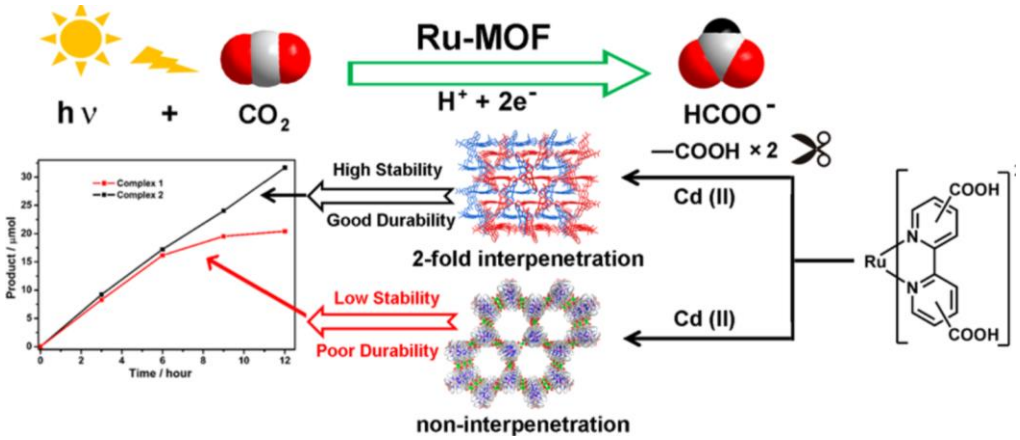


Figure 42. Improvement of stability of photocatalytic Cd (II) MOF by encouragement of interpenetration in the framework.[6]

Furthermore, any reduction of porosity which occurs due to interpenetration can itself provide superior benefits compared to the corresponding highly porous single net framework, as any positive framework-guest interactions arising from functional groups or ligand properties are effectively doubled in the unit cell upon addition of a second net.[7] This can be most strikingly seen in MOF-5, which has moderate hydrogen uptake of 0.5 wt% at 1 bar, 77 K, in its conventional non-interpenetrated form,[8] yet when interpenetration is introduced, the sorption qualities improve, with an uptake of 1.82 wt% under the same conditions, despite a dramatic drop in BET surface area from ~3,000 m^2/g to 1,100 m^2/g.[9]

3.1.2 Classes of Interpenetration

As there are many ways in which nets can interpenetrate, and indeed the number of times this can occur, there are particular naming conventions to aid

descriptions of interpenetrated frameworks. The most simple of these is the degree of interpenetration, Z, described as 2-fold, 3-fold etc., which refers to the number of interpenetrated nets present in the framework, where 2-fold indicates that the framework is formed by two identical interpenetrated nets. This can become more complex, however, as it is sometimes possible to have partially interpenetrated frameworks, as shown in Figure 43, which depicts NOTT-202.[10] This work done previously in the group demonstrates the isolation of a partially interpenetrated structure, where the interpenetrating second net has ~0.75 occupancy throughout the framework. Interestingly, higher temperature conditions resulted in the synthesis of a four-fold interpenetrated analogue.

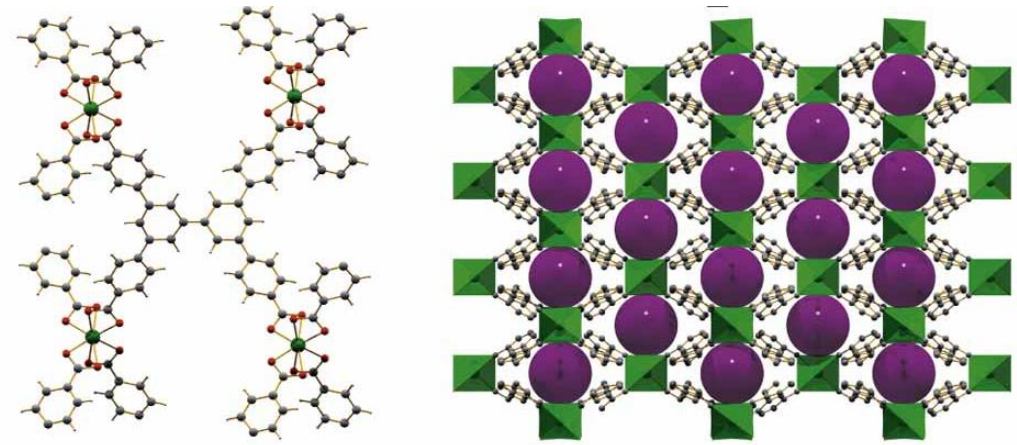


Figure 43. Connectivity of ligand, and overall view of the partially interpenetrated NOTT-202.[10]

More recently, Ferguson *et al*. showed the isolation of non-interpenetrated, partially interpenetrated and two-fold interpenetrated MOFs synthesised from a racemic mixture of ligand $H_2$1 (shown in Figure 44), controlled solely by the solvent used and the reaction time of the solvothermal synthesis. This method could also be used for separation of a racemic mixture, as the non-interpenetrated (α-MUF-9) and fully interpenetrated (β-MUF-9) MOFs were enantiomerically pure.[11]

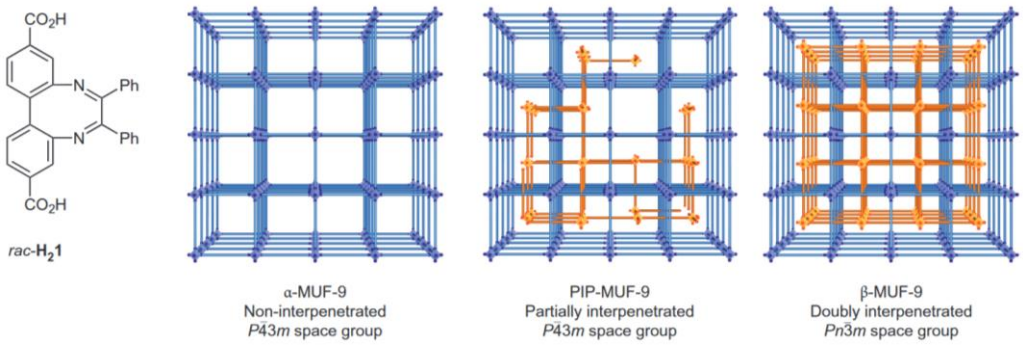


Figure 44. Demonstration of control over interpenetration and partial interpenetration in the MUF-9 series.[11]

The other pertinent information required to effectively describe an interpenetrated framework is how the two nets are systematically related to one another in the framework; this is referred to as the class of interpenetration. There are three different class types, I, II and III, the first two of which can be subdivided into categories a and b.[12] Class I frameworks are those in which the nets are exclusively related to one another by translations, in this instance the degree of interpenetration Z corresponds to the translational degree of interpenetration Z_t. The subclasses a and b are determined by the presence or lack thereof of a full interpenetration vector. For class Ia, all the independent nets are related by a single vector, class Ib therefore are those situations where numerous translational operations must be performed to obtain the different nets.

Class II frameworks are those in which the nets are related solely from symmetry elements present in the space group of the crystal (most commonly inversion centres). The degree of interpenetration now is derived from the non-translational degree Z_n, which is essentially the order of the symmetry element used to generate the interpenetrated array from the single net. The subclasses are now determined, as with class I interpenetration, on the number of symmetry

elements present (IIa structures have a unique full interpenetration symmetry element where IIb structures contain various partial elements. Cases of IIb are extremely rare). Figure 45 shows a comparison between class Ia and IIa structures of the ths topology.

Finally, Class III structures are those in which the interpenetrated nets are generated by both translational and symmetry elements of the single net. The degree of interpenetration is now the product of Z_t x Z_n. There is now no need to further sub-divide this category as there are always multiple elements present.

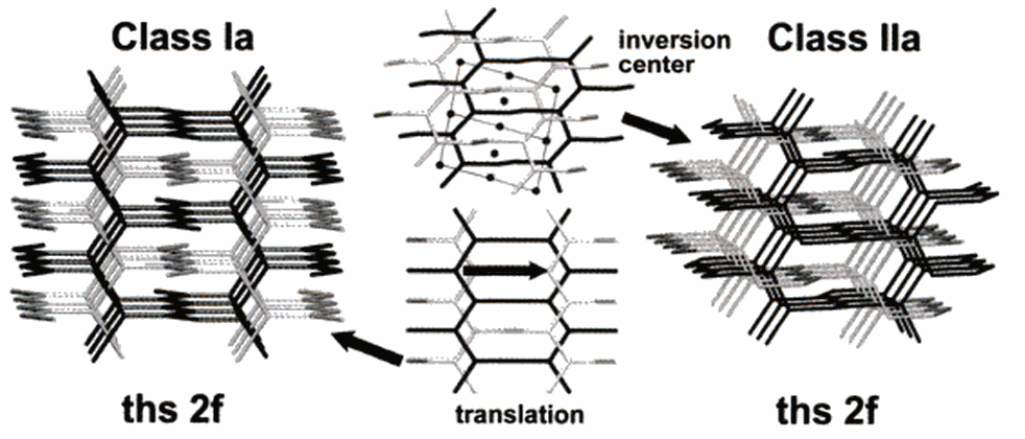


Figure 45. Examples of different classes of interpenetration in the **ths** topology.[12]

In order to compare 3-dimensional metal-organic frameworks in space, it is necessary to give names to the overall description of the periodic net and its connectivity in 3D space (its topology). The naming system commonly followed is the reticular chemistry structural resource's (RCSR's) 3 letters notation.[13] The names come primarily from known chemical compounds, and the similarity of the connectivity of the nodes. For instance, a framework made up of 4-connected nodes in a diamond-like framework is given the symbol **dia**

(lower case, bold). This allows ease of comparison between structurally similar frameworks. There can also be derived nets with extensions after the topology (e.g. **dia-a**, **dia-b**), which are explored in depth by O'Keefe *et. al*.[13]

The control of interpenetration and classes thereof are as such very important to the synthetic MOF chemist as they can prove very difficult to predict or control.

3.1.3 Methods of Preventing Interpenetration

Due to the complexity of crystal growth mechanisms in solution, there is no simple, versatile method of preventing interpenetration within a framework, however there are many methods which have successfully been employed in the past to obtain non-interpenetrated MOFs; a varied selection of these is presented below.

Bulky solvent

One of the most common and logical methods of obtaining a single net framework is centred on the fact that the cause of interpenetration is often due to the large void space in the framework, which allows a second net to inhabit this area, thus causing interpenetration.[1] By filling the pores with a bulky solvent as the MOF is forming, the steric hindrance thus caused when the seed of a second net approaches this space can be sufficient to prevent any level of interpenetration.[14] This has been proven to be an effective method by Lin *et al.*, as seen in Figure 46 below.[15] This also demonstrates the fascinating effect that chirality can have on interpenetration also, as it is only after first introducing interpenetration into the framework by changing to a racemic mixture of ligand that it was necessary to use a bulkier solvent, in this case diethylformamide

(DEF), to obtain the non-interpenetrated racemic framework shown below in green.

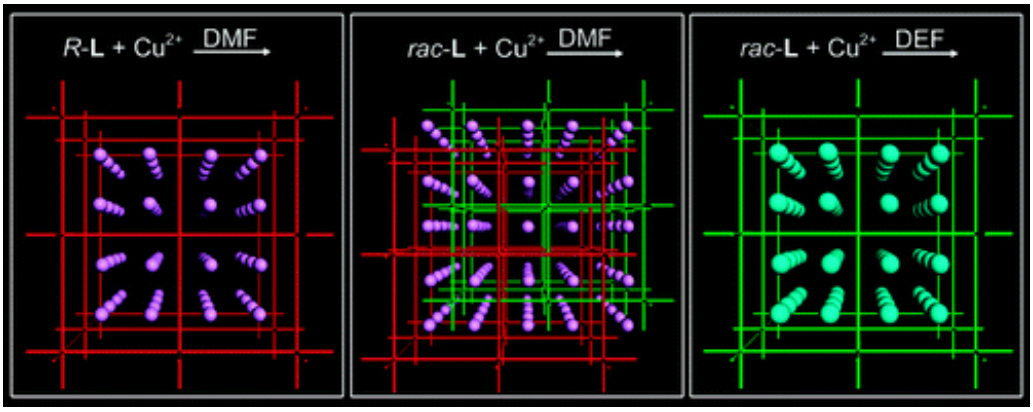


Figure 46. Demonstration of the importance of chirality and solvent templating in the interpenetration of MOFs.[15]

A main advantage of this method is that after the solvothermal synthesis is complete and the framework has been formed, removal of the solvent and subsequent activation leaves completely uninhibited porosity in the framework.

Bulky ligand

A variant on the theory of filling the void space during synthesis of the MOF involves synthesising an analogue to the linker used in the interpenetrated framework, this time incorporating a bulky moiety which can protrude from the ligand into the pore space once the MOF is formed. The extra steric hindrance provided from this extension of the ligand (between both the solvent used in synthesis, and any ligands attempting to occupy the space in between the single net framework) can sometimes prove enough to give the non-interpenetrated framework as a phase pure product. The Hupp group demonstrate this theory excellently in the bromination of 4,4',4'',4'''-benzene-1,2,4,5-tetrayl-terabenzoic acid (shown in Figure 47 below as **L1** and **L2**), to inhibit the formation of interpenetrated pillared MOFs which were present when the non-

brominated ligand was used.[16] The extent of success of this method was also explored, by pillaring the brominated and non-brominated ligands **L1** and **L2** with a variety of struts of increasing length. As shown in Figure 48, this worked highly effectively, and thus formed a series of isoreticular non-interpenetrated MOFs.

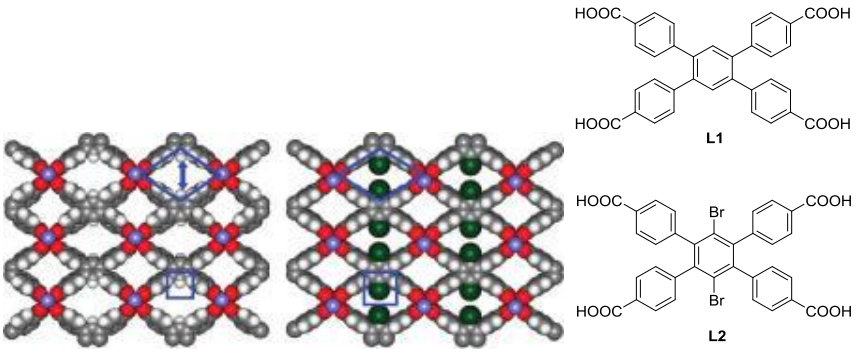


Figure 47. 2D sheets of MOF formed from **L1** and **L2**, with extension of ligand into pore highlighted (top), and set of ligands used to generate 3D interpenetrated and non-interpenetrated MOFs (bottom).[16]

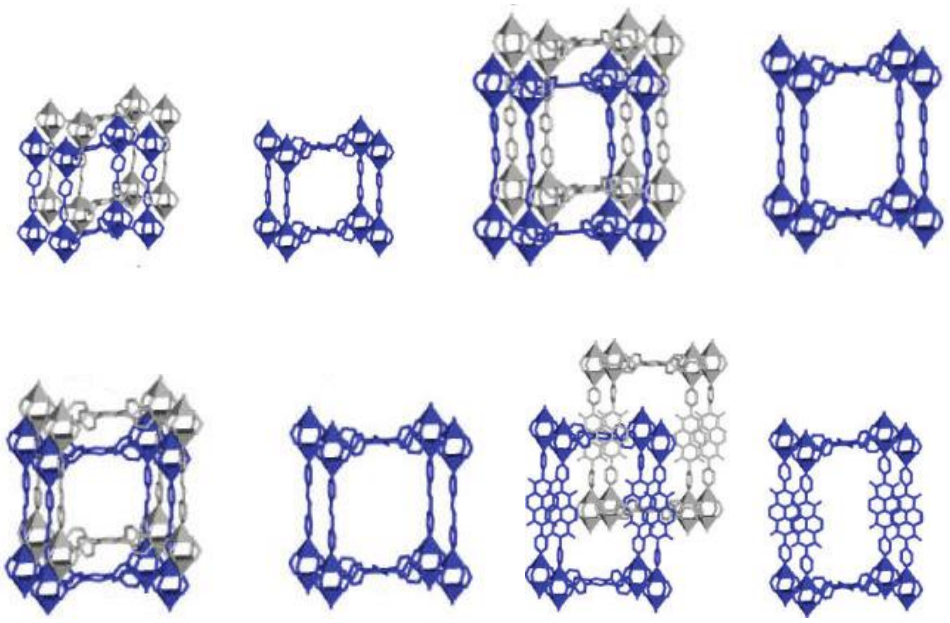


Figure 48. Isoreticular series' of interpenetrated and non-interpenetrated pillared MOFs, demonstrating the striking effect of protruding bromine groups from **L6**.[16]

This method of preventing interpenetration does slightly decrease the idealised porosity of the single net framework, however, as the bulky group used in the

ligand synthesis remains in the pore after activation, therefore reducing porosity a small amount. It can be possible to use a labile group, however, if there is an appropriate functional group to which it can be attached on the original ligand, such as using BOC (tert-butoxycarbonyl) to protect a pendant amine group on a ligand prior to solvothermal synthesis. This thermolabile group can be later removed to generate a non-interpenetrated MOF with enhanced porosity, as first demonstrated by Deshpande *et al.* (shown below in Figure 49).[17] This method of preventing interpenetration does have its drawbacks, however, as it requires two additional steps, a framework stable to the thermolysis conditions, and a protecting group that won't interfere with either the hydrolysis of the carboxylates of the ligand. As such, this method is not as preferable as the use of bulky solvents.

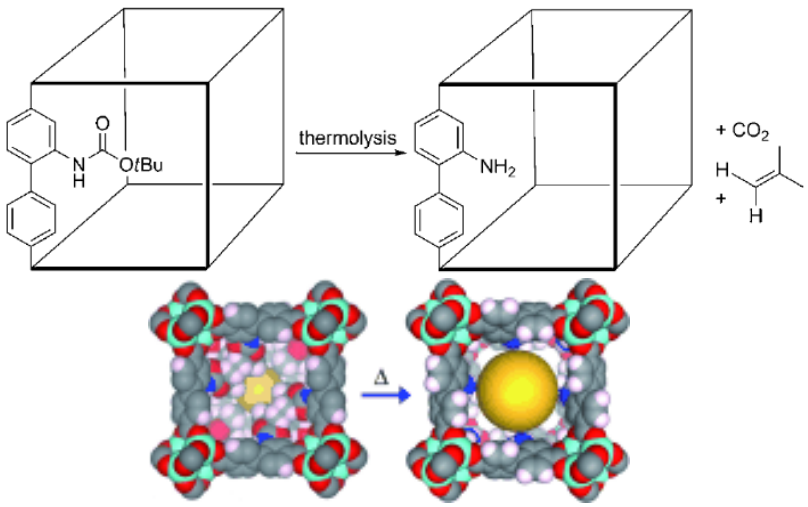


Figure 49. Schematic representation of post-synthetic termolysis of BOC-protected amine group (top), and VDW depiction of the same (bottom).[17]

Temperature and acidity

Alongside these methods of preventing interpenetration with steric bulk and hindrance, are those which utilise other factors which influence the growth of

crystals, such as altering the temperature of synthesis to selectively obtain either the kinetic or thermodynamic product, or changing the acidity of the system, which in turn has major implications on both the bonds which are reversibly forming and breaking during synthesis and the equilibrium of the carboxylic acid/carboxylate anions which determine the rate of reaction and thus the thermodynamic or kinetic product selectivity.

The former method of controlling synthesis by altering the temperature of the system has been shown to work in a variety of cases,[2,18,19,20] such as the Cd MOFs synthesised by the Zaworotko group,[20] and shown in Figure 50. These show how an increase in temperature or concentration can lead to interpenetration, while a low temperature/concentration reaction generates the non-interpenetrated analogue. The effect of temperature here controls whether or not the thermodynamic product is isolated, with higher temperatures preferring the more thermodynamically stable, denser interpenetrated structure, and *vice versa*. The dilution of synthesis conditions simply reduces the probability of a second net forming in the void of the first. This method is less often used, however, as the nuanced changes required in synthesis conditions (±0.05M and ±20 °C in this instance) can be problematic and lead to mixtures of products.

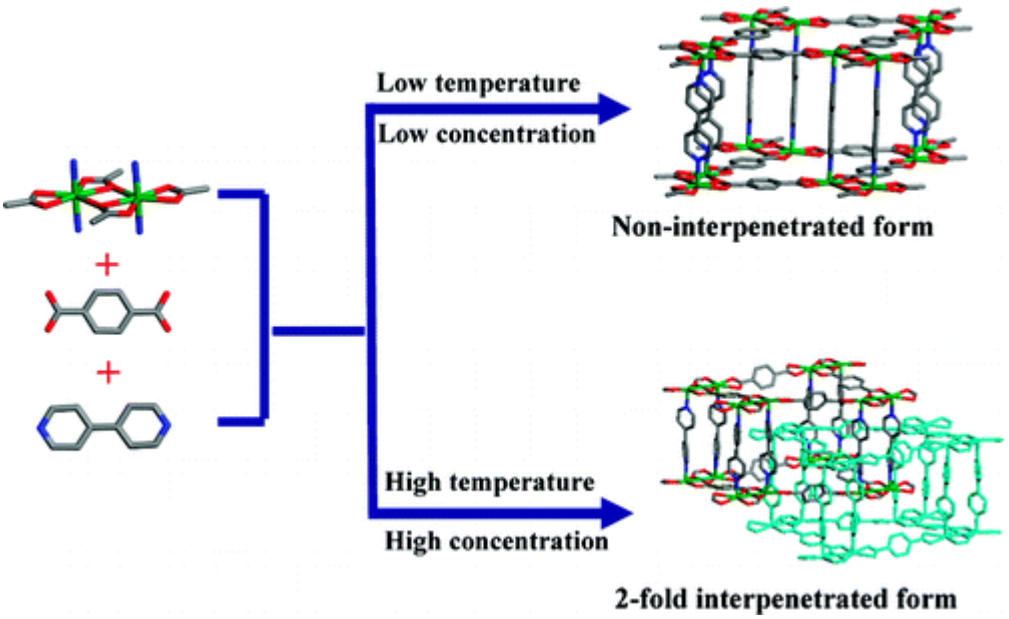


Figure 50. Effect of temperature and concentration on state of interpenetration in MOFs.[20]

As with a change in synthesis temperature, it is also possible to impact the level of interpenetration by varying the acidity of reaction. The most common correlation between acidity and interpenetration is the higher the acid content, the lower the level of interpenetration – this is most likely due to the subsequent reduced rate of deprotonation of ligand, and as such nucleation for MOF crystal growth. This results in fewer independent frameworks forming, and reduces the likelihood of two growing in a catenated fashion. This mirrors the effect when lowering the temperature.[21]

Phase purity problems arising from interpenetration

Due to the wide variety of routes to different MOF structures with various interpenetration levels capable of being formed from the same starting ligand and metal salt, as discussed above, there is often a phase purity problem which arises from the many available products.[20] This is particularly problematic as MOFs are not able to be purified *via* traditional routes due to their inherent

insolubility in organic solvents and general stability. There have been methods devised to separate different MOF structures based upon their density and therefore whether they float in a particular solvent, chosen with a density which lies between the two.[22] Purifying a mixture of compounds is not ideal, however, as it decreases the yield, so often a wide variety of conditions are trialled in order to obtain phase pure products in bulk; the success of which is measured *via* PXRD.

3.1.4 Aims and Objectives

This chapter first describes the synthesis, characterisation and theoretical gas sorption properties of a series of MOFs synthesised from ligand H_4L^1, which differ in their levels and classes of interpenetration, which in turn are controlled by subtle changes to the solvothermal conditions. The most promising candidate of these, the non-interpenetrated structure, is then taken as the base for a series of isoreticular non-interpenetrated frameworks all of **lvt** topology, synthesised from the series of ligands discussed in Chapter 2. The frameworks are all analysed rapidly using computational theory to identify the highest performing MOF, which is subsequently activated and measured experimentally. Problems arising from this are discussed, along with possible methods of overcoming the instability which is prevalent throughout the series.

3.2 Results and Discussion

The synthesis of H_4L^1, as detailed in Chapter 2, is highly versatile due to the central dihalogenated core, and allows for synthesis of a wide variety of tetracarboxylate linkers (the H_4L^X series), which are used throughout this chapter. The shortest un-functionalised ligand, H_4L^1 was the first synthesised and indeed the natural starting place for the generation of a series of frameworks to probe methane and carbon dioxide high pressure working capacities.

Solvothermal synthesis of MFM-191

A solution of H_4L^1 (10 mg, 0.014 mmol) and $Cu(NO_3)_2{\cdot}2.5H_2O$ (25 mg, 0.11 mmol) in dimethylformamide (3 mL), acetonitrile (1 mL), dimethylsulfoxide (1 mL) and 0.1M HCl (1 mL) was heated to 80 °C in a sealed 8 mL glass vial, and maintained at this temperature for 24 hours to yield rhombohedral blue single crystals of MFM-191 with the molecular formula $[Cu_2L^1(H_2O)_2].solv_x$ in a 75% yield. The as-synthesised single crystals were insoluble in organic solvents, and the crystal structure was determined by SCXRD.

3.2.1 Crystal Structure Description of MFM-191

Table 2. Crystallographic information for MFM-191.

Crystal Data	
Formula = $C_{23}H_{15}O_5Cu$	Orthorhombic, *Cmca*
a = 37.7326(9) Å	V = 15119.0 (6) $Å^3$
b = 29.4510(6) Å	Mr = 471.80
c = 13.6053(4) Å	Z = 16
Density = 0.764229 g/cm^3	
Data Collection and Refinement	
Rint = 0.024	$R[F2 > 2\sigma(F2)]$ = 0.044
$wR(F^2)$ = 0.144	

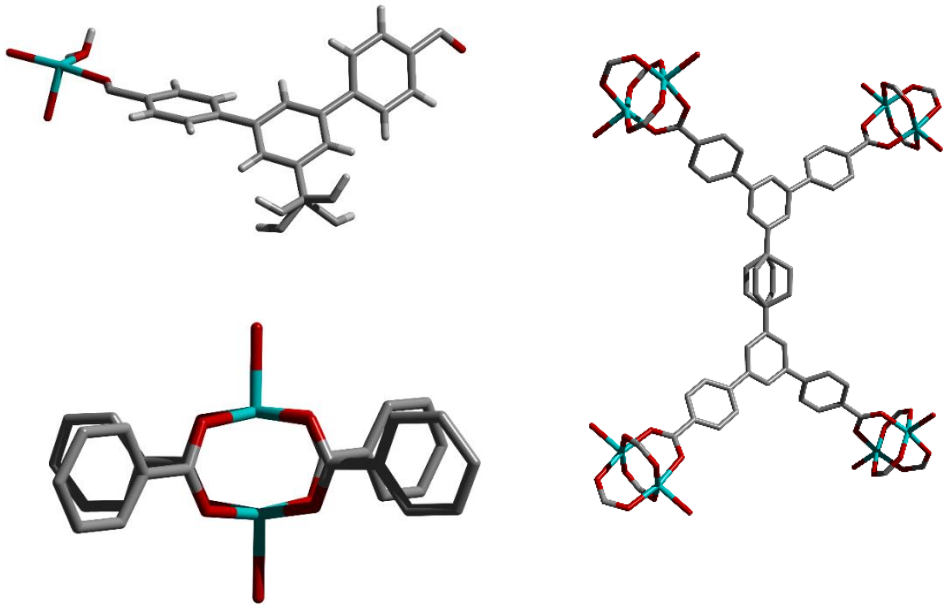


Figure 51. Asymmetric unit and paddlewheel of MFM-191 (left), and coordination mode of ligand L^1 showing the central phenyl ring disordered over two positions.

MFM-191 crystallises in the orthorhombic space group *Cmca*, with unit cell parameters: a = 37.7326(9) Å, b = 29.4510(6) Å and c = 13.6053(4) Å, and a volume of V = 15119.0 (6) $Å^3$. Solving the structure by single-crystal x-ray diffraction techniques showed that the framework contains Cu(II) paddlewheel secondary building units with 4 points of extension. Two Cu(II) ions, joined by carboxylate anions from four separate ligands comprise the $Cu_2(RCO_2)_4$ 'paddlewheel' units (shown in Figure 51). The Cu(II) ions are ostensibly in a square-based pyramidal geometry, with an apical neutral water molecule which can be removed to give a distorted square planar geometry, with each of the four corners binding to an oxygen from four different ligands. The removal of the apical water molecule is energetically favoured due to the Jahn-Teller effect,[23] which applies to metal complexes either in the d^9 configuration (such as copper), or in the d^4 high spin or d^7 low spin state (ie. molecules with a doubly degenerate ground state), and means that the complex must distort along one axis (in this

case the axis with the apical water molecules) to remove this degeneracy and lower the overall energy of the system. This can be seen in the crystal structure by examining the bond lengths (Figure 52), as the four equatorial Cu-O bonds have been shortened to 1.96 Å, while the apical Cu-O bonds are 2.14 Å in length. This lengthening of the apical bond in the crystal structure leads to a situation where the water molecules can be readily removed upon heating under vacuum, thus generating open coordination sites.

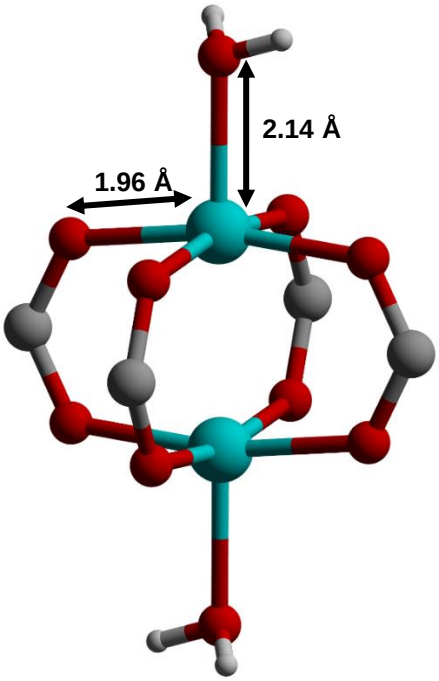


Figure 52. Cu-O distances in MFM-191, demonstrating the Jahn-Teller distortion and lengthening of the Cu-O bonds for the apical water molecules.

These binuclear copper clusters are formed at the four points of extension on each ligand, giving it a 4,4-connected net, as each ligand is connected to four paddlewheels and each paddlewheel is connected to four ligands. The ligand displays some slight twisting between the rings, but overall remains in a predominantly square planar geometry, as shown in Figure 53, which, as it is connected at all four points to paddlewheels which also extend along square planar dimensions, results in a 3 dimensional structure with an **lvt** topology. The

simplified net used to identify the topology is shown in Figure 54, where the connectivity of the paddlewheel (shown in blue) and the ligand (shown in grey) can be easily seen.

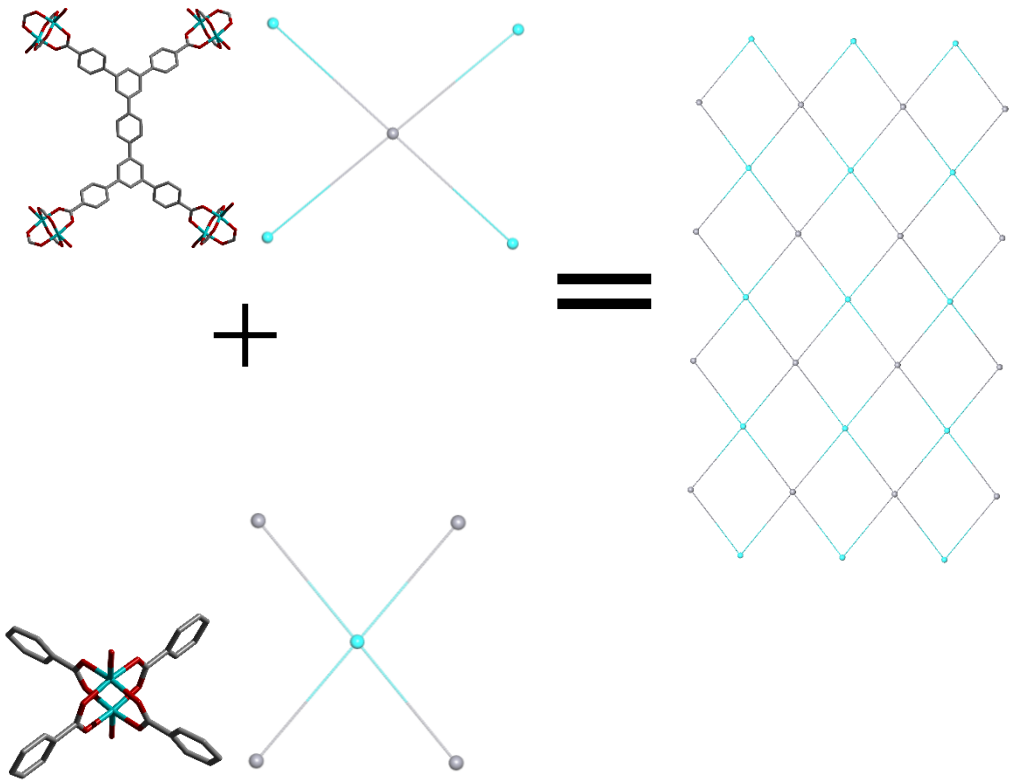


Figure 54. Topological breakdown (left) and overview (right) of **lvt** framework.

When determining the topology, it is necessary to simplify the structure into nodes. In the case of **lvt**, the entire 3D structure can be described by two square planar 4-connected nodes, however it is always prudent to evaluate how accurately the simplification describes the real crystal structure. In the case of MFM-191, for example, an **lvt** topological identification requires the ligand to be simplified to a single 4-connected node, as shown in Figure 54, which is not an entirely accurate representation of the structure. To truly describe the network, the ligand must be considered as two 3-connected nodes, shown in Figure 55, giving it a new topology, which is a 3,4-connected net with stoichiometry $(3\text{-c})_2(4\text{-c})$. This becomes particularly important when

functionalising and extending the central core of the ligand, as an **lvt** topology would be less and less suitable for describing the structures. As shown in Figure 55, even with the shortest ligand (L^1), the description of the it as a two 3-connected nodes gives a network noticeably closer in resemblance to MFM-191. However, simplification of the net does allow comparison with other similar structures in literature with the same compressibility perpendicular to the main pore axis, and therefore this simplification has its advantages, and as such the term **lvt** will be used throughout this thesis.

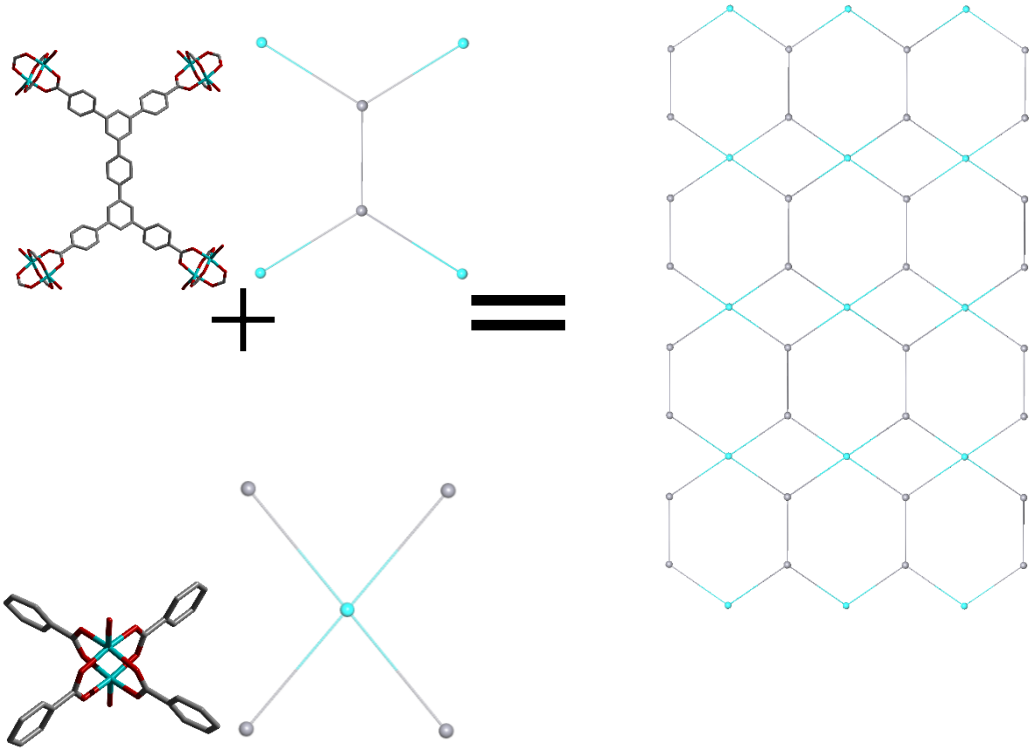


Figure 55. Treatment of ligand H_4L^1 as two 3-connected nodes, resulting in new topology.

Analysis of interpenetration

One of the interesting features of the MFM-191 framework is that it exhibits two-fold interpenetration. As shown in Figure 56, the two nets are identical, and are related to one another by a symmetry operation (inversion), which places this in interpenetration class IIa (subclass a rather than b as there is only a single

symmetry operation relating the two nets). Due to the presence of a second net, the channels down the *a* and *b* axis are blocked, while only the *c* axis remains porous. Figures 56 and 57 display how the two nets are interwoven, the red and blue wire-frame diagrams each depict a single net, and together show the level of interpenetration. The two channels (along the *c* axis) which remain available despite interpenetration have dimensions recorded in table 3.

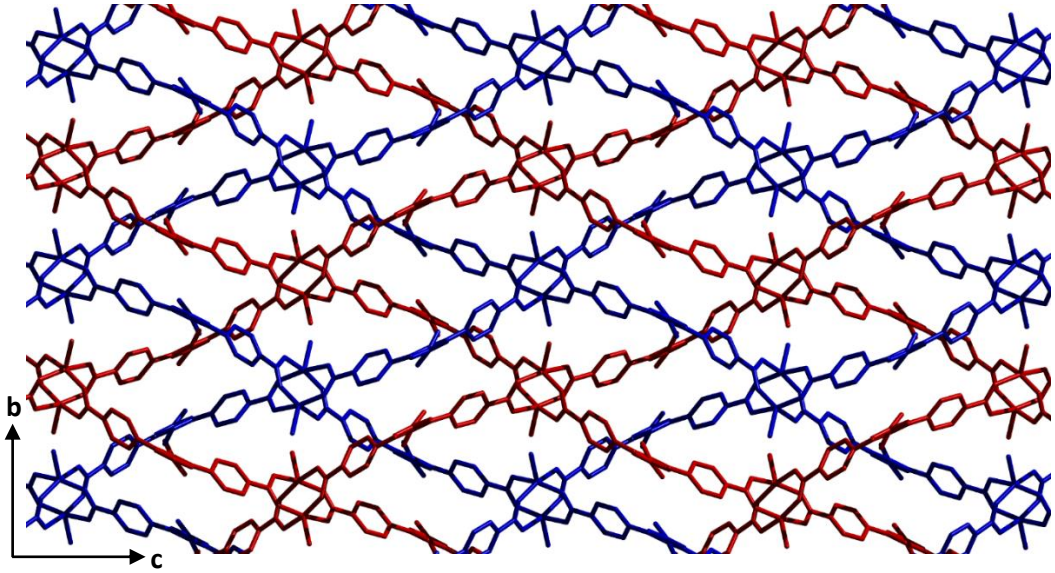


Figure 56. View along the *a* axis depicting interpenetration in MFM-191.

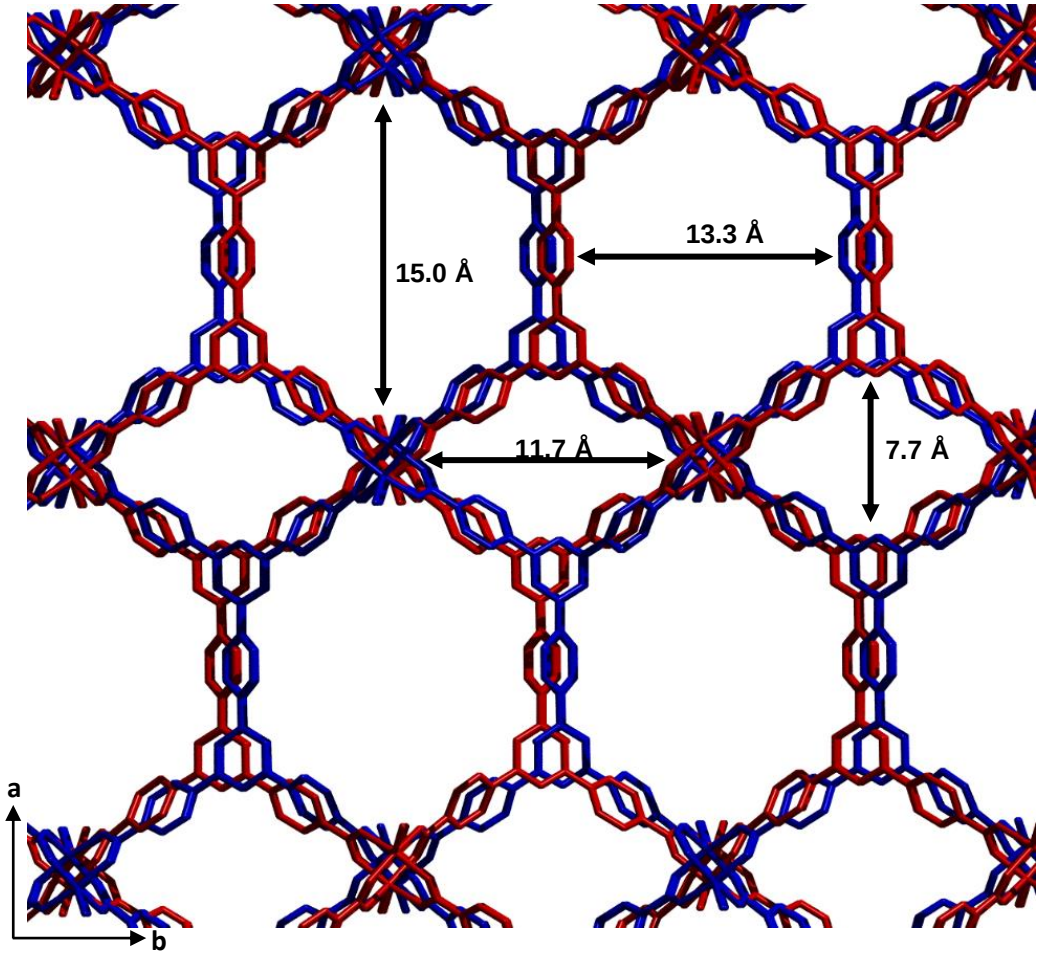


Figure 57. View along the *c* axis depicting pore dimensions in MFM-191. Distances are measured from the centre of each atom.

The 1D pore system along the 001 direction contains a solvent accessible volume of 60.3% of the total cell volume (determined by the volume situated at 1.2 Å from the Van der Waals surface of the framework, as calculated by PLATON SOLV).[24] Therefore the structure was shown to have a reasonably large porosity, with the potential to increase that further if the interpenetration could be avoided.

Further examination of the framework showed the presence of what appeared to be hydrogen bonding between the paddlewheels of adjacent networks (Figure 58) in MFM-191, leading to the hypothesis that a decrease in the pH of the system could disrupt the hydrogen bonding network.

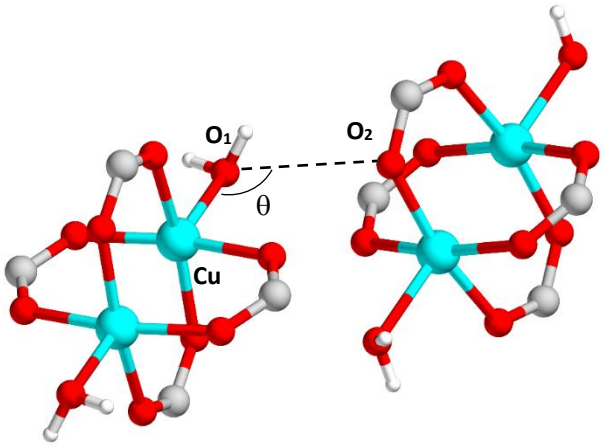


Figure 58. Hydrogen bonding between two paddlewheels from interpenetrating nets in MFM-191.

Table 3. Values from MFM-191 and MFM-192 crystal structures as evidence of H-bonding between paddlewheels.

Distance O_1-O_2 (Å)	2.99
Angle Cu-O-O	102.9°

As shown in Table 3, there is strong evidence of hydrogen bonding in MFM-191 between the apical water molecule on the copper paddlewheel of one net and one of the oxygens from the carboxylate of the second net (typical O_1-O_2 distances in crystal structures lie between 2.16-3.16 Å).[25]

PXRD and TGA of MFM-191

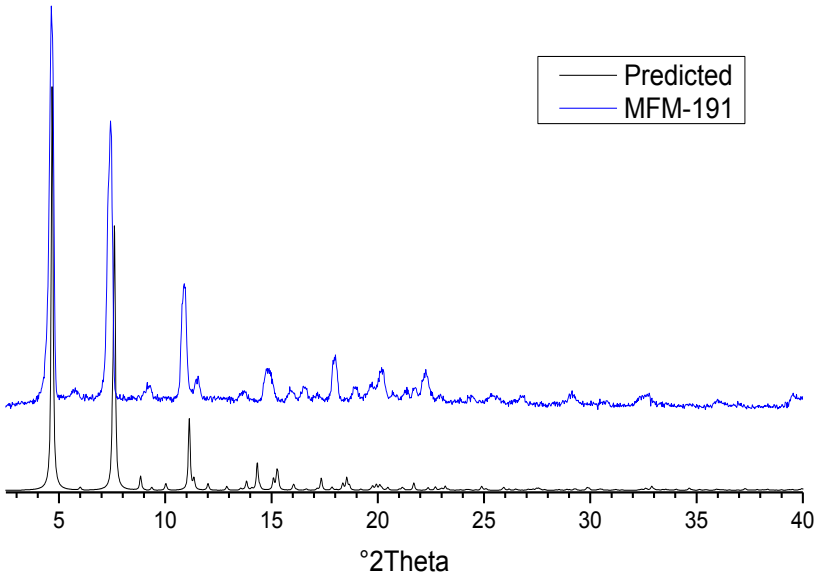


Figure 59. PXRD of simulated and as synthesised MFM-191.

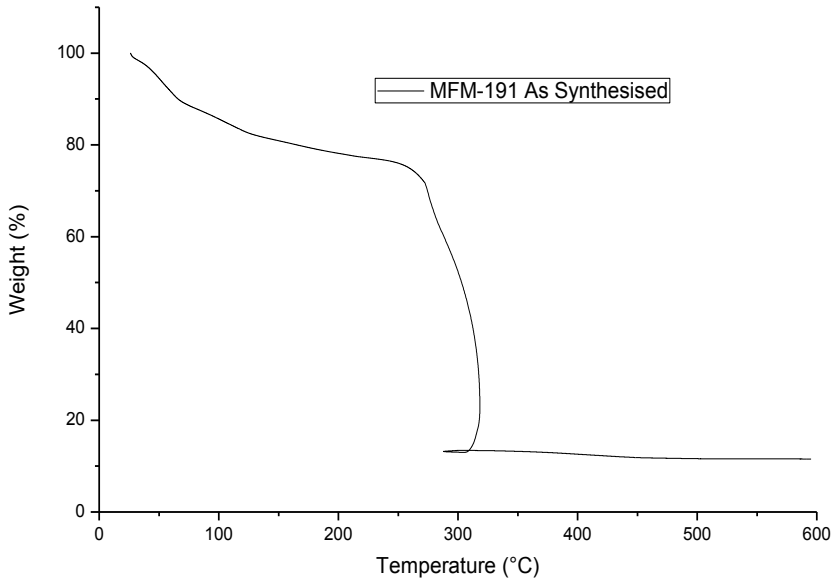


Figure 60. TGA of as synthesised MFM-191 in air.

Solvothermal synthesis of MFM-192

A solution of H_4L^1 (10 mg, 0.014 mmol) and $Cu(NO_3)_2{\cdot}2.5H_2O$ (25 mg, 0.11 mmol) in DEF (3 mL), acetonitrile (1 mL) and 0.1M HCl (1 mL) was heated to 80 °C in an 8 mL glass vial, and maintained at this temperature for 24 hours to yield blue rod shaped single crystals of MFM-192 with the molecular formula $[Cu_2EIB1(H_2O)_2].solv_x$ in an 80% yield. The as-synthesised single crystals were insoluble in organic solvents, and the crystal structure determined by SCXRD. The bulk phase purity of the solid was analysed using powder x-ray diffraction.

3.2.2 Crystal Structure Description of MFM-192.

Table 4. Crystallographic information for MFM-192.

Crystal Data	
Formula = $C_{23}H_{15}O_5Cu$	Orthorhombic, *Pbcm*
a = 9.37961(9) Å	V = 9487.97(15) Å^3
b = 28.3973(2) Å	Mr = 434.89
c = 35.6214(3) Å	Z = 8
Density = 0.608897 g/cm^3	
Data Collection and Refinement	
Rint = 0.0159	$R[F2 > 2\sigma(F2)]$ = 0.0808
$wR(F^2)$ = 0.2641	

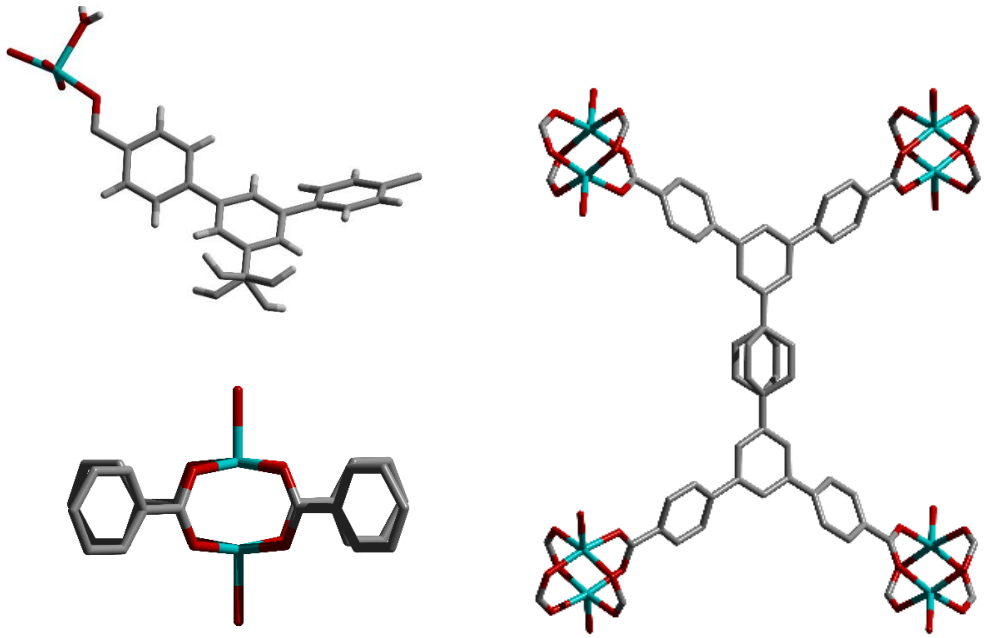


Figure 61. Asymmetric unit and paddlewheel of MFM-192 (left), and coordination mode of ligand L^1 showing the central phenyl ring disordered over two positions.

MFM-192 crystallises in the orthorhombic space group *Pbcm*, with unit cell parameters: a = 9.37961(9) Å, b = 28.3973(2) Å and c = 35.6214(3) Å, and a volume of V = 9487.97(15) $Å^3$. The framework contained the same copper paddlewheel secondary building units as MFM-191 (shown in Figure 61). The 3 dimensional structure of a single net can be described as isoreticular with respect to MFM-191, due to the same 4,4-connectivity and **lvt** topology it exhibits.

Interestingly, the use of a bulkier solvent failed to prevent interpenetration in this instance, and the structure once again is comprised of two interpenetrating nets. However, the change from dimethylformamide (DMF) to diethylformamide (DEF) did have an impact on the class of interpenetration present in the framework, such that the two nets are now related to one another by a single translational operation (rather than the inversion centre in MFM-191), placing the system in class Ia. The use of a bulkier solvent therefore

clearly impacted the growth of the crystal; while the individual nets are retained, the relationship between them is modified, generating a more open 3D pore system with guest accessible channels along the *a*, *b* and *c* axes, suggesting an increase in porosity. The pore dimensions are comparable to MFM-191, and are shown in Figure 62.

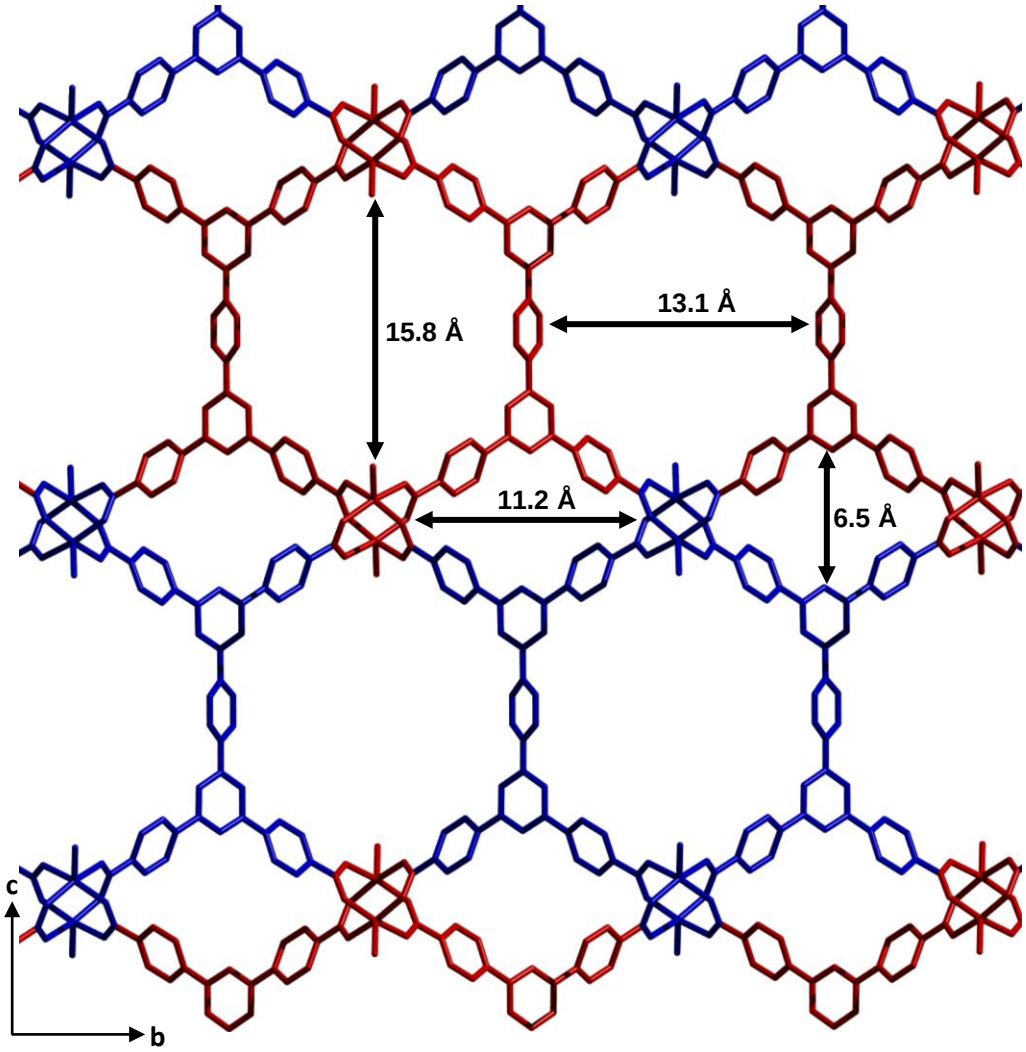


Figure 62. View along the *a* axis, showing the pore dimensions in MFM-192.

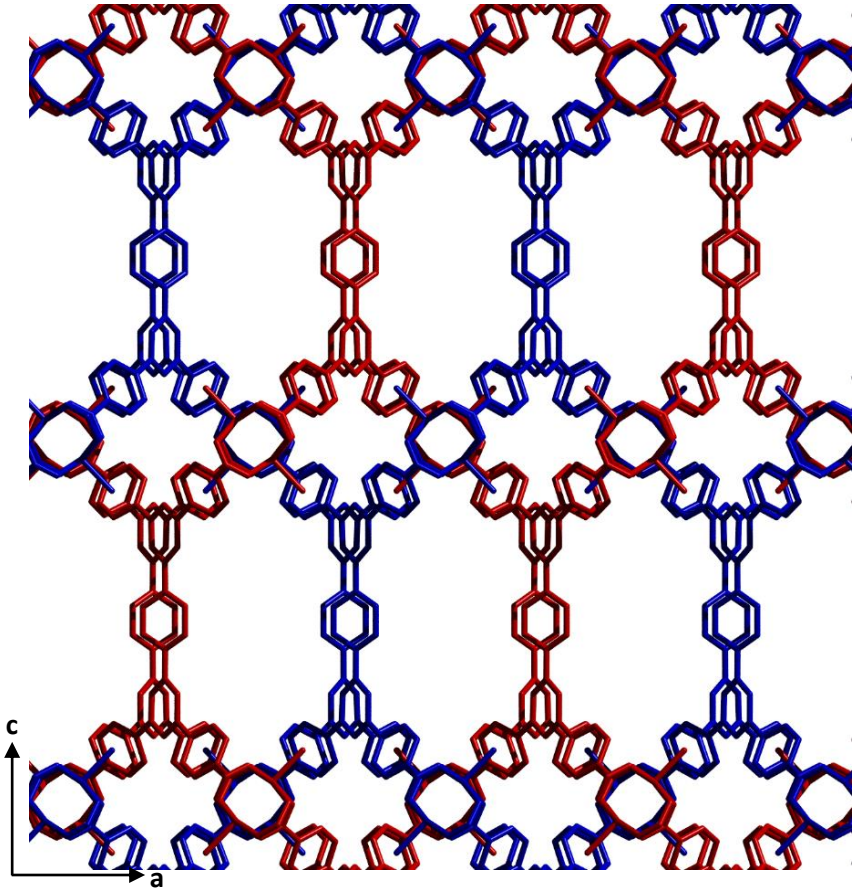


Figure 63. View along the *b* axis, depicting interpenetration in MFM-192.

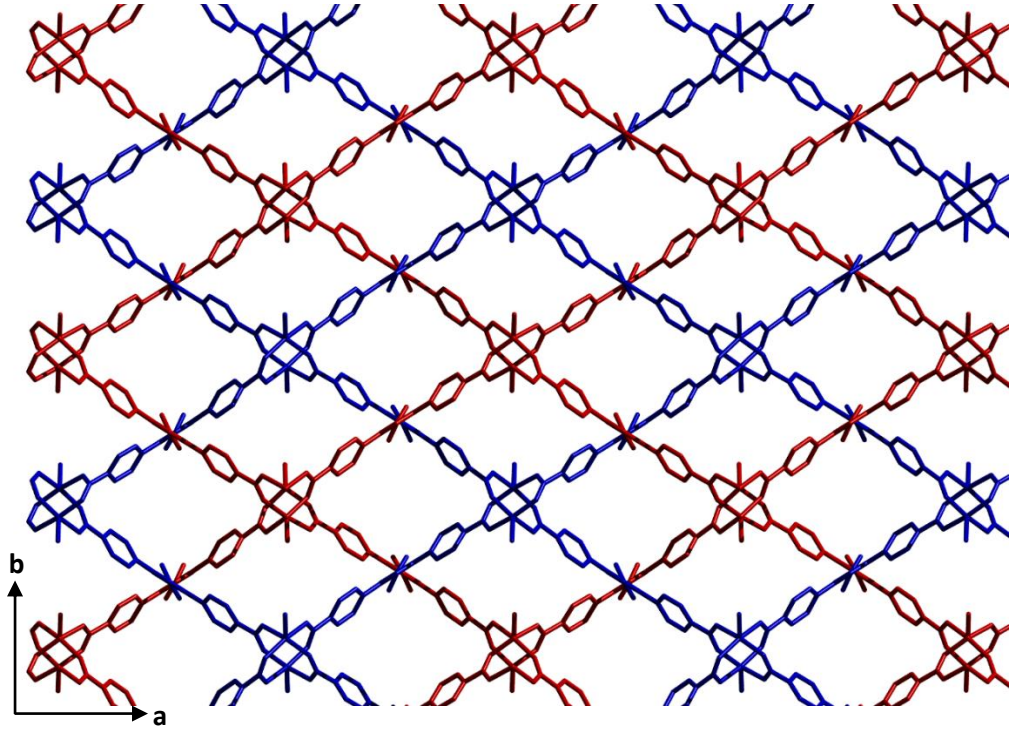


Figure 64. View along the *c* axis, depicting interpenetration in MFM-192.

PXRD and TGA of MFM-192

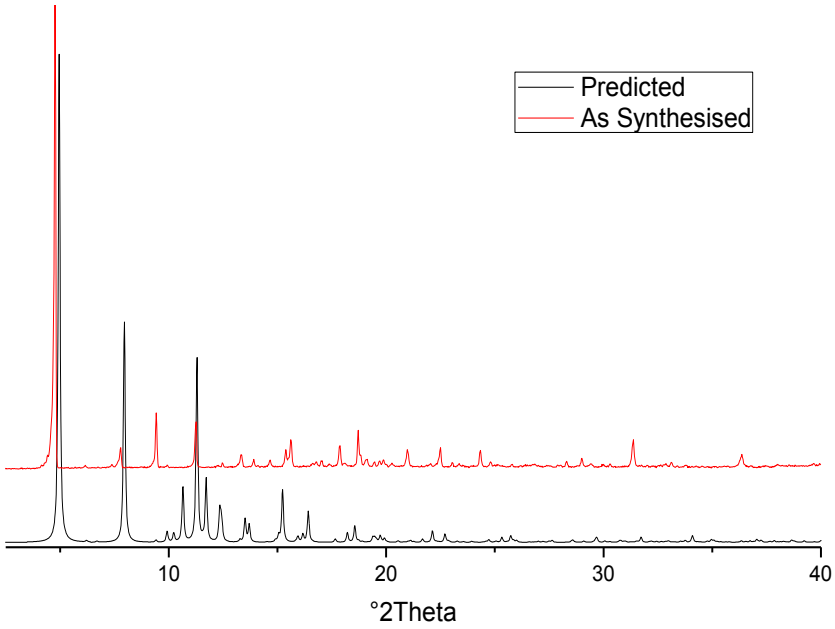


Figure 65. PXRD of simulated and as synthesised MFM-192.

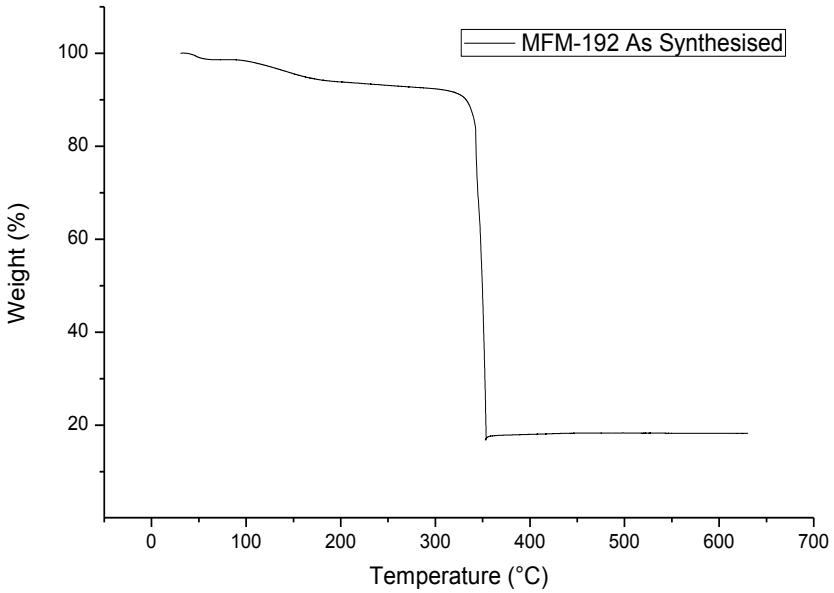


Figure 66. TGA of as synthesised MFM-192 in air.

Comparison of the classes of interpenetration

The difference between class Ia and class IIa can be seen in Figure 67, which shows the inversion centre present in MFM-191, and the translation vector of MFM-192.

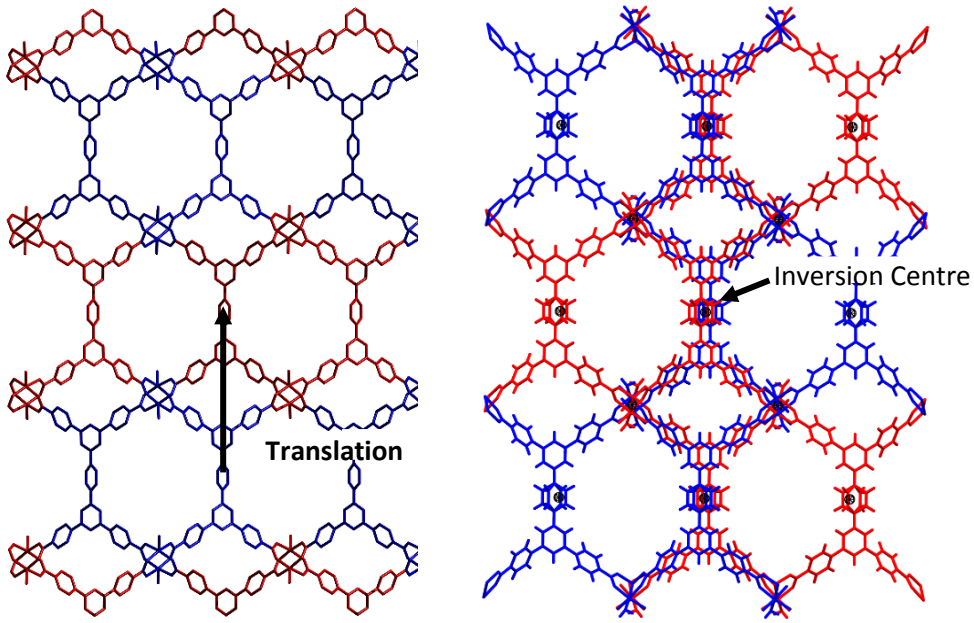


Figure 67. Interpenetration translation vector for MFM-192 (left) and inversion centres in MFM-191 (right) showing the difference in class of interpenetration.

The geometry of the linker in MFM-191 exhibits a degree of distortion throughout the net, so that they are identical yet cannot be mapped onto one another by simple translation. There does remain an inversion centre between the two nets, however (shown in Figure 67), thus placing the type of interpenetration into class II due to this symmetry relationship between them. In MFM-192, the linkers on the two adjacent nets can be superposed onto one another by a simple translation, thus placing the system in class I. As both

structures require only one translation or symmetry operation to transform the single net into its interpenetrated form, they are both of the subclass a.

Further analysis of the distortion present in the net of MFM-191 reveals that the linker displays signs of torsion between the carboxylate and the paddlewheel, which consequently pulls the structure closer together, giving an average distance between the two adjacent nets as 3.99 Å. The single net of MFM-192, however, shows much a much smaller torsion angle between the carboxylate and the paddlewheel, thus expanding the framework's 'wine rack' motif, to give an average distance between the two nets of 7.37 Å. This can be seen in Figures 68 and 69, where the torsion angle increases from 40.2° to 49.1° between MFM-192 and MFM-191.

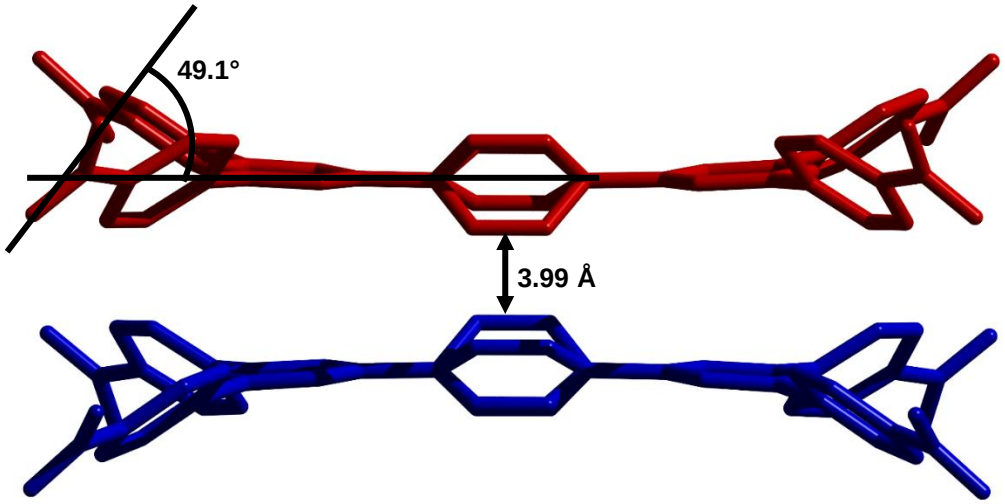


Figure 68. Torsion angle and distance between interpenetrated nets in MFM-191.

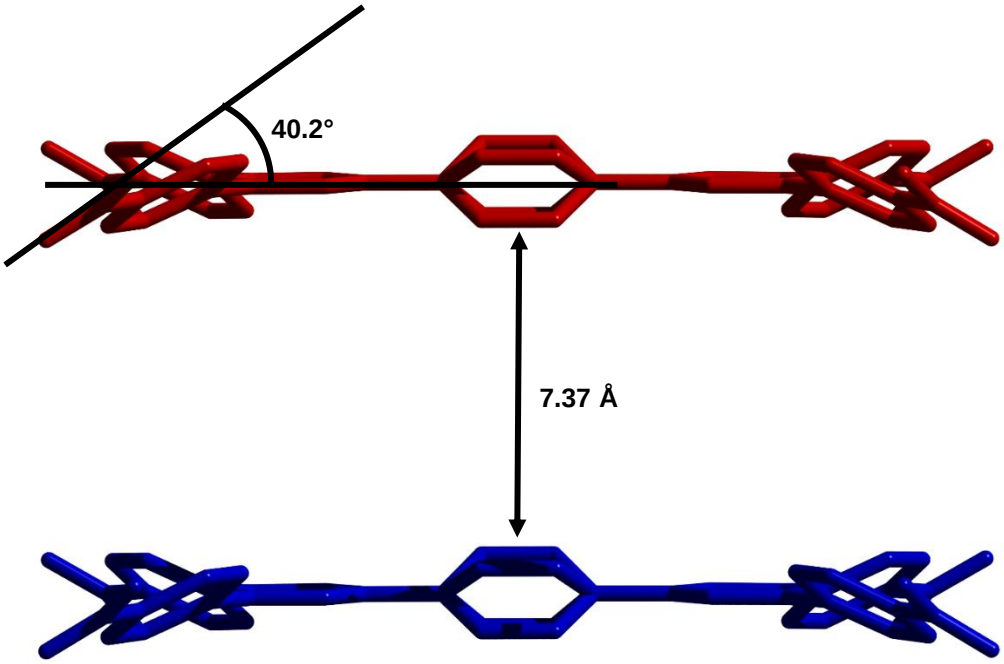


Figure 69. Torsion angle and distance between interpenetrated nets in MFM-192.

Evaluating use of bulky solvent to prevent interpenetration

By calculating the solvent accessible volume with PLATON SOLV,[24] and therefore deducing a theoretical porosity, it was seen that the use of a bulkier solvent had indeed increased the porosity from 60.3% (MFM-191) to 68.9%. This supported the evidence seen in the crystal structure, where the nets are much further apart from one another when viewed down the *b* axis, MFM-192 displaying an average distance of 7.37 Å rather than the 3.99 Å seen in MFM-191.

As discussed earlier, the distances between the paddlewheels in MFM-191 suggested the presence of hydrogen bonding, which might be contributing towards the fact that there is interpenetration in the framework. This, coupled with the knowledge that an increase in acidity would slow the rate of deprotonation and thus nucleation of crystals (an effect which, like dilution of

the system, can lead to prevention of interpenetration), meant the next logical step was to increase acidity in the solvothermal reaction. Both structures so far were synthesised with 1 mL of a very dilute acid (0.1M HCl), therefore in order to increase the acidity there were two options. Either slightly increase the molarity of the 1 mL of acid, or use only a few drops of a highly concentrated acid. The latter approach was taken, and 0.03 mL of 8M HCl was used, as this was thought to have the added benefit of restricting the amount of water present in the synthesis, thereby discouraging hydrogen bonding in the synthesis even further.

Solvothermal synthesis of MFM-193

A solution of H_4L^1 (10 mg, 0.014 mmol) and $Cu(NO_3)_2{\cdot}2.5H_2O$ (25 mg, 0.11 mmol) in DMF (3 mL) and 8M HCl (0.03 mL) was heated to 80 °C in an 8 mL glass vial, and maintained at this temperature for 24 hours to yield blue rhombohedral single crystals of MFM-193 with the molecular formula $[Cu_2EIB1(H_2O)_2].solv_x$ in a 55% yield. The as-synthesised single crystals were insoluble in organic solvents, and the crystal structure was determined by SCXRD. The bulk phase purity of the solid was analysed using powder x-ray diffraction.

3.2.3 Crystal Structure Description of MFM-193

Table 5. Crystallographic information for MFM-193.

Crystal Data	
Formula = $C_{22}H_{16}O_5Cu$	Orthorhombic, *Imma*
a = 29.7895(4) Å	V = 15583.6(7) $Å^3$
b = 37.7231(5) Å	Mr = 206.43
c = 13.8675(5) Å	Z = 16
Density = 0.351988 g/cm^3	
Data Collection and Refinement	
Rint = 0.0547	$R[F2 > 2\sigma(F2)]$ = 0.055
$wR(F^2)$ = 0.198	

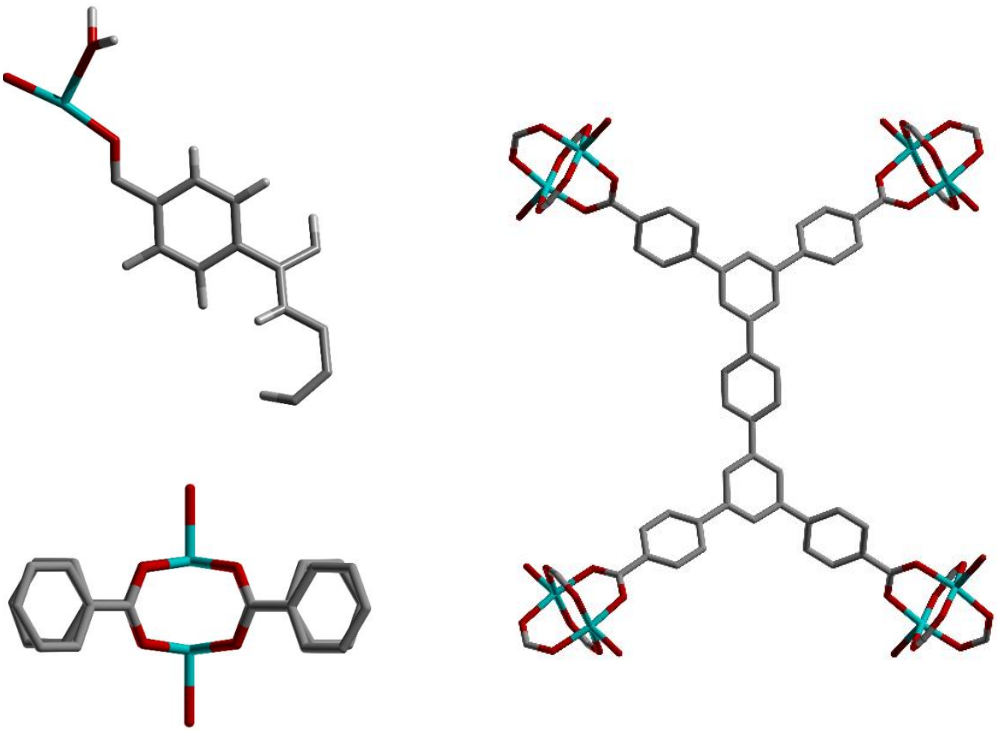


Figure 70. Asymmetric unit and paddlewheel of MFM-193 (left) and coordination mode of L^1 (right).

MFM-193 crystallises in the orthorhombic space group *Imma*, with unit cell parameters: a = 29.7895(4) Å, b = 37.7231(5) Å and c = 13.8675(5) Å, and a volume of V = 15583.6(7) Å^3. The framework contained the same Cu(II) paddlewheel secondary building units as MFM-191 and MFM-192 (shown in Figure 70). The 3 dimensional structure of the single net can be described as isoreticular with respect to these frameworks, due to the same 4,4-connected net and **lvt** topology it exhibits.

The hypothesis that the use of a strong acid might encourage the isolation of a non-interpenetrated framework by slowing the rate of nucleation and disrupting the hydrogen bonding network that was apparently present in the synthesis of the earlier MOFs is supported by the absence of interpenetration in MFM-193. The framework itself is connected in the same way throughout 3D space, and

therefore, as seen in Figures 71 and 72, the *a* and *b* axes become more porous due to the absence of a second net. Analysis of the theoretical solvent accessible volume (calculated from PLATON SOLV)[24] shows that without interpenetration, this ligand and metal system, connected in the **lvt** topology, reaches a high of 81.6% porosity.

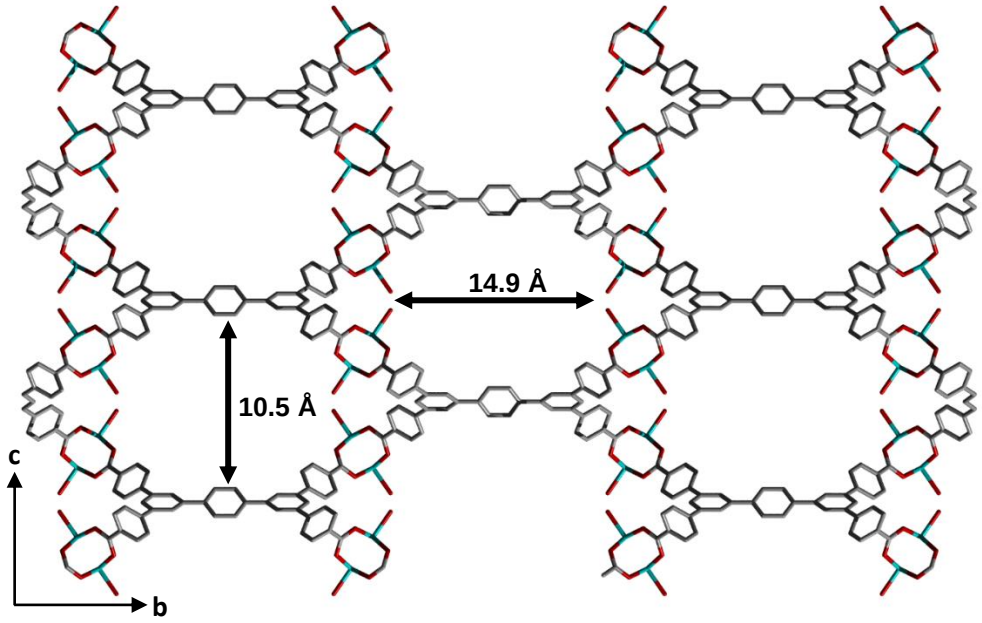


Figure 71. View along the *a* axis showing the size of pore channels in MFM-193.

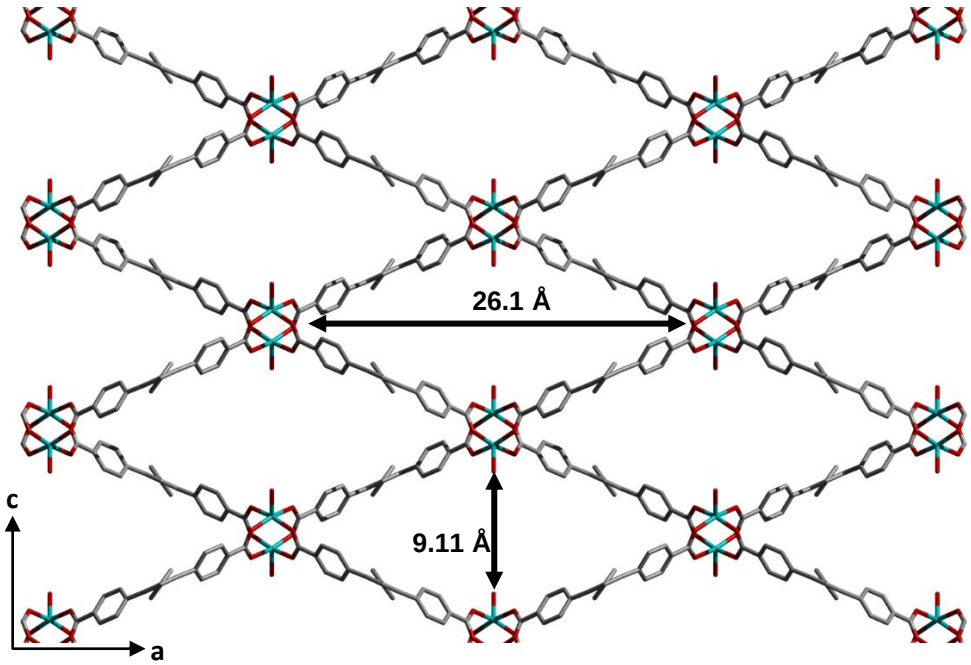


Figure 72. View along the *b* axis showing the size of pore channels in MFM-193.

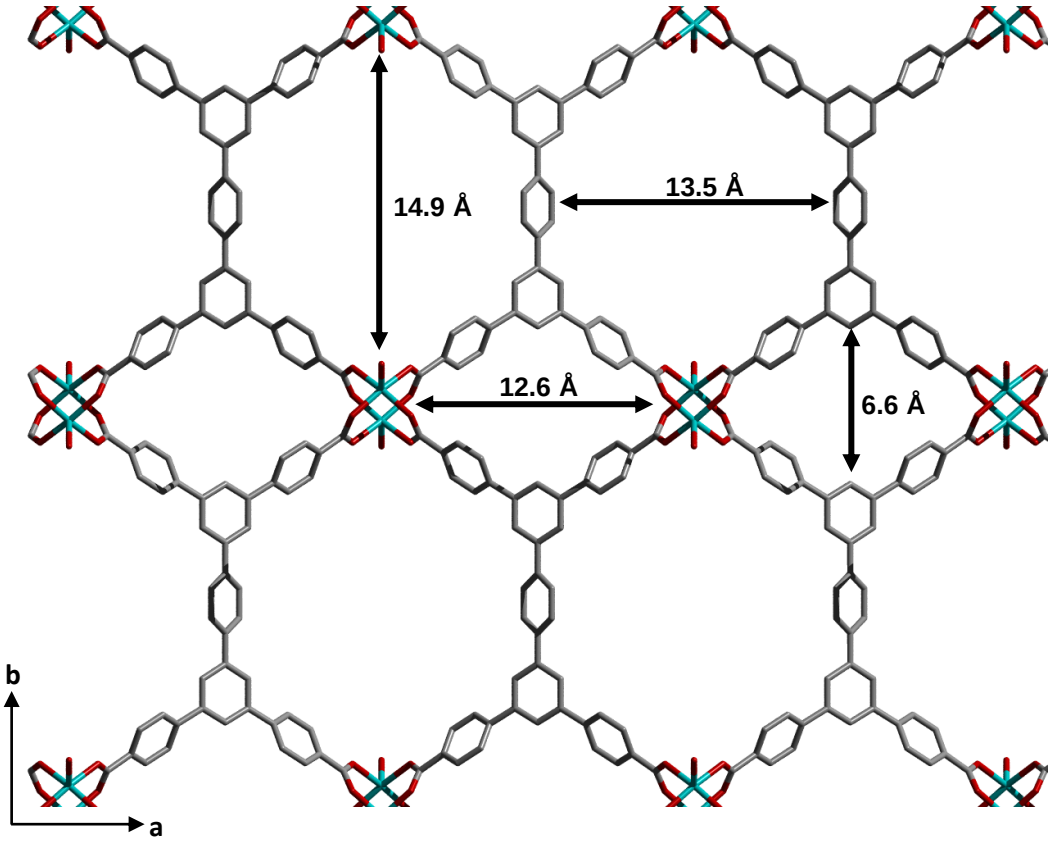


Figure 73. View along the *c* axis showing the size of pore channels in MFM-193.

The pore dimensions down the *c* axis remain comparable to MFM-191 and MFM-192, however now there are two more axes with large pores present, the dimensions of which are shown in Figures 71, 72 and 73. These diagrams illustrate the impact of removing an interpenetrating second net, as the structure gains a 3D networked pore system in comparison to the 1D pore channel present in MFM-191 and MFM-191.

PXRD and TGA of MFM-193

The seemingly disparate diffractograms of MFM-193 predicted and as synthesised are discussed in further detail in Section 3.2.11.

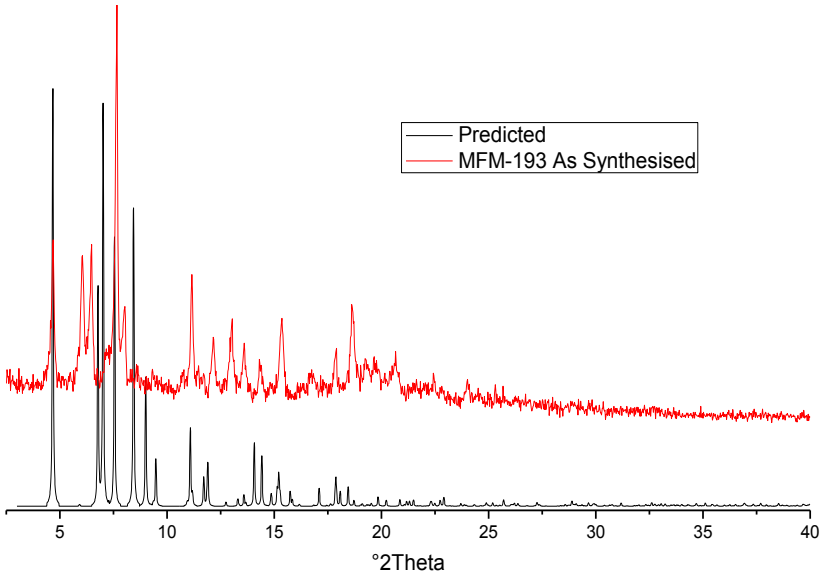


Figure 74. PXRD of simulated and as synthesised MFM-193.

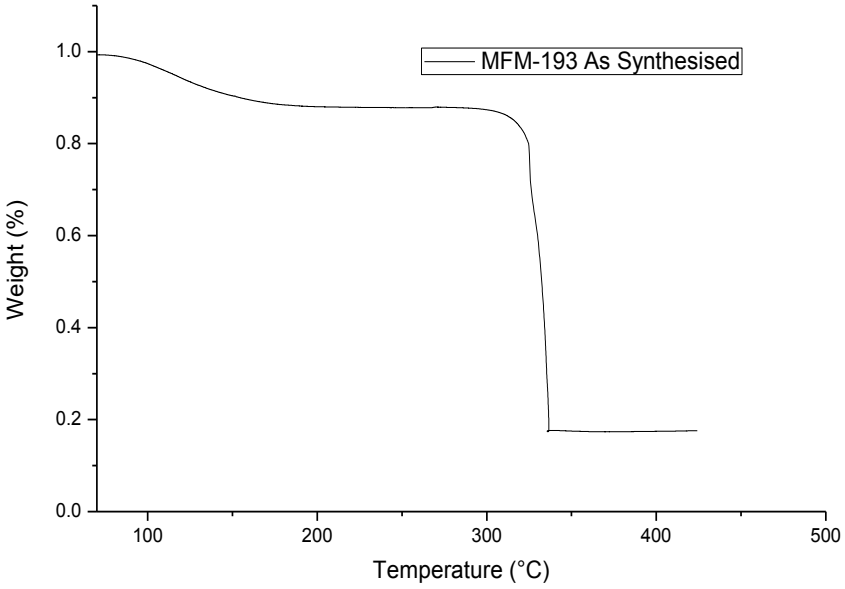


Figure 75. TGA of as synthesised MFM-193 in air.

3.2.4 Comparison of Interpenetrated Frameworks

The impact of interpenetration can be seen in Figure 76, which demonstrates quite strikingly the increase in porosity down a common channel when the class of interpenetration is changed, and when interpenetration is completely removed from the system.

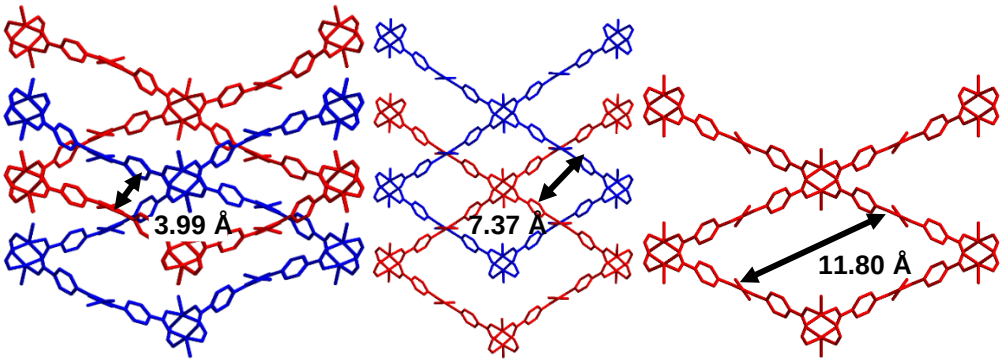


Figure 76. View of MFM-191, MFM-192 and MFM-193 with distances between adjacent nets displayed.

Examining the increase in distance between the two closest parallel ligands from MFM-191 (3.99 Å) to MFM-192 (7.37 Å), to MFM-193 (11.80 Å) not only highlights the increase in porosity, but also suggests the presence of pi-pi stacking in the interpenetrated framework MFM-191, as the distance between phenyl rings from independent nets is close to the expected range (3.3-3.8 Å).[26]

These three isoreticular MOFs generated from a single ligand and metal combination, with subtle changes in solvothermal conditions led to an interesting case to study regarding the interaction between the host and guest molecules inside the MOF. The changes in both porosity and interpenetration, while maintaining the chemical and topological nature of the single net, meant that it would be possible to probe in depth the positive and negative aspects of enlarging pore size, as this increases overall free space in the MOF, but also has the impact of providing less guest-framework interactions for molecules in the centre of the pore.

Determination of effects leading to changes in class of interpenetration

MFM-191 was synthesised using dimethylformamide (DMF), due to the excellent solubility of the ligand in it, its high boiling point which allows for

MOF synthesis at temperatures up to ~120 °C (when the DMF starts decomposing rapidly) and also the lack of solubility of resultant MOFs in it. The logical next step, therefore, was to use diethylformamide, which retains the same benefits as DMF, while inhabiting a much larger space within the MOF, as the extension of the aliphatic chains off the nitrogen group increases the Van-der-Waals radius of the solvent molecule. This did not completely prevent interpenetration, as it may be expected to, however it did lead to a change in class of interpenetration from a less porous Class IIa (MFM-191, 60% porous) to a more open Class Ia framework (MFM-192, 69% porous). The increase in porosity was attributed the extra bulk of the ligand preventing the frameworks from being able to pi-stack, while the retention of interpenetration despite the use of DEF is ascribed to being due to the fact that the pores of the framework were sufficiently large, even in interpenetration, to host DEF without serious steric clashes.

Factors leading to prevention of interpenetration in MFM-193

The two main driving forces which may have prevented interpenetration in the case of MFM-193, are firstly the reduction in the rate of deprotonation of the ligand in the synthesis, thus retarding the growth of the crystals and nucleation and as such reducing the likelihood of two nets interweaving during crystal growth. The second main factor is the disruption of the potential hydrogen bond between adjacent paddlewheels.

3.2.5 Simulated Isotherms for MFM-191, MFM-192 and MFM-193

In order to identify which of these three MOF systems was the most preferential for high pressure uptake, simulated isotherms were calculated (by methods

described in the experimental section) to speedily identify the key features of the host/guest interactions of each framework. The two gases simulated were CO_2 and CH_4, at 273 K and 298 K, as these would provide insight into the working capacity of these frameworks for methane fuelled transport, and CO_2 shipping. Table 6 shows the simulated BET surface areas of the three MOFs calculated from simulated N_2 77 K isotherms, which seem to follow the expected trend where the increase in porosity as the frameworks move from class IIa interpenetration to class Ia to a non-interpenetrated network reflect an increase in BET surface area. The increase upon removal of the interpenetrated net is particularly pronouced.

Table 6. Comparison of BET surface areas across the frameworks MFM-191, MFM-192 and MFM-193.

MOF	Simulated BET Area (m^2/g)	Simulated He Pore Volume (cm^3/g)	Calculated Density from Crystal Structure
MFM-193	6111	2.52	0.355
MFM-192	3073	1.32	0.584
MFM-191	2150	0.98	0.733

3.2.5.1 Simulated CO_2 Isotherms

The change in interpenetration class and level throughout this series of frameworks provided a unique insight into the effect of interpenetration of both high and low pressure gas uptake. This can be seen in Figure 77, where the overall trend of the isotherms suggests a difference in the beneficial effects of increased porosity from the low to the high pressure regime.

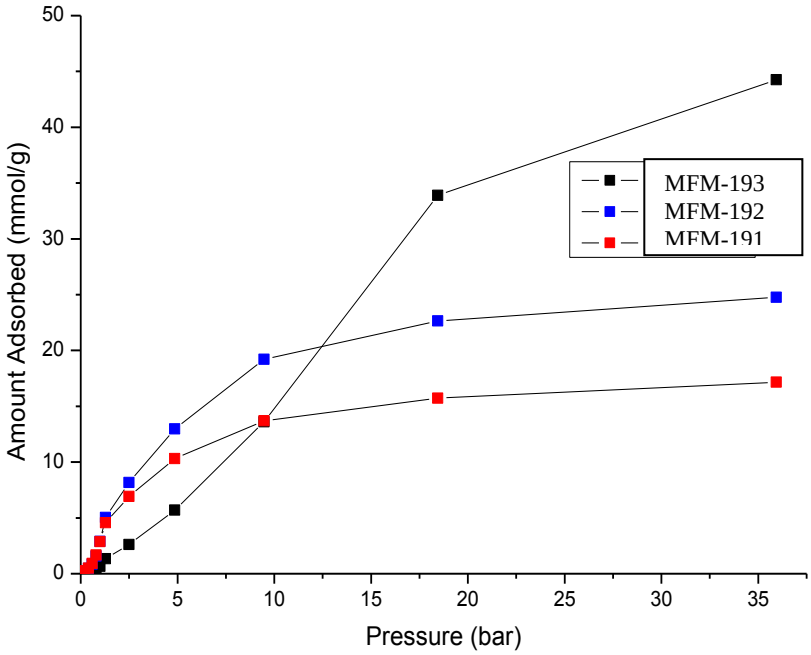


Figure 77. High pressure gravimetric uptake of CO_2 at 298 K in MFM-193, MFM-192 and MFM-191.

As demonstrated in Figure 77 above, in the high pressure region the highly porous MFM-193 exhibits a far superior gravimetric CO_2 uptake, adsorbing 44.26 mmol/g, almost double that of MFM-192 (24.78 mmol/g) and over double the maximum of MFM-191 (17.17 mmol/g). The extent of the impact of porosity can be seen at the highest pressure, where MFM-193 has clearly not saturated, due to the large void space and lack of strong interactions throughout the framework; a Langmuir fit of the curve predicts saturation at 51.08 mmol/g.

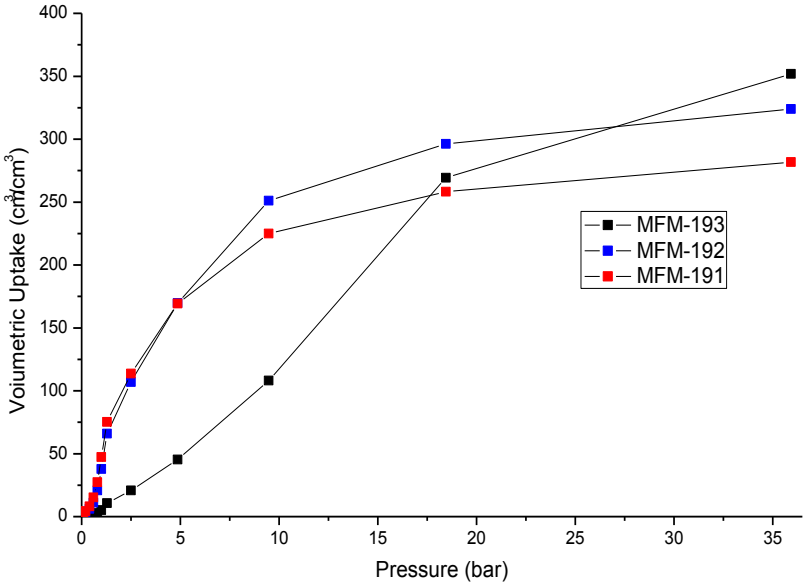


Figure 78. High pressure volumetric uptake of CO_2 at 298 K in MFM-193, MFM-191 and MFM-192.

The order is echoed in volumetric maximum uptake (Figure 78), though to a much lesser degree, with MFM-193 only slightly outperforming MFM-192 and MFM-191, adsorbing 351.9 cm^3/cm^3, compared to 324.0 and 281.8 cm^3/cm^3, respectively. The increase in uptake at high pressures for the more porous, open framework of MFM-193 over the interpenetrated MOFs is to be expected, as at higher pressures the dominant influence on gas storage is the amount of free space within the framework, which follows the same trend shown in the isotherms of MFM-193 > MFM-192 > MFM-191. As seen in the low pressure region in Figures 79 and 80, however, the trend in uptake is vastly different at low pressures.

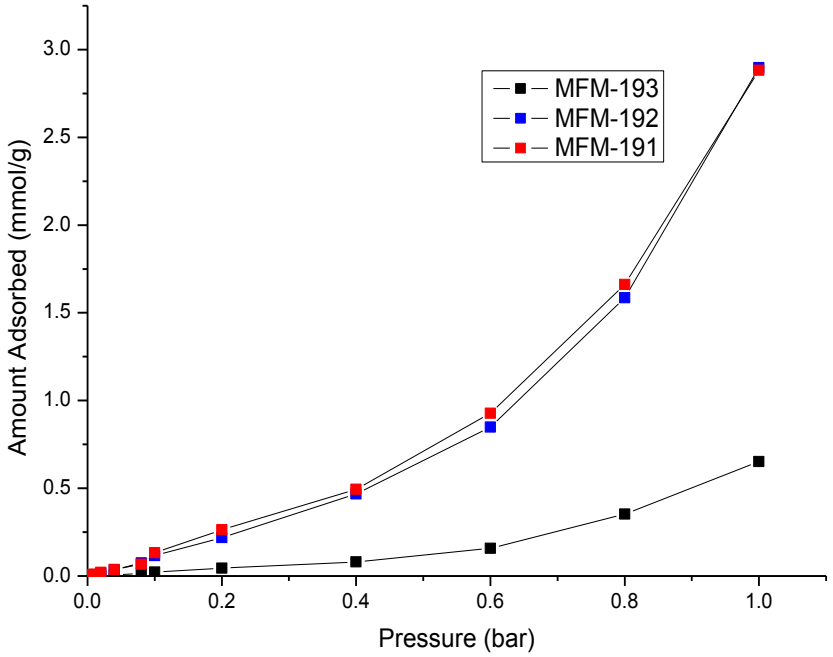


Figure 79. Low pressure gravimetric uptake of CO_2 at 298 K in MFM-193, MFM-192 and MFM-191.

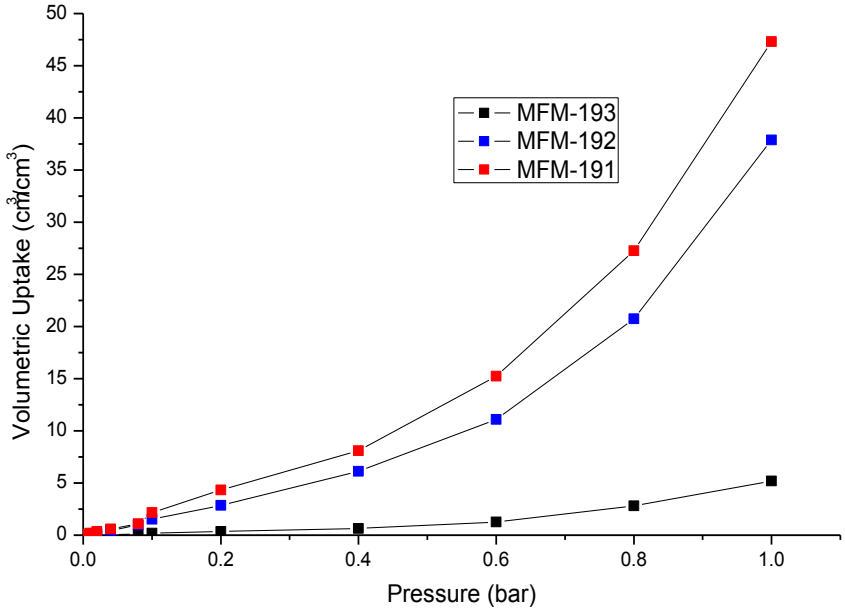


Figure 80. Low pressure volumetric uptake of CO_2 at 298 K in MFM-193, MFM-192 and MFM-191.

In the low pressure region, the level and class of interpenetration become very important, as this is where there are very few gas molecules in the system. Therefore, the dominant effect is the proximity of gas in the centre of the pore to the framework, in particular to the nearest paddlewheel, as these are shown

to have highly favourable interactions with gas molecules, specifically CO_2.[27,28] Figure 81 below demonstrates the distance between adjacent nets in MFM-193, MFM-192 and MFM-191, in which this length appears to be inversly proportional to the gas uptake at very low pressures. The distance decreases from 11.80 Å to 7.37 Å to 3.99 Å for MFM-193, MFM-192 and MFM-191 respectively, as the gas uptake increases from 5.19 to 37.89 to 47.31 cm^3/cm^3 across the series.

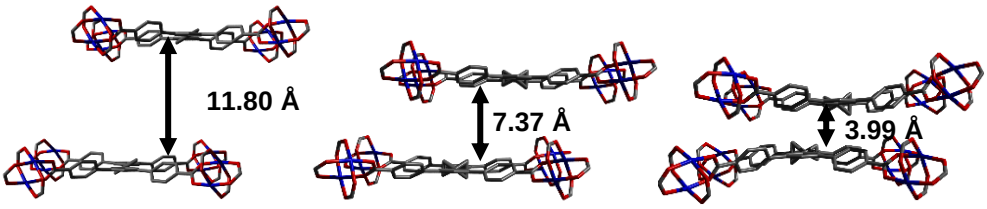


Figure 81. Distance between adjacent nets in the Cu(II) series (left to right: MFM-193, MFM-192, MFM-191).

Most interestingly, the class of interpenetration seems to have a much smaller effect than the level of it, with the closer nets of MFM-191 slightly dominating over MFM-192 in the region <1 bar (47.31 rather than 37.89 cm^3/cm^3 at 298 K). Additionally, the two interpenetrated MOFs perform differently when comparing volumetric as opposed to gravimetric uptake; this is a product of the fact that the density of the frameworks changes across the series quite dramatically: MFM-191 (0.733 g/cm^3)>MFM-192 (0.584 g/cm^3)>MFM-193 (0.355 g/cm^3). This decrease in density positively effects the gravimetric uptake and negatively impacts the volumetric, as for a lighter system, the weight of the gas is proportionally higher, yet for a fixed volume, a less dense framework will contain less molecules to interact with per cm^3, thus inevitably lowering the uptake. MFM-191 demonstrates a better volumetric uptake than MFM-192

(47.31 compared to 37.89 cm^3/g), and a worse gravimetric uptake (2.88 compared to 2.98 mmol/g).

It is certainly worth noting, however, that this presence of an extra net in the pores of the lvt framework more than triples the uptake compared to MFM-193 (5.19 cm^3/cm^3 at 298 K for MFM-193 compared to 37.89 and 47.31 cm^3/cm^3 for MFM-192 and MFM-191).

At pressures higher than 1 bar, the more open structure of MFM-192 begins to improve the performace of this MOF compared to MFM-191 at a steady rate, and the uptakes start to diverge to a large extent at pressures above 2.5 bar. At some pressure between 10 and 18.5 bar the hugely porous network of MFM-193 starts to overtake both the interpenetrated nets, and at the highest pressure simulated (35 bar), the difference between gravimetric and volumetric is not enough to separate the performance of each MOF, as the frameworks diverge from one another sufficiently for this not to affect the order of highest uptake, shown below in Table 7.

Table 7. Comparison of porosity and simulated CO_2 uptake at various pressures at 298 K.

	MFM-193	**MFM-192**	**MFM-191**
Porosity	82.0%	68.9%	60.3%
Crystal Density	0.355	0.584	0.733
Uptake at 1 bar (mmol/g)	0.65	2.90	2.88
Uptake at 1 bar (cm^3/cm^3)	5.19	37.89	47.31
Uptake at 30 bar (mmol/g)	40.82	24.07	16.69
Uptake at 30 bar (cm^3/cm^3)	324.50	314.79	274.00

The vastly different manner in which these frameworks interact with CO_2 at high and low pressure results in a system where from the same ligand and metal

system, different MOFs can be made which are suitable for two distinct applications. The highly porous MFM-193 framework which has extremely high CO_2 uptake at 30 bar is an ideal candidate for CO_2 transport and shipping, while the close interaction between the framework and guest molecules in MFM-191 at 1 bar makes it a possible candidate for natural gas upgrading.

3.2.5.2 Simulated CH_4 Isotherms

As discussed in Chapter 1, one of the most promising applications for metal-organic frameworks is the storage of methane at high pressure (~80 bar) for use in the transport industry. As such, the unique opportunity to probe both different levels and classes of interpenetration presented by these frameworks is ideal for studying high pressure methane isotherms.

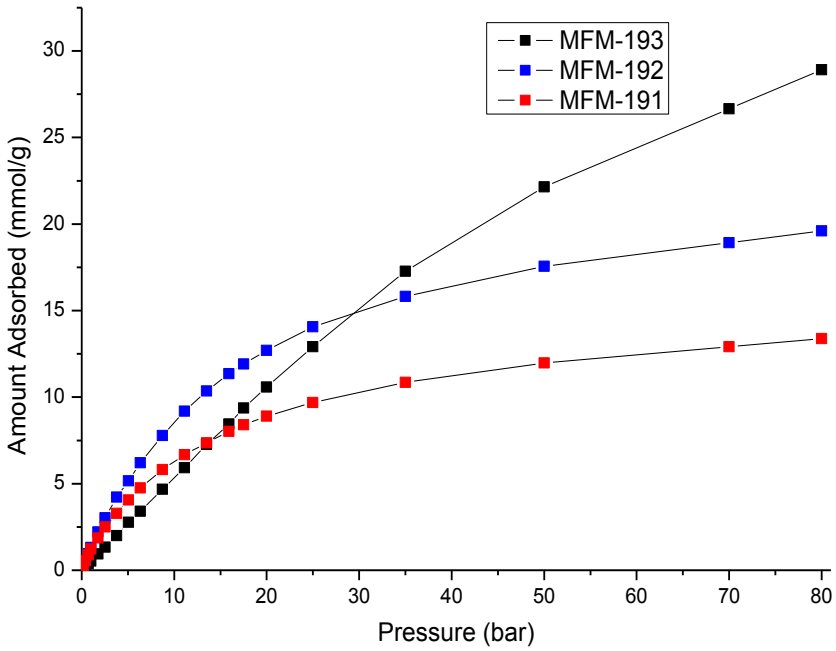


Figure 82. High pressure gravimetric methane isotherms of MFM-193, -192 and -191 at 298 K. *The 80 bar value is extrapolated from a 70 bar simulated isotherm.

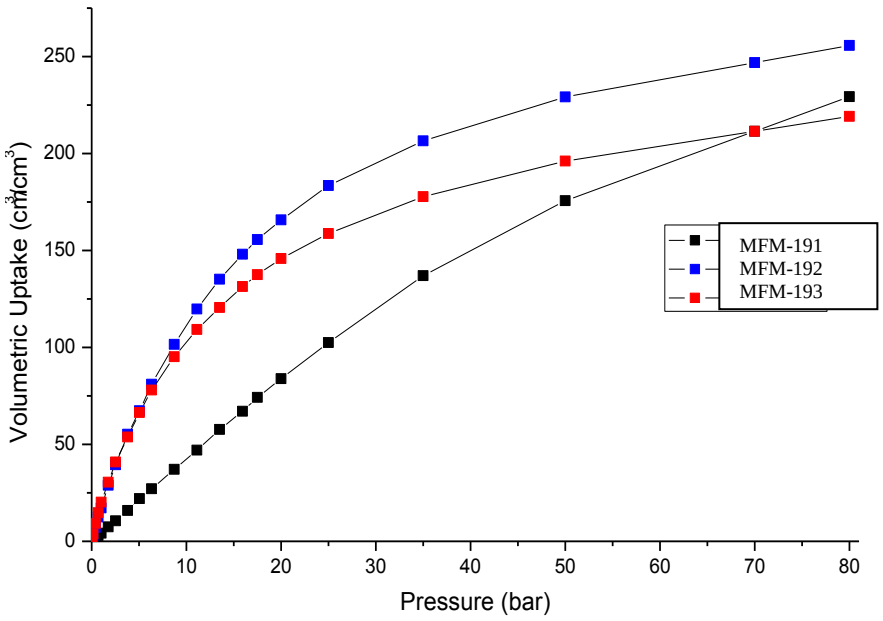


Figure 83. High pressure volumetric methane isotherms of MFM-193, -192 and -191 at 298 K. *The 80 bar value is extrapolated from a 70 bar simulated isotherm.

As shown in Figures 82 and 83, the methane adsorption isotherms reflect the same trend as CO_2, where the highly porous MFM-193 has vastly superior gravimetric uptake at 80 bar, 298 K (28.92 mmol/g compared to 19.60 and 13.38 mmol/g for MFM-192 and -191, respectively). Interestingly, the volumetric uptake is lower for MFM-193 than MFM-192 at 80 bar, which is attributed to the difference in crystal density, furthemore the isotherm of MFM-193 suggests that it is still not fully saturated at 80 bar, due to the extrememly high porosity and BET surface area. Figures 84 and 85 show how this series displays the same order at low pressure as seen for CO_2, with MFM-193 adsorbing the least at 5 bar, 298 K (2.77 mmol/g) compared to MFM-192, which adsorbs 5.16 mmol/g and MFM-191 which adsorbs the most at 4.06 mmol/g.

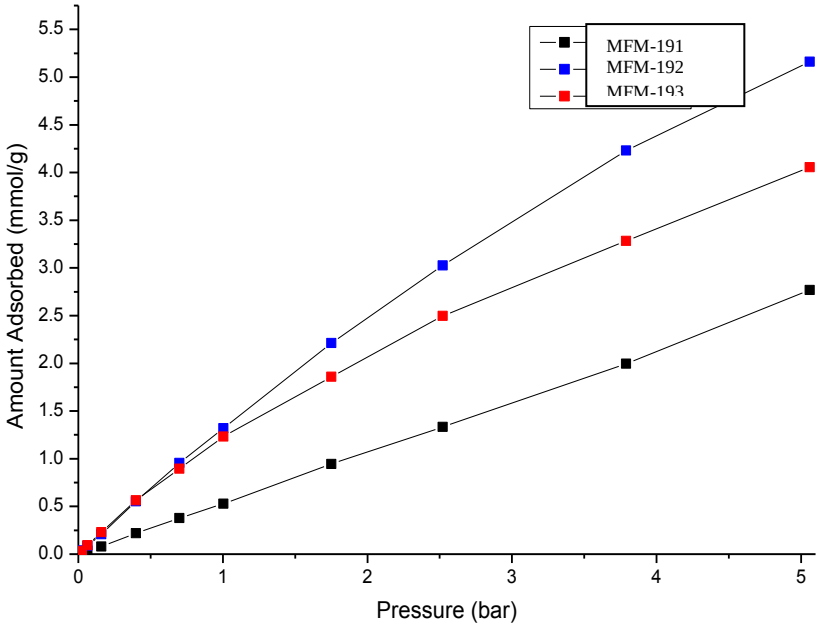


Figure 84. Low pressure gravimetric methane isotherms of MFM-193, MFM-192 and MFM-191 at 298 K.

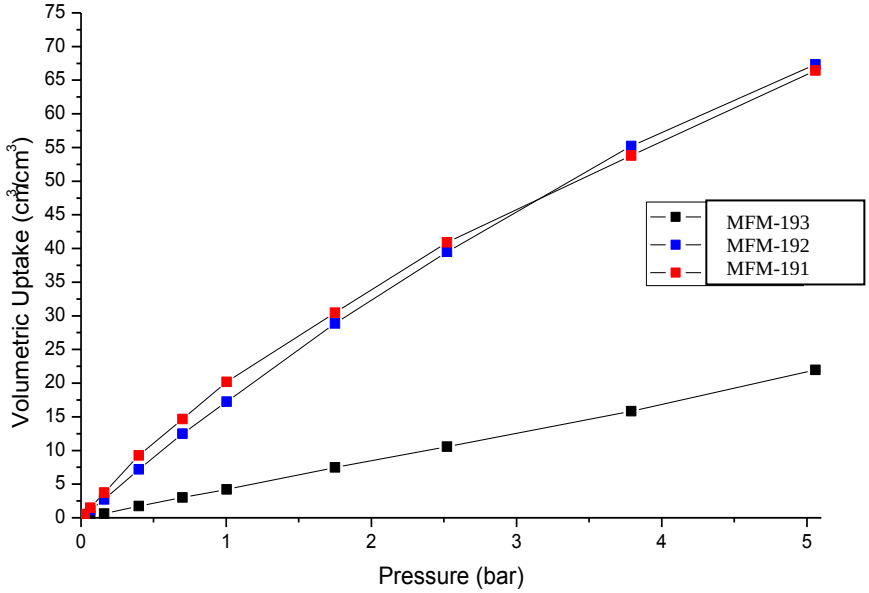


Figure 85. Low pressure volumetric methane isotherms of MFM-193, MFM-192 and MFM-191 at 298 K.

The difference in low and high pressure methane uptake of MFM-193 makes it an ideal candidate for methane storage in transport, where the difference in uptake between 5 and 70 bar (the working capacity) is crucial to enable maximum delivery to the vehicle (as discussed in Chapter 1).

3.2.6 Formation of Isoreticular Series Based Upon MFM-193

The isolation of the non-interpenetrated Cu(II) MOF, MFM-193, paved the way for the generation of an isoreticular series of frameworks based upon non-interpenetrated frameworks with an **lvt** topology. The combination of the flexibility in ligand synthesis (see Chapter 2) and the accessibility of the central core within the framework's pores meant that this was a hugely versatile method of fine tuning the framework properties to enhance interaction with guest molecules, particularly CH_4 and CO_2.

Description of linkers for Cu(II) MOF formation

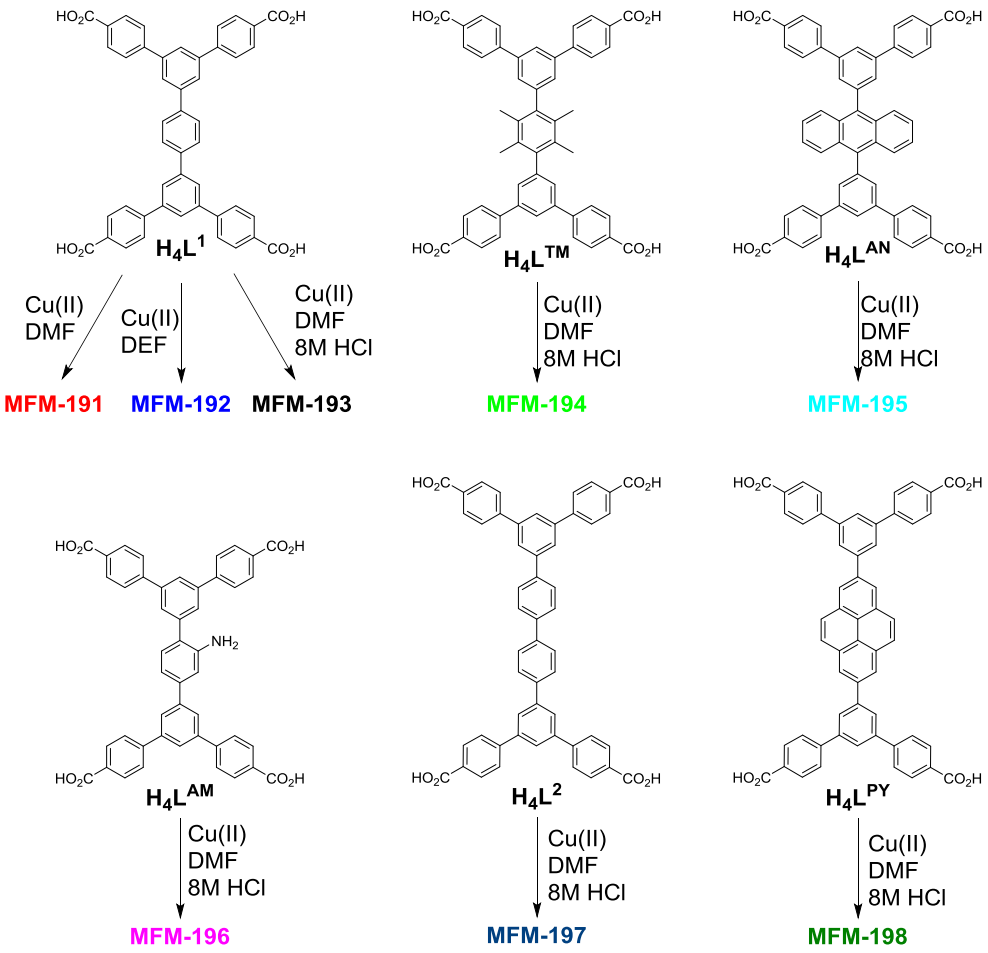


Figure 86. Series of H_4L^X linkers and associated MFM-19X MOFs.

The ligand series shown in Figure 86 demonstrates the versatility of this synthetic method, as there is a clear increase in functionality as you move across the group, from the simple aromatic system of H_4L^1 to the large conjugation system of H_4L^{AN}.

3.2.7 Description of MFM-19X Series

All MOFs in the MFM-19X series crystallised in the orthorhombic space group *Imma*; they are comprised of copper paddlewheels connected to the four extension points of the ligands, resulting in a 4,4-connected net with a **lvt** topology, and are all non-interpenetrated. In this respect they are all isoreticular to MFM-193 and each other; the unique asymmetric units and unit cell parameters for each individual MOF are given below.

MFM-194

A solution of H_4L^{TM} (10 mg, 0.013 mmol) and $Cu(NO_3)_2{\cdot}2.5H_2O$ (25 mg, 0.11 mmol) in DMF (3 mL) and 8M HCl (0.03 mL) was heated to 80 °C in an 8 mL glass vial, and maintained at this temperature for 24 hours to yield blue rhombohedral single crystals of MFM-194 with the molecular formula $[Cu_2L^{TM}(H_2O)_2].solv_x$. The as-synthesised single crystals were insoluble in organic solvents, and the crystal structure was determined by SCXRD. The bulk phase purity of the solid was analysed using powder x-ray diffraction.

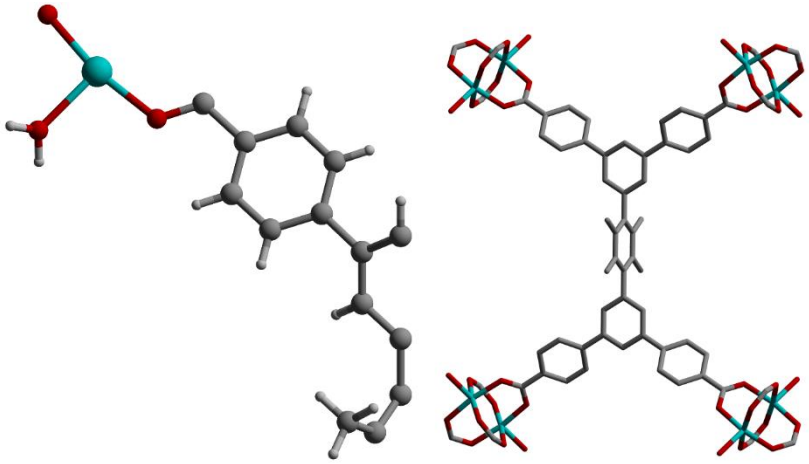


Figure 87. Asymmetric unit (left) and connectivity of ligand (right) of MFM-194.

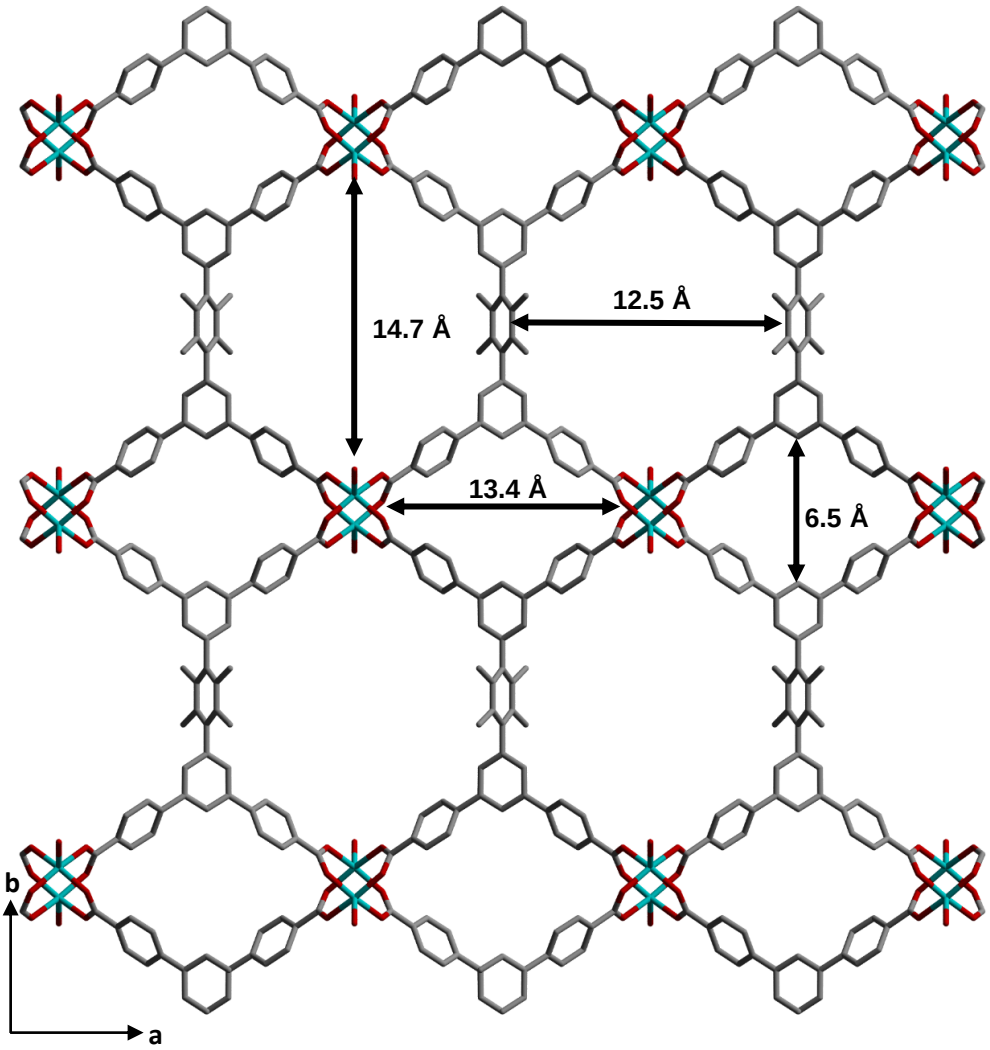


Figure 88. View down *c* axis of MFM-194.

Table 8. Crystallographic information for MFM-194.

Crystal Data	
Formula = $C_{25}H_{19}O_5Cu$	Orthorhombic, *Imma*
a = 37.5058(6) Å	V = 15898.2(7) $Å^3$
b = 29.7789(5) Å	Mr = 462.94
c = 14.2345(5) Å	Z = 8
Density = 0.387 g/cm^3	
Data Collection and Refinement	
Rint = 0.026	$R[F2 > 2\sigma(F2)]$ = 0.061
$wR(F^2)$ = 0.245	

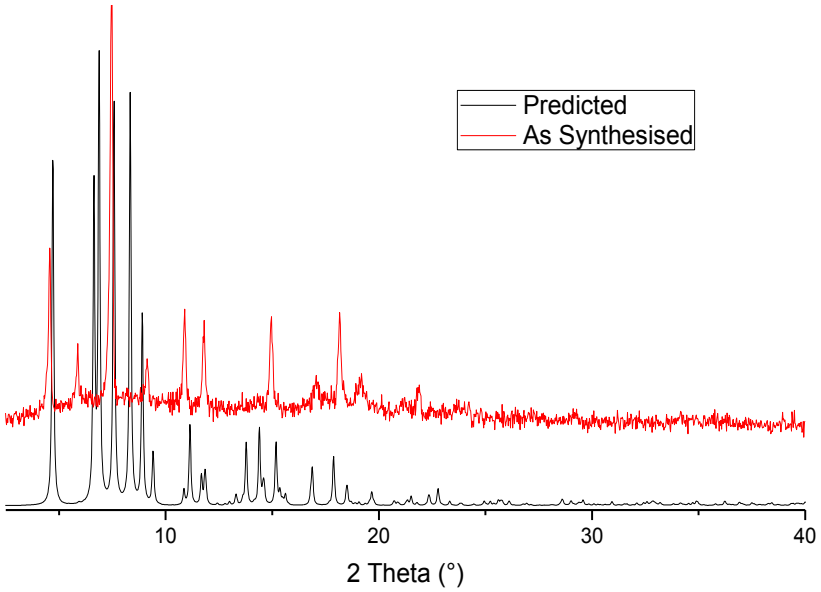


Figure 89. PXRD of simulated and as synthesised MFM-194.

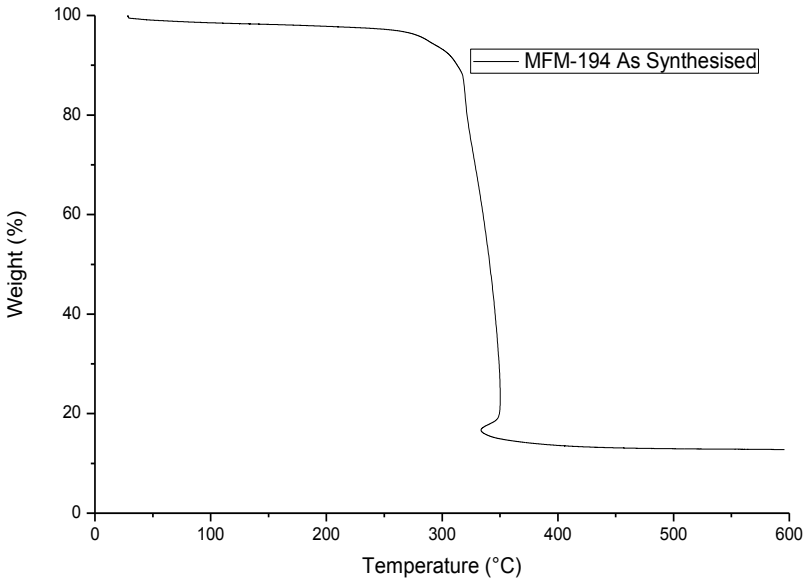


Figure 90. TGA of as synthesised MFM-194 in air.

MFM-195

A solution of H_4L^{AN} (10 mg, 0.012 mmol) and $Cu(NO_3)_2{\cdot}2.5H_2O$ (25 mg, 0.11 mmol) in DMF (3 mL) and 8M HCl (0.03 mL) was heated to 80 °C in an 8 mL glass vial, and maintained at this temperature for 24 hours to yield blue rhombohedral single crystals of MFM-195 with the molecular formula $[Cu_2L^{AN}(H_2O)_2].solv_x$. The as-synthesised single crystals were insoluble in organic solvents, and the crystal structure was determined by SCXRD. The bulk phase purity of the solid was analysed using powder x-ray diffraction.

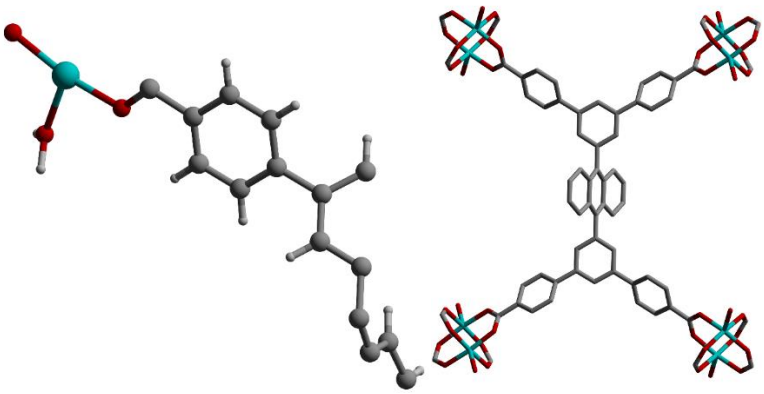


Figure 91. Asymmetric unit of (left) and connectivity of ligand in (right) MFM-195.

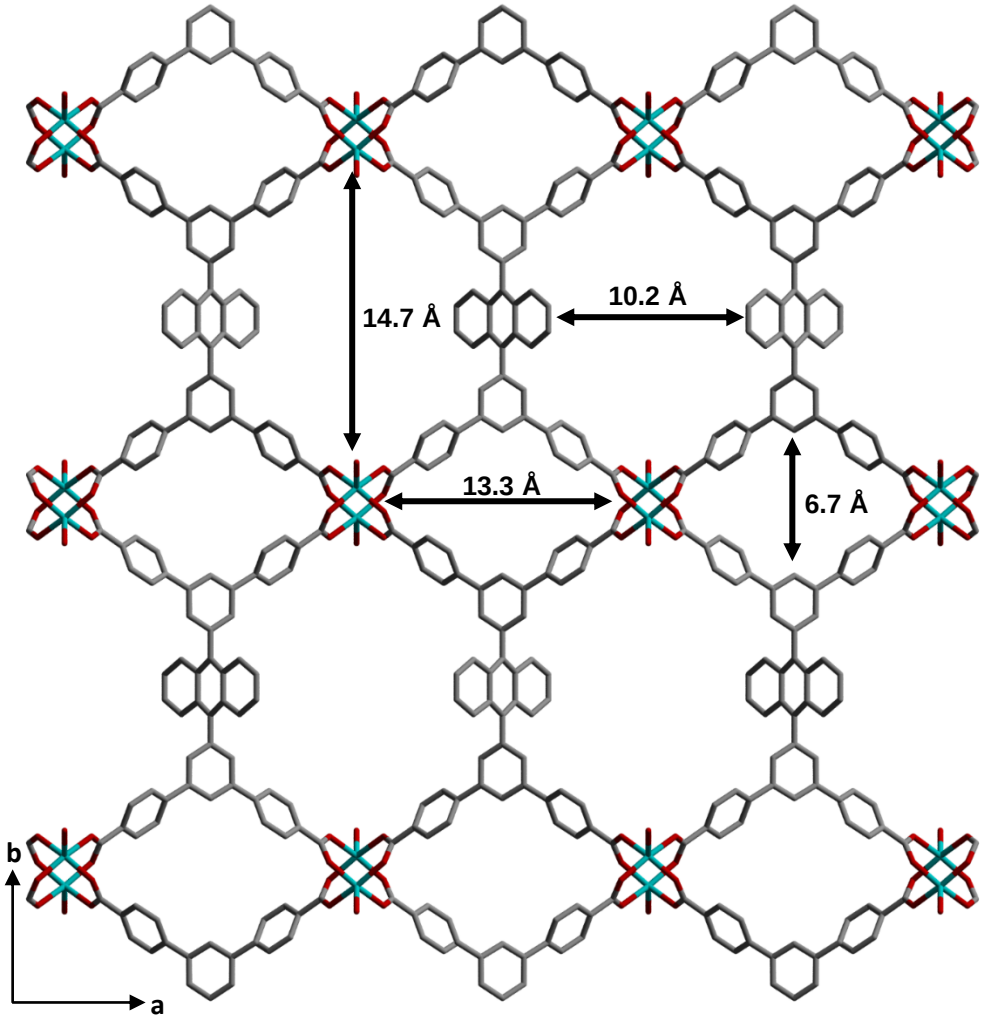


Figure 92. View down *c* axis of MFM-195.

Table 9. Crystallographic information for MFM-195.

Crystal Data	
Formula = $C_{27}H_{17}O_5Cu$	Orthorhombic, *Imma*
a = 37.5973(12) Å	V = 15852.7(13) $Å^3$
b = 29.8057(8) Å	Mr = 484.95
c = 14.1464(11) Å	Z = 8
Density = 0.406 g/cm^3	
Data Collection and Refinement	
Rint = 0.031	$R[F2 > 2\sigma(F2)]$ = 0.078
$wR(F^2)$ = 0.290	

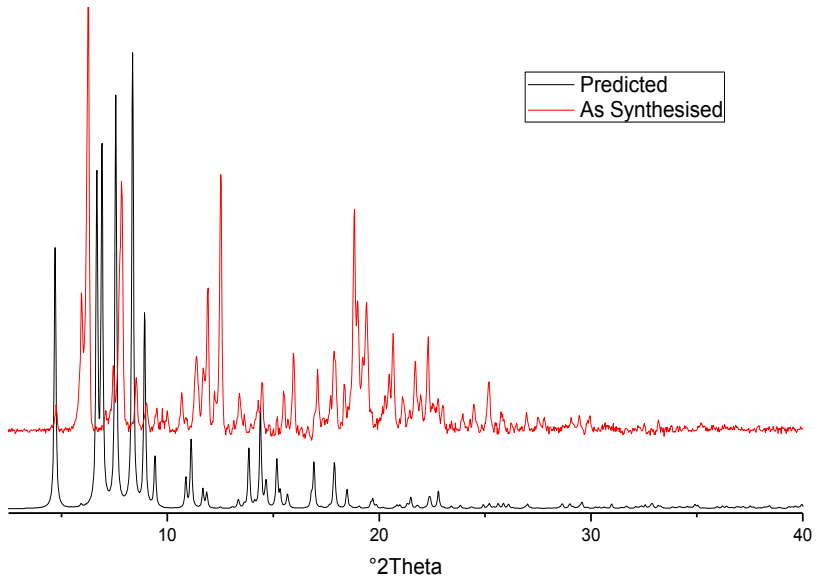


Figure 93. PXRD of simulated and as synthesised MFM-195.

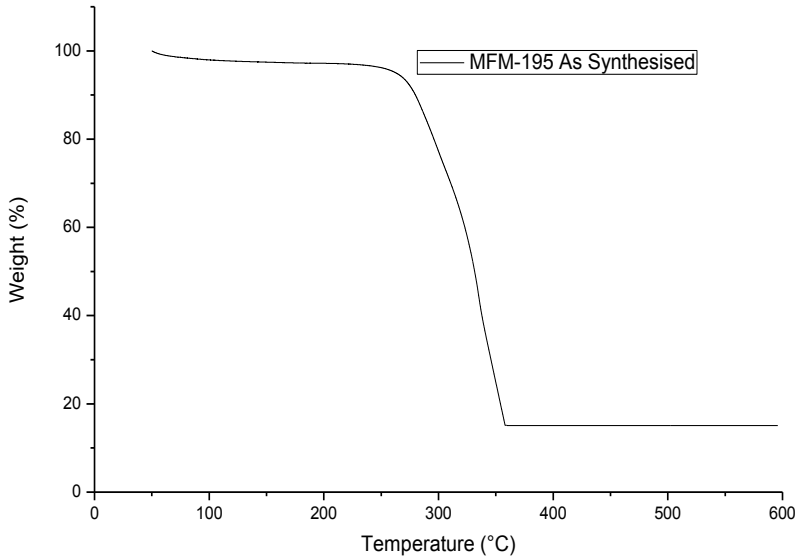


Figure 94. TGA of as synthesised MFM-195 in air.

These data matched that of a MOF published in 2013 by Gole *et al* with the same ligand, metal and topology.[29]

MFM-196

A solution of H_4L^{AM} (10 mg, 0.014 mmol) and $Cu(NO_3)_2{\cdot}2.5H_2O$ (25 mg, 0.11 mmol) in DMF (3 mL) and 8M HCl (0.03 mL) was heated to 80 °C in an 8 mL glass vial, and maintained at this temperature for 24 hours to yield blue

rhombohedral single crystals of MFM-196 with the molecular formula $[Cu_2L^{AM}(H_2O)_2].solv_x$. The as-synthesised single crystals were insoluble in organic solvents, and the crystal structure was determined by SCXRD. The bulk phase purity of the solid was analysed using powder x-ray diffraction.

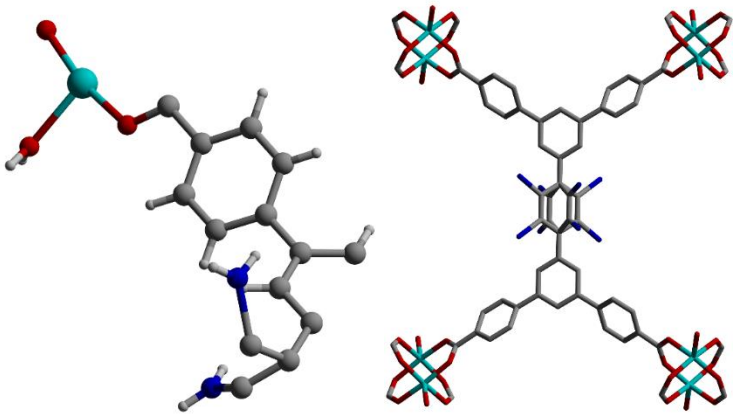


Figure 95. Asymmetric unit (left) of and connectivity of ligand in (right) MFM-196, shown with disorder.

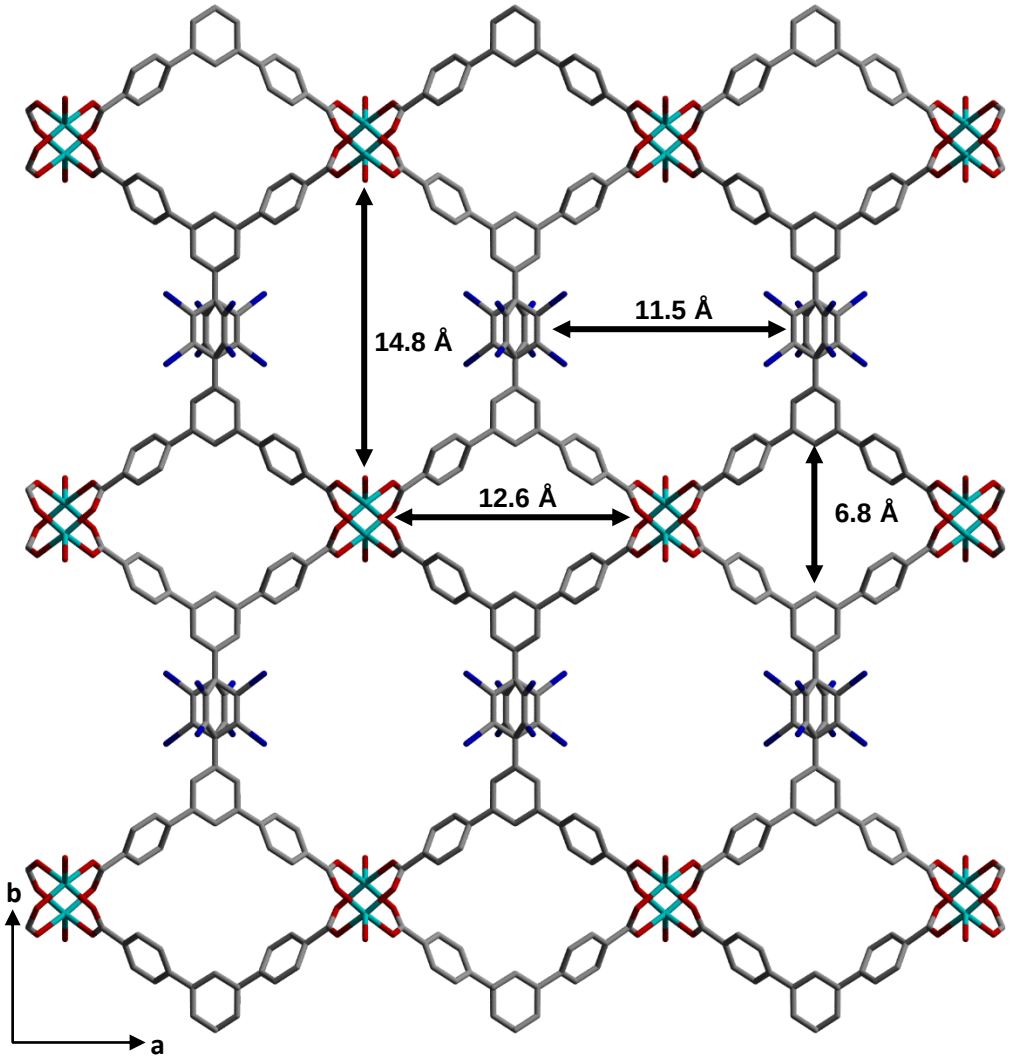


Figure 96. View down *c* axis for MFM-196. Amine group shown disordered over eight positions.

Table 10. Crystallographic information for MFM-196.

Crystal Data	
Formula = $C_{23}H_{11}O_5N_{0.5}Cu$	Orthorhombic, *Imma*
a = 37.6748(4) Å	V = 15843.7(7) $Å^3$
b = 29.8062(5) Å	Mr = 437.86
c = 14.1091(6) Å	Z = 8
Density = 0.370 g/cm^3	
Data Collection and Refinement	
Rint = 0.070	$R[F2 > 2\sigma(F2)]$ = 0.074
$wR(F^2)$ = 0.286	

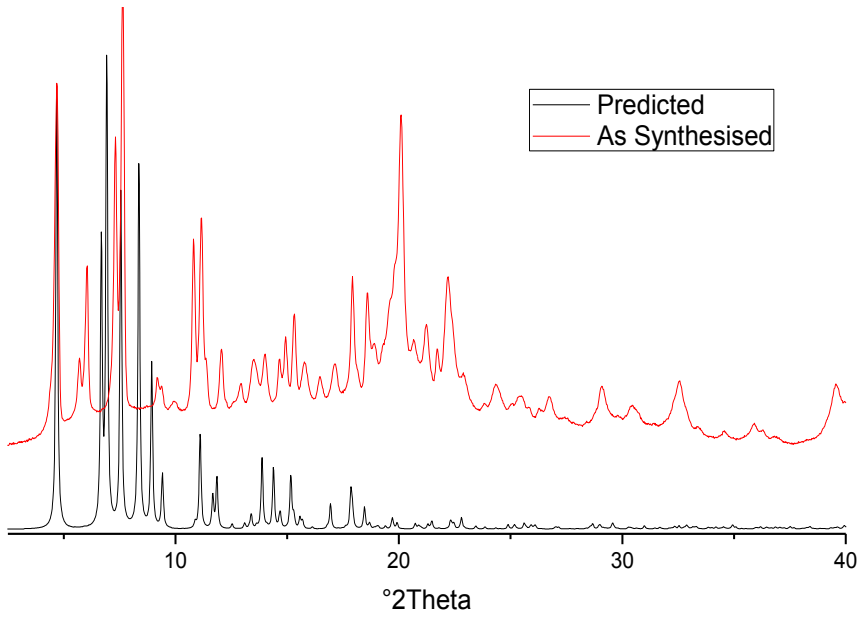


Figure 97. PXRD of simulated and as synthesised MFM-196.

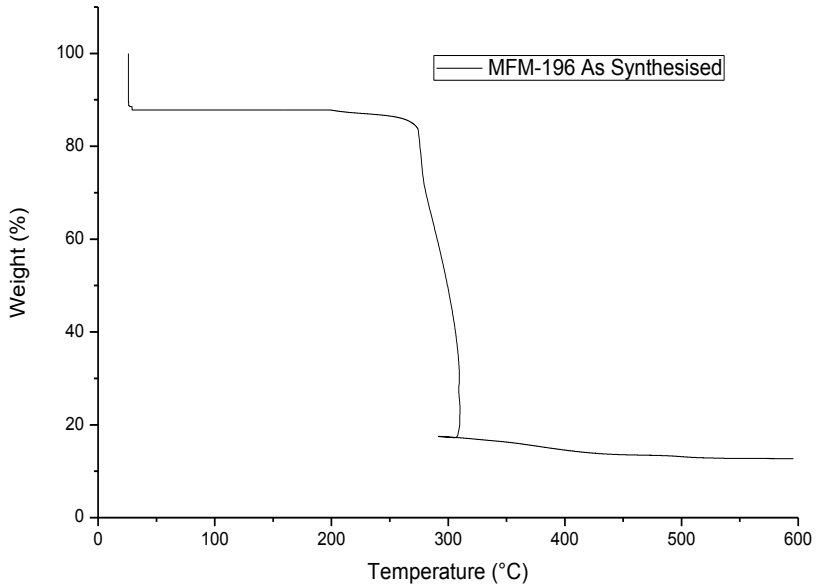


Figure 98. TGA of as synthesised MFM-196 in air.

MFM-197

A solution of H_4L^2 (10 mg, 0.013 mmol) and $Cu(NO_3)_2 \cdot 2.5H_2O$ (25 mg, 0.11 mmol) in DMF (3 mL) and 8M HCl (0.03 mL) was heated to 80 °C in an 8 mL glass vial, and maintained at this temperature for 24 hours to yield blue rhombohedral single crystals of MFM-197 with the molecular formula

$[Cu_2L^2(H_2O)_2].solv_x$. The as-synthesised single crystals were insoluble in organic solvents, and the crystal structure was determined by SCXRD. The bulk phase purity of the solid was analysed using powder x-ray diffraction.

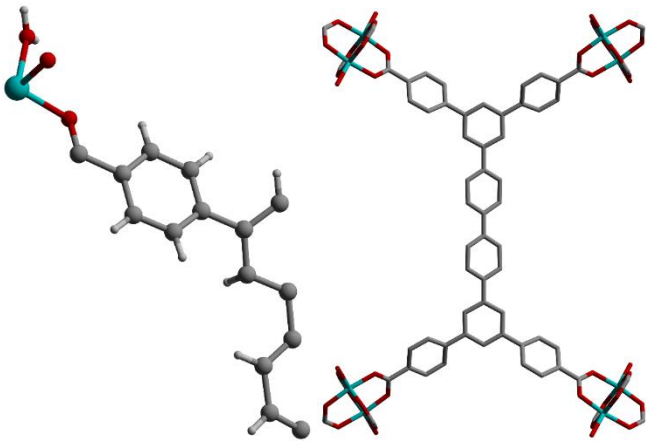


Figure 99. Asymmetric unit of (left) and connectivity of ligand in (right) MFM-197.

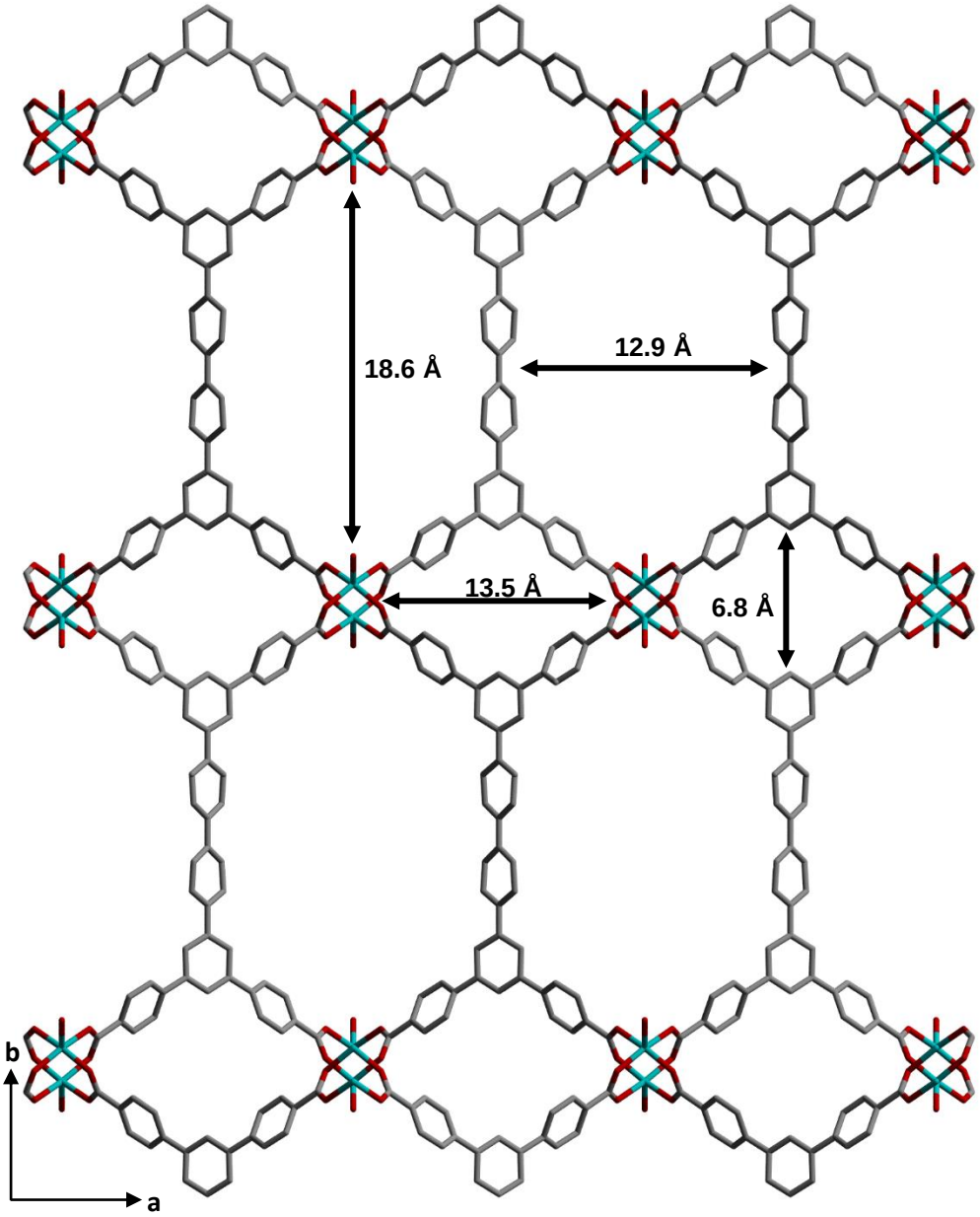


Figure 100. View down *c* axis of MFM-197.

Table 11. Crystallographic information for MFM-197.

Crystal Data	
Formula = $C_{26}H_{17}O_5Cu$	Orthorhombic, *Imma*
a = 45.956(5) Å	V = 21593(7) Å^3
b = 28.879(8) Å	Mr = 472.94
c = 16.270(3) Å	Z = 16
Density = 0.292 g/cm^3	
Data Collection and Refinement	
Rint = 0.173	$R[F2 > 2\sigma(F2)]$ = 0.072
$wR(F^2)$ = 0.231	

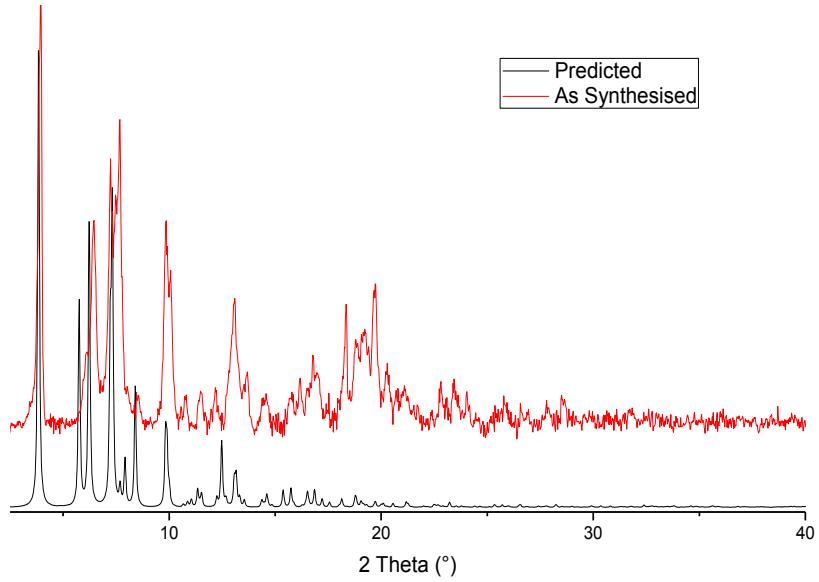


Figure 101. PXRD of simulated and as synthesised MFM-197.

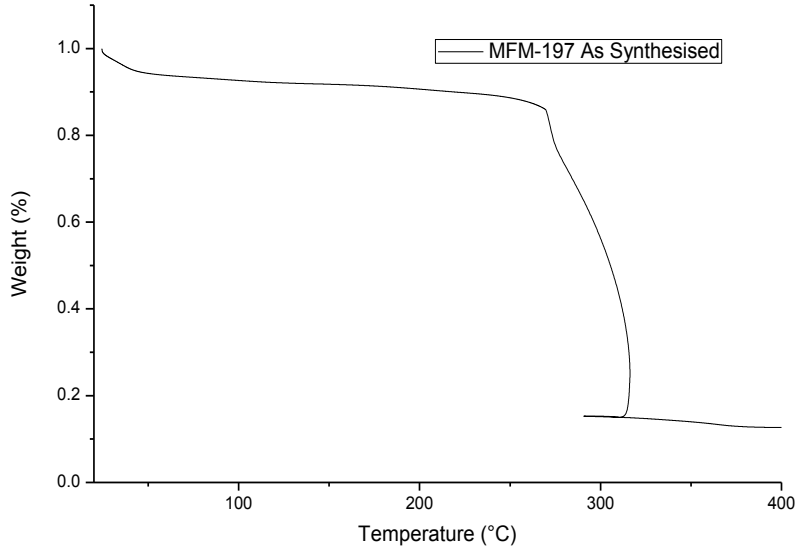


Figure 102. TGA of as synthesised MFM-197 in air.

MFM-198

A solution of H_4L^{PY} (10 mg, 0.013 mmol) and $Cu(NO_3)_2 \cdot 2.5H_2O$ (25 mg, 0.11 mmol) in DMF (3 mL) and 8M HCl (0.03 mL) was heated to 80 °C in an 8 mL glass vial, and maintained at this temperature for 24 hours to yield blue rhombohedral single crystals of MFM-198 with the molecular formula

$[Cu_2L^{PY}(H_2O)_2].solv_x$. The as-synthesised single crystals were insoluble in organic solvents, and the crystal structure was determined by SCXRD. The bulk phase purity of the solid was analysed using powder x-ray diffraction.

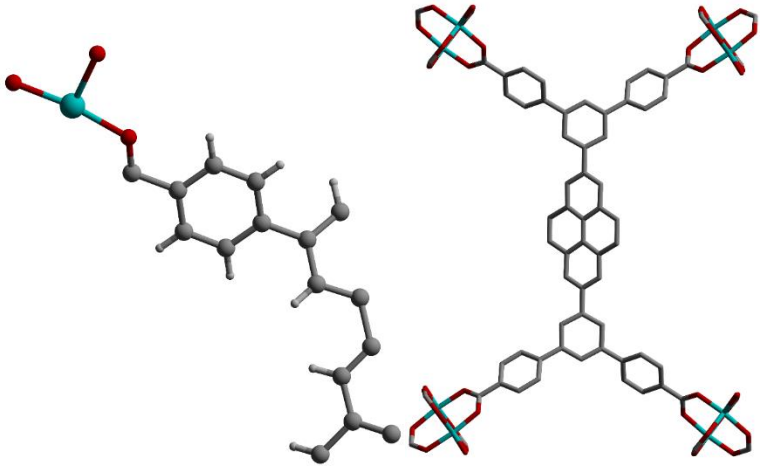


Figure 103. Asymmetric unit of (left) and connectivity of ligand in (right) MFM-198.

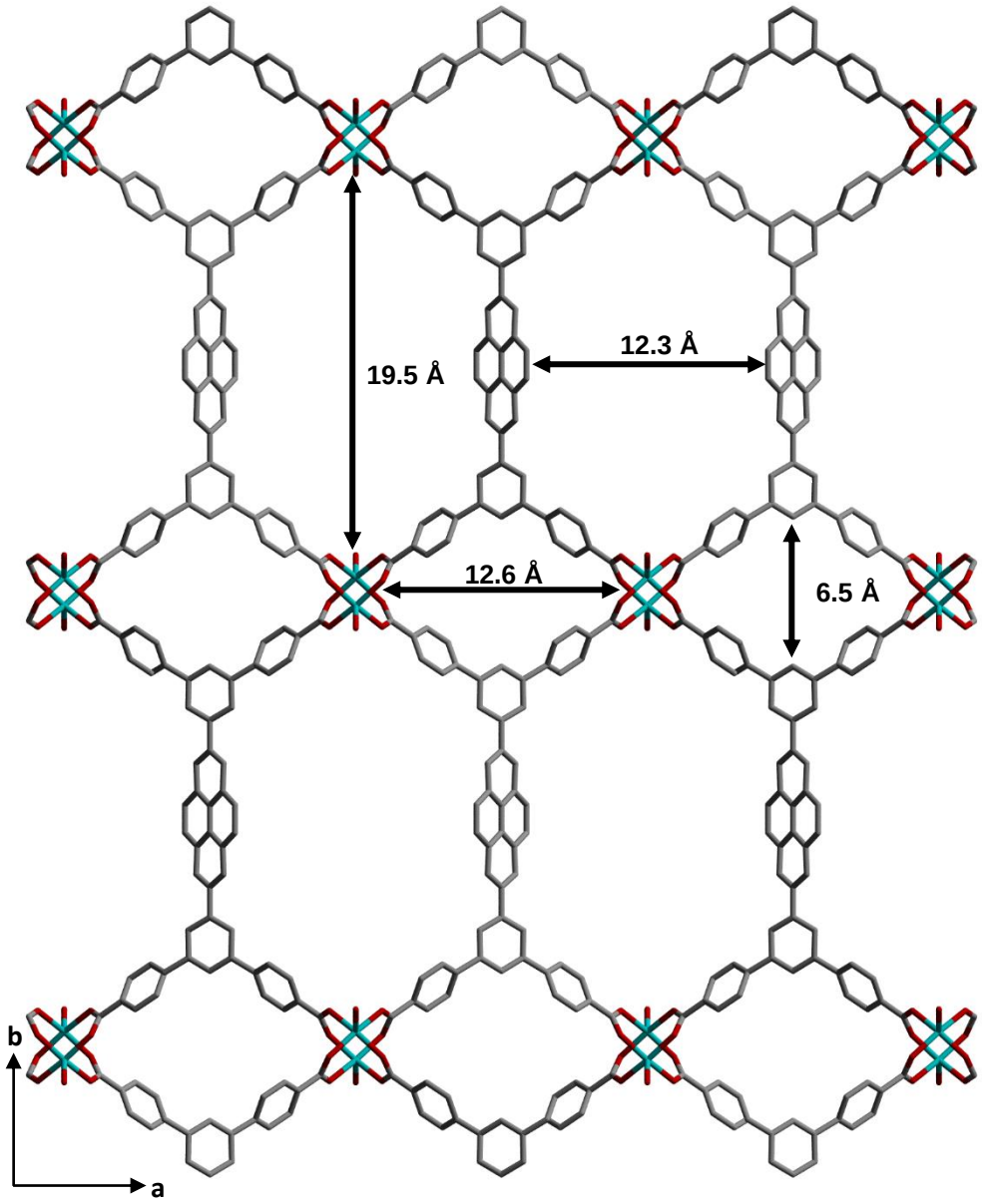


Figure 104. View down *c* axis of MFM-198.

Table 12. Crystallographic information for MFM-198.

Crystal Data	
Formula = $C_{28}H_{17}O_5Cu$	Orthorhombic, *Imma*
a = 46.439(4) Å	V = 18687(7) Å^3
b = 29.789(6) Å	Mr = 496.96
c = 13.509(4) Å	Z = 16
Density = 0.352 g/cm^3	
Data Collection and Refinement	
Rint = 0.132	$R[F2 > 2\sigma(F2)]$ = 0.120
$wR(F^2)$ = 0.384	

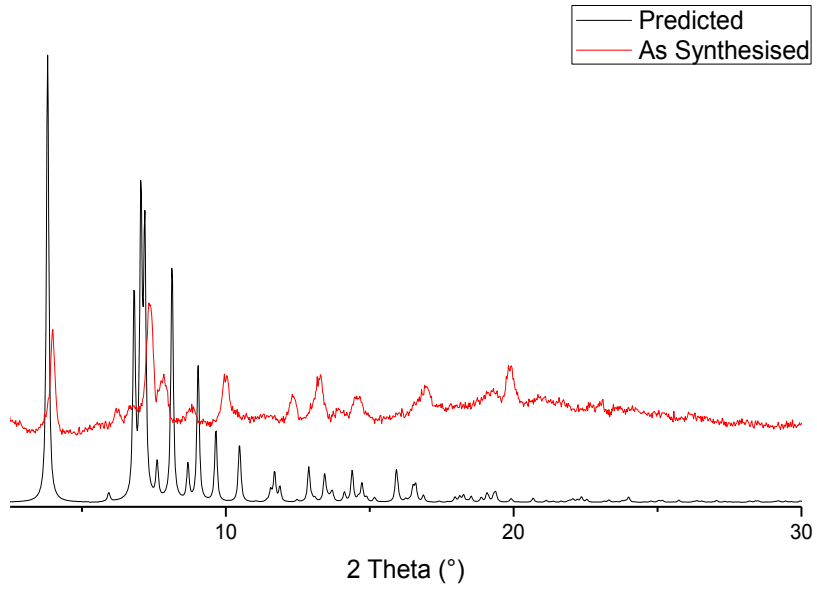


Figure 105. PXRD of simulated and as synthesised MFM-198.

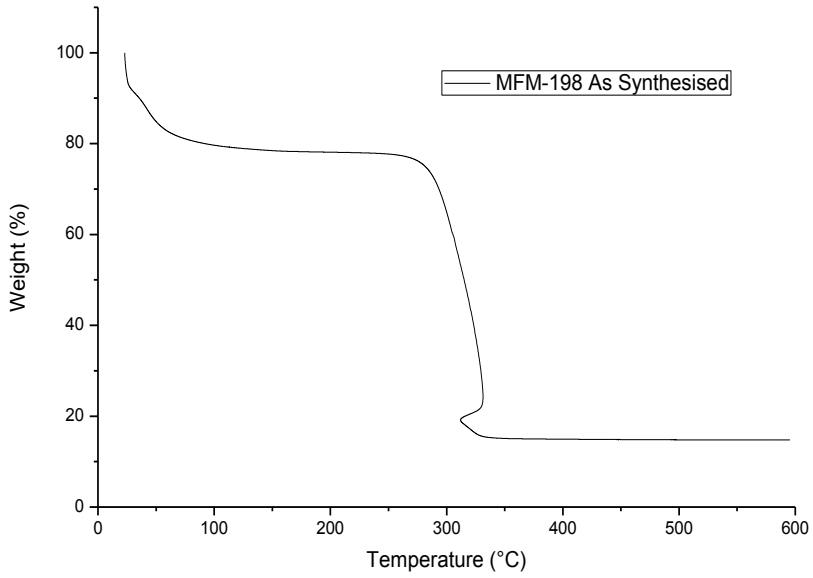


Figure 106. TGA of as synthesised MFM-198 in air.

3.2.8 Simulated Isotherms for Isoreticular Copper Series

In order to swiftly assess the efficacy of functionalising the core of the ligand and extending the pore size, simulated isotherms were calculated, as with the MFM-191, -192 and -193 frameworks.

Table 13 shows the simulated BET surface areas of the isoreticular series, which seem to follow the expected trend where the increase in pore size and porosity as the ligand is extended by an extra phenyl ring reflect an increase in BET surface area. Additionally, the extension of the ligand into the pore by functionalisation (for example, the anthracene moiety in MFM-195) results in a slight decrease in BET surface area.

Table 13. Comparison of BET surface areas across the MFM-19X series.

MOF	Porosity	BET Area (m^2/g)	He Pore Volume (cm^3/g)	Calculated Density
MFM-193	82%	6111	2.52	0.355
MFM-194	81%	5947	2.30	0.387
MFM-195	79%	5490	2.19	0.406
MFM-196	82%	7055	2.47	0.367
MFM-197	87%	13452	3.19	0.292
MFM-198	83%	7119	2.58	0.352

3.2.8.1 Comparison of Simulated Isotherms – CO_2

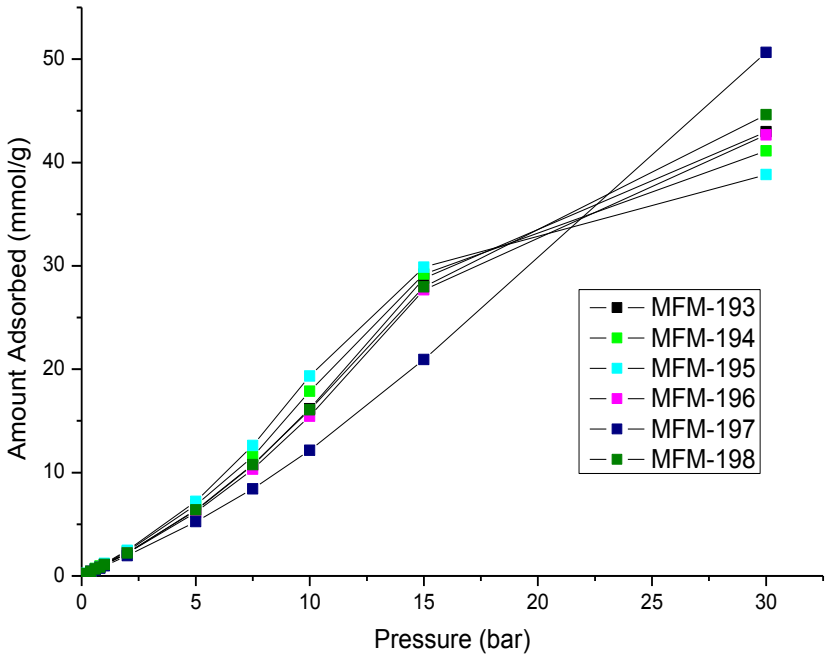


Figure 107. Simulated gravimetric CO_2 isotherms for non-interpenetrated MFM-19X series at 298 K.

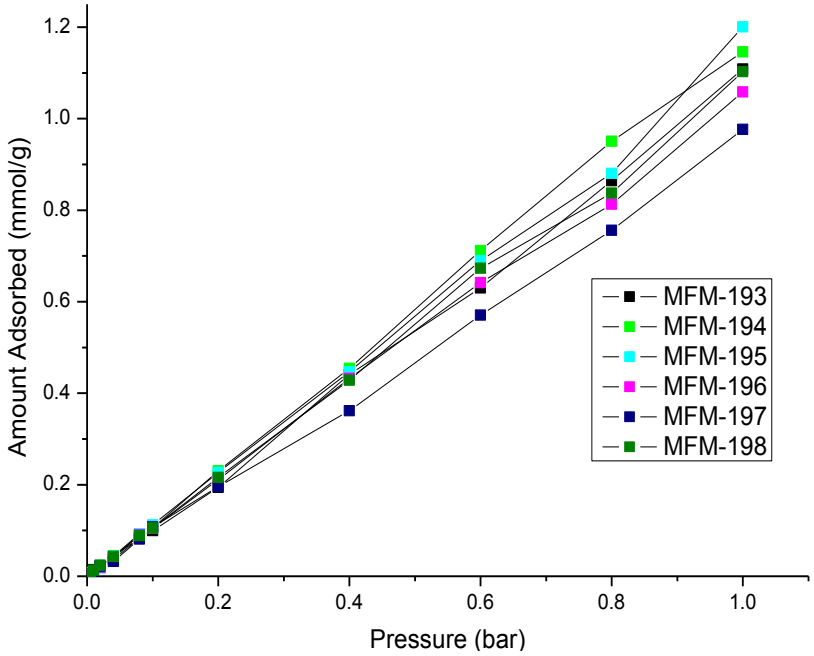


Figure 108. Simulated low pressure gravimetric methane isotherms for non-interpenetrated MFM-19X series at 298 K.

The simulated high and low pressure gravimetric isotherms (Figures 107 and 108) of the non-interpenetrated copper series follow a similar pattern to the H_4L^1 based structures discussed earlier in the Chapter, where an increase in porosity results in an increase in gravimetric uptake, which is a combined result of a decrease in density and an increase in pore volume available for storage of gases.

At lower pressures, as previously observed, the large pore volume results in less favourable uptake at low loading. This effect, combined with functionalisation, also leads to an ordering of the frameworks at low pressure which reflects the intrusion into the pore of the central core (most pronounced for the anthracene and tetramethyl functionalised ligands), and hence an increase in the interaction with the guest CO_2 molecules.

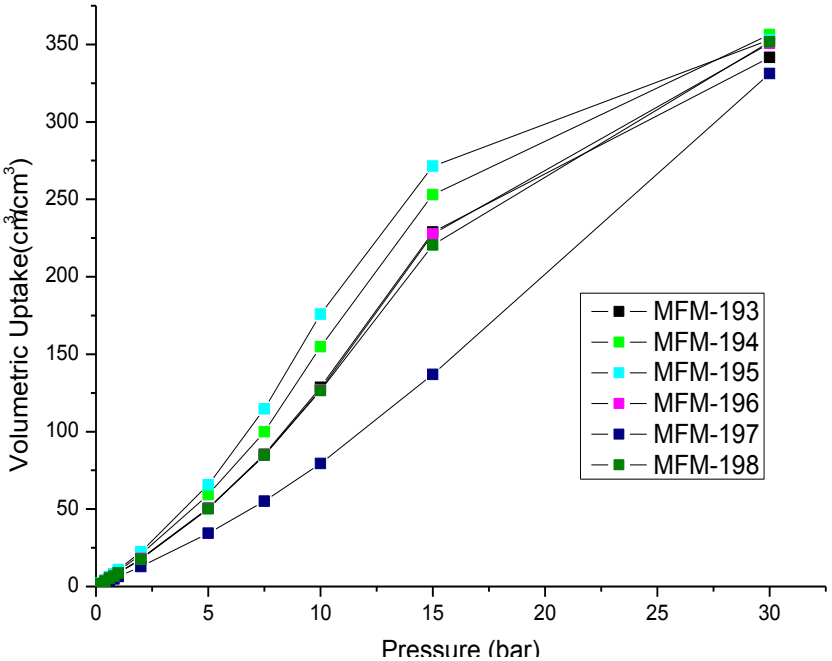


Figure 109. Simulated volumetric CO_2 isotherms for MFM-19X series at 298 K.

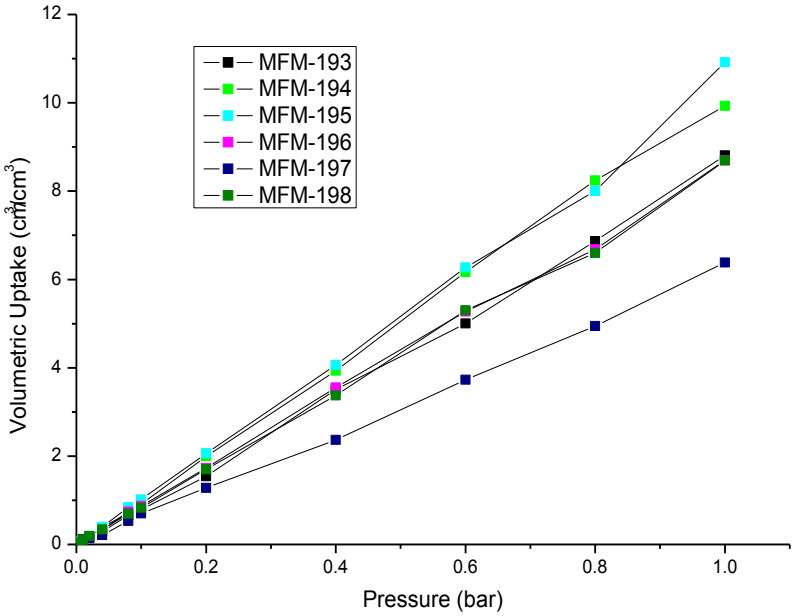


Figure 110. Simulated low pressure volumetric CO_2 isotherms for MFM-19X series at 298 K.

The volumetric uptake (Figures 109 and 110) shows very little difference at high pressures between the entire series (due to the negative effect of lower crystal density). This, coupled with the fact that at low pressures the difference is quite

pronounced between the highly porous MFM-197 and functionalised MFM-195, provides further scope on the premise of choosing MOFs for a specific purpose. For low pressure uptake, the ideal MOF would be one which is highly functionalised and, as discussed earlier, interpenetrated – for example, an anthracene functionalised equivalent of MFM-191 would prove ideal for low pressure uptake. However, for high pressure applications, the features which seem most relevant are pore size and functionalisation. Interestingly, the pendant amine group in MFM-196 did not increase the uptake as much as could have been expected when comparing to literature examples.[30,31] The most effective increase was seen with the addition of the anthracene moiety, this is most likely due to the increased interaction between the highly aromatic anthracene group and CO_2, partially *via* a small charge transfer from the ring system to the CO_2 molecule, and partially *via* dispersion interactions.[32,33]

Table 14. Comparison of porosity and CO_2 uptake at various pressures in the non-interpenetrated Cu(II) MOF series at 298 K.

	MFM-193	**MFM-194**	**MFM-195**	**MFM-196**	**MFM-197**	**MFM-198**
Central Core	Phenyl	Tetramethyl	Anthracene	Amine	Biphenyl	Pyrene
Porosity	81.6%	81%	79%	82%	87%	83%
Crystal Density	0.355	0.387	0.406	0.367	0.292	0.352
Uptake at 1 bar (mmol/g)	1.11	1.15	1.20	1.06	0.98	1.10
Uptake at 1 bar (cm^3/cm^3)	8.81	9.93	10.92	8.70	6.38	8.69
Uptake at 30 bar (mmol/g)	42.98	41.12	38.82	42.67	50.65	44.62
Uptake at 30 bar (cm^3/cm^3)	341.69	356.38	353.00	350.74	331.24	351.73

As seen in Table 14, there is a significant impact on the maximum uptake of CO_2 at various pressures dependant on how the MOF is functionalised, resulting in three clear leaders when analysing the low pressure uptake (both volumetric and gravimetric), the high pressure volumetric uptake, and the high pressure gravimetric uptake. For pressures up to 1 bar, the anthracene functionalised MOF, MFM-195, exhibits the highest uptake both gravimetrically and volumetrically (1.20 mmol/g and 10.92 cm^3/cm^3), followed closely by MFM-194 (1.15 mmol/g and 9.93 cm^3/cm^3), this effectively demonstrates how, at low pressures, extension of a ligand into a pore as large as those found in this series (~15 Å by 10 Å) is highly beneficial. This is further supported by the fact that the lowest uptake at pressures up to 1 bar is MFM-197 (0.98 mmol/g and 6.38 cm^3/cm^3), due to the lengthening of pore size to 20 Å.

The variety of functionalisation across the series allows selection of the highest uptake at 30 bar, where there is a clear leader in gravimetric uptake, MFM-197 (50.65 mmol/g compared to the closest, MFM-198, at 44.62 mmol/g), and a different leader for volumetric uptake, MFM-194 (356.38 cm^3/cm^3). This is due to the variation in crystal density across the series, which, while not as extreme as in the interpenetrated series (values range from 0.292-0.406 g/cm^3 rather than 0.355-0.733 g/cm^3), still separates the order of maximum uptake. The MOFs differ to a far lesser extent volumetrically due to the smaller discrepancy between crystal densities, resulting in MFM-197 as the preferential MOF candidate for high pressure uptake, due to the lack of a large trade-off between gravimetric and volumetric uptake.

3.2.8.2 Comparison of Simulated Isotherms – CH_4

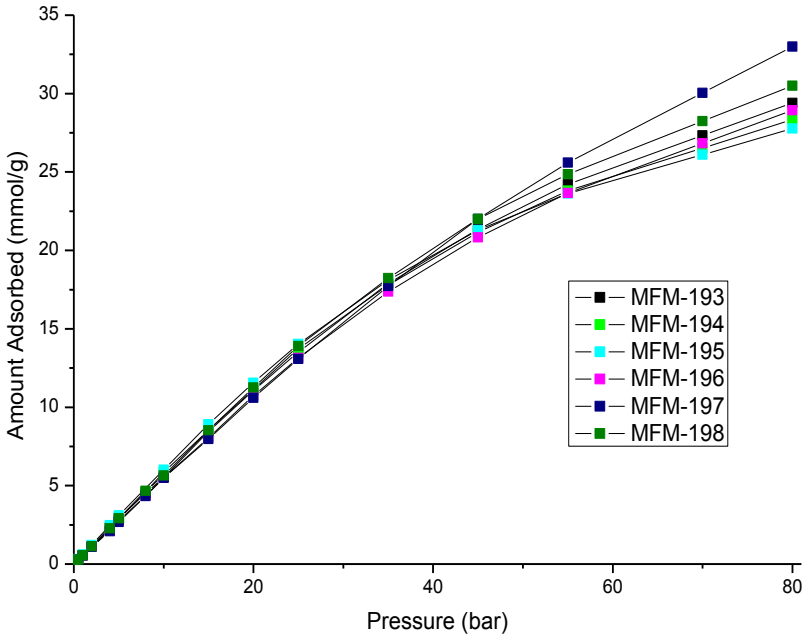


Figure 111. Simulated gravimetric methane isotherms for MFM-19X series at 298 K. *The 80 bar value is extrapolated from a 70 bar simulated isotherm.

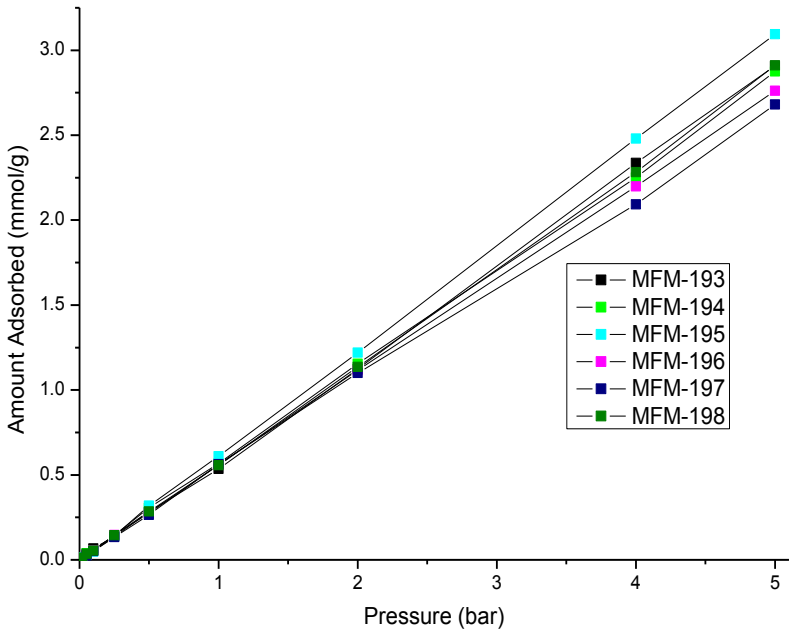


Figure 112. Simulated low pressure gravimetric methane isotherms for MFM-19X series at 298 K.

Surprisingly, the gravimetric isotherms show little difference at low pressure loadings (Figure 112), despite the various functionalisation of the central core.

The difference becomes more pronounced as the pressure reaches 80 bar (Figure 111), where the extension of the pore size and increase in porosity leads to a difference of over 5 mmol/g between the highest and lowest uptake, MFM-197 (33.00 mmol/g) and MFM-195 (27.77 mmol/g). This is attributed to the fact that pore width in MFM-195 is the smallest of the entire series (10.2 Å, instead of the average width of 13.0 Å), which enhances the low pressure interaction with guest molecules in the MOF, but hinders the maximum uptake, whereas MFM-197 has the largest pore cross-section area with a pore that measures 18.6 Å by 12.9 Å, thus providing a boost in high pressure uptake values. This consequently means that the working capacity is increased by a dual effect in MFM-197, as it has the largest difference in uptake from 5-80 bar. This shows great promise for the utilisation of this method to fine-tune MOFs for specific purposes based solely around interpenetration (as shown earlier) and extension of ligands in an isoreticular fashion, as demonstrated here.

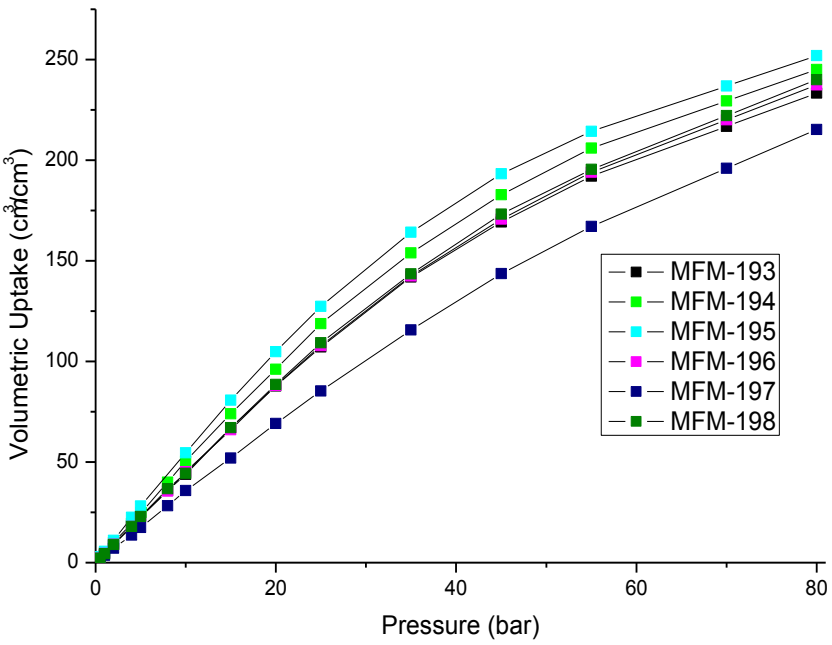


Figure 113. Simulated volumetric methane isotherms for MFM-19X series at 298 K. *The 80 bar value is extrapolated from a 70 bar simulated isotherm.

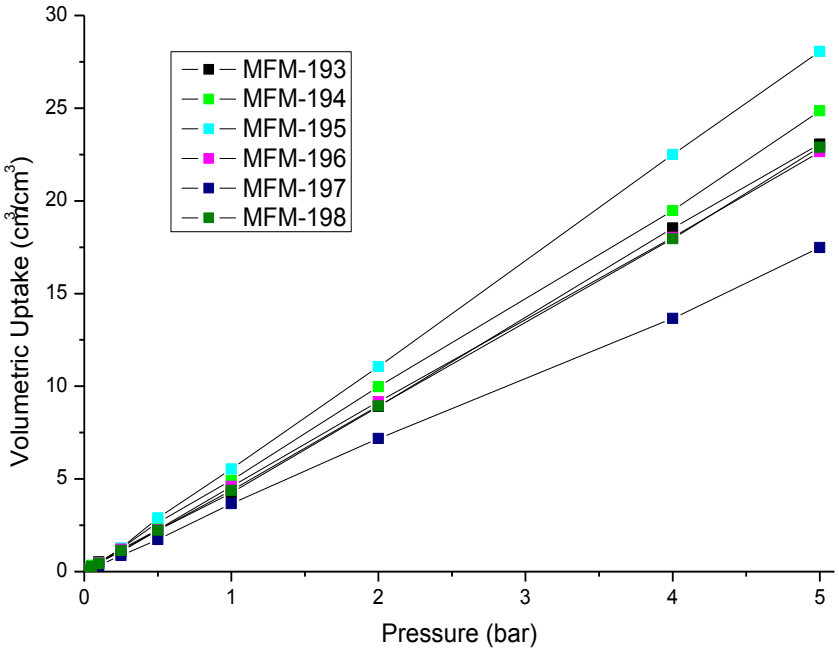


Figure 114. Simulated low pressure volumetric methane isotherms for MFM-19X series at 298 K.

Interestingly, the volumetric isotherms (Figures 113 and 114) have almost the complete reverse order of which framework has the highest capacity, with the anthracene containing MOF adsorbing the most, volumetrically, and that generated from the H_4L^2 ligand adsorbing the least. At low pressure, however, as opposed to the gravimetric isotherms, the trend is largely the same, with MFM-197 adsorbing far less than the other MOFs. This reflects the same trend found earlier in the interpenetrated series, therefore the working capacity might be highest for MFM-197 despite the relatively low volumetric uptake. Interestingly, it is in the low pressure region that the functionalisation of the ligand core has the largest effect, with MFM-195 (the anthracene functionalised MOF) displaying an increased affinity to methane (a result which echoes the trend of higher methane binding energy with increased aromaticity discussed in Section 2.1.2), and MFM-198 adsorbing far more than the 'plain' L^2 MOF.

3.2.9 Applications – CO_2 Shipping

For CO_2 transportation, the most important feature of the framework is the maximum uptake at 30 bar, and thus the deliverable quantity when releasing the pressure. In order for the system to be relevant for industrial use, the quantity should approach, and preferably exceed at 298 K the amount of CO_2 able to be stored in a pressurised container at the same pressure at 263 K. Table 15 below shows the values of CO_2 storage for a steel tank kept at temperatures low enough to maintain liquefaction of CO_2, versus the uptake of gaseous CO_2 at room temperature and 30 bar of the MFM-19X series and leading reported MOFs. All of the values are presented volumetrically, as for large scale shipping, this is the limiting factor.

Table 15. Comparison of total molar volumetric uptake of MOFs versus current technology. All MOFs are quoted at 298 K.

MOF/Container	**Pressure (bar)**	**Total Molar Uptake (mol/m^3)**
Tank at 223 K	7	26,248
Tank at 263 K	26.5	22,354
Tank at 298 K	30	1,458
MFM-191	30	12,755
MFM-192	30	14,656
MFM-193	30	15,257
MFM-194	30	15,913
MFM-195	30	15,762
MFM-196	30	15,661
MFM-197	30	14,790
MFM-198	30	15,706
HKUST-1[34]	30	9,418
IRMOF-1[35]	30	14,036
IRMOF-3[35]	30	11,062
IRMOF-6[35]	30	10,545
IRMOF-11[35]	30	10,591
MOF-177[36]	30	14,552
MOF-200[37]	30	7,566
MOF-505[38]	30	10,118

As can be seen from Table 15, the MOFs shown in this Chapter do not quite meet or exceed the capacity of a tank of liquid CO_2 at 263 K, or indeed at 223 K. However, it is evident that they far exceed the uptake of a steel tank at the same temperature, and certainly highlight the possibility of shipping CO_2 in bulk quantities in porous media such as MOFs. The ability to keep the gas at 298 K, as opposed to 263 or 223 K, brings the cost down by a considerable 2 million dollars per ship per year, and saves 72 GJs of energy for every filling cycle.[39] Additionally, the quantity able to be shipped *via* this method is over 10 times higher than the amount in a bare tank under the same conditions, thus making it feasible to ship large quantities at a time. The range of uptake throughout the MFM-19X series is quite tight (~3,000 mol/m^3 spread), as the lower crystal densities of the highly porous frameworks somewhat counter the increase in uptake when comparing them volumetrically. However, it is clear that the series as a whole slightly outperforms current reported MOFs, with the highest recorded uptake so far belonging to MOF-177 (14,552 mol/m^3), and the highest calculated uptake in the MFM-19X series being the tetramethyl functionalised MFM-194, with a maximum uptake of 15,913 mol/m^3, ~70% of the quantity of liquid CO_2 in a refrigerated tank at 263 K (22,354 mol/m^3).

3.2.10 Applications – CH_4 Storage for Vehicular Transport

Table 16 shows the working capacity of the MFM-19X series in comparison to leading MOF candidates in the literature. Comparison of the L^1 series, MFM-191, -192 and -193, highlights the equal importance of low uptake at low pressure as well as maximising high pressure uptake. MFM-192 has the highest volumetric maximum uptake (256 compared to 233 cm^3/cm^3 for MFM-193), however the strong interactions at low pressure (an uptake of 68 compared to

23 cm^3/cm^3 for MFM-193) for this system reduce the overall working capacity such that MFM-193 is the leader for both gravimetric and volumetric working capacities, despite its much lower crystal density.

Table 16. Comparison of methane working capacities to those in literature at 298 K.

	Crystal Density	Uptake at 80 bar (cm^3 cm^{-3})	Working Capacity 5-80 bar (cm^3 cm^{-3})	Uptake at 80 bar (wt%)	Working Capacity 5-80 bar (wt%)
MFM-191	0.733	219	153	21.4	14.9
MFM-192	0.584	256	188	31.4	23.1
MFM-193	0.355	233	210	47.1	42.4
MFM-194	0.387	245	220	45.4	40.8
MFM-195	0.406	252	224	44.4	39.5
MFM-196	0.367	237	215	46.3	41.9
MFM-197	0.292	215	198	52.8	48.5
MFM-198	0.352	240	217	48.8	44.2
MOF-519[40]	0.953	279	230	21.0	17.3
Al-soc-MOF-1[41]	0.34	222	201	46.7	42.3
HKUST-1[34]	0.881	272	200	22.2	16.3
MOF-520[40]	0.586	231	194	28.2	23.7
MOF-205[37]	0.38	205	186	38.6	35.0
MOF-177[36]	0.427	205	185	34.4	31.0
PCN-14[42]	0.819	250	178	21.9	15.6
Cu-tbo-MOF-5[43]	0.595	216	175	26.0	21.1
Bulk CH_4	N/A	83	79	N/A	N/A

There are a number of factors which govern the best framework for use in transport, and indeed many properties a structure must exhibit for ideal working capacity. For example, the maximum wt% uptake amongst the series discussed in this chapter is MFM-197, owing to its higher BET surface area and porosity. However, due to the low crystal density of this framework (0.292 g/cm^3) compared to MFM-192 and MFM-191 (0.584 and 0.733 g/cm^3 respectively),

the volumetric capacity is greatly reduced compared to these other frameworks. In fact the highest uptake in this respect is MFM-192, which takes up 256 cm^3 cm^{-3}, a volumetric capacity higher than MFM-193, despite the huge difference in wt % uptake. Even more important, however, is the difference in uptake between 5 and 70 bar, as this provides the 'working capacity', which has a target value to be exceeded of 50 wt% and 264 cm^3/cm^3, as set by the American DoE. This value dramatically changes the ideal properties of the MOF again, as now there is seemingly a trade-off between the porosity and crystal density of the MOF, where high porosity and large pores are needed for both the maximum uptake at high pressure and minimum uptake at low pressure (due to the distance between the framework and the centre of the pores), yet these inevitably reduce the crystal density, as the increasing void space decreases the weight present in a set volume. The fact, therefore, that the non-interpenetrated frameworks have such high volumetric capacities (between 198 and 224 cm^3/cm^3) is incredibly promising when coupled with their high gravimetric uptake (between 39 and 49 wt%), as these are both approaching the targets set by the DoE.

The series discussed above is informative when analysing the optimum framework for methane storage, as the maximum uptake can clearly be increased by introducing more aromaticity into the ligand, which interacts with the methane molecules by a C-H-pi weak hydrogen bond, the strength of which increases in line with aromaticity (as discussed in Chapter 2).[44] This can be seen by comparing the 'bare' ligand in MFM-193 to the more complex aromaticity of MFM-195, where the maximum volumetric uptake increases from 233.29 to 251.89 cm^3/cm^3 across the two (the gravimetric uptake decreases slightly due to an increase in crystal density). This same increase due to aromaticity can be

seen again with the extended 'bare' MFM-197, and subsequently functionalised MFM-198, where the maximum volumetric uptake increases hugely between the two, from 215.29 to 239.92 cm^3/cm^3.

Furthermore, the impact of increasing the pore size is shown here, as it is shown to decrease the overall volumetric uptake marginally (noteably different to the increase seen by functionalising the core of the ligand), but hugely increase the gravimetric uptake. Therefore, to get the ideal situation of a framework with both volumetric and gravimetric working capacities over the DoE targets, the framework must have large pores, a very high porosity and, most importantly, a large degree of aromaticity in the ligand core. The MOF synthesised here which meets all of these criteria is MFM-198, and it can be seen to clearly be the most suitable candidate for a material in which the trade-off between volumetric and gravimetric working capacity still places it in a favourable position and indeed potentially an industrially relevent material.

The department of energy's targets for volumetric and gravimetric capacity are shown in Table 17, comparison of the highest performing MOFs from the MFM-19X series with the targets show that, at 273 K (isotherms shown in Appendices), these MOFs show theoretical isotherms which exceed the gravimetric working capacity, and come within 10 cm^3/cm^3 of the set volumetric working capacity.

Table 17. Comparison of DoE targets and calculated results for methane uptake in select MOFs from the MFM-19X series (the working capacities for these MOFs is calculated between 5 and 80 bar).

	DoE Targets	**MFM-193**		**MFM-195**		**MFM-197**		**MFM-198**	
Temp. (K)		273	298	273	298	273	298	273	298
Grav. Working Capacity (wt %)	50	49.7	41.8	44.9	39.5	59.8	48.5	52.3	44.2
Vol. Working Capacity (cm^3/cm^3)	264	246	207	254.6	223.8	243.8	197.8	256.9	217.0

Perhaps the most encouraging result of the MFM-19X series was MFM-198, which, as shown in Table 17, not only comes the closest to achieving the DoE volumetric capacity target at 273 K (257 cm^3/cm^3 compared to 264 cm^3/cm^3), but also exceeds the gravimetric working capacity of 50 wt% (MFM-198 has a working capacity of 52 wt% at 273 K), thus making it the best 'compromise' out of the series.

3.2.11 Isolation and Purification of Phase Pure Compounds

While the ability to access a wide variety of frameworks from the same ligand and metal combination is advantageous for tuning host-guest interactions and as such enabling selection of suitable MOFs for particular applications, it can also be problematic for phase purity. Multiple phases and morphologies can form at the boundaries of the subtle changes in conditions needed to change from one framework to another.

Purification of MFM-191, MFM-192 and MFM-193

While the main driving force behind the change in interpenetration is a simple change from one solvent to another, initial results of different single crystal

morphologies came from an extensive test of a variety of conditions, which often resulted in mixed phases. Therefore, many solvothermal conditions were explored to obtain pure bulk materials of MFM-191, MFM-192 and MFM-193. The transition from interpenetrated MOFs to a non-interpenetrated MOF by increasing the acidity was another which may be expected to generate a variety of impure mixed phases en route to a pure compound. Indeed, as Figure 115 shows, initial attempts at synthesis of a pure compound led to a pattern with varied quite dramatically from the predicted pattern (from the SCXRD data).

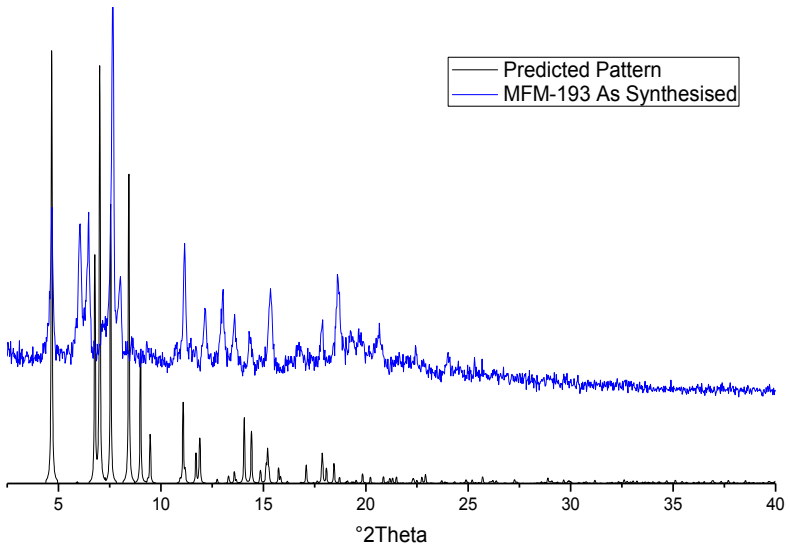


Figure 115. Predicted pattern (from SCXRD data) and experimental pattern for MFM-193.

It is quite usual to observe slight changes in peak position and intensity when comparing experimental patterns to their corresponding predicted ones, as the difference in collection temperature (typcially 120 K for SCXRD, and 298 K for PXRD) and the solvent content of the pores leads to unit cell dimension variations. However, the pattern is usually a close resemblence, and are picked up within the scope of indexing rather quickly. The nature of the **lvt** framework,

with the easily flexible 'wine-rack' motif, may account for a larger change in unit cell parameters over the 178 K difference in collection temperature.

In order to assess this, the pattern was indexed and refined using Pawley refinement of the unit cell parameters, starting from the values from the crystal structure. It was found that a good fit was obtained when the *c* axis was lengthened to 15.47 Å (and increase of 1.60 Å), with a corresponding decrease in *a* of 0.75 Å and *b* of 0.12 Å. The conservation of the orthorhombic symmetry is a clear sign that this reflected accurately a change in the MOF over this large temperature difference. Figure 116 below shows the MFM-193 framework, along the *b* axis, and illustrates the expansion and contraction of cell parameters, while Figure 117 shows the corresponding Pawley fit, with a reliable GoF of 1.67; Rwp 7.20, Rexp 4.26.

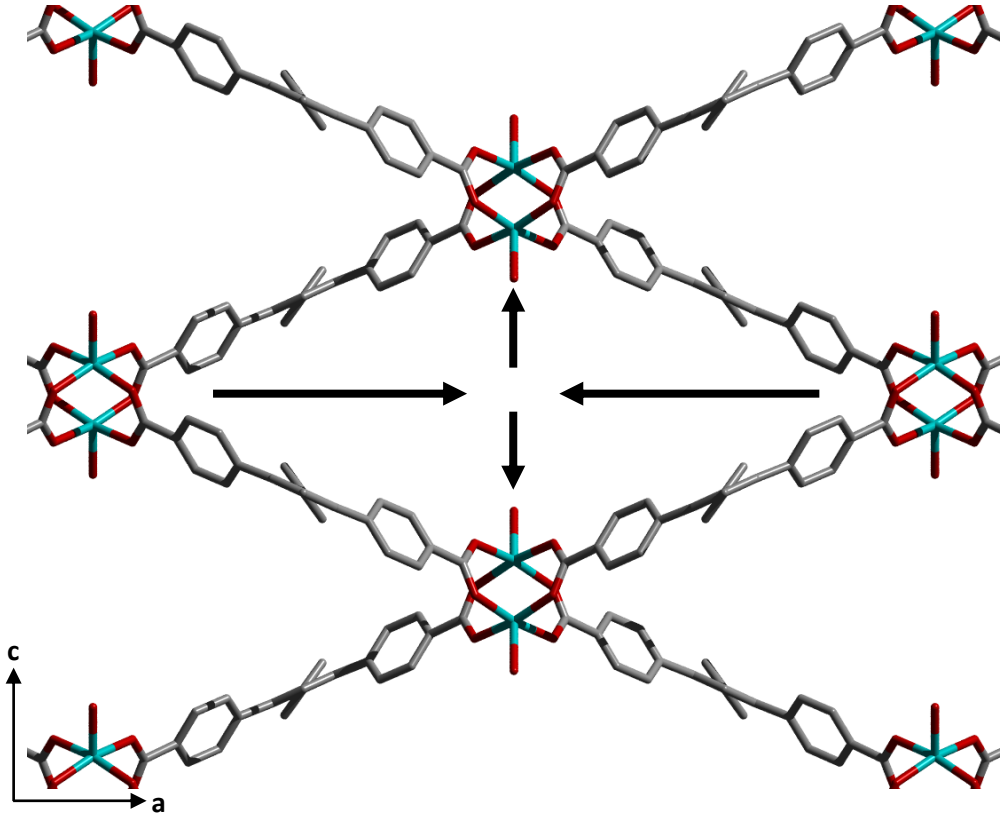


Figure 116. View along *b* axis, showing main directions of cell expansion and contraction from SCXRD at 120 K to PXRD at 298 K.

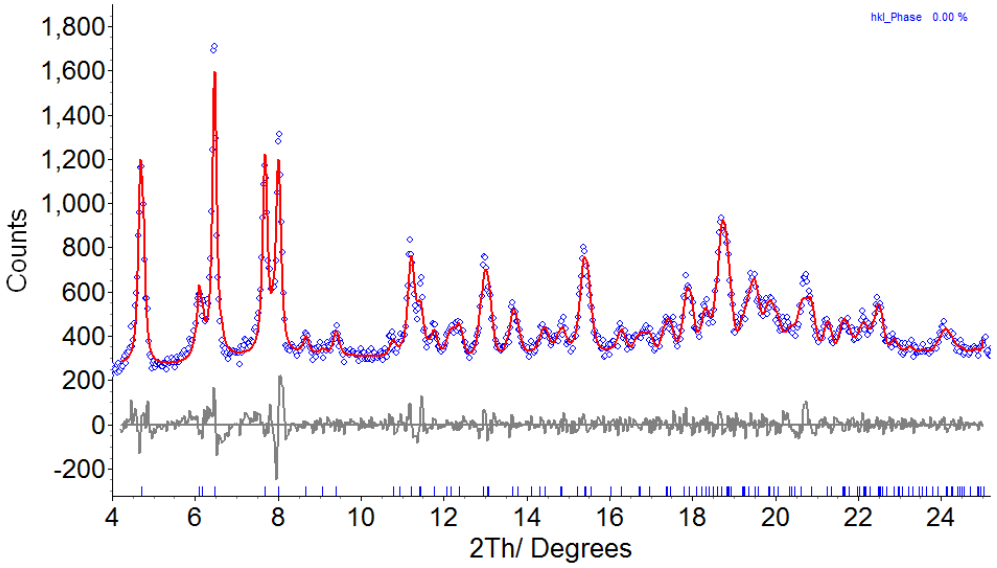


Figure 117. PXRD and Pawley fit for expansion of *c* axis in MFM-191. The blue circles are Y_{obs}, the red line is Y_{calc} and the grey line is the difference.

Cell expansion in the MFM-19X series

The rest of the non-interpenetrated series displayed a similar flexing motion in their room temperature PXRDs, these are tabulated below in Table 18.

Table 18. Comparison of shifts in cell axes across the MFM-19X non-interpenetrated series. All PXRD cells were obtained via Pawley refinement of data to a GoF < 2.

MOF	Cell Axes from SCXRD @ 120 K			Cell Axes from PXRD @ 298 K		
	a	b	c	a	b	c
MFM-193	29.7895	37.7231	13.8675	29.0444	37.6045	15.4659
MFM-194	29.7789	37.5058	14.2345	29.9858	38.6750	14.5879
MFM-195	29.8057	37.5973	14.1464	29.0843	35.4856	15.1081
MFM-196	29.8062	37.6748	14.1091	28.3104	36.8582	14.3023
MFM-197	28.879	45.956	16.270	31.0109	47.9490	17.1657
MFM-198	29.789	46.439	13.509	28.8934	45.5862	15.0650

3.2.12 Activation of MFM-19X Series

By using reticular chemistry to obtain many structures which could then be probed using simulated isotherms to assess which were suited for specific purposes, it was possible to identify key targets for activation and analysis on gas sorption instruments to recreate the highly promising predicted isotherms. This also ensures the counter-productive method of purely simulating a series of MOFs which are not ever realised for use in real world applications is avoided. The combination of versatile organic synthesis and rapid computational work proved extremely useful in this case, and indeed can be used in similar situations where the synthetic method allows for such functionalisation across a range of ligands.

The most interesting framework synthesised was clearly MFM-197, as it had both gravimetric and volumetric methane working capacities which approached and even exceeded the DoE targets. It also exhibited favourable high pressure CO_2 isotherms, and therefore was the ideal candidate for activation and assessment of the realisation of these simulated high pressure isotherms.

Activation attempt of MFM-197

A 50 mg (when wet) sample of MFM-197 was prepared as described in Section 3.2.7, washed with hot DMF (~50 mL) and soaked in acetone for 5 days (the acetone was replaced daily to ensure maximum exchange of residual DMF in the pores). This ‘acetone exchanged’ sample was then loaded into a glass micromeritics sample tube and placed on the SmartVacPrep degasser where it was heated to 100 °C under dynamic vacuum for 18 hours. The sample was seen

to change from a deep green colour to a light green, which usually suggests decomposition (Figure 118 shows a PXRD which confirms a loss of crystallinity). The sample was placed on a 3-flex gas sorption analyser for further analysis to check the stability and extent of potential collapse as suggested by the colour. Figure 111 shows the N_2 77 K isotherm, which was used to calculate the BET surface area shown below.

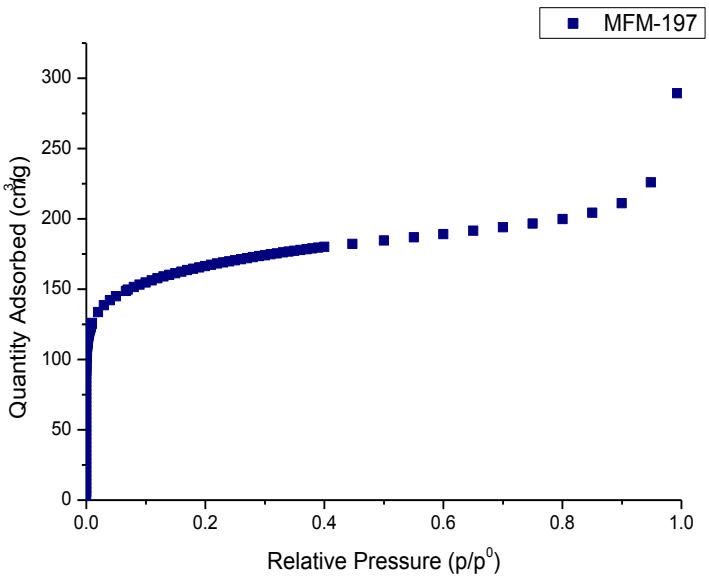


Figure 118. N_2 isotherm collected at 77 K for MFM-197.

The BET surface area calculated from the isotherm above was 606.76 m^2/g (see Experimental Section for BET plot). As seen in Figure 118, the quantity adsorbed is less than would be expected for a MOF with such large porosity. Other similar frameworks would adsorb anything above 2,000 cm^3/g, whereas this MOF reaches a maximum of around 200 cm^3/g (the spike in quantity adsorbed at pressures near $p/p^0 = 1$ is due to condensation of N_2 in the tube, and therefore is not a value to be considered here). Furthermore, analysis of the BET surface area calculated for MFM-197 shows it clearly is not stable to standard

activation methods, as the value is far lower than the predicted 13,452 m^2/g. This difference is too much to attribute it to errors in calculation or slight defects throughout the framework, and instead is evidence that the highly porous nature of the framework, coupled with the long, flexible ligand led to a collapse of the framework. Further evidence of a loss of crystallinity can be seen in Figure 119, which shows the PXRD patterns of the sample before and after activation. There is clearly some retention of long range order, which explains the BET, but the structure has clearly collapsed to a large extent.

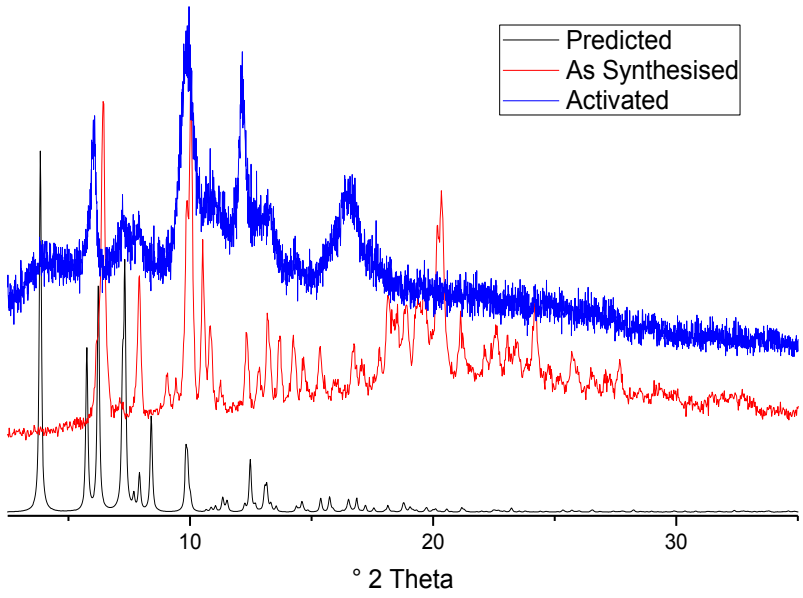


Figure 119. Predicted, as synthesised and activated PXRD patterns of MFM-197.

There are several known methods which can be employed to attempt to retain porosity lost during conventional activation methods, such as supercritical CO_2 drying,[45] or simply activating at a lower temperature, however, with MFM-193 also exhibiting favourable simulated isotherms (particularly in the working capacity of CH_4, which would be higher than current literature values), this was chosen to be explored for its stability next. The shorter nature of the ligand, and

subsequent lower porosity and less flexibility of the framework as a whole was theorised to provide some stability over MFM-197.

Activation attempt of MFM-193

A 50 mg (when wet) sample of MFM-193 was prepared as described in Section 3.2.7 and exchanged with acetone in the same manner as MFM-197. This acetone exchanged sample was then loaded into a glass micromeritics sample tube and placed on the SmartVacPrep degasser where it was heated to 100 °C under vacuum for 18 hours. The sample was seen to change from a deep green colour to a light blue, which still suggested a certain amount of decomposition (Figure 121 shows a PXRD confirming a loss of crystallinity). The sample was placed on a 3-flex gas sorption analyser for further analysis to check the stability and extent of potential collapse as suggested by the colour. Figure 120 shows the N_2 77 K isotherm, which was used to calculate the BET surface area shown below.

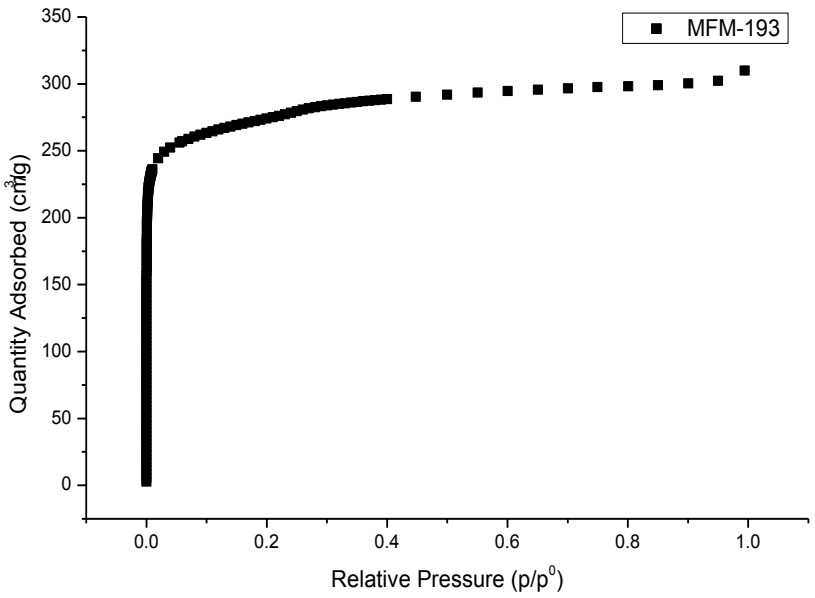


Figure 120. N_2 isotherm collected at 77 K for MFM-193.

The BET surface area calculated from the N_2 77 K isotherm was 1,038 m^2/g (see Experimental Section for BET plot). As seen by the increase in quantity adsorbed in Figure 120 and the related increase in BET surface area, clearly the MOF generated from the shorter ligand H_4L^1 was more stable than MFM-197, as the BET surface area increased where it should have decreased if both frameworks behaved in the same manner. However, this surface area is still far below the theoretical 6,111 m^2/g calculated based on the ideal crystal structure, thus suggesting that the framework is still not applicable for use in industry as the potential maximum is still not accessible under standard conditions. The loss of short range order throughout the structure is echoed in the PXRD pattern shown below in Figure 121.

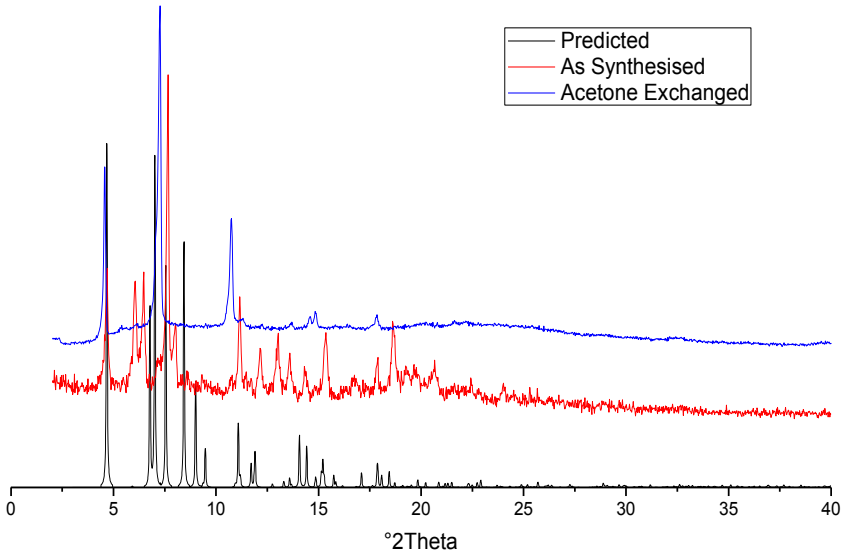


Figure 121. Predicted, as synthesised and activated PXRD patterns of MFM-193.

The shorter ligand saw an increase in strength of framework, due to less degrees of freedom being present, and brought the huge discrepancy between measured and calculated BET surface areas up from the measured value being only 4.5%

of the theoretical for MFM-197 to the measured value being 17% of the ideal for MFM-193. Therefore, a further way of strengthening the framework could be to reintroduce interpenetration, hence MFM-191 becoming the next candidate for conventional activation.

Activation attempts of MFM-191

A 50 mg (when wet) sample of MFM-191 was prepared and exchanged with acetone in the same manner as MFM-197. This acetone exchanged sample was then loaded into a glass micromeritics sample tube and placed on the SmartVacPrep degasser where it was heated to 100 °C under vacuum for 18 hours. The sample was seen to change from a deep green colour to a light green, which suggested framework collapse (Figure 123 shows a PXRD with a significant decrease in crystallinity when activated). The sample was placed on the 3-flex for further analysis to check the stability and extent of potential collapse as suggested by the colour. Figure 115 shows the N_2 77 K isotherm, which was used to calculate the BET surface area shown below.

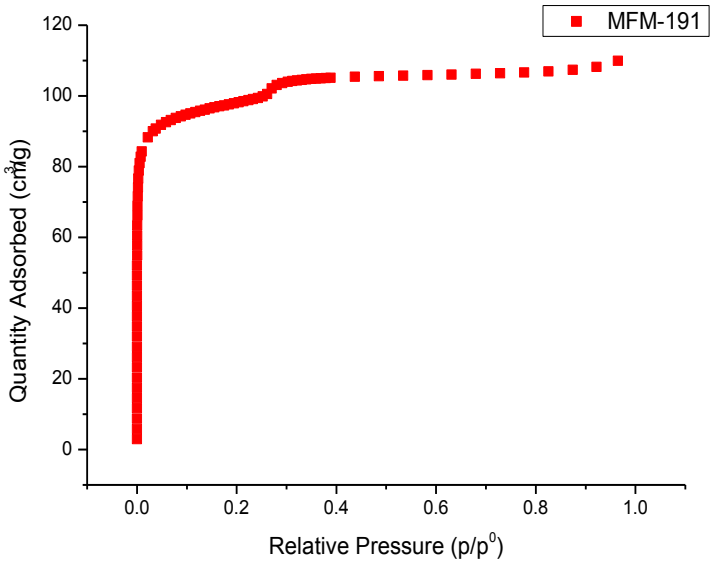


Figure 122. N_2 isotherm collected at 77 K for MFM-191.

The BET surface area calculated from the N_2 77 K isotherm shown in Figure 122 was 290 m^2/g. The BET for this framework was much lower than expected, as the increase in stability that might come from interpenetration was theorised to lead to a BET which is a greater percentage of the ideal value. As it was, this value stood at 13% of the ideal value of 2,150 m^2/g. This is still more than MFM-197, but less than MFM-193. MFM-191 was activated using supercritical CO_2 drying in order to determine the cause of this lack of stability, possibly inherent to the framework. This was important, as it would ascertain whether or not the sample was capable of realising the theorised values, which were incredibly promising for both CO_2 shipping and methane storage for use in vehicular transport.

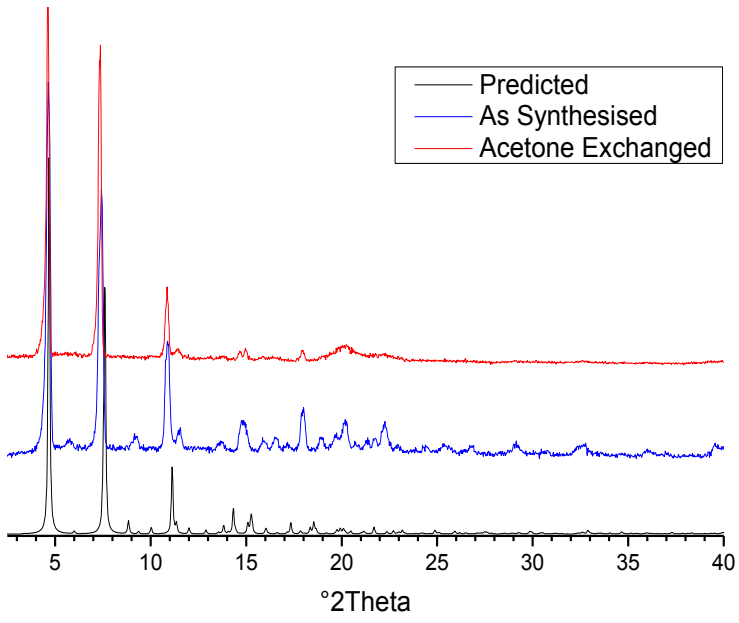


Figure 123. Predicted, as synthesised and activated PXRD patterns of MFM-191.

Supercritical CO_2 activation

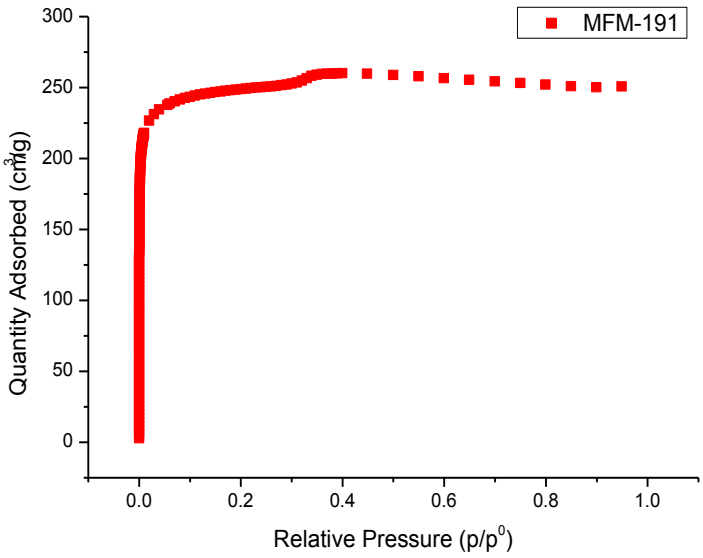


Figure 124. N_2 isotherm collected at 77 K for MFM-191 after $scCO_2$ activation.

The BET surface area calculated from the isotherm shown in Figure 124 was 911 m^2/g. Supercritical activation clearly increased the BET surface area of the sample, and hence retained more porosity than the conventional method. The percentage of the ideal BET surface area was now 42%, which is a large increase from the conventional method, but still vastly lower than ideal. This was still not high enough to give the promising isotherms calculated theoretically, but showed how by changing the ligand, activation method and interpenetration level it was possible to change the permanent porosity from less than 5% of the ideal to over 40%.

A thorough analysis of the **lvt** topology suggested that this instability is something inherent in the topology, as it is highly flexible. A deformation analysis performed on the topology at Lawrence Berkley National Laboratory (Figure 125)[46] shows how the framework is flexible along all axes, as indicated

by the flat lines on the graph. This is in stark contrast to, for example **pcu** (the topology of the highly stable MOF-5),[47] which is rigid along all axes and angles, and as such is absent of straight lines in the deformation graph below.

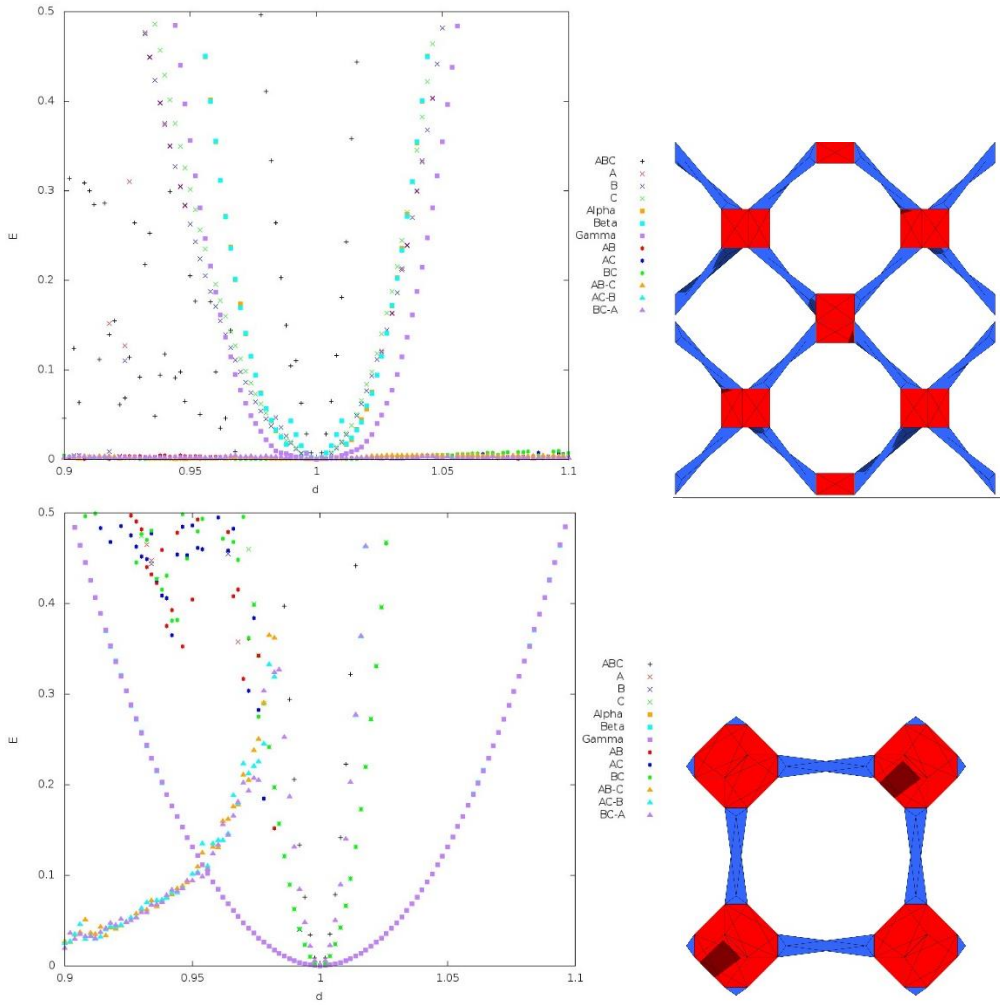


Figure 125. Deformation analysis graph of flexible **lvt** topology (top) and rigid **pcu** topology (bottom).[46]

3.3 Conclusion

This chapter discussed the advantages of co-operation of synthetic and computational work to optimise MOFs for specific purposes, with particular emphasis on the unique opportunity to probe not only the introduction and removal of interpenetration in frameworks, but also the change to a different class of interpenetration. It was evident from this investigation that for low

pressure CO_2 uptake, the interpenetrated framework MFM-192 (class Ia) was preferential, due to the proximity of the centre of the pore to the framework, resulting in interactions of the gas molecule and the MOF even at very low loadings. The high pressure methane uptake, however, favoured the more porous non-interpenetrated framework MFM-193, which had the highest simulated BET surface area of the three MOFs generated from the ligand H_4L^X, and therefore had the maximum void space to host such a vast quantity of methane molecules. The calculated methane isotherm suggested that if this was realised experimentally, MFM-193 would have the highest recorded methane uptake to date.

Further discussion centred on the ability to generate a large variety of isoreticular functionalised frameworks via versatile ligand synthesis, which led to rapid screening of these samples to identify those which exceeded the promising result already shown by MFM-193. Careful analysis of the simulated isotherm resulted in the most porous framework, MFM-197, exhibiting a working capacity for methane which could potentially prove industrially relevant for use in methane fuelled vehicles. This result echoed the trend seen in the earlier MOFs, as the functionalisation of the ligand led to better low pressure uptake (due to a combination of the functionality interacting with the gas molecule, but also the extension of the ligand into the pore, acting in a similar manner to the gas uptake as the interpenetration did for MFM-191 and MFM-192), while the extension of the ligand and subsequent extension of the pore and raising of the overall porosity and BET surface area led to record high pressure uptake.

There was also discussion on the trade-off between volumetric and gravimetric uptake due to the lowering of crystal density usually brought about by an increase in porosity. This provided a premise of choosing MOFs for a specific purpose. For low pressure uptake, the anthracene derivative (MFM-195) seemed most appropriate of the non-interpenetrated MOFs due to the extension into the pore. However, for high pressure applications, the feature which seemed most relevant was pore size, and then functionality to a lesser extent, thus resulting in MFM-197 and MFM-198 as the most promising high pressure uptake candidates.

The chapter culminated in the various activation methods used to attempt to obtain the same isotherms and BET surface area as were computationally calculated. The initial attempts were with MFM-197, as this had the highest methane gravimetric working capacity, but swiftly moved towards frameworks with smaller pores which may have been more stable. While shortening the ligand increased the permanent porosity due to the decrease in flexibility, and hence increase in stability, the results were still far below those calculated, and indeed far below current literature values. The highest proportion of theoretical permanent porosity realised was 42%, for MFM-191 (the least porous and hence most stable) activated from supercritical CO_2, and with a change in synthesis conditions to move away from molecules which might bind and not be removed from the paddlewheel. While this was a large increase from the miniscule 4.5% proportion of BET surface area attained by MFM-197, it still suggested that copper **lvt** frameworks were potentially not suitable for industrial gas uptake applications, and therefore a more stable framework with an SBU with higher metal-oxygen bond enthalpies was required. It is possible that with further

reduction of the ligand size a framework might be accessible which demonstrates a degree of stability, however the ligands synthesised in this thesis were ideal candidates for the synthesis of some Zr(IV) MOFs, as these are well known for their stability throughout literature, and using the ligand library already synthesised, MOFs with stable permanent porosity, high BET surface areas and decent high pressure storage of methane and CO_2 could be easily attainable.

3.4 Experimental

3.4.1 Solvothermal Syntheses of MFM-19X Series

Solvothermal synthesis of MFM-191

A solution of H_4L^1 (10 mg, 0.014 mmol) and $Cu(NO_3)_2{\cdot}2.5H_2O$ (25 mg, 0.11 mmol) in DMF (3 mL), acetonitrile (1 mL), dimethylsulfoxide (1 mL) and 0.1M HCl (1 mL) was heated to 80 °C in a sealed 8 mL Wheaton vial, and maintained at this temperature for 24 hours to yield rhombohedral blue single crystals. These were washed several times with hot DMF, and soaked in acetone over several days to give $[Cu_2L^1(H_2O)_2]{\cdot}(H_2O)_3$, MFM-191 (11 mg, 85% yield). Elemental analysis – Expected: C 59.80; H 3.93, Found (average): C 58.26; H 3.81; N 0.

Solvothermal synthesis of MFM-192

A solution of H_4L^1 (10 mg, 0.014 mmol) and $Cu(NO_3)_2{\cdot}2.5H_2O$ (25 mg, 0.11 mmol) in DEF (3 mL), acetonitrile (1 mL) and 0.1M HCl (1 mL) was heated to

80 °C in an 8 mL Wheaton vial, and maintained at this temperature for 24 hours to yield blue rod shaped single crystals. These were washed several times with hot DMF, and soaked in acetone over several days to give $[Cu_2L^1(H_2O)_2]\cdot(H_2O)_3$, MFM-192 (8 mg, 62% yield). Elemental analysis – Expected: C 59.80; H 3.93, Found (average): C 62.38; H 3.51; N 0.

Solvothermal synthesis of MFM-193

A solution of H_4L^1 (10 mg, 0.014 mmol) and $Cu(NO_3)_2\cdot 2.5H_2O$ (25 mg, 0.11 mmol) in DMF (3 mL) and 8M HCl (0.03 mL) was heated to 80 °C in an 8 mL Wheaton vial, and maintained at this temperature for 24 hours to yield rhombohedral blue single crystals. These were washed several times with hot DMF, and soaked in acetone over several days to give $[Cu_2L^1(H_2O)_2]$, MFM-193 (10 mg, 86% yield). Elemental analysis – Expected: C 63.52; H 3.48, Found (average): C 63.58; H 3.27.

Solvothermal synthesis of MFM-194

A solution of H_4L^{TM} (10 mg, 0.013 mmol) and $Cu(NO_3)_2\cdot 2.5H_2O$ (25 mg, 0.11 mmol) in DMF (3 mL) and 8M HCl (0.03 mL) was heated to 80 °C in an 8 mL Wheaton vial, and maintained at this temperature for 24 hours to yield rhombohedral blue single crystals. These were washed several times with hot DMF, and soaked in acetone over several days to give $[Cu_2L^{TM}(H_2O)_2]\cdot((CH_3)_2CO)_4(H_2O)$, MFM-194 (11 mg, 72% yield). Elemental analysis – Expected: C 63.31; H 5.48 Found (average): C 65.13; H 4.44; N <0.3

Solvothermal synthesis of MFM-195

A solution of H_4L^{AN} (10 mg, 0.012 mmol) and $Cu(NO_3)_2{\cdot}2.5H_2O$ (25 mg, 0.11 mmol) in DMF (3 mL) and 8M HCl (0.03 mL) was heated to 80 °C in an 8 mL Wheaton vial, and maintained at this temperature for 24 hours to yield rhombohedral blue single crystals. These were washed several times with hot DMF, and soaked in acetone over several days to give $[Cu_2L^{AN}(H_2O)_2]{\cdot}(H_2O)_2$, MFM-195 (11 mg, 91% yield). Elemental analysis – Expected: C 64.47; H 3.81, Found (average): C 62.76; H 2.69; N <0.3.

Solvothermal synthesis of MFM-196

A solution of H_4L^{AM} (10 mg, 0.014 mmol) and $Cu(NO_3)_2{\cdot}2.5H_2O$ (25 mg, 0.11 mmol) in DMF (3 mL) and 8M HCl (0.03 mL) was heated to 80 °C in an 8 mL Wheaton vial, and maintained at this temperature for 24 hours to yield rhombohedral blue single crystals. These were washed several times with hot DMF, and soaked in acetone over several days to give $[Cu_2L^{AM}(H_2O)_2]{\cdot}((CH_3)_2CO)_4$, MFM-196 (10 mg, 64% yield). Elemental analysis – Expected: C 62.36; H 4.96; N 1.25, Found (average): C 63.24; H 4.68; N 0.3.

Solvothermal synthesis of MFM-197

A solution of H_4L^2 (10 mg, 0.013 mmol) and $Cu(NO_3)_2{\cdot}2.5H_2O$ (25 mg, 0.11 mmol) in DMF (3 mL) and 8M HCl (0.03 mL) was heated to 80 °C in an 8 mL Wheaton vial, and maintained at this temperature for 24 hours to yield rhombohedral blue single crystals. These were washed several times with hot DMF, and soaked in acetone over several days to give $[Cu_2L^2(H_2O)_2]{\cdot}((CH_3)_2CO)_2(H_2O)_3$, MFM-197 (8 mg, 55% yield). Elemental

analysis – Expected: C 62.42; H 4.70; N 0.00 Found (average): C 61.67; H 4.18; N 0.45.

Solvothermal synthesis of MFM-198

A solution of H_4L^{PY} (10 mg, 0.013 mmol) and $Cu(NO_3)_2{\cdot}2.5H_2O$ (25 mg, 0.11 mmol) in DMF (3 mL) and 8M HCl (0.03 mL) was heated to 80 °C in an 8 mL Wheaton vial, and maintained at this temperature for 24 hours to yield rhombohedral blue single crystals. These were washed several times with hot DMF, and soaked in acetone over several days to give $[Cu_2L^{PY}(H_2O)_2]{\cdot}(H_2O)_1$, MFM-198 (9 mg, 68% yield). Elemental analysis – Expected: C 66.46; H 3.59, Found (average): C 67.36; H 3.45; N<0.3

3.4.2 Single Crystal Structure Determination for MFM-19X Series

Single crystals were analysed on either a Supernova, Dual Atlas diffractometer, held at 119.99(10) K during data collection, or on an Agilent GV1000 CuKα1 X-Ray diffractometer at 120.15(10) K. All structures were solved by direct methods using Olex2,[48] with the ShelXD[49] structure solution program, refined with the ShelX[50] refinement package using least squares minimisation. The H atoms on the apical water molecules could not be located, but are included in the formula sum. The unit cells contain a large region of disordered solvent due to the high porosity of the frameworks, which could not be modelled as discrete molecules. As such, the PLATON SQUEEZE[24] function was used to calculate the diffraction contribution of these molecules, and mask them to produce a new set of solvent-free diffraction intensities which were used in the final refinement

stages. The final formula was calculated from CHN analyses combined with TGA.

3.4.3 Crystal Data for MFM-19X Series

Crystallographic Information for MFM-191

Crystal Description	
Blue rectangular crystals	Crystal Size: 50x20x10 μm
Crystal Data	
Formula = $C_{23}H_{15}O_5Cu$	Orthorhombic, *Cmca*
a = 37.7326(9) Å	V = 15119.0 (6) $Å^3$
b = 29.4510(6) Å	Mr = 434.89
c = 13.6053(4) Å	Z = 16
Density = 0.764 g/cm^3	
Data Collection and Refinement	
F(000) = 3552	Rint = 0.024
$R[F2 > 2\sigma(F2)]$ = 0.046	$wR(F^2)$ = 0.215
43755 reflections; 7784 unique, 6972 with $I > 2\sigma I$	GOF = 0.998
μ = 0.96 mm^{-1}	Max/min residual electron density after PLATON SQUEEZE = 0.5/-0.5 e A^{-3}
Electrons found in solvent accessible volume: 2080	

Crystallographic Information for MFM-192

Crystal Description	
Blue rhombohedral crystals	Crystal Size: 50x50x10 μm
Crystal Data	
Formula = $C_{23}H_{15}O_5Cu$	Orthorhombic, *Pbcm*
a = 9.37961(9) Å	V = 9487.97(15) $Å^3$
b = 28.3973(2) Å	Mr = 434.89
c = 35.6214(3) Å	Z = 8
Density = 0.608897 g/cm^3	
Data Collection and Refinement	
F(000) = 1776	Rint = 0.0159
$R[F2 > 2\sigma(F2)]$ = 0.0808	$wR(F^2)$ = 0.2641
53853 reflections; 9728 unique, 8472 with $I > 2\sigma I$	GOF = 1.106
μ = 0.77 mm^{-1}	Max/min residual electron density after PLATON SQUEEZE = 3.3/-0.5 e A^{-3}
Electrons found in solvent accessible volume:1354	

Crystallographic Information for MFM-193

Crystal Description	
Blue rhombohedral crystals	Crystal Size: 80x80x30 μm
Crystal Data	
Formula = $C_{23}H_{15}O_5Cu$	Orthorhombic, *Imma*
a = 29.7895(4) Å	V = 15583.6(7) Å^3
b = 37.7231(5) Å	Mr = 434.89
c = 13.8675(5) Å	Z = 16
Density = 0.371 g/cm^3	
Data Collection and Refinement	
F(000) = 1776	Rint = 0.024
$R[F2 > 2\sigma(F2)]$ = 0.059	$wR(F^2)$ = 0.222
17257 reflections; 7937 unique, 5624 with $I > 2\sigma I$	GOF = 1.014
μ = 0.47 mm^{-1}	Max/min residual electron density after PLATON SQUEEZE = 0.6/-0.3 e A^{-3}
Electrons found in solvent accessible volume: 3083	

Crystallographic Information for MFM-194

Crystal Description	
Blue rhombohedral crystals	Crystal Size: 100x100x20 μm
Crystal Data	
Formula = $C_{25}H_{19}O_5Cu$	Orthorhombic, *Imma*
a = 37.5058(6) Å	V = 15898.2(7) Å^3
b = 29.7789(5) Å	Mr = 462.94
c = 14.2345(5) Å	Z = 16
Density = 0.387 g/cm^3	
Data Collection and Refinement	
F(000) = 1904	Rint = 0.026
$R[F2 > 2\sigma(F2)]$ = 0.061	$wR(F^2)$ = 0.245
34623 reflections; 8187 unique, 5993 with $I > 2\sigma I$	GOF = 1.150
μ = 0.47 mm^{-1}	Max/min residual electron density after PLATON SQUEEZE = 0.7/-0.3 e A^{-3}
Electrons found in solvent accessible volume: 3871	

Crystallographic Information for MFM-195

Crystal Description	
Blue rhombohedral crystals	Crystal Size: 100x100x20 μm
Crystal Data	
Formula = $C_{27}H_{17}O_5Cu$	Orthorhombic, *Imma*
a = 37.5973(12) Å	V = 15852.7(13) $Å^3$
b = 29.8057(8) Å	Mr = 484.95
c = 14.1464(11) Å	Z = 16
Density = 0.406 g/cm^3	
Data Collection and Refinement	
F(000) = 1984	Rint = 0.031
$R[F2 > 2\sigma(F2)]$ = 0.078	$wR(F^2)$ = 0.290
20365 reflections; 8154 unique, 5512 with $I > 2\sigma I$	GOF = 1.083
μ = 0.48 mm^{-1}	Max/min residual electron density after PLATON SQUEEZE = 1.5/-0.3 e A^{-3}
Electrons found in solvent accessible volume: 3436	

Crystallographic Information for MFM-196

Crystal Description	
Blue rhombohedral crystals	Crystal Size: 120x120x20 μm
Crystal Data	
Formula = $C_{23}H_{11}O_5N_{0.5}Cu$	Orthorhombic, *Imma*
a = 37.6748(4) Å	V = 15843.7(7) $Å^3$
b = 29.8062(5) Å	Mr = 437.86
c = 14.1091(6) Å	Z = 16
Density = 0.370 g/cm^3	
Data Collection and Refinement	
F(000) = 1796	Rint = 0.070
$R[F2 > 2\sigma(F2)]$ = 0.074	$wR(F^2)$ = 0.286
99336 reflections; 13951 unique, 6967 with $I > 2\sigma I$	GOF = 1.039
μ = 0.26 mm^{-1}	Max/min residual electron density after PLATON SQUEEZE = 0.6/-0.5 e A^{-3}

Crystallographic Information for MFM-197

Crystal Description	
Blue rhombohedral crystals	Crystal Size: 100x100x20 μm

Crystal Data	
Formula = $C_{26}H_{17}O_5Cu$	Orthorhombic, *Imma*
a = 45.956(5) Å	V = 21593(7) Å^3
b = 28.879(8) Å	Mr = 472.94
c = 16.270(3) Å	Z = 16
Density = 0.292 g/cm^3	
Data Collection and Refinement	
F(000) = 1952	Rint = 0.173
$R[F2 > 2\sigma(F2)]$ = 0.072	$wR(F^2)$ = 0.231
28917 reflections; 11132 unique, 2734 with $I > 2\sigma I$	GOF = 0.790
μ = 0.35 mm^{-1}	Max/min residual electron density after PLATON SQUEEZE = 0.4/-0.5 e A^{-3}
Electrons found in solvent accessible volume: 5557	

Crystallographic Information for MFM-198

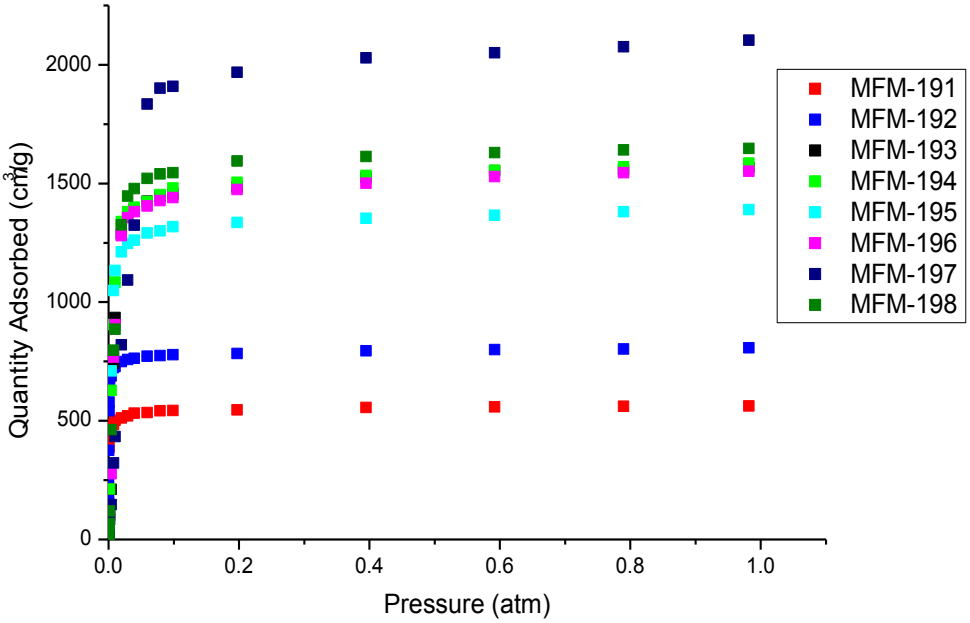
Crystal Description	
Blue rhombohedral crystals	Crystal Size: 80x80x15 μm
Crystal Data	
Formula = $C_{28}H_{17}O_5Cu$	Orthorhombic, *Imma*
a = 46.439(4) Å	V = 18687(7) Å^3
b = 29.789(6) Å	Mr = 496.96
c = 13.509(4) Å	Z = 16
Density = 0.352 g/cm^3	
Data Collection and Refinement	
F(000) = 2016	Rint = 0.132
$R[F2 > 2\sigma(F2)]$ = 0.120	$wR(F^2)$ = 0.384
23679 reflections; 9428 unique, 2342 with $I > 2\sigma I$	GOF = 0.866
μ = 0.41 mm^{-1}	Max/min residual electron density after PLATON SQUEEZE = 0.7/-0.9 e A^{-3}
Electrons found in solvent accessible volume: 4831	

3.4.4 Simulation Details for MFM-19X Series

All computational isotherms were simulated by Dr. Matthew Lennox and Joe Glover (who calculated the simulation details as part of his Master's Project), using the methods detailed below.

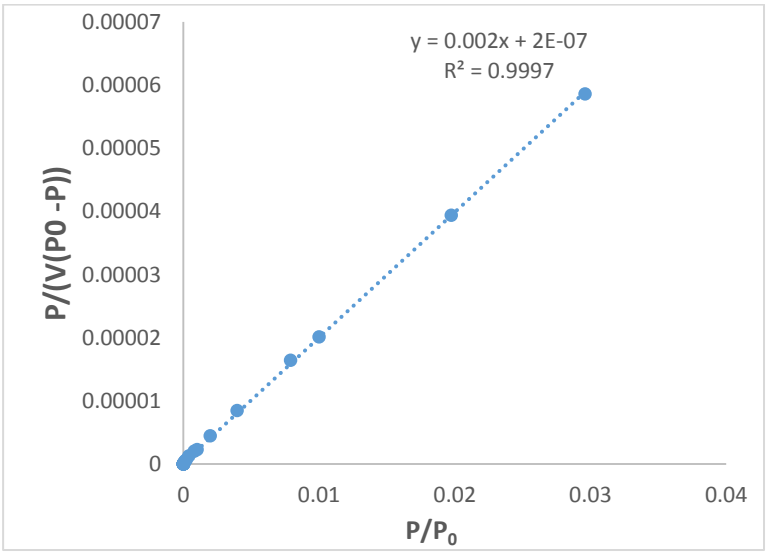
The adsorption of N_2 at 77 K and CH_4 and CO_2 at 273 K and 298 K was simulated using the grand canonical Monte Carlo simulations implemented in the MuSiC software package[51] and using translation, rotation and energy-biased insertion and deletion moves. All simulations were allowed at least 8×10^6 equilibration steps, followed by 12×10^6 production steps for each pressure point. The frameworks were treated as rigid, with atoms kept fixed at their crystallographic positions. Lennard-Jones parameters for the framework atoms were taken from the OPLS[52] force field with the exception of the metals, for which UFF parameters[53] were used. Nitrogen was simulated as a rigid molecule using the TraPPE model,[54] incorporating both Lennard-Jones parameters and partial charges. Previous work has shown that nitrogen-MOF electrostatic contributions play only a minor role in nitrogen adsorption[55] and, as such, only the electrostatic interactions between nitrogen molecules were included in our simulations. BET surface areas were calculated following the consistency criteria of Rouquerol and co-workers[56] using a pressure range of $0.008 < P/P_0 < 0.06$. For CO_2 and CH_4, the Lennard-Jones parameters – and, in the case of CO_2, partial charges – were taken from the TraPPE force field.[57]

3.4.5 Simulated N_2 Isotherms for MFM-19X Series

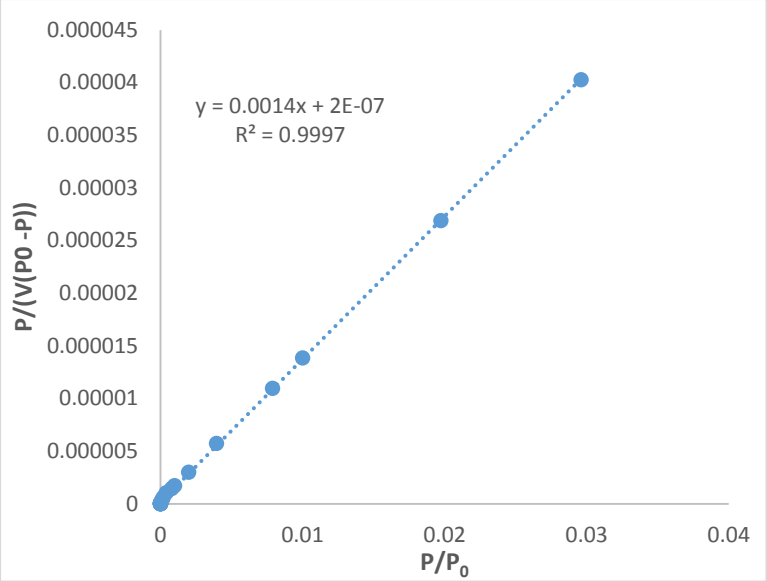


3.4.6 BET Plots and Rouquerol Plots for MFM-19X Series

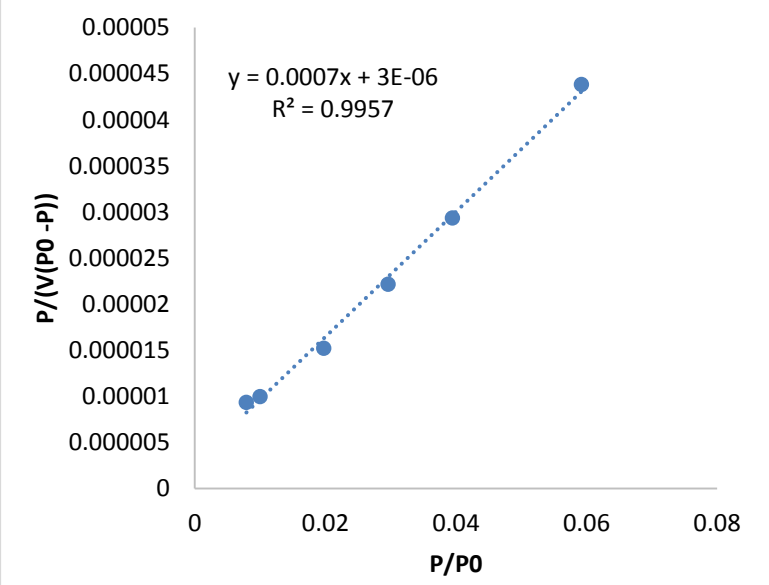
Linear section of BET plot used for MFM-191



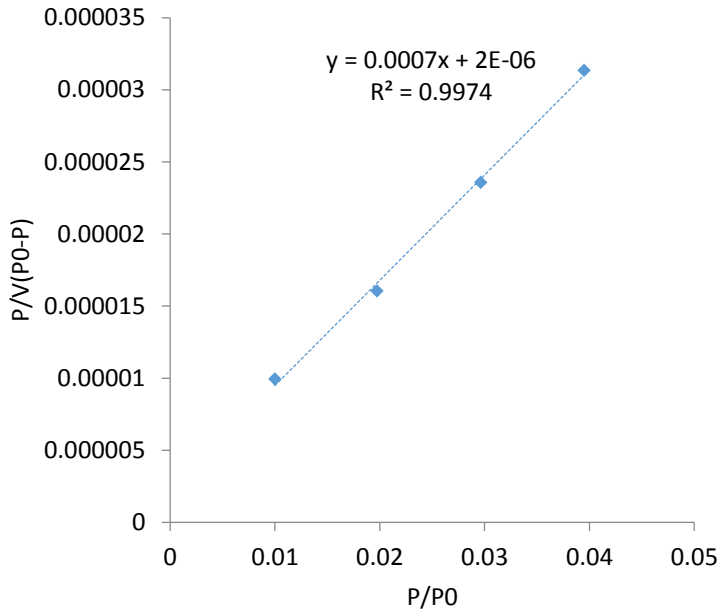
Linear section of BET plot used for MFM-192



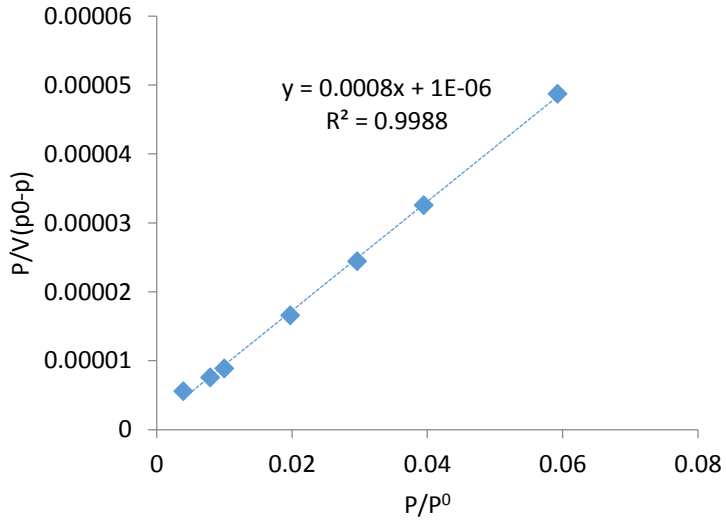
Linear section of BET plot used for MFM-193



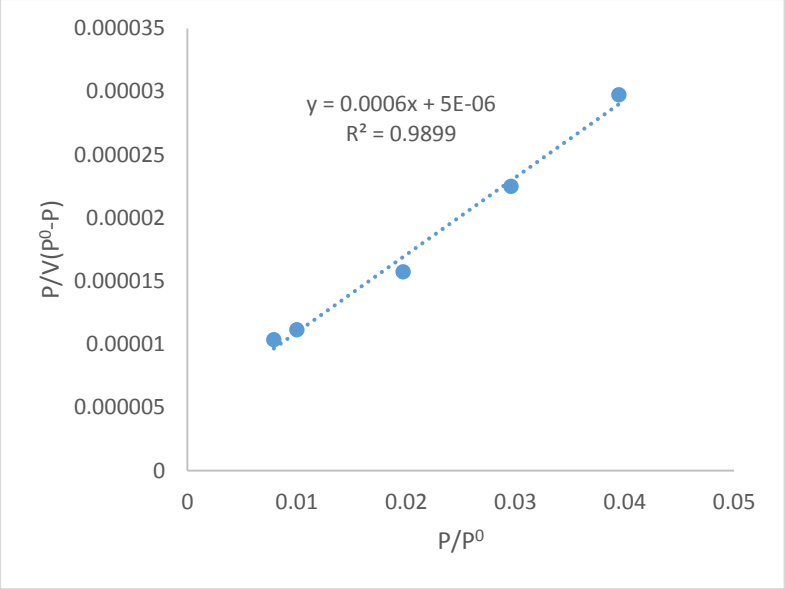
Linear section of BET plot used for MFM-194



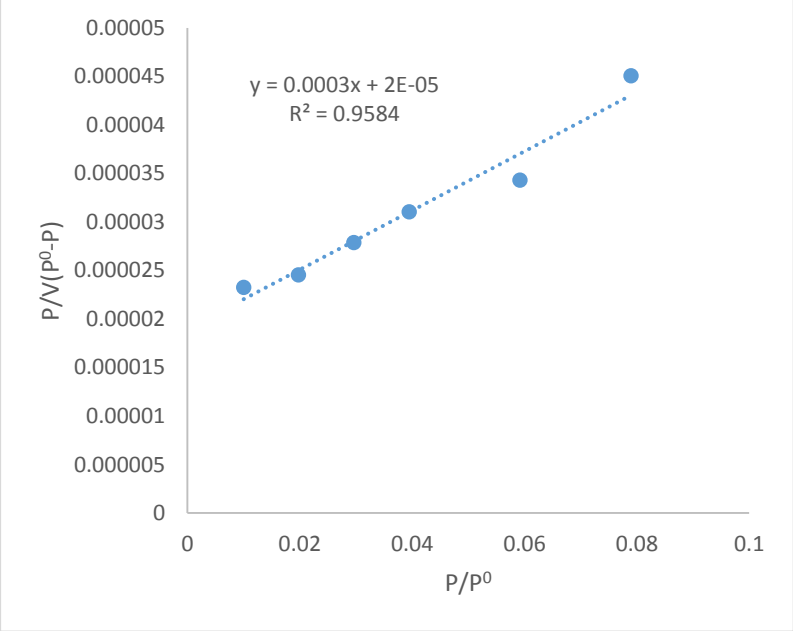
Linear section of BET plot used for MFM-195



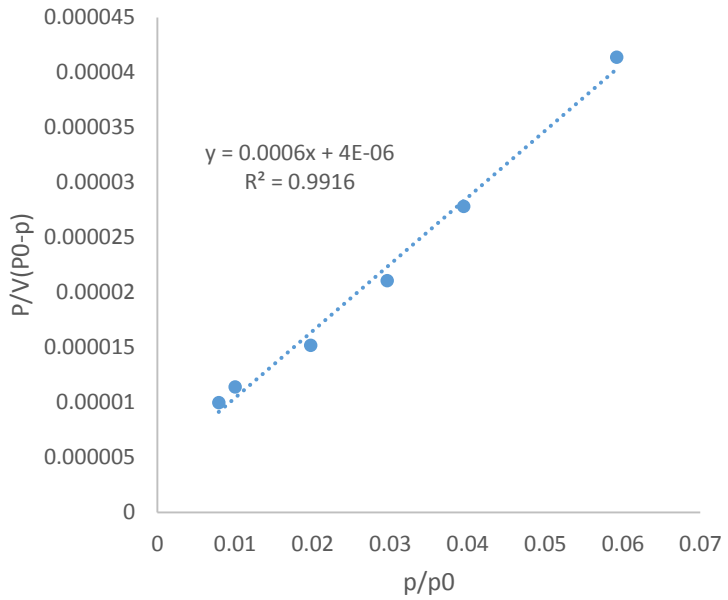
Linear section of BET plot used for MFM-196



Linear section of BET plot used for MFM-197



Linear section of BET plot used for MFM-198

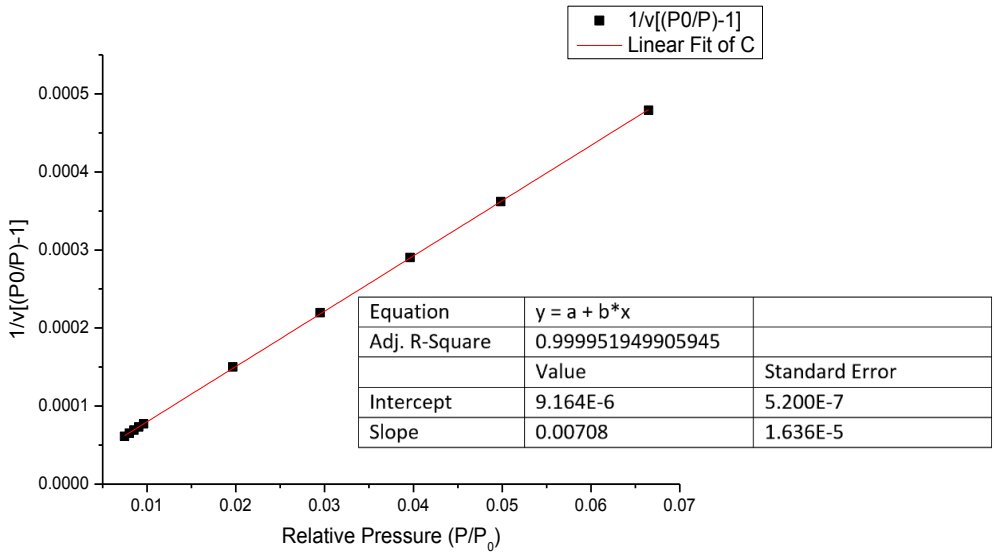


3.4.7 Gas Adsorption Measurements on MFM-19X Series

The samples were activated on a Micromeritics SmartVacPrep degasser, and subsequent BET measurements were made on a Micromeritics 3-Flex gas sorption analyser, using ultra-high purity N_2.

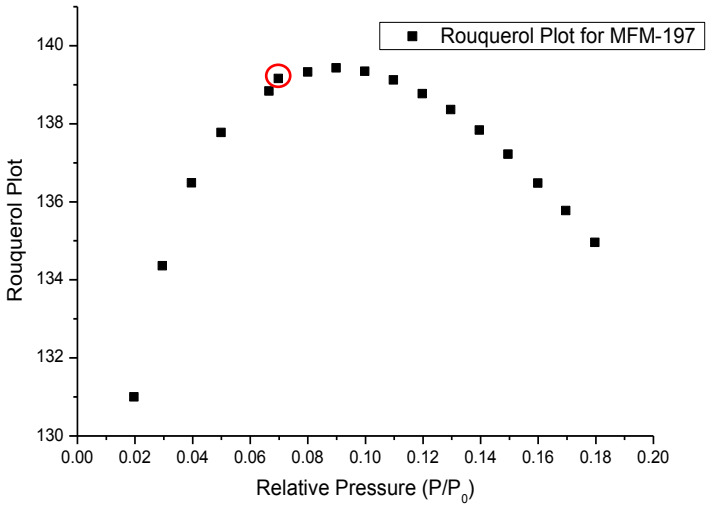
3.4.8 Experimental BET Plots

Linear section of experimental BET plot used for MFM-197

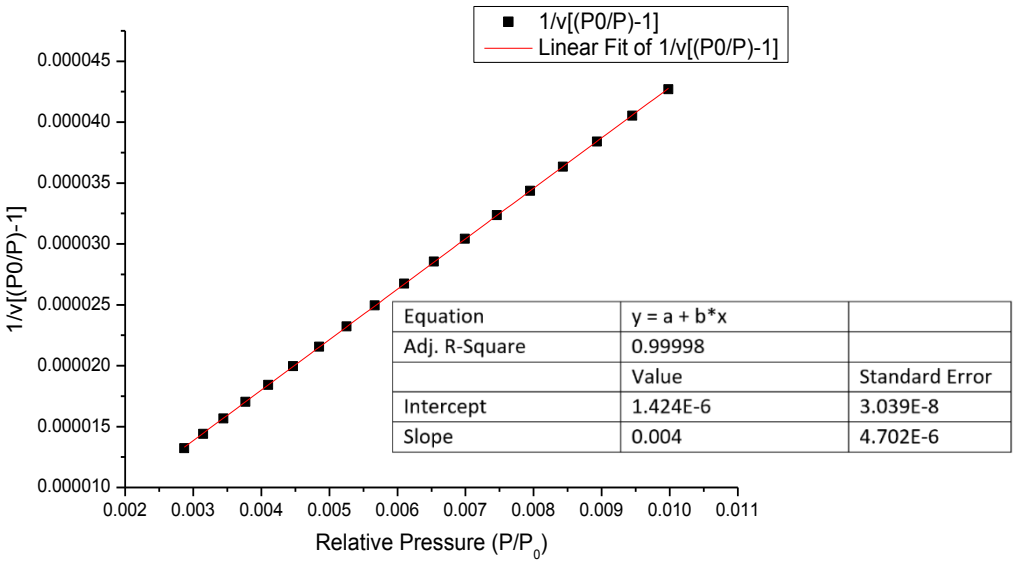


Equation	y = a + b*x	
Adj. R-Square	0.999951949905945	
	Value	Standard Error
Intercept	9.164E-6	5.200E-7
Slope	0.00708	1.636E-5

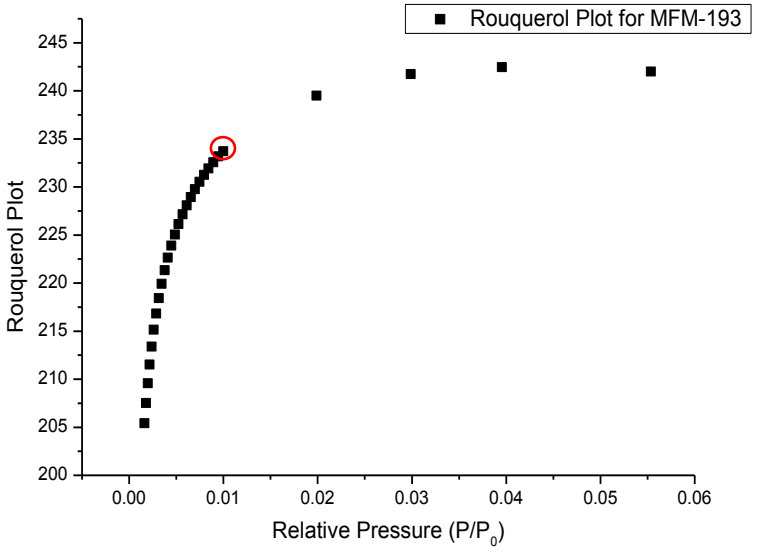
Rouquerol consistency criterion for MFM-197 (circled value used for highest pressure)



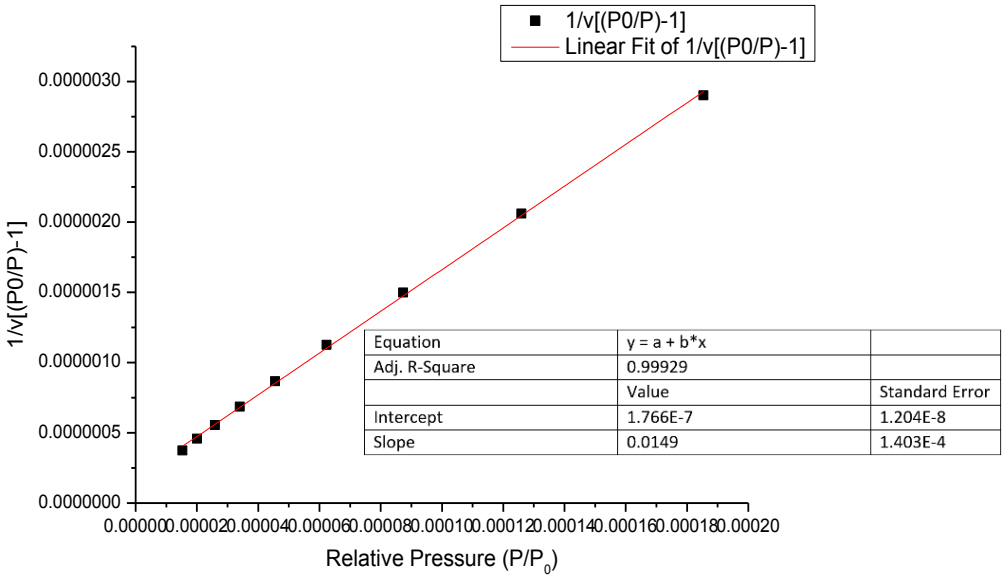
Linear section of experimental BET plot used for MFM-193



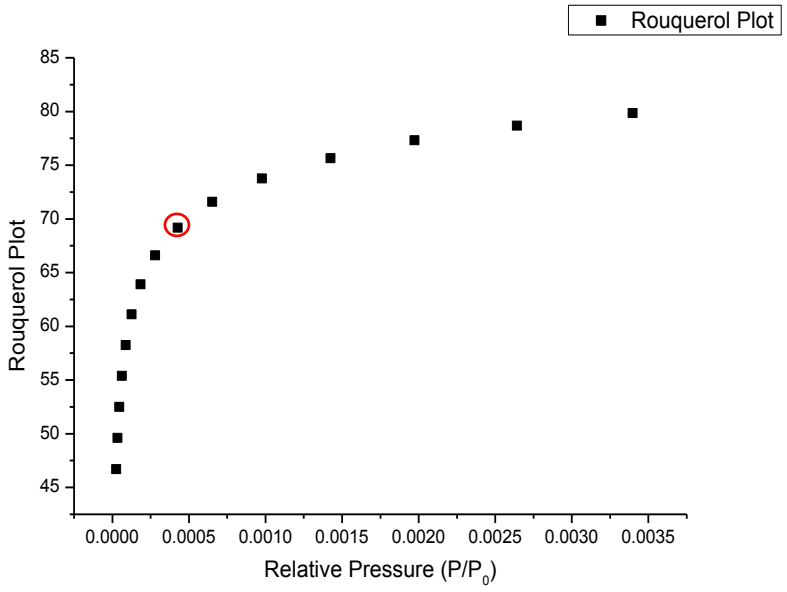
Rouquerol consistency criterion for MFM-193 (circled value used for highest pressure)



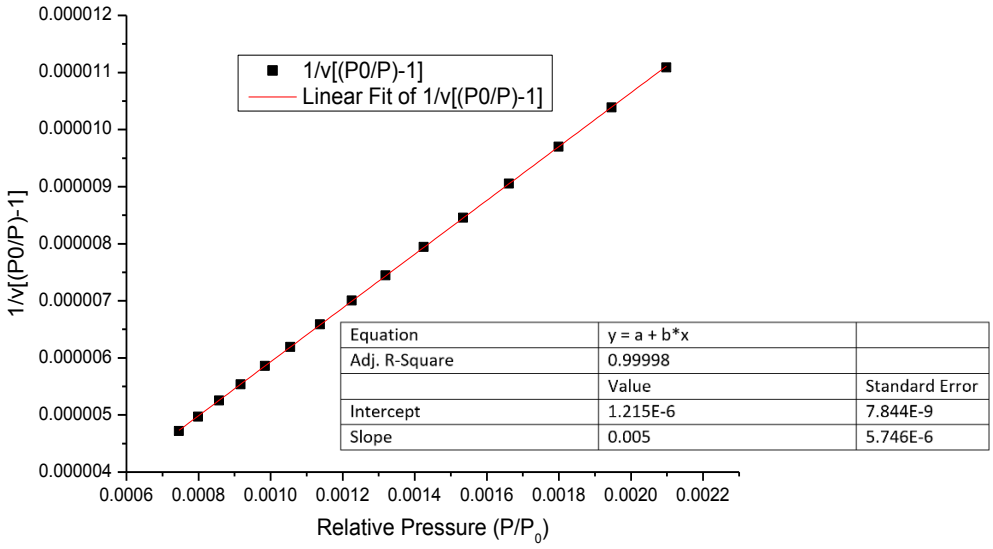
Linear section of experimental BET plot used for MFM-191



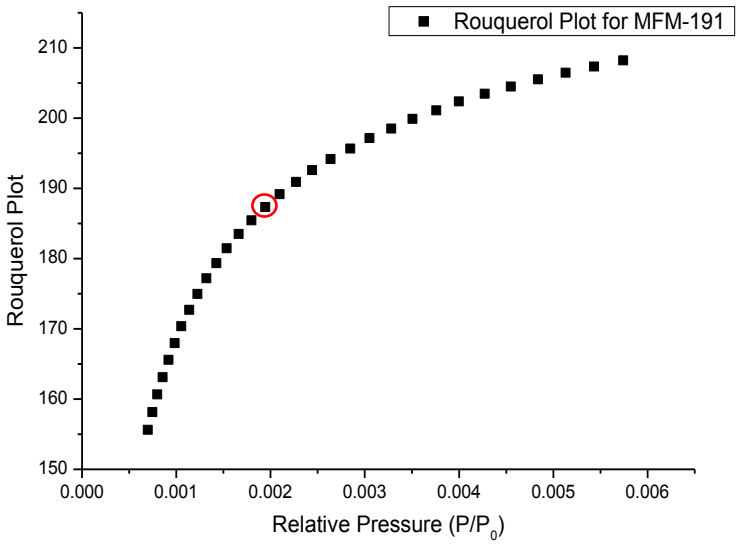
Rouquerol consistency criterion for MFM-191 (circled value used for highest pressure)



Linear section of experimental BET plot used for MFM-191 activated from supercritical CO_2



Rouquerol consistency criterion for MFM-191 activated from supercritical CO_2 (circled value used for highest pressure)



References

1. Batten, S. R. & Robson, R., *Angew. Chemie Int. Ed.,* **1198,** *37,* 1460–1494.
2. Aggarwal, H., Lama, P. & Barbour, L. J., *Chem. Commun.* **2014,** *50,* 14543–14546.
3. Prasad, T. K. & Suh, M. P., *Chem. - A Eur. J.* **2012,** *18,* 8673–8680.
4. Lin, X. *et al., J. Am. Chem. Soc.* **2009,** *131,* 2159–71.
5. Chen, B., Eddaoudi, M., Hyde, S. T., O'Keeffe, M. & Yaghi, O. M., *Science* **2001,** *291,* 1021–3.
6. Zhang, S., Li, L., Zhao, S., Sun, Z. & Luo, J., *Inorg. Chem.* **2015,** *54,* 8375–8379.
7. Han, S. S., Jung, D.-H. & Heo, J., *J. Phys. Chem. C* **2013,** *117,* 71–77.
8. Saha, D., Deng, S. & Yang, Z., *J. Porous Mater.* **2009,** *16,* 141–149.
9. Chen, B. *et al., J. Mater. Chem.* **2010,** *20,* 3758.
10. Yang, S. *et al. Nat. Mater.* **2012,** *11,* 1–7.
11. Ferguson, A. *et al., Nat. Chem.* **2016,** *8,* 250–257.
12. Braga, D., Grepioni, F. & Wiley InterScience (Online service). *Making crystals by design : methods, techniques and applications*. (Wiley-VCH, **2007**).
13. O'Keeffe, M., Peskov, M. A., Ramsden, S. J. & Yaghi, O. M., *Acc. Chem. Res.* **2008,** ***41,*** 1782–1789.
14. Song, F., Wang, C., Falkowski, J. M., Ma, L. & Lin, W., *J. Am. Chem. Soc.* **2010,** *132,* 15390–15398.
15. Ma, L. & Lin, W., *J. Am. Chem. Soc.* **2008,** *130,* 13834–5.

16. Farha, O. K., Malliakas, C. D., Kanatzidis, M. G. & Hupp, J. T., *J. Am. Chem. Soc.* **2010,** *132,* 950–952.

17. Deshpande, R. K., Minnaar, J. L. & Telfer, S. G., *Angew. Chemie Int. Ed.* **2010,** *49,* 4598–4602.

18. Jiang, H.-L., Tatsu, Y., Lu, Z.-H. & Xu, Q., *J. Am. Chem. Soc.* **2010,** *132,* 5586–5587.

19. Sun, D. *et al.*, *Chem. Commun.* **2005,** *36,* 5447.

20. Zhang, J., Wojtas, L., Larsen, R. W., Eddaoudi, M. & Zaworotko, M. J., *J. Am. Chem. Soc.* **2009,** *131,* 17040–17041.

21. Jiang, H. L., Makal, T. A. & Zhou, H. C., *Coord. Chem. Rev.* **2013,** *257,* 2232–2249.

22. Farha, O. K., Mulfort, K. L., Thorsness, A. M. & Hupp, J. T., *J. Am. Chem. Soc* **2008,** *130,* 8598–8599.

23. Deeth, R. J. *et al.*, *Dalt. Trans.* **2006,** *101,* 1092–1100 (2006).

24. Van Der Sluis, P. & Spek, A. L., *Acta Crystallogr. Sect. A* **1990,** *6,* 194–201.

25. Steiner, T., *Angew. Chemie Int. Ed.* **2002,** *41,* 48–76.

26. Janiak, C., *J. Chem. Soc. Dalt. Trans.* **2000,** 3885–3896.

27. Bhatia, S. K. & Myers, A. L., *Langmuir* **2006,** *22,* 1688–700.

28. Maloney, A. G. P., Wood, P. A. & Parsons, S., *CrystEngComm* **2016,** *18,* 3273–3281.

29. Gole, B., Bar, A. K., Mallick, A., Banerjee, R. & Mukherjee, P. S., *Chem. Commun. (Camb).* **2013,** *49,* 7439–41.

30. Lee, H. M., Youn, I. S., Saleh, M., Lee, J. W. & Kim, K. S., *Phys. Chem. Chem. Phys.* **2015**, *17,* 10925–33.

31. Orestes, E. *et al.*, *Phys. Chem. Chem. Phys.* **2014,** *16,* 17213.

32. Chen, L., Cao, F. & Sun, H., *Int. J. Quantum Chem.* **2013,** *113,* 2261–2266.

33. Lee, H. M., Youn, I. S., Saleh, M., Lee, J. W. & Kim, K. S., *Phys. Chem.* **2015,** *17,* 10925–10933.

34. Chui, Lo, Charmant, Orpen & Williams. *Science* **1999,** *283,* 1148–50.

35. Eddaoudi, M. *et al.*, *Science* **2002,** *295,* 469–72.

36. Chae, H. K. *et al.*, *Nature* **2004,** *427,* 523–527.

37. Furukawa, H. *et al.*, *Science.* **2010,** 329.

38. Chen, B., Ockwig, N. W., Millward, A. R., Contreras, D. S. & Yaghi, O. M. *Angew. Chemie Int. Ed.* **2005,** *44,* 4745–4749.

39. Skagestad, R. *et al.* Ship transport of CO_2. (**2014**).

40. Gándara, F., Furukawa, H., Lee, S. & Yaghi, O. M., *J. Am. Chem. Soc.* **2014,** *136,* 5271–5274.

41. Alezi, D. *et al.*, *J. Am. Chem. Soc.* **2015,** *137,* 13308–13318.

42. Ma, S. *et al.*, *J. Am. Chem. Soc.* **2008,** *130,* 1012–1016.

43. Spanopoulos, I. *et al.*, *J. Am. Chem. Soc.* **2016,** *138*, 1568–1574.

44. Gou, Q. *et al.*, *Phys. Chem. Chem. Phys.* **2014,** *16*, 13041.

45. Nelson, A. P., Farha, O. K., Mulfort, K. L. & Hupp, J. T. S *J. Am. Chem. Soc.* **2009,** *131*, 458–460.

46. Martin, R. Database of MOF materials analyzed for flexibility. (**2013**). Available at: http://www.nanoporousmaterials.org/flexibility/database.html.

47. Mohamed Eddaoudi, Hailian Li, and & O. M. Yaghi., *J. Am. Chem. Soc.*, **2000**, 122, 1391–1397.

48. Dolomanov, O. V, Bourhis, L. J., Gildea, R. J., Howard, J. A. K. & Puschmann, H. *J. Appl. Crystallogr.* **2009,** *42*, 339–341.

49. Sheldrick, G. M., *Acta Crystallogr. A.* **2008,** *64*, 112–22.

50. Sheldrick, G. M. *et al. Acta Crystallogr. Sect. C Struct. Chem.*, **2015,** *71*, 3–8.

51. Gupta, A., Chempath, S., Sanborn, M. J., Clark, L. A. & Snurr, R. Q., *Mol. Simul.* **2003,** *29*, 29–46.

52. Jorgensen, W. L., Laird, E. R., Nguyen, T. B. & Tirado-Rives, J., *J. Comput. Chem.* **1993,** *14*, 206–215.

53. Rappe, A. K., Casewit, C. J., Colwell, K. S., Goddard, W. A. & Skiff, W. M., *J. Am. Chem. Soc.* **1992,** *114*, 10024–10035.

54. Potoff, J. J. & Siepmann, J. I., *AIChE J.* **2001,** *47*, 1676–1682.

55. K. S. W. & Snurr*, R. Q. *J. Am. Chem. Soc.*, **2007**, 129, 8552–8556.

56. Rouquerol, J., Llewellyn, P. & Rouquerol, F. in *Studies in Surface Science and Catalysis*, **2007,** *160*, 49–56.

57. M. G. M. & Siepmann*, J. I. *J. Phys. Chem. B*, **1998**, *102*, 2569–2577.

CHAPTER 4

Highly connected inorganic secondary building units as a gateway to permanently highly porous materials

4.1 Introduction

4.1.1 Selection of Secondary Building Units for Stability Enhancement in MOFs

As discussed in Chapter 3, there are a number of methods available to access the full permanent porosity of an unstable MOF. One method is to enhance the stability of an existing MOF, such as introducing interpenetration to reduce the void space and provide structural support throughout the framework.[1] Another is to alter the activation process to enable a gentler method of removing the solvent from the pores. For example, using a solvent with a lower surface tension, or activating *via* supercritical CO_2 – a solvent with zero surface tension, and thus the smallest amount of strain possible to put on the framework.[2] However, when these methods don't work, a highly stable framework may be synthesised from the same starting ligand, in combination with a metal known to form stable SBUs. There are two main factors to consider when selecting SBUs for stable frameworks: the oxophilicity of the metal, and therefore the strength of the bond it will form with a carboxylate; and the connectivity of the SBU cluster (ie. the number of carboxylate groups from linkers participating in its formation), as the higher this number, the more bonds that need to be broken to decompose the framework.

Prioritising oxophilicity in secondary building unit selection

Due to the nature of the carboxylate anion as a hard Lewis base, it can be reasonably predicted that it will form stronger bonds with hard Lewis acids, such as early transition metals with a high oxidation state on the metal cation, and weaker bonds with later transition metals. This is seen when evaluating the

oxophilicity of the metal ions, shown in Figure 126, and the consequent strength of the M-O bond that forms in the process of synthesising a MOF.

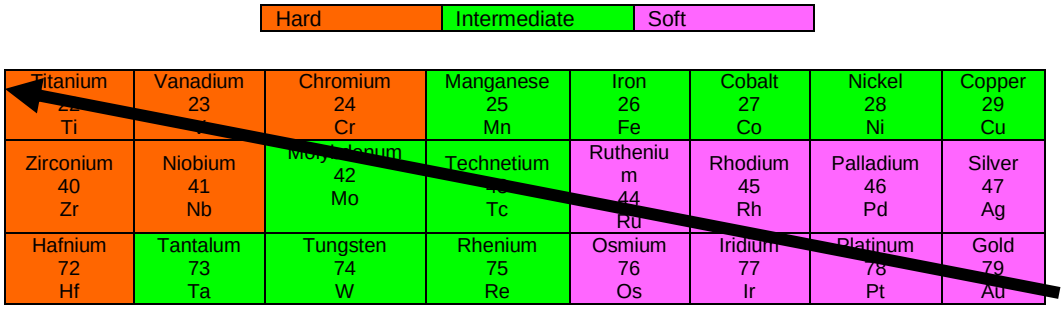


Figure 126. Trend in oxophilicity across the transition metals in the periodic table.

This method of producing more stable MOFs using metals with high oxophilicity to form stronger bonds has been reported many times in literature. One such example is shown below in Figure 127, where Loeb *et al*. synthesised a stable MOF from a rotaxane-based ligand which had been used in previous synthetic attempts with cadmium, though had produced a framework which was highly unstable due to the weak nature of the Cd-O bond. By taking the same ligand, dibenzo-[24]crown-8 ether, a stable rotaxane-based MOF was formed with a series of lanthanides (Sm, Eu, Gd and Tb), which are hard Lewis acids and therefore form strong metal-oxygen bonds.[3]

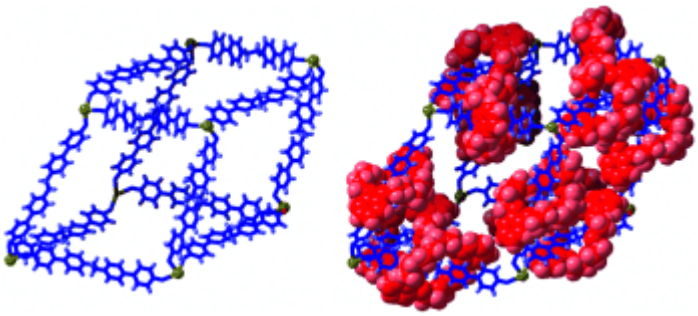


Figure 127. A single "cube" unit of the 3D network with the crown-ether wheels removed (left), and with crown-ether wheels included (right).[3]

4.1.2 Utilising Highly Connected Secondary Building Units to Stabilise MOFs

An extra advantage of employing oxophilic SBUs with high individual ion charge (hard Lewis acids) is the extra connectivity often gained from this process due to the need for additional charge balancing. For example, the copper paddlewheel SBU contains two Cu(II) ions, and is therefore balanced by four carboxylates (with a charge of 1- each), which, as they bind in a bidentate fashion, readily form a small SBU with apical neutral molecules to satisfy geometrical binding requirements. Secondary building units which incorporate a Zr(IV) cation, on the other hand, need a larger number of constituent atoms to satisfy the charge balance and binding requirements of both the ligand and the metal. This in turn generates a network of highly connected topology containing a large number of bonds to be broken to cause framework collapse. Figure 128 shows how this method of topological control was employed by the Zhou group to synthesise highly stable frameworks from a 12-connected Zr(IV) SBU and ligands which have been extended to over 4 nm, a point where linkers of this size would usually form unstable networks with SBUs with fewer points of extension.[4] The framework they synthesise from H_4TCP-3 (PCN-230 in Figure 128) demonstrates stability between pH 0-12, and as such has the highest pH tolerance of all porphyrin containing MOFs, despite the huge length of the ligand and the mesoporous nature of the framework.

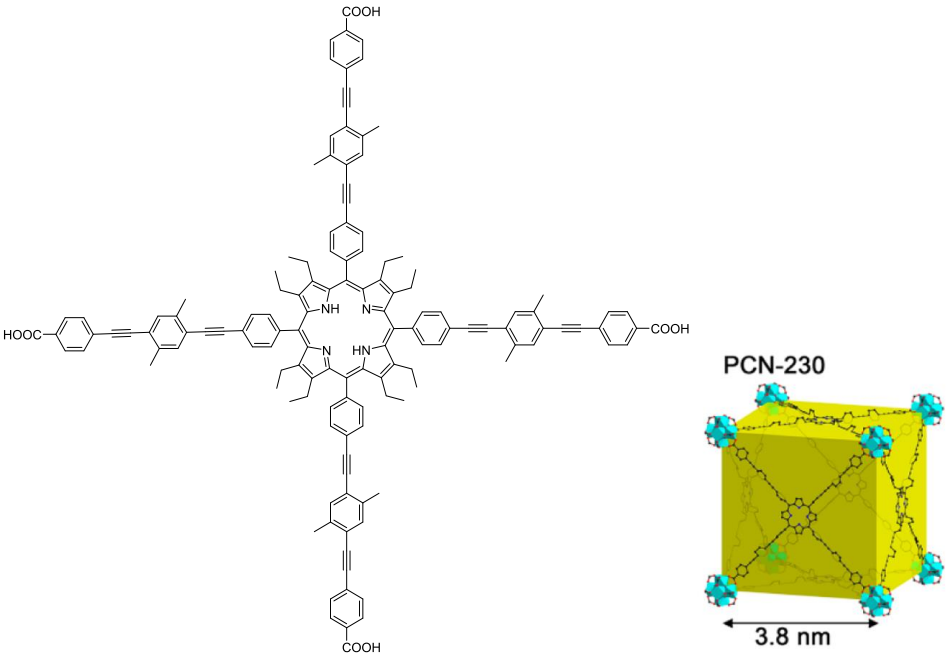


Figure 128. Structure of H_4TCP-3 (left) and highly stable mesoporous porphyrinic MOF (right).[4]

A further implication of the use of highly connected nodes with multiple points of extension is the resultant complex network topology that can often geometrically forbid interpenetration.[5]

4.1.3 Interesting Features of Zr(IV) Structures in Literature

While it is generally accepted that Zr(IV) structures will generate a stable framework due to the oxophilicity and connectivity of the cluster, it has been shown that in a number of different cases, the structural stability can be significantly less than expected. A study, performed by DeCoste *et al.*, revealed that many structures with the $Zr_6O_4(OH)_4$ cluster, as found in UiO-66, can become unstable to water, acid and even protic solvents such as methanol and isopropanol (Figure 129).[6] This decrease in stability was found to be a product of extension and functionalisation of the ligand, following the trend from UiO-66 (formed from H_2BDC and Zr(IV), and stable from pH 1-14), to UiO-67 (synthesised from 4,4'-biphenyldicarboxylate, and susceptible

to chemical degradation from water and HCl), to a MOF synthesised from 2,2'-bypyridine-5,5'-dicarboxylate, which showed structural collapse when soaked in methanol or isopropanol.

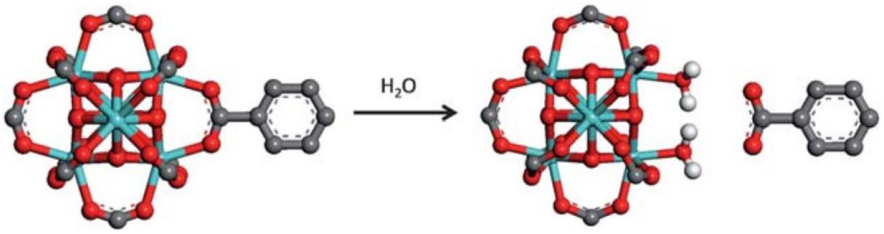


Figure 129. Proposed mechanism for breakdown of Zr structure in water.[6]

Another interesting feature of Zr(IV) MOFs is the nature of the binding oxygen atoms in Zr_6-based nodes, as precise location of the protons (needed for charge balance), can be difficult due to the location of the hydrogen atoms so close to heavy Zr(IV) ions in the crystal structure. However, a recent study by the Hupp group combined methods of quantum mechanics and experimental IR data (DRIFTS) to elucidate the proton topology in the NU-1000 framework, as shown in Figure 130.[7] It was found that the nature of the bridging and terminal oxygen atoms were mixed; rather than an entirely H_2O cluster, with charge balance provided by bridging oxo anions, or an entirely hydroxyl terminated cluster, with bridging μ_3-OH entities, the cluster formula $[Zr_6(\mu_3{-}O)_4(\mu_3{-}OH)_4(OH)_4(OH_2)_4]^{8+}$ was preferred, with the ability for the nature of the ions to change to accommodate post-synthetic modification, and thus balance the charges appropriately.

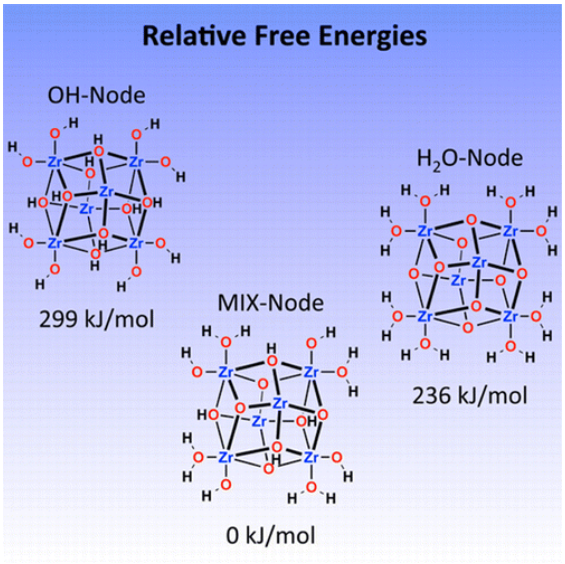


Figure 130. Relative stabilities of Zr_6-based nodes, with the mixed node showing clear preference.[7]

4.1.4 Aims and Objectives

This chapter details the synthesis, characterisation and gas sorption properties of a Zr(IV) MOF synthesised from the same ligand (H_4L^1) used in the MFM-19X Cu(II) series, which is shown to have exceptional thermal and chemical stability, thus providing a more promising candidate for real world applications than the unstable Cu(II) **lvt** MOFs. The chapter then moves on to discuss another Zr(IV) MOF with equal stability and gas sorption properties, generated from H^4L^{1P}, detailed in Chapter 2 as synthesised from a cheap, quick and green synthetic route. This provides an even more practical approach to an ideal industrial application scenario if the gas sorption properties could be improved slightly, suggestions for which is where the chapter concludes.

4.2 Results and Discussion

Solvothermal synthesis of MFM-421

A suspension of H_4L^1 (16 mg, 0.023 mmol), $ZrCl_4$ (24 mg, 0.103 mmol) and benzoic acid (600 mg, 4.91 mmol) in DEF (3 mL) was heated to 120 °C in a

sealed 15 mL pressure vessel, and maintained at this temperature for 24 hours to yield small, white needles of MFM-421 $[Zr_6L^1{}_2(\mu_3\text{-}OH)_8(OH)_8]$ in a 60% yield. The as-synthesised single crystals were insoluble in organic solvents, and the structure of MFM-421 was determined by SCXRD using synchrotron radiation as the size of the crystals was very small. Without the use of benzoic acid as a modulator, the reaction did not yield crystals large enough for characterisation. The bulk phase purity of the solid was analysed using powder x-ray diffraction.

4.2.1 Crystal Structure Description of MFM-421

Table 19. Crystallographic information for MFM-421.

Crystal Data	
Formula = $C_{11.5}H_{8.5}O_4Zr_{0.75}$	Hexagonal, *P6/mmm*
a = 40.301(2) Å	V = 28592(3) $Å^3$
c = 20.327(2) Å	Mr = 279.11
Density = 0.377 g/cm^3	Z = 24
Data Collection and Refinement	
Rint = 0.484	$R[F2 > 2\sigma(F2)]$ = 0.098
$wR(F^2)$ = 0.338	

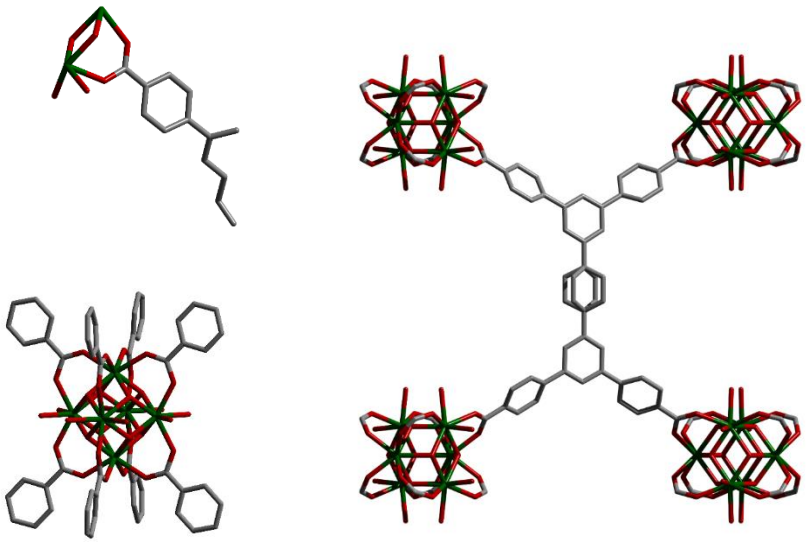


Figure 131. Asymmetric unit and the $[Zr_6L^1{}_2(\mu_3{-}O)_4(\mu_3{-}OH)_4(OH)_4(OH_2)_4]$ SBU of MFM-421 (left) and coordination mode of L^1, showing the central phenyl ring disordered over two positions (right).

MFM-421 crystallises in the hexagonal space group *P*6/*mmm*, with unit cell parameters: a = 40.301(2) Å and c = 20.327(2) Å, and V = 28592 (3) Å^3. Solving the structure by single-crystal x-ray diffraction techniques shows that the framework contains SBUs with 8 points of extension. The equatorial Zr(IV) ions are coordinated to two oxygen atoms coming from two separate ligands, four bridging mixed μ_3-OH/μ_3-O anions between the adjacent Zr(IV) ions (the mixed nature as discussed in the introduction to this Chapter),[7] and two hydroxyl groups bound protruding into the pores. The remaining two axial Zr(IV) ions are bound to four oxygen atoms from four separate ligands which bridge to adjacent Zr(IV) ions and four hydroxo anions (Figure 131). These hexanuclear, 8-connected Zr(IV) clusters are formed at the four points of extension on each ligand, giving a 3D MOF of **csq** topology, which is quite rare, and only seen in MOFs with the 8-connected zirconium SBU present in this structure.[8,9] Due to the highly connected topology, the framework is non-interpenetrated, which makes it hugely porous, with a calculated solvent accessible volume of 82.2% (calculated by PLATON SOLV).[10] As shown in Figures 132 and 133, the structure is highly porous down all axes, particularly *c*, which has a large, 36.8 Å diameter pore.

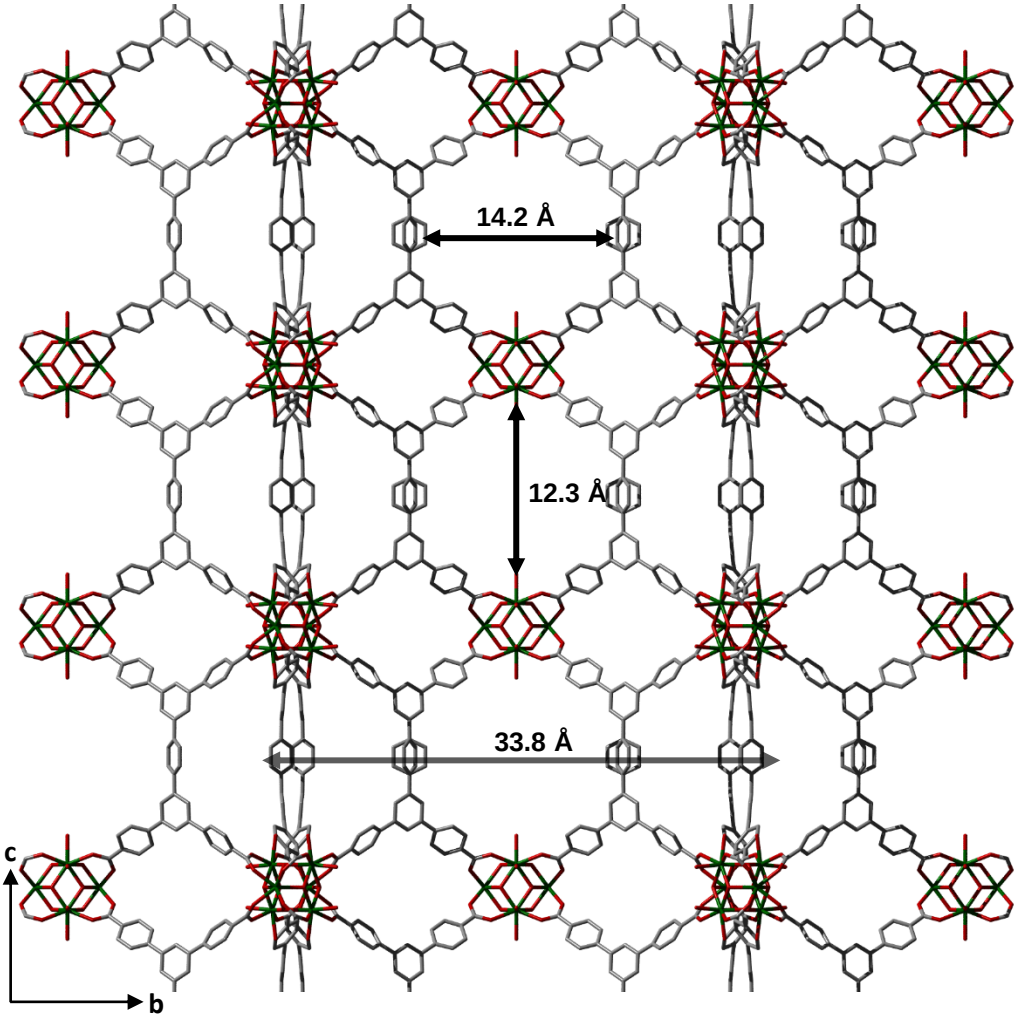


Figure 132. View down the *a* axis of MFM-421, with pore size distances indicated.

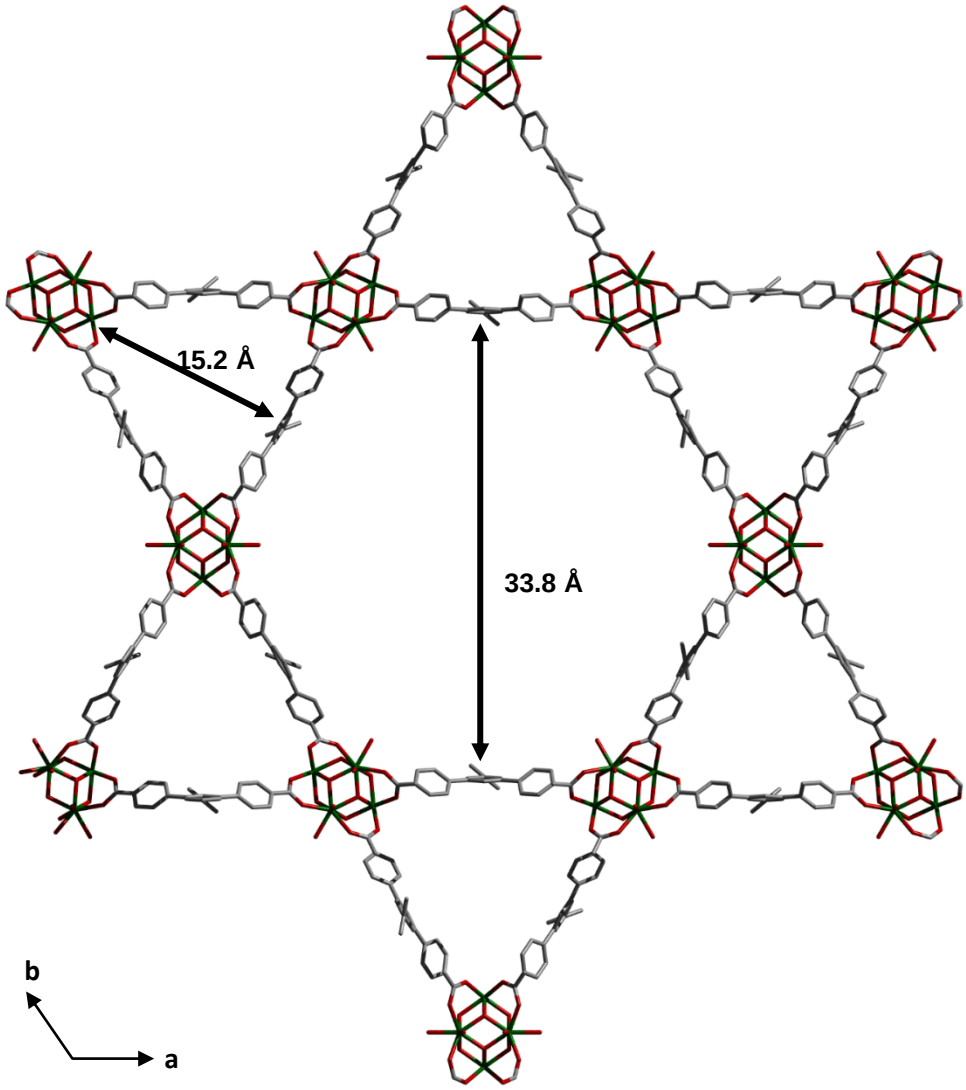


Figure 133. View down the *c* axis of MFM-421, with pore size distances indicated.

Perhaps the most notable aspect of this MOF is its high thermal and chemical stability (see PXRD and TGA data below). In addition to its **csq** topology which forbids interpenetration (hence avoiding the phase purity issues present in the Cu(II) MOF series), the stability of MFM-421 is thought to arise from the highly connected Zr(IV) nodes, which require more bonds to be broken to result in the destruction of the crystal structure. The oxophilicity of the Zr(IV) ions also contributes to the stability, as they form a very strong bond with the carboxylate groups from the ligand, with a bond enthalpy of 760 kJ/mol for Zr-O, compared to 343 kJ/mol for Cu-O.[11]

Stability of MFM-421

The high potential porosity of the framework matched that of MFM-193 in Chapter 3, demonstrating a solvent accessible volume (calculated by PLATON SOLV) of 82.2%, compared to the 81.6% calculated for MFM-193, and as such was of great interest for high pressure storage of guest molecules inside the MOF. This was particularly interesting as MFM-193 showed great promise computationally, yet was unable to be activated by conventional methods. Therefore, MFM-421 needed to be stable to desolvation, and ideally more stable than the Cu(II) MOF series as a whole, to ensure sustained storage of gas molecules through a range of conditions.

To test and compare thermal stability, a TGA was performed on an 8 mg sample of MFM-421 (shown in Figure 134). It is evident, when comparing it to the Cu(II) series, that this MOF is much more thermally stable, up to 500 °C, as opposed to 300-350 °C for the MFM-19X series. This was a promising result that the framework might be suitable for real-world applications.

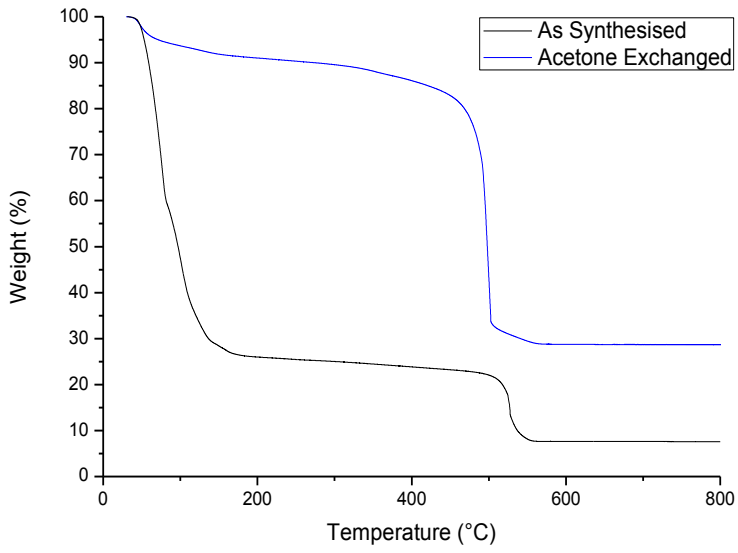


Figure 134. Thermo-gravimetric analyses of MFM-421 in air.

In order to further ascertain the stability of the framework, multiple PXRD patterns were collected at various stages of the activation process, to track the stability and, if there was any instability, allow opportunity to remedy it. Figure 135 shows these PXRD patterns, and indeed highlights how, upon solvent exchange with methanol, the diffractogram decreases in intensity and shows strong signs of collapse, whereas upon exchange with acetone (Figure 136) the sample remains crystalline. This echoes results seen in literature upon extension and functionalisation of Zr_6-based structures.[6] The fact that upon swapping to acetone the sample remained crystalline was encouraging for the realisation of an ideal permanent porosity.

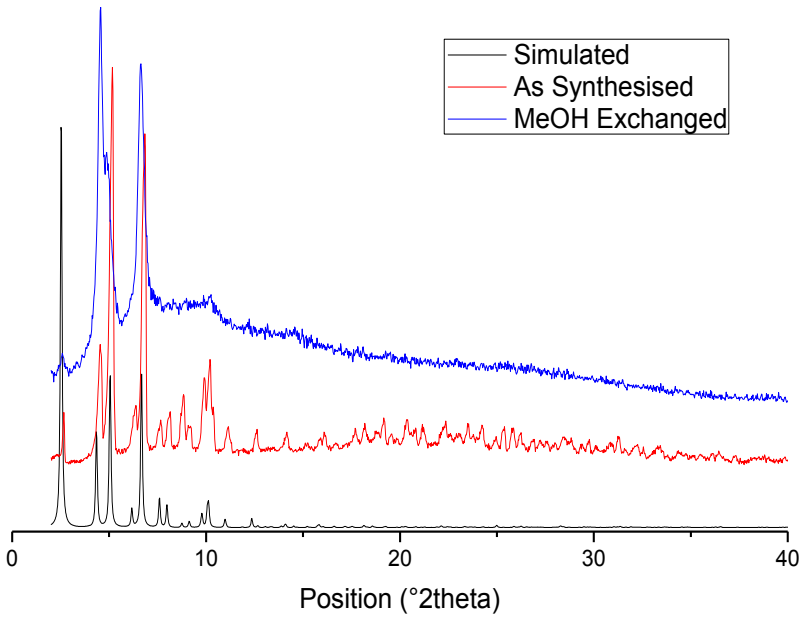


Figure 135. Overlaid PXRD patterns of MFM-421 simulated from single crystal data, as synthesised and methanol exchanged, showing loss of crystallinity.

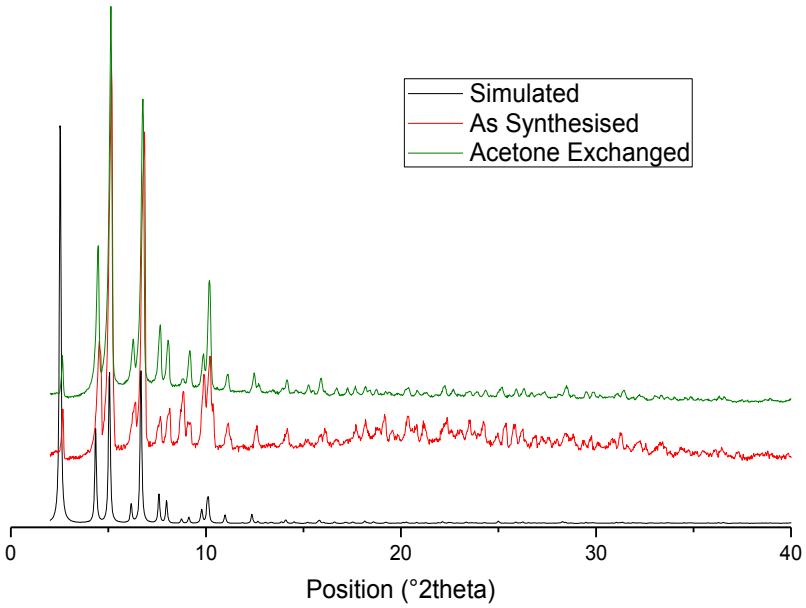


Figure 136. Overlaid PXRD patterns of MFM-421 simulated from single crystal data, as synthesised and acetone exchanged, showing the retention of crystallinity.

To further test the stability of this compound, a 40 mg acetone exchanged sample was activated by heating to 120 °C under dynamic vacuum in a Schlenk flask for 24 hours. Figure 137 shows how this sample retained its crystallinity, showing promise for during activation.

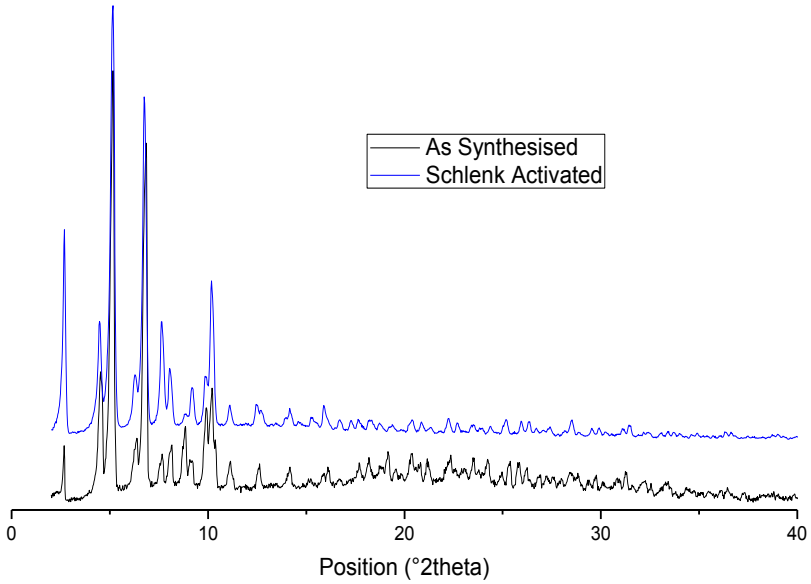


Figure 137. PXRD patterns of MFM-421 after activation in a Shlenk flask and subsequent exposure to ambient conditions, compared to as synthesised pattern.

4.2.2 Gas Sorption Measurements of MFM-421

Following these promising PXRD and TGA results, an 80 mg (when wet) sample of MFM-421 was prepared and exchanged with acetone by soaking for 5 days, with fresh acetone replacement every 24 hours. This acetone exchanged sample was then loaded into a glass micromeritics sample tube and placed on the SmartVacPrep degasser where it was heated to 120 °C under dynamic vacuum for 18 hours. The sample was placed on the 3-flex for further analysis to check the stability, Figure 138 shows the nitrogen isotherm at 77 K, which was used to calculate the BET surface area shown below.

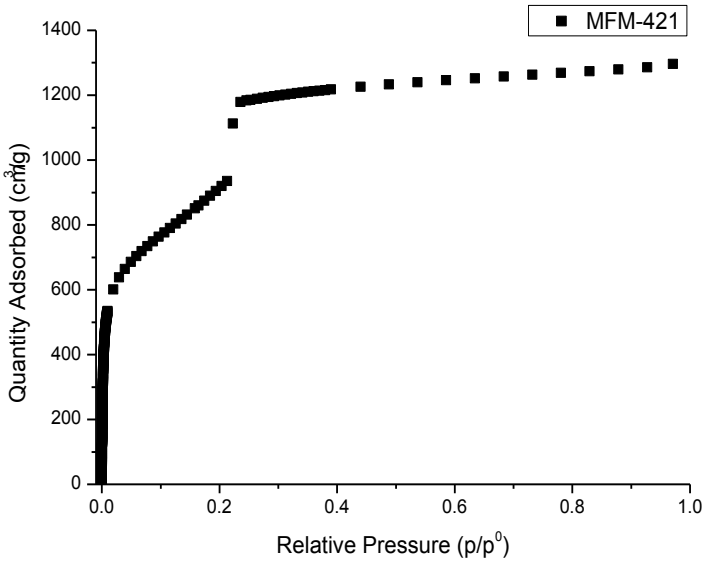


Figure 138. Nitrogen isotherm of MFM-421 at 77 K, used to calculate BET surface area and pore size distribution.

The isotherm (Figure 138) shows a distinct type IV isotherm profile, indicating the permanent porosity and mesoporous nature of MFM-421, which was assigned as the retention of the 3.38 nm diameter pore down the *c* axis. The BET surface area calculated from Figure 138 was 3,300 m^2/g (BET plot and Rouqerol

consistency check in Experimental Section), and the pore volume was calculated to be 2.00 cm^3/g.

4.2.2.1 High Pressure CH_4 Isotherms of MFM-421

A 70 mg acetone exchanged sample of MFM-421 was placed in a high pressure gas sorption measurement kit (Xemis), which would enable methane isotherms up to 80 bar. This was to allow the sample to reach maximum uptake, and to assess it for its potential to be used in methane storage in vehicles, as the huge pore should provide optimum working capacity conditions with a large difference between high pressure uptake, and very low uptake at low pressure.

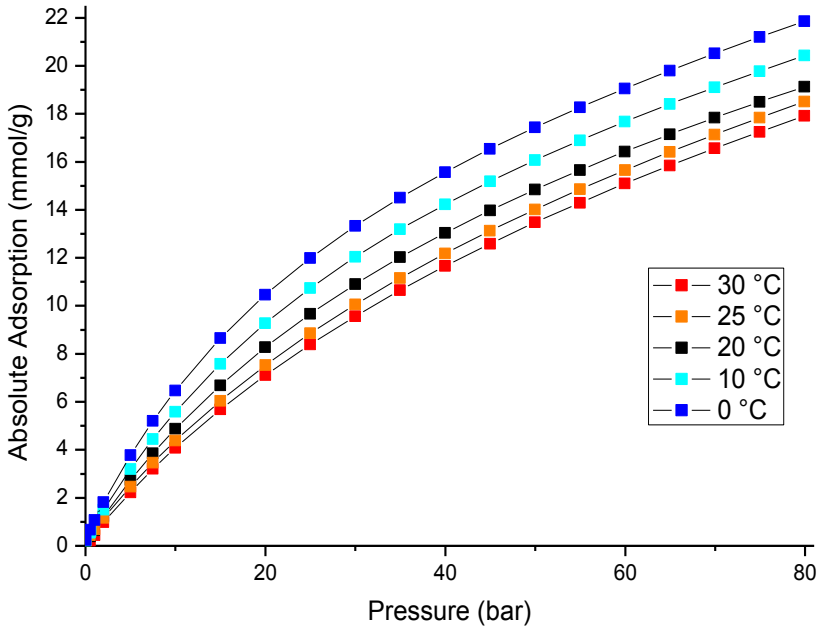


Figure 139. High pressure gravimetric methane isotherms for MFM-421 at various temperatures.

As shown in Figure 139, the gravimetric uptake changes by 3.94 mmol/g between the values of 30 and 0 °C at the highest pressure loading (from 17.91 to 21.85 mmol/g), yet only 1.56 mmol/g at 5 bar (2.22 to 3.78 mmol/g), which suggests the working capacity will increase as the temperature is lowered. This reflects the poor host/guest interactions at low loadings due to the 34 Å pore down the *c* axis, and how this actually benefits the working capacity of this MOF. It is also evident, however, that the isotherm has not plateaued at 80 bar, indicating that the MOF has not reached saturation, again possibly due to the large pore which can continue to accommodate methane at even the highest pressures.

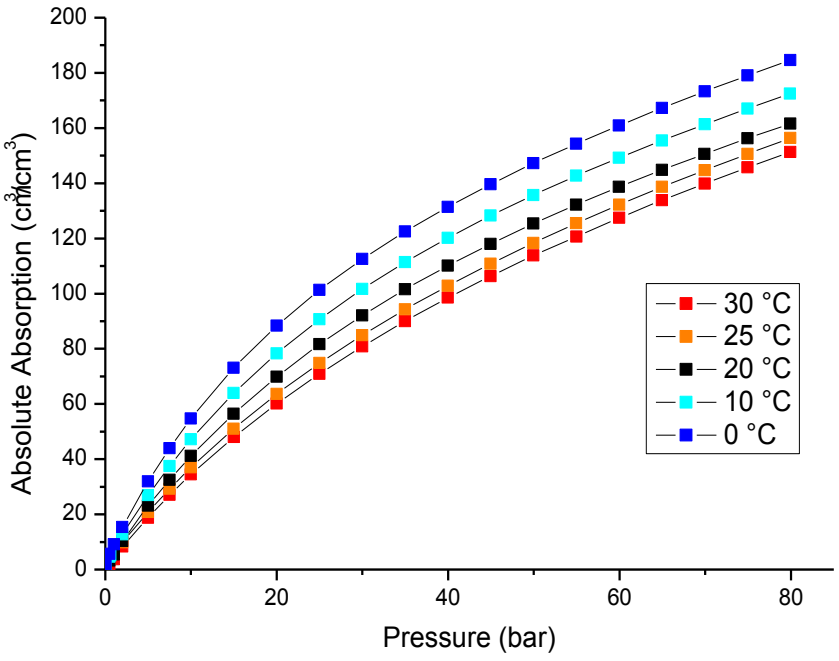


Figure 140. High pressure volumetric methane isotherms for MFM-421 at various temperatures.

The volumetric uptake, shown in Figure 140, echoes the gravimetric in both the high and low pressure regions, which is to be expected as the crystal density stays constant, unlike the Cu(II) MOF series discussed earlier. There is again evidence that the working capacity will improve at lower temperatures, with the difference between 30 and 0 °C uptake at 5 bar being 13.2 cm^3/cm^3 (from 18.7 to 31.9 cm^3/cm^3), and the difference at 80 bar raising to 33.3 cm^3/cm^3 (from 151.30 cm^3/cm^3 at 30 °C to 184.58 cm^3/cm^3 at 0 °C). The shape of the isotherm, coupled with the uniform nature of the increase again supports the theory that the MOF has not reached saturation at 80 bar at any of these temperatures.

In comparison to the non-interpenetrated Cu(II) MOF series discussed in Chapter 3, both the gravimetric and volumetric uptakes at 80 bar are surprisingly much lower. Considering simply the porosity, this is quite unexpected, as the porosity of this framework is exactly the same as MFM-193 at 82%. The main pore diameter down the *c* axis is roughly twice the size of that in MFM-193 (a uniform 33.8 Å compared to 23.0 by 11.8 Å), which may suggest even higher uptake at 80 bar than that seen in MFM-193, as there is more volume in the centre of the pore to host the gas molecules. However, this is evidently not the case, a possible reason for which could be that the isotherm of MFM-421 has clearly not plateaued, and therefore the maximum uptake has not been reached, which might approach and exceed that of MFM-193. The second possible reason for the difference in uptake can be seen in a comparison of the BET surface areas and pore volumes, in Table 20.

Table 20. Comparison of BET surface area and pore volume for MFM-421 and MFM-193.

	MFM-421	**MFM-193 (Simulated)**
BET Surface Area	3,300 m^2/g	6,111 m^2/g
Pore Volume	2.00 cm^3/g	2.52 cm^3/g
Porosity (calculated by PLATON SOLV)[12]	82.2%	81.6%

The BET surface area and pore volume data suggest that MFM-421 might have lower overall uptake, even after it has plateaued, as the BET surface area implies roughly half the amount of accessible framework surface per gram of material, and the pore volume suggests a smaller maximum uptake due to the reduction in space inside the MOF, despite the large pore down the *c* axis. The huge difference in BET surface area does suggest that the MOF may have suffered partial framework collapse. However, this was investigated by post-sorption PXRD, and found not to be the case, as the PXRD was still largely crystalline (see Figure 141 below).

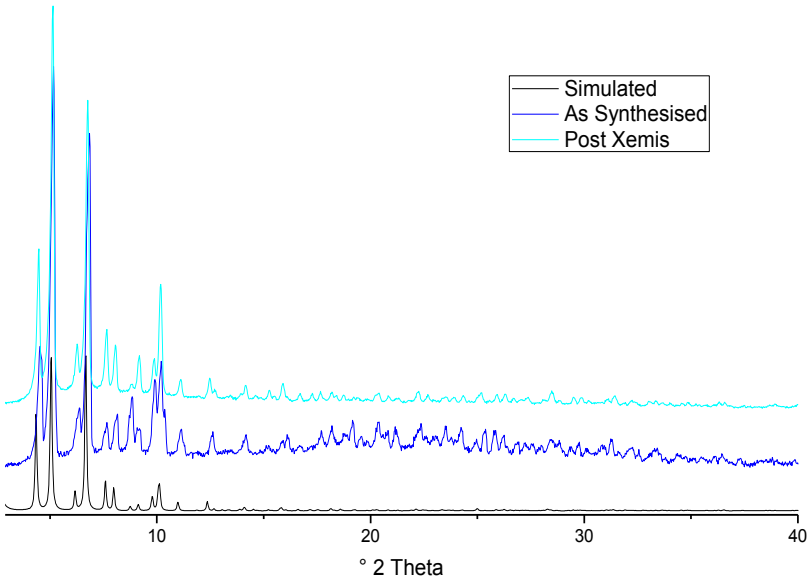


Figure 141. Post sorption PXRD of MFM-421 demonstrating retention of crystallinity.

Further evidence to suggest an accurate BET measurement for this MOF can be seen when comparing the value to that of isoreticular MOFs, PCN-222 and NU-1000 (shown in Figure 142),[8,9] which exhibit surface areas of 2,200 and 2,300 m^2/g with ligands proportionally slightly smaller than H_4L^1.

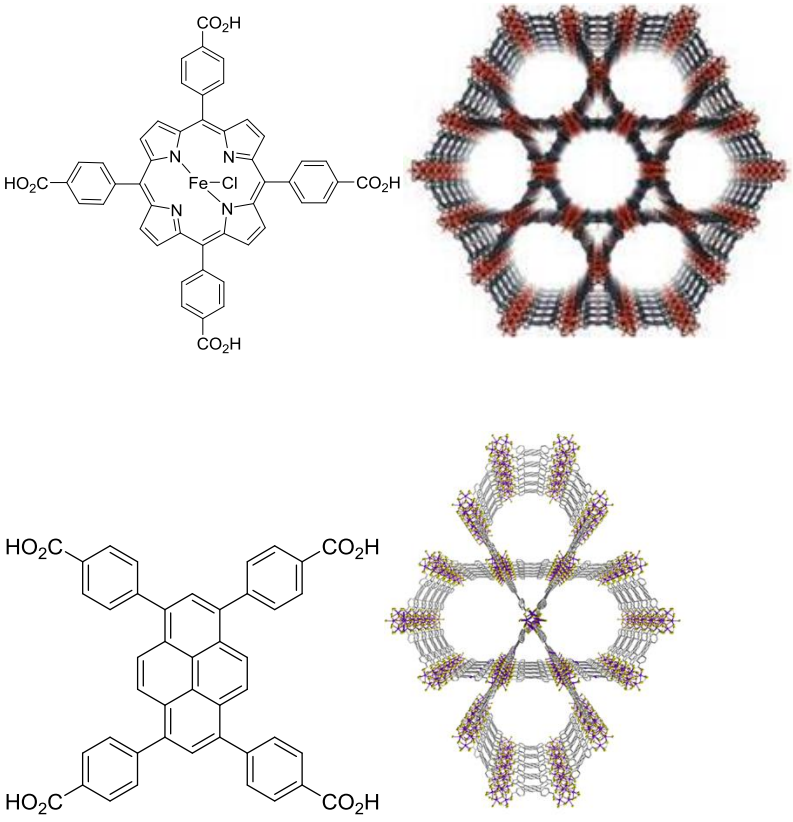


Figure 142. Fe-TCPP ligand and PCN-222 structure (top) and TBAPy ligand and NU-1000 structure (bottom), Zr MOFs of the same **csq** topology as MFM-421.[8,9]

However, the total gas uptake at the highest pressure reached, 80 bar, is still lower than those calculated from the Cu(II) structures in Chapter 2, and as such there must be further factors to consider than an over-estimation of the gas storage capacities of the MFM-19X series by computational methods. By analysing the CH_4 sorption plots, it can be seen that at 273 K and 80 bar, MFM-421 has not plateaued, yet at pressures any higher or temperatures any lower, the scenario is impractical for use in vehicular transport. Therefore it can be

seen that as interactions between the framework and the pore become less important in the mesoporous range, and the overall structure resembles more of a standalone void, the gas storage properties at accessible pressures are negatively impacted. The distance between the centre of the pore and the structure is of course still small enough for there to be a beneficial impact of this over a compressed gas cylinder, but this trend of increased porosity starting to reduce gas uptake at accessible pressures should be considered in the design of new MOFs.

4.2.2.2 High Pressure CO_2 isotherms of MFM-421

The large BET surface area, evident stability, and mesoporous nature of MFM-421 also make it an interesting candidate for studying high pressure CO_2 capture for CO_2 storage for shipping to offshore geostorage locations. This is an area relatively little studied in MOFs, due to the reasons discussed in Chapter 1, and the synthetic cost of most suitable MOFs, as they typically require larger ligands to generate structures with large pores and porosity. The versatility of the synthetic route to these ligands, discussed in Chapter 2, may also prove useful for fine tuning the properties of carbon dioxide uptake.

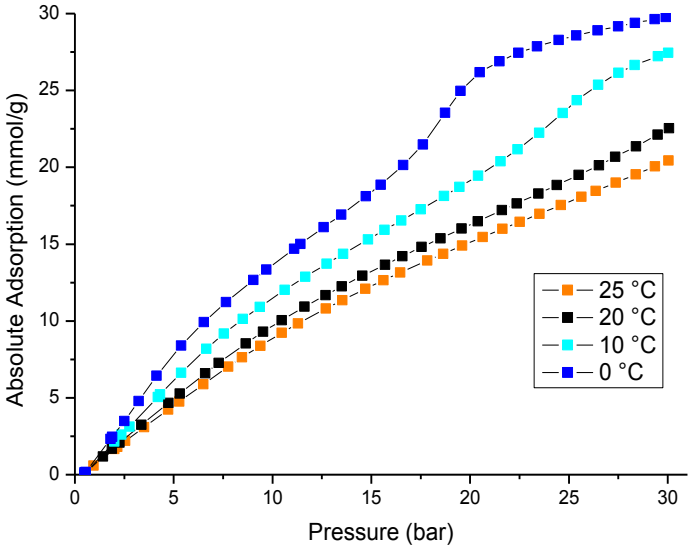


Figure 143. High pressure gravimetric uptake of CO_2 at various temperatures in MFM-421.

The low temperature CO_2 isotherms (Figure 143) display the same type IV behaviour as seen in with N_2 at 77 K (Figure 138). This is indicitive of a mesoporous framework, however it is typically seen in much lower temperature isotherms, as this is where the gas approaches saturation near the higher pressures. It is therefore interesting to start to observe this at 283 K, as this suggests that the system is beginning to resemble that of the bulk fluid at this temperature and pressure, indicating that this system is far superior to the storage of CO_2 in a bare tank under the same conditions. Similar trends have been seen in literature – as the capacity of a MOF system increases, the shape of the isotherm becomes more sigmoidal. This is most noticeable for MOF-177, which is the current highest reported uptake of CO_2, and starts to display this sigmoidal shape even at room temperature.[13]

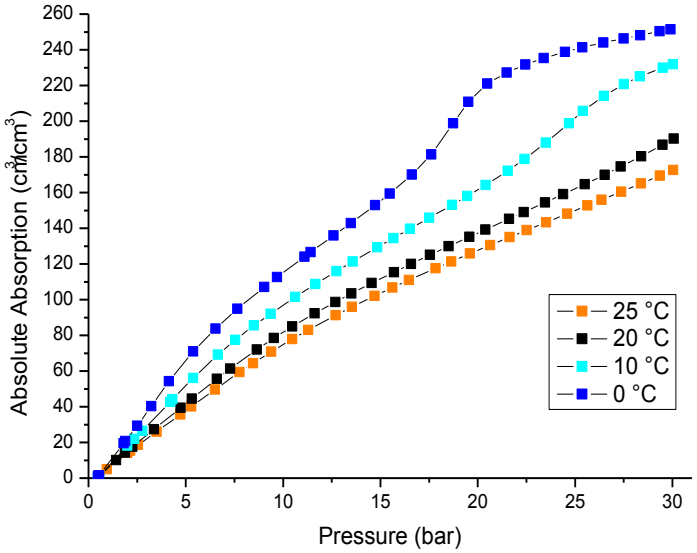


Figure 144. High pressure volumetric uptake of CO_2 at various temperatures in MFM-421.

As the crystal density of MFM-421 is so low, it is expected that the volumetric uptake would suffer from this, and as seen in Figure 144, there is certainly a detrimental effect to the overall capacity from the low crystal density, which places it below the calculated capacities of the MFM-19X series. Table 21 shows a comparison between MFM-421 and the MFM-19X series, as these were unstable to conventional activation methods, but showed great potential for CO_2 shipping in the carbon capture chain for power stations which need to relocate their waste CO_2 over large distances. The exceptional stability of MFM-421 is particularly needed in this application, as the benefit from a storage tank with MOF versus a compressed cylinder at low temperature would build with every use of the tank, providing a saving of 72 GJ with every loading cycle (saving up to $2M per ship per year).[14]

Table 21. Comparison of porosity and CO_2 of uptake for at various pressures of MFM-421 and the simulated MFM-19X series at 298 K.

	MFM-421	MFM-193	MFM-192	MFM-191
Porosity	**82.2%**	81.6%	68.9%	60.3%
Crystal Density	0.377	0.355	0.584	0.733
Uptake at 1 bar (mmol/g)	0.59	0.65	**2.90**	2.88
Uptake at 1 bar (cm^3/cm^3)	4.95	5.19	37.89	**47.31**
Uptake at 30 bar (mmol/g)	20.44	**40.82**	24.07	16.69
Uptake at 30 bar (cm^3/cm^3)	172.65	**324.50**	314.79	274.00

As seen with the methane uptake, Table 21 shows again how the high porosity alone does not grant MFM-421 an extremely high uptake such as those calculated for the Cu(II) **lvt** structures. The overall maximum gravimetric uptake lies just above that of MFM-191, which is much less porous on account of the interpenetrated net which halves the pore volume down two of the axes. The reason for the discrepancy in overall uptake is again attributed to the large pore down the *c* axis of MFM-421, which acts more like a void as would be found inside a regular cylinder, rather than the framework-enchanced pore volume as found in the Cu(II) MOF series.

Before comparing these values to literature values and evaluating the potential industrial use of this MOF, it is worth considering all of the practicalities and current limiting factors to the use of MOFs in industrial roles. As discussed in Chapter 2, one of these key factors is the cost of synthesis, both of the ligand and of the actual MOF itself. This is particularly the case for high pressure uptake of both methane and carbon dioxide, where the cheap ligands to synthesise or buy (BTC, TA) tend to generate structures which are ultra-microporous (HKUST, IRMOF-1) and therefore often do not have sufficient

pore volume (>1.8 cm^3/g) to be used for high pressure gas sorption and storage. Ideal materials have large pores, and therefore typically require ligands which themselves are large and complex, preferably with additional functionality. This requires extra cost and effort in the ligand synthesis, thus producing materials which may be exceptional at gas storage, but are impractical for industrial use. The ligands used so far in this chapter and the last have fallen into this category of large and highly functionalised, with subsequent MOFs exhibiting promising isotherms (both simulated and experimental), yet they are also extremely expensive to synthesise, despite the relatively versatile method shown in Chapter 2. Therefore, to make a system which is not only theoretically useful, but realistically plausible for industrial application, the two-step ligand synthesis of H_4L^{1P} detailed in Section 2.2.2 is incredibly promising. Therefore, this linker was reacted with Zr(IV), with the aim of producing a structure isoreticular to that of MFM-421, as this demonstrated great stability and an attainable permanent porosity which is accessible *via* conventional activation methods.

4.2.3 MFM-422

Solvothermal Synthesis of MFM-422

A suspension of H_4L^{1P} ligand (16 mg, 0.022 mmol), $ZrCl_4$ (24 mg, 0.103 mmol) and benzoic acid (600 mg, 4.91 mmol) in diethylformamide (3 mL) was heated to 120 °C in a sealed 15 mL pressure vessel, and maintained at this temperature for 24 hours to yield small, white needles of MFM-422 $[Zr_6L^{1P}_{2.5}(\mu_3\text{-}OH)_6(\mu_3\text{-}O)_2(OH)_4]\cdot solv_x$ in a 65% yield. The as-synthesised single crystals were insoluble in organic solvents, and were fully characterised by SCXRD using

synchrotron radiation as the size of the crystals was very small. Without the use of benzoic acid as a modulator, the reaction did not yield crystals large enough for characterisation. The bulk phase purity of the solid was analysed using powder x-ray diffraction.

Crystal Structure Description of MFM-422

Table 22. Crystallographic Information for MFM-422.

Crystal Data	
Formula = $C_{13.625}H_9N_{0.625}O_4Zr_{0.75}$	Hexagonal, *P*6/*mmm*
a = 54.4240(18) Å	V = 102004(7) Å^3
c = 39.7655(9) Å	Mr = 314.145
Density = 0.487	Z = 24
Data Collection and Refinement	
Rint = 1.978	$R[F2 > 2\sigma(F2)]$ = 0.110
$wR(F^2)$ = 0.326	

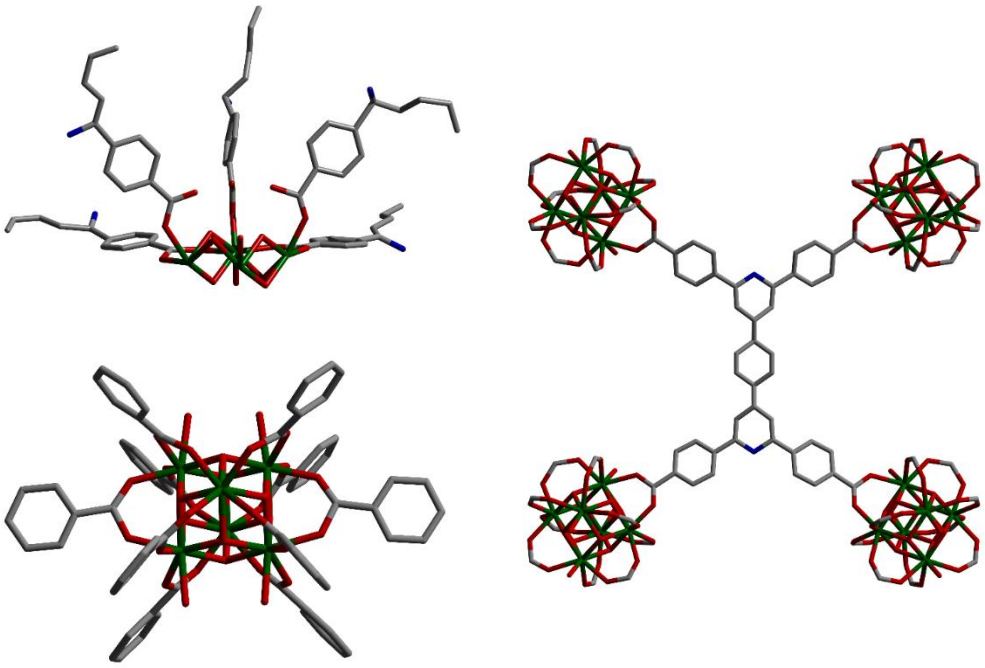


Figure 145. Asymmetric unit and the $[Zr_6L^{1P}_{2.5}(\mu_3{-}O)_4(\mu_3{-}OH)_4(OH)_2(OH_2)_2]$ SBU of MFM-421 (left) and coordination mode of L^{1P} (right).

MFM-422 crystallised in the hexagonal space group *P*6/*mmm*, with cell parameters: *a* = 54.4240(18) Å and *c* = 39.7655(9) Å, and *V* = 102,004 (7) Å^3.

Solving the structure by single-crystal x-ray diffraction techniques showed that the framework contained SBUs with 10 points of extension. The two apical Zr(IV) ions are coordinated to four oxygen atoms from four separate ligands, leaving the other half of the carboxylates from the four ligands to bind to the four equatorial Zr(IV) ions. These four equatorial ions bind to two separate ligands through a single oxygen-zirconium bond on each, and to one terminal OH/H_2O, as shown in Figure 145. All of the Zr cations in the cluster are joined by a total of eight bridging μ_3-OH/μ_3–O anions, as the interchangeable nature of the oxygen ions in the cluster enables charge balancing from the extra two ligands which replace the 4 terminal OH anions in MFM-421, as described in the introduction to this Chapter.[7]

These hexanuclear zirconium clusters are formed at the four points of extension on each ligand, giving it a 4,10-connected net, as shown in Figure 146. The 3D network formed by the MOF has an unknown topology. Due to the highly connected nature of the topology, the framework is non-interpenetrated, which makes it very porous, with a calculated solvent accessible volume of 79% (calculated by PLATON SOLV).[10] The structure is highly porous down all axes, and forms an overlapping triangular circles grid, where each circle has six overlapping neighbours, forming a 'flower of life' design, which is strikingly different to the structure of MFM-421. The difference in framework produced was most likely due to the presence of the pyridyl ring, which itself can act as modulator by binding with Zr(IV) ions in the synthesis, and also raises the pH of the solution due to the basic nature of the pyridyl moiety.

Figures 146 and 147 show the framework, which is highly porous, and is of a topology which shows great promise for gas uptake as it has many cages for

framework-guest interactions. The main pore channel down the *c* axis (Figure 140) measures 29 Å in diameter, and is lined with two types of cages, a square cage measuring 17.3 x 15.3 Å (Figure 146), and a triangular cage of 15.5 Å width; both of these cages constitute ideal sites for gas sorption.

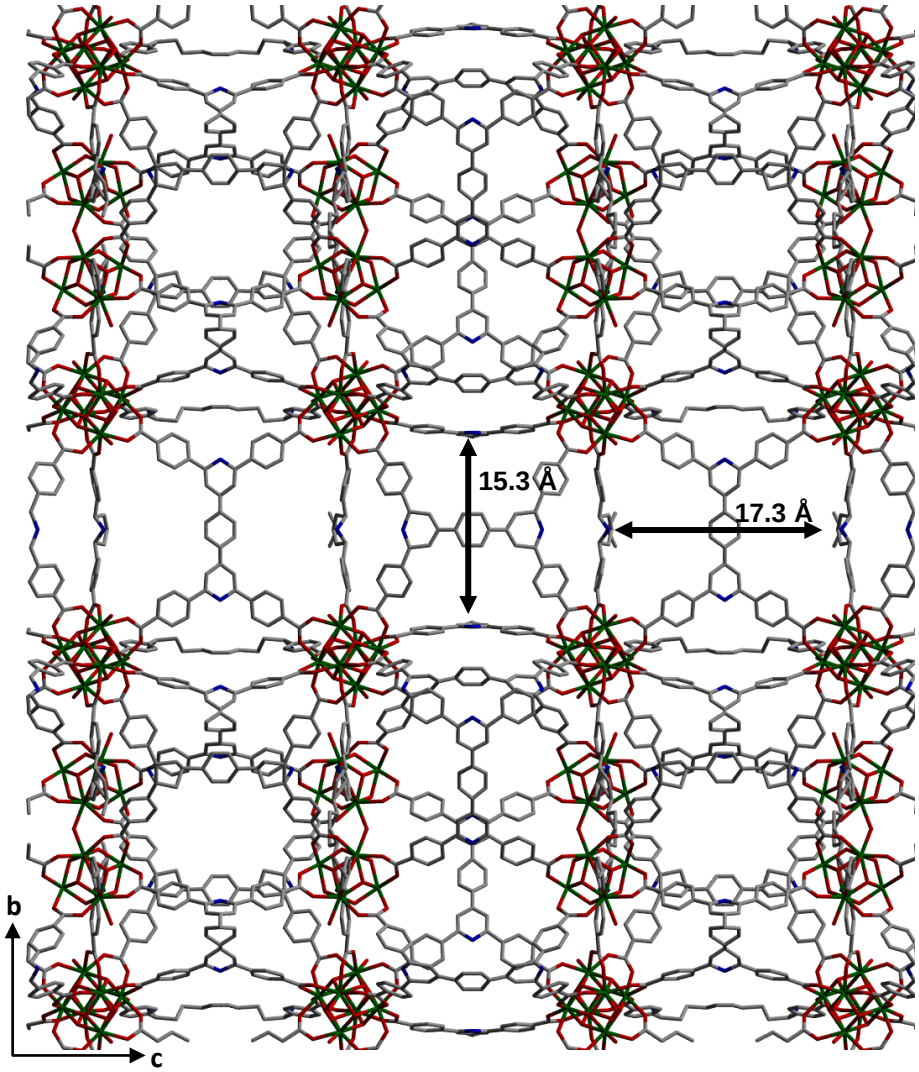


Figure 146. View down the *a* axis of MFM-422, with cage sizes indicated.

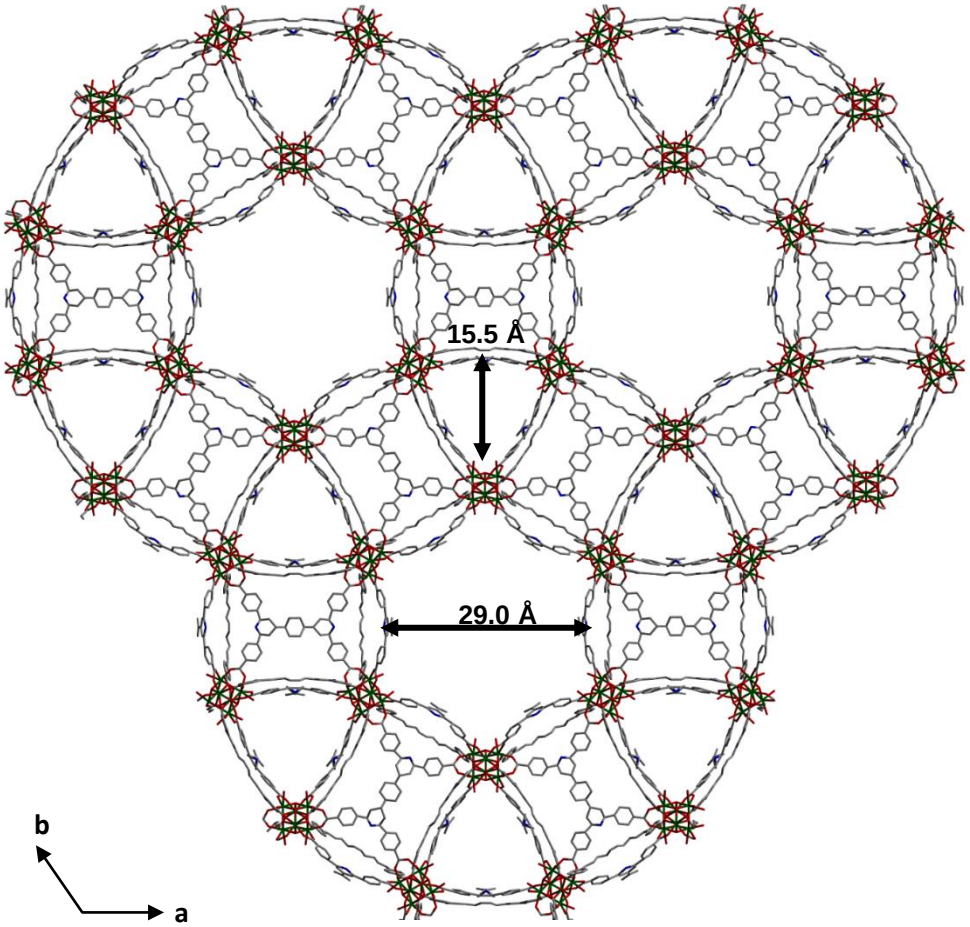


Figure 147. View down the *c* axis of MFM-422, with pore size indicated, demonstrating the high porosity of the non-interpenetrated framework.

As with MFM-421, the crystals of MFM-422 are thermally and chemically very robust; as it has a very similar SBU with many strong Zr-O bonds which hold the framework together. There are also fewer equatorial terminal hydroxo anions, which could lead to enhanced stability over MFM-421, particularly if the hypothesis that the methanol exchange caused framework collapse due to insertion of methanol into the cluster was correct.

Thermal and chemical stability of MFM-422

The framework of MFM-422, while different to that of MFM-421, is still incredibly porous, and again exhibits a very large pore down the *c* axis of several nanometers. This made it an interesting candidate for high pressure storage of

methane and carbon dioxide, as it would have different uptakes to MFM-421, but still could be very promising for industrial applications, particularly with the ease of ligand synthesis. The first step in assessing the importance of this structure was to test the stability to activation, and to other conditions which might render a material impractical for real world usage.

To test and compare thermal stability, a TGA was performed on a 7 mg sample of MFM-422, as shown in Figure 148. The MOF shows thermal stability similar to that of MFM-421, up to just below 500 °C in the acetone exchanged sample.

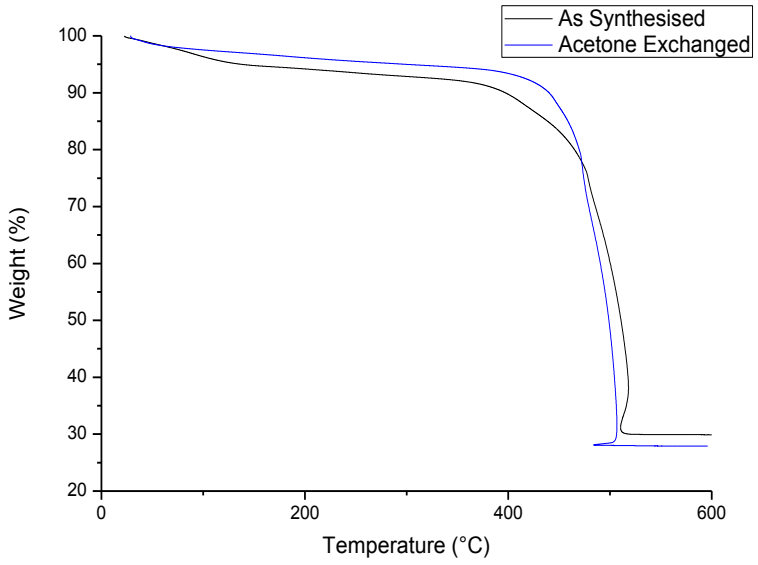


Figure 148. Thermo-gravimetric analyses of MFM-422 in air.

In order to further ascertain the stability of the framework, PXRD patterns were collected, as with MFM-421, to ensure retention of crystallinity throughout the activation process. As shown in Figure 149, the PXRD patterns show that the MOF remains crystalline after acetone exchange and after activation at 120 °C under dynamic vacuum in a Schlenk flask for 24 hours.

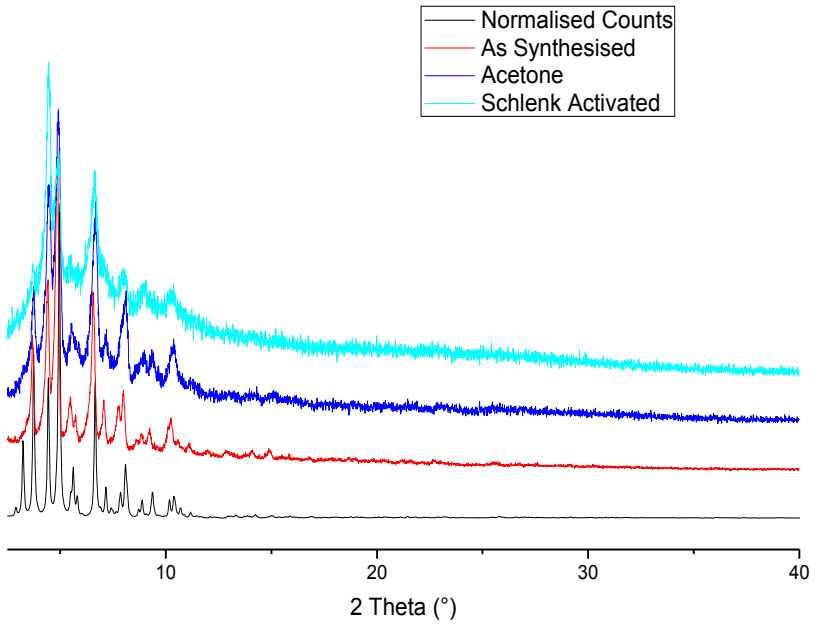


Figure 149. Overlaid PXRD patterns of MFM-422 simulated from single crystal data, as synthesised, acetone exchanged and Schlenk activated.

4.2.4 Gas Sorption Measurements of MFM-422

A 60 mg sample of MFM-422 was prepared and exchanged with acetone. This acetone exchanged sample was then loaded into a glass micromeritics sample tube and placed on the SmartVacPrep degasser where it was heated to 120 °C under dynamic vacuum for 18 hours. The sample was seen to change from a dark yellow colour when wet with acetone to a light cream colour when activated. This activated sample was then placed on a Tristar gas sorption analyser. Figure 150 shows the N_2 isotherm at 77 K, which was used to calculate the BET surface area shown below.

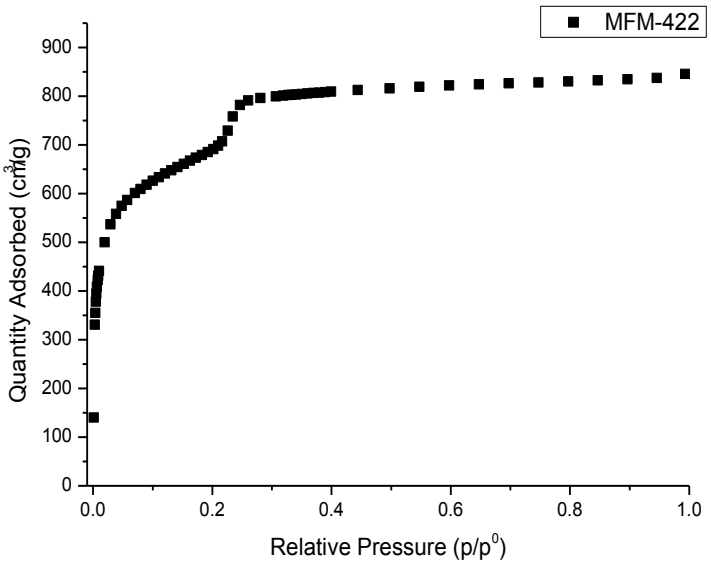


Figure 150. N_2 isotherm of MFM-422 at 77 K used to calculate BET surface area.

The BET surface area calculated from the N_2 isotherm shown in Figure 150 was 2,500 m^2/g, and showed that this sample was clearly stable to activation, and had a permanent porosity which could be used for the storage of gas. As with MFM-421, the isotherm was type IV, which suggests the retention of the 2.9 nm pore down the *c* axis. The pore volume could not be calculated due to the lack of points in the low pressure region (this was due to the equipment the isotherm was measured on).

4.2.4.1 High Pressure CH_4 Isotherms of MFM-422

The sample was placed on a high pressure gas sorption measurement kit (Xemis) and methane and carbon dioxide isotherms were measured up to 80 and 30 bar respectively, in an attempt to saturate the MOF and allow the calculation of working capacities, and subsequent assessment of the potential impact of the relatively cheap and easily synthesisable material.

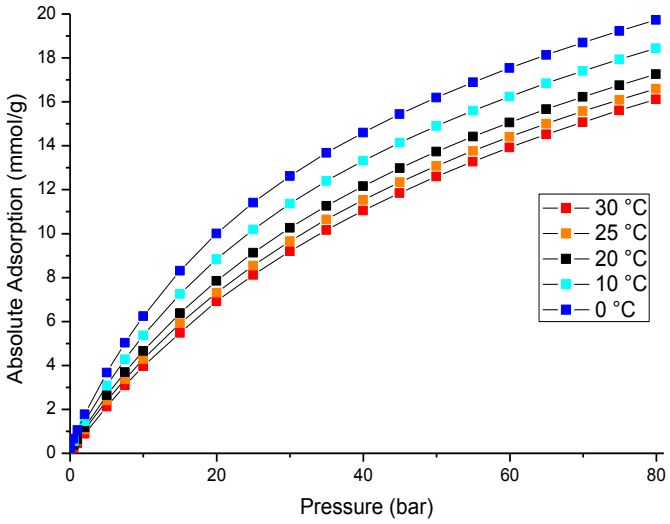


Figure 151. Gravimetric methane isotherms for MFM-422 at various temperatures.

As shown in Figure 151, the gravimetric uptake changes by just over 3.5 mmol/g between the values of 30 and 0 °C at the highest pressure loading (from 16.12 mmol/g at 30 °C and 80 bar, to 19.73 mmol/g at 0 °C), yet only about 1.5 mmol/g at 5 bar(from 2.12 at 30 °C to 3.67 mmol/g at 0 °C), which suggests the working capacity will increase as the temperature is lowered, just as with MFM-421, reflecting the poor host/guest interactions at low loadings due to the mesoporosity of the MOF, and how this actually benefits the working capacity. The isotherm again does not plateau at 80 bar, indicating that the MOF has not reached saturation.

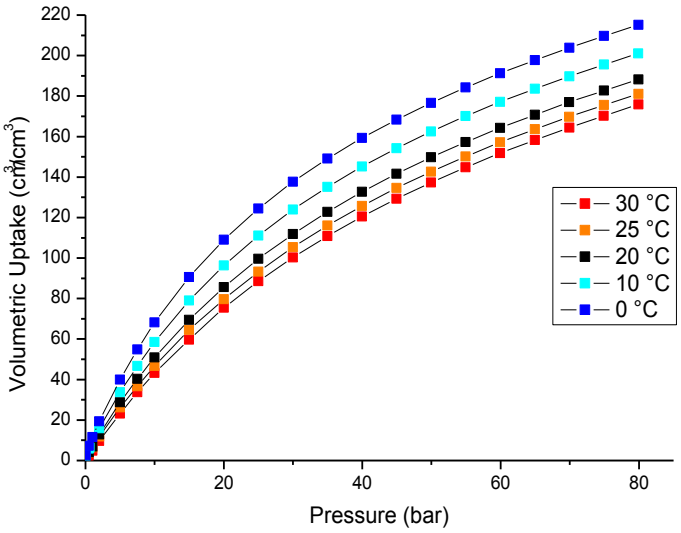


Figure 152. Volumetric methane isotherms for MFM-422 at various temperatures.

As shown in Figure 152, there is just under a 40 cm^3/cm^3 increase at 80 bar across the temperature range, from 175.79 cm^3/cm^3 at 30 °C to 215.15 cm^3/cm^3 at 0 °C. This maximum uptake at 0 °C is over 30 cm^3/cm^3 more than that of MFM-421 (184.57 cm^3/cm^3), probably a result of the higher crystal density (0.487 g/cm^3, as opposed to 0.377 g/cm^3), which improves the volumetric uptake and slightly negatively impacts the gravimetric.

As seen with MFM-421, the gravimetric and volumetric uptakes are lower than those calculated for the non-interpenetrated copper series, MFM-19X. This supports the theory that a large solvent accessible volume (calculated from PLATON SOLV)[12] is not the sole factor which governs a great high pressure uptake, and the presence of a singular, giant pore is less beneficial than a network of smaller pores interlinked to enable maximum gas/framework interactions. However, the large pore does lead to a working capacity that is

very close to the maximum uptake, resulting in very little wasted 'dead' volume of methane at low pressure.

Interestingly, the lower BET surface area of MFM-422 compared to MFM-421 (800 m^2/g less) does not impact the uptake dramatically, and indeed the volumetric working capacity is actually 25 cm^3/cm^3 higher at 298 K, while the gravimetric working capacity is only 3.1 wt% lower – suggesting that this is not solely due to the difference in crystal density between the two MOFs. It is proposed that the proportional increase in uptake for MFM-422 is a combined effect of a smaller main pore down the *c* axis (a 10 Å reduction in diameter) and the positive impact the pyridyl group has on interaction with guest methane molecules.[15]

4.2.4.2 High Pressure CO_2 Isotherms of MFM-422

A set of high pressure carbon dioxide isotherms were collected at various temperatures to enable comparison to the current literature records for MOFs in this application.

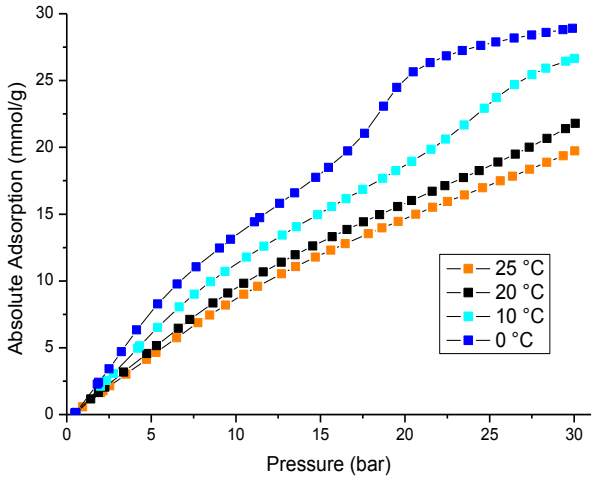


Figure 153. High pressure gravimetric uptake of CO_2 at various temperatures in MFM-422.

As with MFM-421, MFM-422 shows a good affinity for CO_2 uptake at high pressures (Figure 154). Again, the low temperature isotherm is sigmoidal in shape, highlighting the impact the MOF has on the CO_2 to enable it to resemble bulk fluid at this temperature.

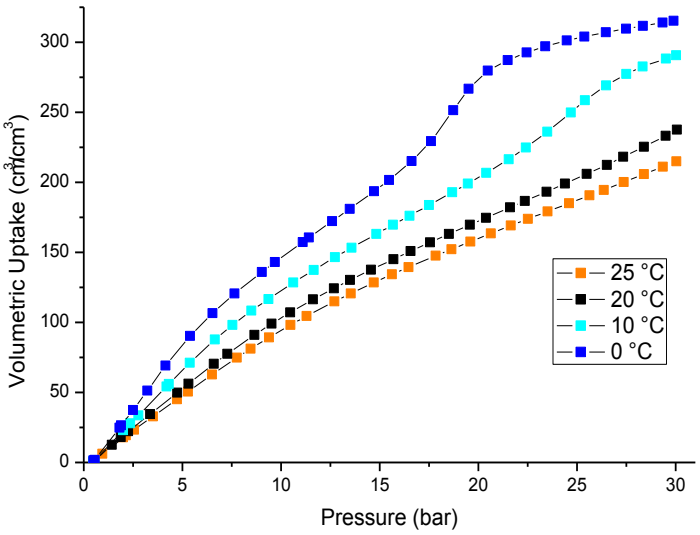


Figure 154. High pressure volumetric uptake of CO_2 at various temperatures in MFM-422.

The slightly higher crystal density of MFM-422 than that of MFM-421 leads to a higher maximum volumetric uptake, seen in Figure 154. Despite the increase in maximum uptake, there is still very little uptake at low pressures, thus presenting a higher working capacity and signifying how in these structures with incredibly large pores, extra functionality, such as a pyridyl group, is highly beneficial as they do not impact the uptake at low pressures significantly, yet at maximum loading their impact can be seen to a greater extent.

Table 23 shows a comparison between the two Zr(IV) MOFs presented in this chapter and the Cu(II) MOF series discussed in Chapter 3. This helps to build a

more complete picture of how, despite the fragile nature of the Cu(II) structures which were computationally theorised to have extremely promising high pressure isotherms, it is possible to use a different metal known for producing highly stable frameworks to synthesise structures which can match and even outperform some of the Cu(II) structures which were unable to attain their simulated capacities. Most importantly, the comparison between the two Zr(IV) MOFs allows for analysis of the synthetically preferential pyridyl MOF, as this offers many key advantages in preparation.

Table 23. Comparison of the Zr(IV) structures to the H_4L^1 Cu(II) MOF series for CO_2 uptake at various pressures and 298 K.

	MFM-422	**MFM-421**	**MFM-193**	**MFM-192**	**MFM-191**
Porosity	79%	82.2%	81.6%	68.9%	60.3%
Crystal Density (g/cm^3)	0.487	0.377	0.355	0.584	0.733
Uptake at 1 bar (mmol/g)	0.57	0.59	0.65	2.90	2.88
Uptake at 1 bar (cm^3/cm^3)	6.18	4.95	5.19	37.89	47.31
Uptake at 30 bar (mmol/g)	19.72	20.44	40.82	24.07	16.69
Uptake at 30 bar (cm^3/cm^3)	215.05	172.65	324.50	314.79	274.00

The overall gravimetric and volumetric maximum adsorption values of MFM-422 (Table 23) are both incredibly close to those given by MFM-421 – an interesting result given the decrease in BET surface area for MFM-422. Furthermore, given the difference in crystal density and how the loss in overall gravimetric uptake (a 3.66% decrease from MFM-421 to MFM-422) is lower than the positive gain in volumetric uptake (a 24.56% increase from MFM-421 to MFM-422), then proportionally MFM-422 seems to have better gas uptake properties. This is most likely due to a combination of a slightly smaller main

pore running down the *c* axis (although the size of it is still in the mesoporous range and so has some negative impact on host/guest interactions) and higher crystal density of MFM-422.

4.2.5 Applications – CO_2 Shipping

The impressive uptake of CO_2 at high pressure, coupled with the thermal and chemical stability of both of these Zr(IV) MOFs make them ideal candidates for CO_2 transportation, where the maximum uptake at 30 bar is essential for a decent deliverable quantity when shipping the CO_2 to off-shore locations. Table 24 below shows a comparison of total gravimetric uptake for the MFM-19X series, the MFM-42X series, and a selection of the best performing literature MOFs, all at 298 K, versus CO_2 stored in a cylinder, as this is the current technology proposed for CO_2 shipping.

Table 24. Comparison of total molar uptake of MOFs versus current technology. All MOFs are quoted at 298 K.

MOF/Container	Crystal Density	Pressure (bar)	Total Molar Uptake (mol/m^3)
Tank at 223K	N/A	7	26,248
Tank at 263K	N/A	26.5	22,354
Tank at 298K	N/A	30	1,458
MFM-191	0.733	30	12,755
MFM-192	0.584	30	14,656
MFM-193	0.355	30	15,257
MFM-194	0.387	30	15,913
MFM-195	0.406	30	15,762
MFM-196	0.367	30	15,661
MFM-197	0.292	30	14,790
MFM-198	0.352	30	15,706
MFM-421	0.377	30	7,708
MFM-422	0.487	30	9,605
HKUST-1[16]	0.881	30	9,418
IRMOF-1[17]	0.648	30	14,036
IRMOF-3[17]	0.593	30	11,062
IRMOF-6[17]	0.540	30	10,545
IRMOF-11[17]	0.720	30	10,591
MOF-177[18]	0.427	30	14,552

MOF-200[19]	0.222	30	7,566
MOF-505[20]	0.992	30	10,118

As seen in Table 24 above, the MFM-19X series' computational data stand out as leading MOFs in high pressure CO_2 storage, however they were seen to be unstable to activation. The Zr(IV) MOFs, on the other hand, displayed enhanced stability, and were capable of adsorbing sufficient quantities of CO_2 compared to a bare tank to be worthy of consideration in CO_2 shipping. Comparison of MFM-421 and MFM-422 to literature MOFs under the same conditions, shows that they exhibit lower volumetric uptake than most, due to the low crystal density of the Zr(IV) frameworks. However, as the main driving factor for replacing an empty tank with MOF is the cost saving aspect over the need for refrigeration of CO_2, the crystal density is worth considering as this is directly related to the amount of MOF in each cylinder, and as such the cost of installation and overall efficiency of the system. Therefore, comparing the crystal densities, it is clear that while the Zr(IV) MOFs might not adsorb as much CO_2 volumetrically, most other MOF structures are considerably more dense, and as such would require more MOF to fill the cylinder, and therefore would operate at a much higher cost. This cost implication is more important still for MFM-422, which has a cheap, versatile synthetic route, and therefore makes it an ideal candidate.

4.2.6 Applications – CH_4 Storage for Vehicular Transport

Comparison of MFM-421 with L^1 Cu(II) structures

Table 25 shows a comparison between the working capacities of the MFM-421 and the interpenetrated series of Cu(II) MOFs discussed in Chapter 3 (MFM-191 to 193), as these are all synthesised from the same ligand, H_4L^1. These are also interesting for comparison because MFM-192 has a similar BET surface area to MFM-421, while MFM-193 has similar porosity and crystal density. This helps identify the core factors governing high working capacity, and further aids the ability to hone and optimise MOFs for particular applications. As seen in Table 25, the 298 K volumetric working capacity of MFM-421, between 5-80 bar, is on average lower than those of the copper MOF series (136 cm^3/cm^3 compared to 153 cm^3/cm^3 188.38 cm^3/cm^3 and 210 cm^3/cm^3 for MFM-191, -192 and -193). This is due to the vastly lower BET surface area in comparison to MFM-193, and much lighter crystal density than MFM-192 and MFM-191.

Table 25. Comparison of methane working capacities at 298 K between MFM-191, -192, -193 and -421; all synthesised from H_4L^1.

	Crystal Density (g cm^{-3})	**Uptake at 80 bar (cm^3 cm^{-3})**	**Working Capacity 5-80 bar (cm^3 cm^{-3})**	**Uptake at 80 bar (wt%)**	**Working Capacity 5-80 bar (wt%)**
MFM-191	0.733	219.09	153	21.40	14.9
MFM-192	0.584	255.73	188	31.36	23.1
MFM-193	0.355	233.29	210	47.06	42.4
MFM-421	0.377	156	136	29.7	25.7

The low crystal density, however, is beneficial to the gravimetric uptake. MFM-421 takes second place among the compared MOFs above, out-performing

MFM-192, which has a similar BET surface area, giving a working capacity at 298 K of 25.7 wt% compared to 23.1 wt%. This is highly encouraging, as MFM-421 is proven to be highly stable compared to the MFM-19X series. The value is still a lot lower than MFM-193 (25.7 wt% *versus* 42.4 wt% for MFM-193 at 298 K), which signifies the importance of BET surface area over porosity, as this is the only factor which separates these two MOFs. They have incredibly similar crystal densities (0.377 and 0.355 for MFM-421 and MFM-193, respectively), and share very similar values for solvent accessible volume calculated by PLATON SOLV, at 82.2% and 81.6% of the unit cell volumes of MFM-421 and MFM-193.

The uptake, therefore, is clearly negatively impacted by topologies where the porosity mainly comes from one large pore, as in the case of MFM-421, which is of **csq** topology, and has a main pore size of 33.8 Å. Furthermore, the intersecting pores themselves are very large, measuring 14.2 by 12.3 Å, and are comparable in size to the main pores in MFM-193 (14.9 by 13.5 Å).

A beneficial topology for maximum uptake and working capacity would appear to be one which contains many smaller sized pores, enabling gas molecules to interact with more of the framework, as in the case of MFM-193, which is of **lvt** topology. This framework contains one 'main pore' axis, with a major pore size of 14.9 by 13.5 Å and a minor pore size of 12.6 by 6.6 Å. This main pore channel is intersected by slightly smaller pores, which average 11.5 Å across (with the exception of a long, tapered pore which measures 26.1 Å, though is diamond in shape, and therefore interacts with guest molecules much before the end of the pore). The highly networked nature of this framework allows for

maximum porosity without compromising interactions between the framework and the guest molecules inside the MOF.

Comparison of Zr(IV) MOFs to high-performing literature MOFs

Table 26 shows a comparison between the two Zr(IV) MOFs described in this Chapter, the Cu(II) MOF series from Chapter 3, and a selection of literature MOFs which exhibit the highest recorded volumetric and gravimetric working capacities (5-80 bar) at 298 K to date.

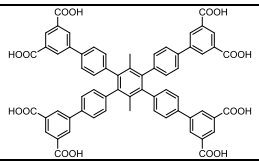
Table 26. Comparison of methane working capacities of MFM-422 and MFM-421 with current literature MOFs, ordered by gravimetric working capacity at 298 K.

	Crystal Density (g cm^{-3})	**Uptake at 80 bar (cm^3 cm^{-3})**	**Working Capacity 5-80 bar (cm^3 cm^{-3})**	**Uptake at 80 bar (wt%)**	**Working Capacity 5-80 bar (wt%)**
MFM-191	0.733	219.09	152.66	21.40	14.91
MFM-192	0.584	255.73	188.38	31.36	23.10
MFM-193	0.355	233.29	210.23	47.06	42.41
MFM-194	0.387	245.07	220.21	45.35	40.75
MFM-195	0.406	251.89	223.78	44.43	39.47
MFM-196	0.367	237.31	214.66	46.30	41.88
MFM-197	0.292	215.29	197.80	52.79	48.51
MFM-198	0.352	239.92	217.03	48.81	44.15
MFM-421	0.377	156	136	29.7	25.7
MFM-422	0.487	181	155	26.6	22.8
MOF-519[21]	0.953	279	230	21.0	17.3
Al-soc-MOF-1[22]	0.34	222	201	46.7	42.3
HKUST-1[16]	0.881	272	200	22.2	16.3
MOF-520[21]	0.586	231	194	28.2	23.7
MOF-205[19]	0.38	205	186	38.6	35.0
MOF-177[18]	0.427	205	185	34.4	31.0
PCN-14[23]	0.819	250	178	21.9	15.6
Cu-tbo-MOF-5[24]	0.595	216	175	26.0	21.1
Bulk CH_4	N/A	83	79	N/A	N/A

There is a very clear distinction between volumetric and gravimetric working capacity when comparing these Zr(IV) MOFs, as the volumetric capacity is greatly effected by the low crystal density, and therefore MFM-421 and MFM-422 perform lower than the other MOFs reviewed here. However, it is worth noting the increase of working capacity from 79 cm^3/cm^3 for bulk CH_4 in a cylinder to 135.5 cm^3/cm^3 for MFM-421 and 155 cm^3/cm^3 for MFM-422, demonstrating the hugely positive impact these MOFs have over cylinder storage. The gravimetric working capacity of MFM-421, however, is the fourth highest of MOFs reported to date, and, most importantly, is above both MFM-191 and MFM-192, which therefore shows promise for this method of synthesising a framework which approaches the extrememly promising results computationally calculated for the MFM-19X series. Also of note is the comparison to HKUST-1, as it is the only MOF among this list which is as cheap and easy to make as MFM-422 (as shown in Table 27).

Table 27. Comparison of cost of synthesis (on laboratory scale) of MOFs reviewed for CH_4 storage.

	Ligand	**Cost of Ligand**	**Steps to Ligand**	**Metal**	**Cost of Metal**
Al-soc-MOF-1[22]	3,3",5,5"-tetrakis(4-carboxyphenyl)-p-terphenyl (H_4L^1)	£42.77/g	3*	$Al(NO_3)_3{\cdot}9H_2O$	£0.10/g
MFM-193	H_4L^1	£11.68/g	6*	$Cu(NO_3)_2.2.5H_2O$	£0.08
MOF-205[19]	2,6-Naphthalenedicarboxylic acid	£2.02/g	0	$Zn(OAc)_2{\cdot}2H_2O$	£0.11/g
MOF-177[18]	H_3BTB (1,3,5-tris(4-carboxyphenyl)benzene)	£3.10/g**	2*	$Zn(OAc)_2{\cdot}2H_2O$	£0.11/g
MFM-421	H_4L^1	£11.68/g	6*	$ZrCl_4$	£0.36/g
MOF-520[21]	H_3BTB (1,3,5-tris(4-carboxyphenyl)benzene)	£3.10/g**	2*	$Al(NO_3)_3{\cdot}9H_2O$	£0.10/g
MFM-422	H_4L^{1P}	£0.51/g	2	$ZrCl_4$	£0.36/g

Cu-tbo-MOF-5[24]		£13.60/g	6*	$Cu(NO_3)_2.2.5H_2O$	£0.08
MOF-519[21]	H_3BTB (1,3,5-tris(4-carboxyphenyl)benzene)	£3.10/g**	2*	$Al(NO_3)_3.9H_2O$	£0.10/g
HKUST-1[16]	Trimesic Acid	£0.28/g	0	$Cu(NO_3)_2.2.5H_2O$	£0.08
PCN-14[23]	5,5'-(9,10-Anthracenediyl)di-isophthalic acid	£25.32/g	2*	$Cu(NO_3)_2.2.5H_2O$	£0.08
IRMOF-1[17]	Terephthalic Acid	£0.09/g	0	$Zn(OAc)_2.2H_2O$	£0.11/g
IRMOF-3[17]	3-Aminoterephthalic acid	£0.82/g	0	$Zn(OAc)_2.2H_2O$	£0.11/g
IRMOF-6[17]	1,2-dihydrocyclobutabenzene-3,6-dicarboxylic acid	£0.75/g	6*	$Zn(OAc)_2.2H_2O$	£0.11/g
IRMOF-11[17]	4,5,9,10-tetrahydropyrene-2,7-dicarboxylic acid	£0.84	3*	$Zn(OAc)_2.2H_2O$	£0.11/g
MOF-200[19]	1,3,5-Tris(4′-carboxy[1,1′-biphenyl]-4-yl)benzene (H_4BBC)	£3.37/g	3*	$Zn(OAc)_2.2H_2O$	£0.11/g
MOF-505[20]	Biphenyl-3,3′,5,5′-tetracarboxylic acid (H_4BPTC)	£1.09	4*	$Cu(NO_3)_2.2.5H_2O$	£0.08

As Table 27 shows, MFM-422 and HKUST-1 are by far the cheapest and easiest MOFs to synthesize from those published which show the highest CH_4 working capacities. Therefore the comparison of these two MOFs is vital to progressing towards MOFs as storage materials for alternative fuel. As shown earlier in Table 26, the volumetric working capacity of HKUST-1 outperforms MFM-422 (200 cm^3/cm^3, compared to 154.88 cm^3/cm^3), yet its gravimetric working capacity is lower (16.3 wt.% compared to 22.78 wt%). Therefore, the synthesis of this Zr(IV) MOF provides a choice between selecting a material with high volumetric, or high gravimetric working capacity.

The cheap and concise synthesis of a zirconium MOF which not only demonstrates competitive gravimetric uptake, but also exhibits exceptional stability both thermally and chemically is a further step towards realisation of the commercialisation of MOFs as porous host materials for methane storage. As seen in Table 26, the best performing MOF in literature to date, and closest to the DoE targets, is Al-soc-MOF-1. Further evaluation of this MOF reveals that it is synthesised using the ligand referred to in this thesis as H_4L^1, which is of extreme importance, as Chapter 2 details a more versatile synthesis of this ligand which could allow for functionalisation and extension of the ligand to reach and even exceed the target values which Al-soc-MOF-1 comes so close to attaining. Of even greater significance, however, is the analogous pyridyl ligand used to synthesise MFM-422, which, with refinement of solvothermal synthesis conditions to balance the difference in pH and modulation of MOF synthesis, should theoretically be capable of forming the same MOF structure, but at a cost which is a fraction of that involved in Al-soc-MOF-1. This could form the basis of a truly industrially viable MOF for use in methane fuelled transport.

4.3 Conclusion

This chapter evaluated the trade-off between MOFs which were theoretically impressive in sorption, but ultimately unstable to activation (the MFM-19X series), and MOFs synthesised from the same ligand (H_4L^1) which were capable of realising their full gas sorption potential due to the thermal and chemical stability, but did not exhibit the same calculated record-breaking uptake as those which were unstable to activation.

The chapter started with the evaluation of MFM-421, a zirconium structure synthesised from the same ligand as the MFM-191,2,3 interpenetration series, and explored the limits of stability of this structure, which was found to be superior to the Cu(II) MOFs. These improvements were attributed to the Zr-O bonds, which are stronger than Cu-O bonds, due to the more oxophilic nature of zirconium. High pressure CH_4 and CO_2 sorption measurements were discussed, as the highly porous nature of the framework suggested potential for excellent sorption measurements at high pressure due to the space available in the crystal structure. Comparison of both the CO_2 and CH_4 isotherms with the MFM-19X series showed that this non-interpenetrated zirconium structure did not reach the same potential simulated for the non-interpenetrated framework MFM-193, although it did outperform the interpenetrated structures gravimetrically (the volumetric uptake suffered due to low crystal density in comparison to MFM-192). The apparent discrepancy in sorption properties was ascribed to the main pore channel being too large (34 Å in diameter) for optimum host-guest interactions, thus resulting in a situation where gases in the centre of the pore are too far away to interact with the framework walls. This 'over-porosity' was also evident in the lack of saturation in any of the isotherms measured to the highest pressure possible on the equipment setup. Overall, while the slight decrease in uptake was undesirable, the synthesis of a MOF which was highly stable, and outperformed many literature MOFs (particularly for gravimetric methane uptake), was encouraging, and lead to evaluation of the cost of MOF synthesis for realistic industrial potential.

The second half of the chapter, therefore, was centred on the synthesis of a novel Zr(IV) MOF, MFM-422, from an analogous ligand (H_4L^{1P}). The expected

isoreticular framework was not obtained, presumably as a result of to the binding nature of the pyridyl groups interacting with the Zr(IV) ions as the crystal grew, resulting in an SBU with ten points of extension rather than eight. The MOF crystallised in a 'flower of life' design, with a topology different to that of MFM-421, although the porosity and dimensions of the framework were comparable and therefore also suitable for high pressure CH_4 and CO_2 storage. Analysis of the high pressure isotherms showed them to be very similar in nature to MFM-421, with only the crystal density separating the two in order of highest uptake. MFM-421 displayed the highest gravimetric uptake due to its slightly lower crystal density, while MFM-422 had higher volumetric uptake due its higher density. This was hugely successful, therefore, as a method of synthesising a highly stable framework, countering the instability of the MFM-19X series and also considerably reducing the cost of both ligand and MOF synthesis, with scale-up conditions in DMF resulting in highly crystalline samples.

Finally, the chapter ended by comparing these Zr(IV) MOFs to literature MOFs and current technology for CO_2 shipping and transport. It was evident that there would be some balance between the huge potential savings per shipment due to the removal of refrigeration costs, and the cost of one-time installation of MOF in the tank. This trade-off extended to the choice of MOF, as the volumetric requirements of the ship meant that MOFs with higher crystal densities would store more CO_2 (on average a trend seen across the MOFs in literature), and therefore reduce the cost per shipment, while those with lower crystal densities would require less MOF per tank, and therefore reduce the capital cost. Additionally, factoring in the cost of MOF synthesis resulted in HKUST-1

providing a good middle ground for higher capital cost and lower running cost, and MFM-422 providing the balance on the other side. This mirrored the results seen in methane uptake, where HKUST-1 is a benchmark for a cheap, efficient MOF for volumetric working capacity of methane, and MFM-422 provides the most robust realistic industrial potential of a MOF with high gravimetric uptake.

4.4 Experimental

4.4.1 Preparation of MFM-42X

Solvothermal Synthesis of MFM-421

A suspension of H_4L^1 (16 mg, 0.023 mmol), $ZrCl_4$ (24 mg, 0.103 mmol) and benzoic acid (600 mg, 4.91 mmol) in DEF (3 mL) was heated to 120 °C in a sealed 15 mL pressure vessel, and maintained at this temperature for 24 hours to yield small, white crystalline needles. These were washed several times with hot DMF to give $[Zr_6L^1{}_2(\mu_3{-}O)_4(\mu_3{-}OH)_4(OH)_4(OH_2)_4]$, MFM-421 (20 mg, 39% yield). Elemental analysis – Expected: C 49.49; H 3.07 Found (average): C 47.88; H 3.05;

Solvothermal Synthesis of MFM-422

A suspension of H_4L^{1P} ligand (16 mg, 0.022 mmol), $ZrCl_4$ (24 mg, 0.103 mmol) and benzoic acid (600 mg, 4.91 mmol) in diethylformamide (3 mL) was heated to 120 °C in a sealed 15 mL pressure vessel, and maintained at this temperature for 24 hours to yield small, white crystalline needles. These were washed several times with hot DMF to give $[Zr_6L^{1P}{}_{2.5}(\mu_3{-}O)_4(\mu_3{-}OH)_4(OH)_2(OH_2)_2]$, MFM-422 (25 mg, 45% yield). Elemental analysis – Expected: C 52.09; H 2.97; N 2.79 Found (average): C 50.82; H 2.81; N 2.53

4.4.2 Crystal Structure Descriptions of MFM-42X

Crystallographic Information for MFM-421

Crystal Description	
White Needles	Crystal Size: 30x10x5 μm
Crystal Data	
Formula = $C_{92}H_{68}O_{32}Zr_6$	Hexagonal, *P6/mmm*
a = 40.301(2) Å	V = 28592(3) Å^3
c = 20.327(2) Å	Mr = 2232.88
Density = 0.377 g/cm^3	Z = 3
Data Collection and Refinement	
F(000) = 3300	Rint = 0.484
$R[F2 > 2\sigma(F2)]$ = 0.098	$wR(F^2)$ = 0.338
71795 reflections; 5414 unique, 2480 with $I > 2\sigma I$	GOF = 0.989
μ = 0.16 mm^{-1}	Max/min residual electron density after PLATON SQUEEZE = 0.9/-0.7 e A^{-3}
Electrons found in solvent accessible volume: 2661	

Crystallographic Information for MFM-422

Crystal Description	
White Needles	Crystal Size: 25x10x5 μm
Crystal Data	
Formula = $C_{109}H_{72}N_5O_{32}Zr_6$	Hexagonal, *P6/mmm*
a = 54.4240(18) Å	V = 102004(7) Å^3
c = 39.7655(9) Å	Mr = 2513.16
Density = 0.487	Z = 3
Data Collection and Refinement	
F(000) = 14856	Rint = 1.978
$R[F2 > 2\sigma(F2)]$ = 0.110	$wR(F^2)$ = 0.326
1652821 reflections; 93297 unique, 5592 with $I > 2\sigma I$	GOF = 1.147
μ = 0.19 mm^{-1}	Max/min residual electron density = 0.9/-0.7 e A^{-3}

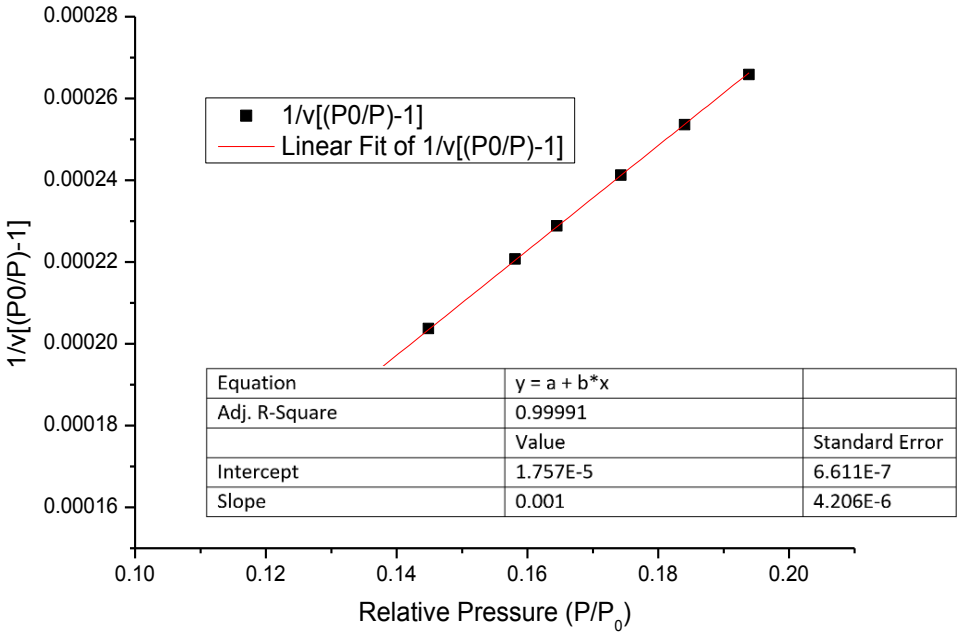
4.4.3 Gas Adsorption Measurements on MFM-19X Series

The samples were activated on a Micromeritics SmartVacPrep degasser, and subsequent BET measurements were made on a Micromeritics 3-Flex gas sorption analyser (MFM-421), or a Micromeritics Tristar (MFM-422) using ultra-high purity N_2. High pressure measurements were made on a Hiden

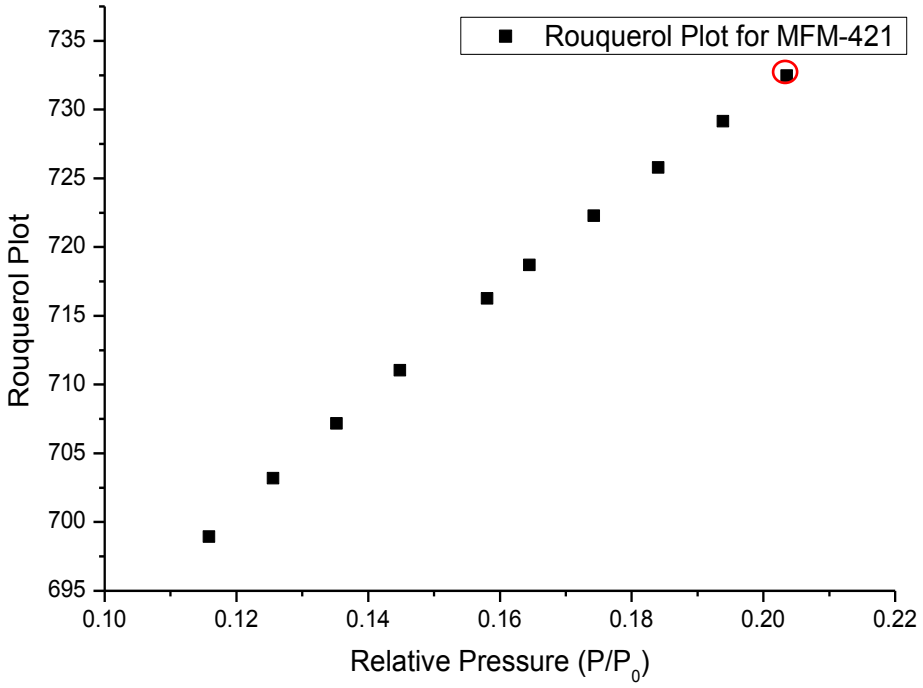
Xemis, using high purity CH_4, CO_2 and He (for buoyancy corrections). Sample skeletal density was calculated by multiple helium isotherms (0-100 bar) performed at 0, 10, 20 and 30 °C. MFM-421 was determined to have a skeletal density of 1.98 g/cm^3, and MFM-422 was calculated to have a skeletal density of 2.30 g/cm^3. Conversion of excess adsorption to total adsorption was performed by subtracting the density of the appropriate gas at appropriate temperature and pressure from the excess adsorption plot.

4.4.4 BET Surface Plots

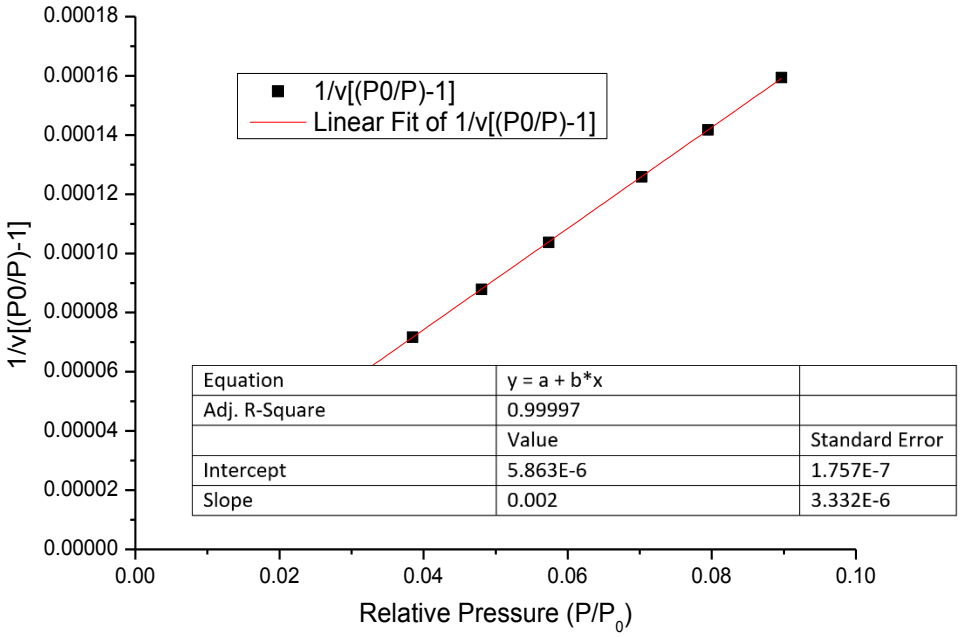
Linear section of experimental BET plot used for MFM-421



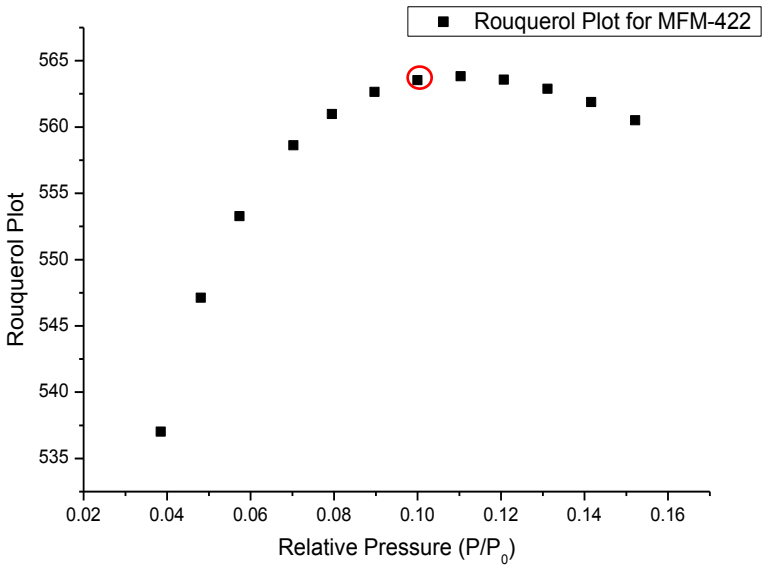
Rouqerol consistency criterion for MFM-421 (Circled value used as highest pressure)



Linear section of experimental BET plot used for MFM-422



Rouqerol consistency criterion for MFM-422 (Circled value used as highest pressure)



References

1. Zhang, S., Li, L., Zhao, S., Sun, Z. & Luo, J., *Inorg. Chem.* **2015,** *54,* 8375–8379.
2. Nelson, A. P., Farha, O. K., Mulfort, K. L. & Hupp, J. T., *J. Am. Chem. Soc.* **2009,** *131,* 458–460.
3. Hoffart, D. J. & Loeb, S. J., *Angew. Chemie Int. Ed.* **2005,** *44,* 901–904.
4. Liu, T. F. *et al.*, *J. Am. Chem. Soc.* **2015,** *137,* 413–419.
5. Batten, S. R. *et al.*, *CrystEngComm* **2001,** *3,* 67.
6. DeCoste, J. B. *et al.*, *J. Mater. Chem. A* **2013,** *1,* 5642.
7. Planas, N. *et al.*, *J. Phys. Chem. Lett.* **2014,** *5,* 3716–3723.
8. Feng, D. *et al.*, *Angew. Chemie* **2012,** *124,* 10453–10456.
9. Mondloch, J. E. *et al.*, *J. Am. Chem. Soc.* **2013,** *135,* 10294–7.
10. Spek, A. L., *Acta Crystallogr. D. Biol. Crystallogr.* **2009,** *65,* 148–55.
11. Dean, J. A. (John A. & Lange, N. A. *Lange's handbook of chemistry*. (McGraw-Hill, **1992**).
12. Van Der Sluis, P. & Spek, A. L., *Acta Crystallogr. Sect. A* **1990,** *46,*

194–201.

13. Millward, A. R. & Yaghi, O. M. *J. Am. Chem. Soc.* **2005,** *127,* 17998–9.
14. Skagestad, R. *et al.* 2th International Conference on Greenhouse Gas Control Technologies, **2014**, *63,* 2638-2644.
15. Gou, Q. *et al. Phys. Chem. Chem. Phys.* **2014,** *16,* 13041.
16. Chui, Lo, Charmant, Orpen & Williams. *Science* **1998,** *283,* 1148–50.
17. Eddaoudi, M. *et al., Science* **2002,** *295,* 469–72.
18. Chae, H. K. *et al., Nature* **2004,** *427,* 523–527.
19. Furukawa, H. *et al., Science.* **2010**, 329.
20. Chen, B., Ockwig, N. W., Millward, A. R., Contreras, D. S. & Yaghi, O. M. *Angew. Chemie Int. Ed.* **2005,** *44,* 4745–4749.
21. Gándara, F., Furukawa, H., Lee, S. & Yaghi, O. M., *J. Am. Chem. Soc.* **2014,** *136,* 5271–5274.
22. Alezi, D. *et al., J. Am. Chem. Soc.*, **2015,** *137,* 13308–13318.
23. Ma, S. *et al., J. Am. Chem. Soc.* **2008,** *130,* 1012–1016.
24. Spanopoulos, I. *et al., J. Am. Chem. Soc.* **2016,** *138,* 1568–1574.

Chapter 5

Conclusion

5.1 Conclusion

The storage of gases at high pressure inside MOFs as an alternative to standard cylinder storage is an area which is in the process of moving from an academic curiosity to a realistic industrial opportunity. This is due to their high BET surface areas, functionalities and great potential for CH_4 and CO_2 interactions. This thesis details the synthesis and characterisation of a Cu(II) series of frameworks (MFM-19X) and two Zr(IV) frameworks, MFM-421 and MFM-422.

A tetracarboxylate ligand, H_4L^1 has been synthesised *via* a versatile synthetic pathway which was then used to generate a series of ligands of increasing functionality and length, named in this thesis as the H_4L^X series. The method of ligand synthesis was evaluated in terms of efficiency and cost, and an analogous ligand, based around rapid molecular weight increase via simultaneous double pyridine cyclisation was synthesised, H_4L^{1P}. This synthetic route avoided precious metal cross-coupling reactions and shortened the steps from six down to two. Comparison of all ligands synthesised with those used in MOFs with leading high pressure sorption revealed that, while the pathway to H_4L^1 was more versatile than one used for the same and similar ligands in literature, it was still overall one of the more expensive ligands, due to its complexity and functionality. H_4L^{1P}, on the other hand, was identified amongst these ligands from top performing MOFs as being among the top three cheapest ligands to make, costing £0.51/g to make on a laboratory scale, slightly more than the ubiquitous H_3BTB and H_2BTC, which cost £0.28/g and £0.09/g, respectively. This made it an ideal candidate for high pressure storage, as scale up could lead to an affordable MOF for industrial use.

Assembly of H_4L^1 with Cu(II) paddlewheel SBUs afforded three highly porous frameworks, two of which were interpenetrated. MFM-191 and MFM-192 were doubly interpenetrated, with the relationship of the nets defined as class IIa and class Ia, respectively. The increase of acid content in the solvothermal synthesis yielded the non-interpenetrated framework MFM-193. Using these solvothermal conditions, a range of non-interpenetrated isoreticular frameworks were synthesised, resulting in the MFM-19X series. Simulated isotherms were calculated for the entire series, covering N_2 at 77 K for BET surface area calculations, and CO_2 and CH_4 at 273 K and 298 K to predict the applicability of these frameworks for high pressure storage of gases. Of this series, the two interpenetrated frameworks showed the best host-guest interactions at low pressures for CO_2 (47.31 and 37.89 cm^3/cm^3 at 1 bar for MFM-191 and MFM-192, respectively) and CH_4 (20.18 and 17.24 cm^3/cm^3 at 1 bar). This was due to the additional net which lowered porosity, but resulted in more orbital overlap between the framework and the guest molecules. The non-interpenetrated series (MFM-193 to -198) showed enhanced abilities to store gas at high pressures, with simulated isotherms predicting respectable CO_2 uptakes (between 331.24-356.38 cm^3/cm^3 throughout the series), and exceptional CH_4 working capacity, with the highest overall performing MOF (MFM-198) predicted to exceed the DoE requirements for gravimetric working capacity between 5-80 bar at 273 K (with 52 wt% compared to the target of 50 wt%), and come close to the volumetric working capacity under the same conditions (obtaining a value of 257 cm^3/cm^3 compared to the target of 264 cm^3/cm^3). This demonstrated the power of highly versatile synthetic routes to reticular frameworks, coupled with rapid computational screening to identify the most promising candidates for

high pressure gas storage. However, activation attempts on these MOFs resulted in the collapse of the framework, with BETs among the non-interpenetrated frameworks all measuring under 650 m^2/g. Indeed, even the least porous framework (and therefore the least likely to collapse), MFM-191, activated from supercritical CO_2 displaying signs of partial framework collapse, with a BET of 911 m^2/g, compared to the theoretical 2,150 m^2/g, demonstrating the clear need for a more stable framework which can be used in high pressure applications.

The use of Zr(IV), a highly oxophilic metal known to form stable SBUs, was utilised as a solution to the problem of instability inherent throughout the Cu(II) frameworks. Consequently, MFM-421 and MFM-422 were synthesised by the separate solvothermal reactions of H_4L^1 and H_4L^{1P} with Zr(IV). MFM-421 was a non-interpenetrated structure, highly porous down all axes, which consisted of 8-connected Zr(IV) SBUs, and was shown to have thermal and chemical stability surpassing that of the Cu(II) MOF series. Furthermore, activation of the sample led to a measured BET surface area of 3,300 m^2/g, indicating access to stable permanent porosity. MFM-422 was not isostructural to MFM-421, despite the analogous ligand, this was attributed to the binding nature of the pyridyl in the MOF synthesis process. Instead, it consisted of 10-connected Zr(IV) SBUs, forming a structure which was also highly porous down all axes and non-interpenetrated. It was shown to have comparable stability thermally to MFM-421, and upon activation gave a measured BET surface area of 2,500 m^2/g, thus again demonstrating the permanent porosity retained in the activation process. High pressure CO_2 and CH_4 isotherms of these two structures were measured, and compared with literature values to assess their potential. MFM-421 was found to have the fourth highest gravimetric working capacity (25.7

wt%), and MFM-422 the sixth (22.8 wt%), placing them both in the top ten MOFs for methane storage for use in vehicular transport. Additional analysis of cost implications resulted in MFM-422 providing an alternative choice to HKUST-1 when choosing the most cost effective MOF for working capacity, with HKUST-1 providing the most affordable choice for volumetric uptake, and MFM-422 for gravimetric.

High pressure CO_2 storage capabilities of these MOFs was seen as a new potential option for CO_2 shipping of waste CO_2 to off-shore destinations, allowing flexible routes for the uncertain future of CO_2 geostorage. Of the Cu(II) MOFs discussed, that with the greatest potential was MFM-194, (the tetramethyl functionalised framework), which had a maximum uptake of 15,913 mol/m^3 at 30 bar, 298 K, totalling ~70% of the quantity of liquid CO_2 in a refrigerated tank at the same pressure and 263 K (22,354 mol/m^3). This therefore provided a theoretical alternative, however the instability of the framework rendered it not feasible. As such, MFM-422 was the most appealing alternative, providing a modest uptake at 298 K, 30 bar of 9,605 mol/m^3, ~40% of a tank at 263 K, yet over 600% of a bare tank at 298 K, thus providing an alternative capable of saving the extra cost and implications of dealing with liquid CO_2.

In summary, this thesis explores the use of versatile ligand synthesis for rapid synthesis of MOF structures, in pursuit of frameworks which push the boundaries of theoretical upper limits of high pressure gas sorption. By doing so, a novel route to a green ligand suitable for sustainable MOF chemistry is shown, and its corresponding highly stable Zr(IV) MOF, which displays similar

behaviour towards CH_4 and CO_2 as HKUST-1, thus providing another, more robust, cost effective solution to gas sorption needs.

Further research into synthesising an analogous Al(III) MOF to Al-soc-MOF-1 (formed with a ligand of the same geometry as H_4L^{1P}), would be highly beneficial, as this is the current leader in gravimetric CH_4 working capacity at 298 K between 5-80 bar, yet is synthesised with a ligand that costs thousands of pounds per kilogram. Therefore, the synthesis of an analogous MOF with H_4L^{1P}, which is less than 1.2% of the cost following the route published in literature, is an incredibly valuable target.

Appendices

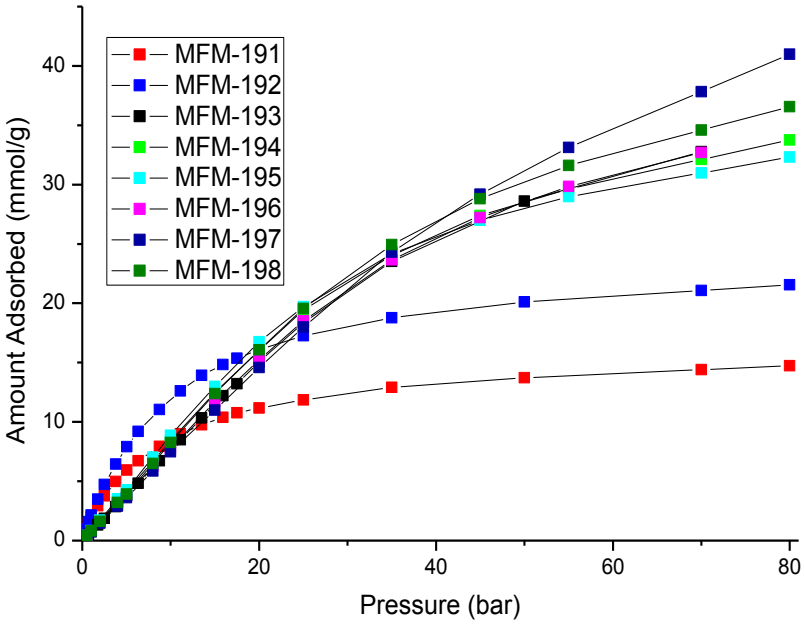


Figure A1. Gravimetric CH_4 isotherms for MFM-19X series at 273 K.

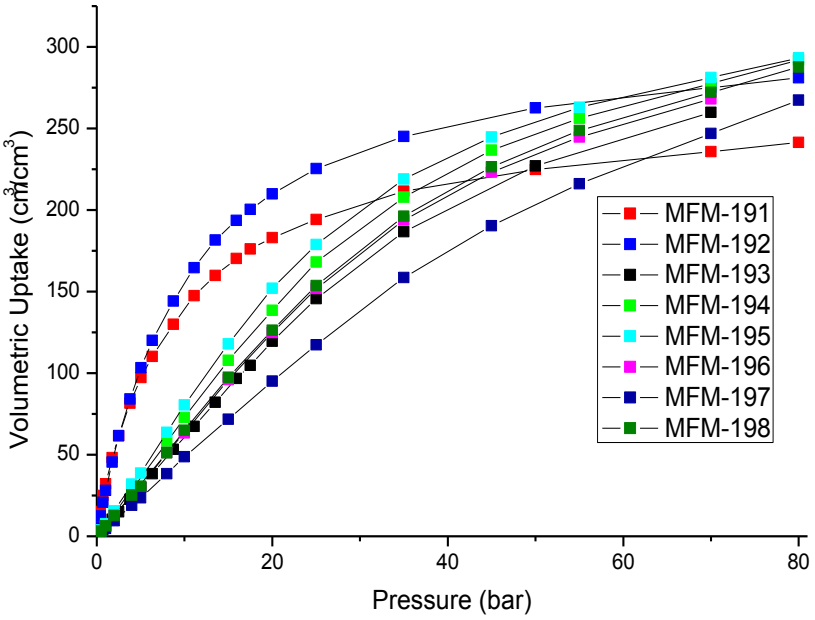


Figure A2. Volumetric CH_4 isotherms for MFM-19X series at 273 K.

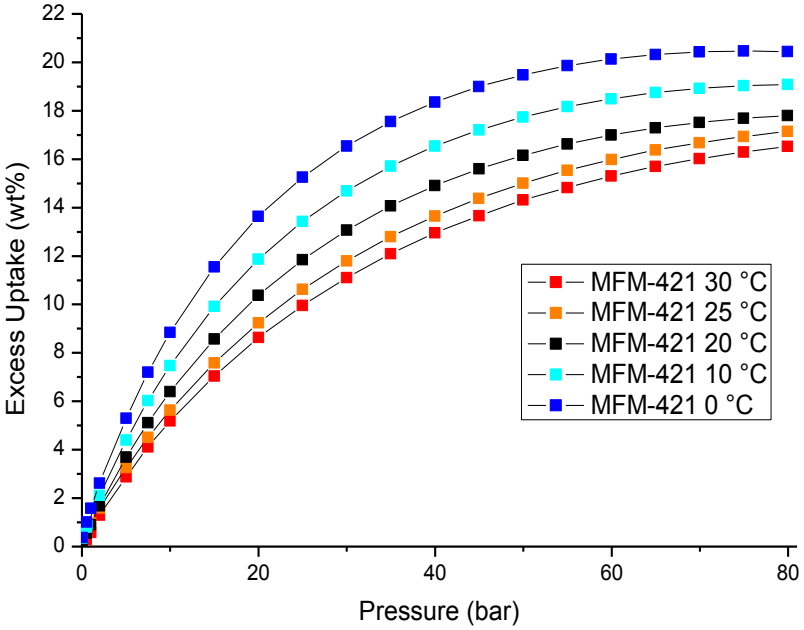


Figure A3. Excess gravimetric adsorption of CH_4 for MFM-421 at various temperatures.

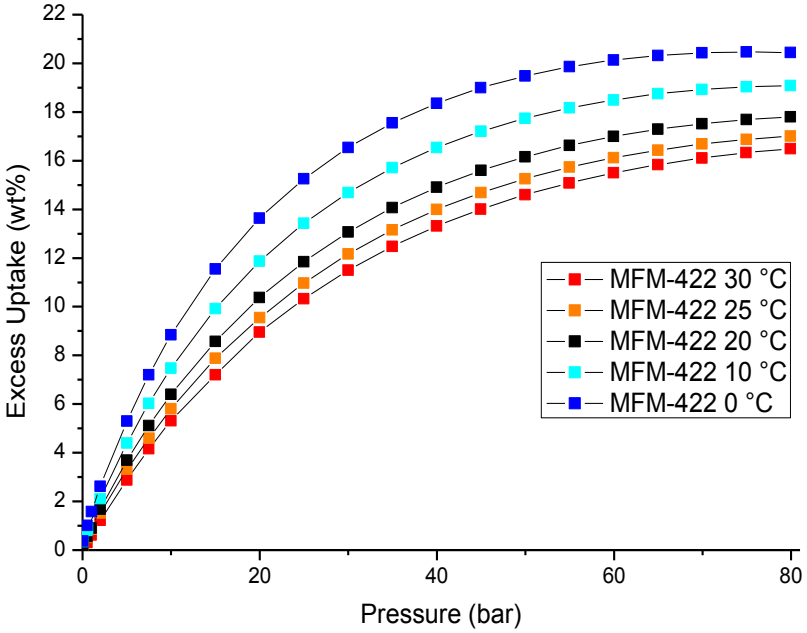


Figure A4. Excess gravimetric adsorption of CH_4 for MFM-422 at various temperatures.

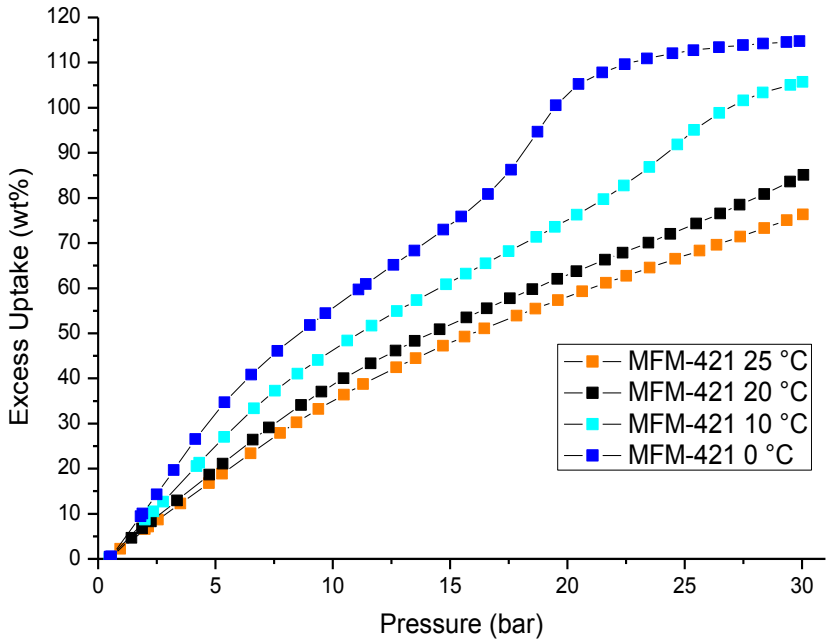


Figure A5. Excess gravimetric adsorption of CO_2 for MFM-421 at various temperatures.

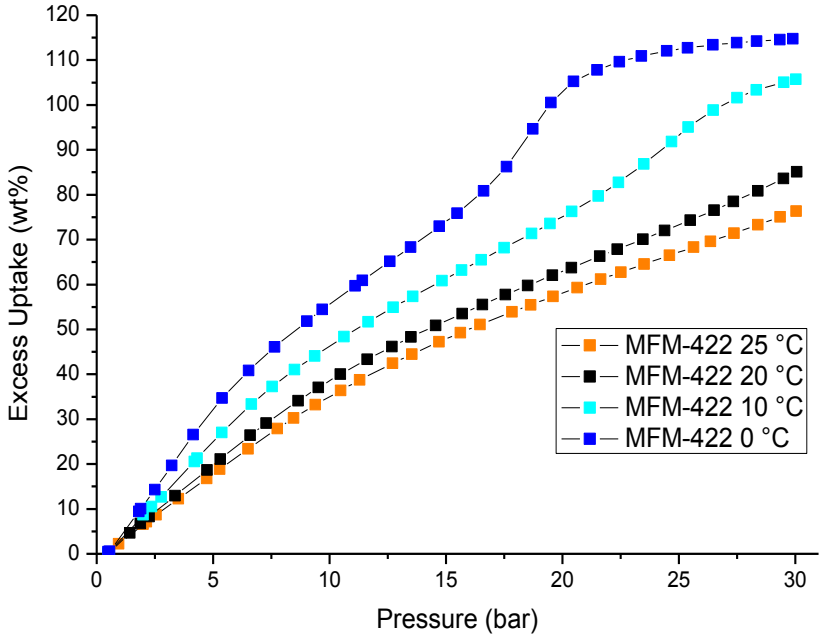


Figure A6. Excess gravimetric adsorption of CO_2 for MFM-422 at various temperatures.

Rxn No.	Metal Salt	Ligand	Amount of Metal	DMF	MeCN	DMSO	Acid Used	Amount of Acid	Molarity of Acid
1	Cu(NO3)2	10	26.18	2	0.67	0.67	HCl	0.67	0.1
2	Cu(NO3)2	10	26.18	3	1	1	HCl	1	0.1
3	Cu(NO3)2	50	130.9	15	5	5	HCl	5	0.1
4	Cu(NO3)2	50	130.9	15	5	0	HCl	5	0.1
5	CuCl2	10	15	3	1	0	HCl	1	0.05
6	Cu(NO3)2	10	26.18	3	1	1	HCl	1	0.1
7	Cu(NO3)2	10	26.18	3	1	1	HCl	1	0.05
8	Cu(NO3)2	10	26.18	3	1	0	HCl	1	0.08
9	Cu(NO3)2	10	26.18	3	1	0	HCl	1	0.05
10	Cu(NO3)2	10	26.18	3	1	0	HNO3	1	0.1
11	Cu(NO3)2	10	26.18	5	0	0	HBF4	0.1	8
12	Cu(NO3)2	10	26.18	3	0	0	HBF4	0.09	8
13	Cu(NO3)2	10	26.18	3	0	0	HBF4	0.25	8
14	Cu(NO3)2	100	265	30	0	0	HBF4	0.3	8
15	Cu(NO3)2	10	26	3	0	0	HBF4	0.09	8
16	Cu(NO3)2	10	26.18	5	0	0	HBF4	0.25	8
17	Cu(NO3)2	10	26.18	3	1	0	HCl	1	0.1
18	Cu(NO3)2	10	26.18	3	1	0	HCl	1	0.2
19	Cu(NO3)2	10	26.18	3	1	0	HCl	0.1	1
20	Cu(NO3)2	15	26.18	3	1	1	HCl	1	0.1
21	Cu(NO3)2	10	26.18	3	1	1	HCl	1	0.05
22	Cu(NO3)2	10	26.18	3	1	0	HCl	1	0.05
23	Cu(NO3)2	12	26.18	3	0	0	HCl	1	0.1
24	Cu(NO3)2	10	26	3	1	1	HCl	1	0.1
25	Cu(NO3)2	10	26	3	1	1	HCl	0.5	0.1
26	Cu(NO3)2	10	26	3	1	0	HCl	0.1	1
27	Cu(NO3)2	20	26	3	1	0	HCl	1	0.05
28	Cu(NO3)2	20	26	3	0	0	HCl	1	0.05
29	Cu(NO3)2	10	15	2	1	0	HCl	1	0.01
30	Cu(NO3)2	10	15	2	1	0	None	1	0
31	Cu(NO3)2	10	26	3	0	0	HCl	0.09	8
32	Cu(NO3)2	10	26	3	0	0	HCl	0.15	8
33	Cu(NO3)2	10	26	3	1	1	HCl	1	0.05
34	Cu(NO3)2	10	26	3	1	1	HCl	1	0.01
35	Cu(NO3)2	10	26	3	0	0	HCl	0.09	8
36	Cu(NO3)2	10	26	3	1	0	HCl	0.09	8
37	Cu(NO3)2	10	26	3	0	1	HCl	0.5	0.1
38	Cu(NO3)2	10	26	3	1	1	HCl	0.5	0.1
39	Cu(NO3)2	10	26.18	3	1	0	HCl	1	0.1
40	Cu(NO3)2	10	26.18	3	1	0	HCl	1	0.03
41	Cu(NO3)2	10	26.18	3	0	0	HBF4	0.18	8
42	Cu(NO3)2	10	26	3	0	0	HNO3	0.09	6